Re-Road *End of life strategies of asphalt pavements*

Performance Modelling of Reclaimed Asphalt – Final Report

Sabine Werkmeister et al.

SEVENTH FRAMEWORK PROGRAMME

The research leading to these results has received funding from the European Community's Seventh Framework Programme (FP7/2007–2013) under grant agreement n° 218747.

Re-road – End of life strategies of asphalt pavements

Deliverable 5.5
Performance Modelling of RA – Final Report

EUROPEAN COMMISSION
DG RESEARCH

A FP7 Collaborative Project
Work programme:
Sustainable Surface Transport
SST.2007.1.2.2 End of life strategies
for vehicles/vessels and infrastructures

SEVENTH FRAMEWORK PROGRAMME

TECHNISCHE UNIVERSITÄT DRESDEN

Sabine Werkmeister
Sabine.Werkmeister@tu-dresden.de

Markus Oeser
oeser@isac.rwth-aachen.de

Gustavo Canon Falla
Gustavo_Adolfo.Canon_Falla@tu-dresden.de

Anita Blasl
Anita.Blasl@tu-dresden.de

The University of Nottingham

Davide Lo Presti, Andrew Collop, Gordon Airey
Davide.Lopresti@nottingham.ac.uk

TU Delft Delft University of Technology

Mirella Villani, Cor Kasbergen, Tom Scarpas
m.m.villani@tudelft.nl

artesis

Wim van den Bergh
wim.vandenbergh@artesis.be

UCD DUBLIN

Ciaran McNally
ciaran.mcnally@ucd.ie

Eanna Fallon
eanna.fallon@ucdconnect.ie

Executive summary

A deeper insight into the mechanics of asphalts composed of recycled and new components were to be researched in the framework of work package 5 (WP5) „performance and modelling“ of the “Re-Road” project sponsored by the European Union. For this reason a comprehensive material test program was conducted to investigate and understand the elastic, visco-plastic and visco-elastic deformation as well as the fatigue performance of asphalt mixes containing RA and to determine the input parameters required for numerical simulations.

The objective of WP5 was to evaluate the performance of two asphalt mixtures with RA in comparison to a virgin asphalt mixture. A prerequisite was to design and select representative RA mixes with nearly identical grading and clearly different amounts of aged and unaged binders (chapter 2). It was decided to work with Stone Mastic Asphalt (SMA). As reference material (Material I) SMA 11 S was chosen. For Material II and III reclaimed asphalt replacement levels of 20 M.-% and 40 M.-% were envisaged but had to be reduced to 15 M.-% and 30 M.-% due to problems during material production. The chosen reclaimed asphalt was open porous asphalt (PA) and provided by WP2. Virgin binder for all asphalt materials was PmB 25/55-55A. Aggregates of all materials came from the same source. A total of 20 ton asphalt were produced and tested in WP5.

The results obtained from the material test program form the basis for models describing the constitutive characteristics of asphalt materials.

In this report the major outcomes from the research within WP5 are presented.

The comprehensive material characterisation was conducted by all partners involved in WP5. Each partner conducted different laboratory tests on bituminous binders and asphalt mixtures and selected the most qualified sampling for his laboratory tests. The mechanical properties and the performance characteristics of three asphalt mixes and different binders were determined within the research by using appropriate testing methodologies (chapter 4). In section 4.1 the different sample preparations are shortly described for each conducted performance test on asphalt mixtures. The sample preparation of the binder samples is included in section 4.2.

The results of the laboratory performance tests as well as the determination of input parameters required for numerical simulations and the pavement design life calculation are summarised and discussed in chapter 5. For the pavement design life calculation and numerical simulations input parameters like fatigue curves, master curves and Cole-Cole Plots for the asphalt mixtures are required for TUD model, while constant strain-rate tests and Creep & Recovery curves are required for UNOTT model.

Model development and pavement design life calculation had to be done independent from each other by the partners TU Dresden and University of Nottingham in cooperation with TU Delft. Two different viso-elastic models, both using different input parameters, have been developed. Chapter 6 and chapter 7 contain the description and calibration of the developed models.

The model validation is following depicted in chapter 8. In this chapter the results of wheel tracker tests conducted at UC Dublin and TU Dresden are explained.

The results of the wheel tracking tests carried out at UC Dublin showed that the use of increased levels of RA in the asphalt mixtures resulted in increased resistance to permanent deformation. Based on the average reported vales, it can be see that the use of 15 % RA resulted in a 53 % reduction in permanent deformation and the use of 30 % RA resulted in a 72 % decrease.

The results of the Hamburg Wheel Tracking Tests (HWTT) carried out at TU Dresden demonstrate that the level of permanent deformation observed for all three materials was relatively low. In addition, it could be established that the use of increased levels of RA in the asphalt mixtures resulted in increased resistance to permanent deformation. A relatively high plastic deformation was observed during the post compaction period.

The results of the HWTT were used to validate the plastic model developed at TU Dresden. The results of the simulation show the lowest plastic deformation in terms of a calculated rut depth for Material III followed by Material II. Material I exhibits the highest plastic deformation using the strain approach. This agrees with the results from the HWWT and the theory that postulated that the existence of RA in the mix improves the resistance against rutting of the mix. Additional investigation suggests that a stress approach provides a better fit with the experimental data compared to the elastic strain approach. The results of the simulation show the lowest plastic deformation in terms of a calculated rut depth for Material I followed by Material II and III. However, further experimental data is needed to improve and fine tune the model in order to confirm the validity of the plastic model.

Based on the wheel tracker test results, the models developed at TU Dresden and University of Nottingham in cooperation with TU Delft are validated.

The outcomes of the pavement design life calculation of asphalt pavement containing reclaimed asphalt are presented in chapter 9.

A description of a numerical tool developed for the pavement design life calculation follows in chapter 10.The numerical tool developed at TU Dresden will be capable of predicting plastic deformations (rut depth) in asphalt layers.

Table of contents

1 Introduction 26
1.1 Aim of the Research 26
1.2 Background 27
1.3 Organisation of WP5 28

2 Materials tested 29
2.1 Material Selection 29
2.1.1 Preliminary Analysis 29
2.2 Asphalt Production 30
2.3 Mixes Properties 31

3 Characterisation of Bituminous Mixtures 33
3.1 Complex Modulus 33
3.1.1 Complex Modulus Representation 34
3.2 Permanent Deformation 36
3.3 Fatigue 37

4 Laboratory Performance Tests 38
4.1 Laboratory Performance Tests on bituminous Asphalt Mixes 38
4.1.1 Repeated Load Triaxial Tests at Technical University Dresden 38
4.1.1.1 Asphalt Sample Preparation 42
4.1.1.2 Cyclic Compression Tests 42
4.1.1.3 Permanent Deformation Tests 45
4.1.2 Experimental Programme at University of Nottingham 47
4.1.2.1 Experimental Settings 47
4.1.2.2 Specimen Manufacture - Compression Tests 47
4.1.2.3 Specimen Manufacture - Tension Tests 55
4.1.2.4 Specimen Manufacture - Compression Tests 55
4.1.2.5 Specimen Manufacture - Tension tests 56
4.1.3 Indirect Tensile Tests at Technical University Dresden 57
4.1.3.1 Asphalt Sample Preparation 58
4.1.4 Indirect Tensile Tests at University College Dublin 58
4.1.4.1 Compaction 58
4.1.4.2 Coring 60
4.1.4.3 Specimen Preparation 60
4.1.4.4 Specimen Testing 61
4.2 Laboratory Performance Tests on bituminous Binders 63
4.2.1 Bitumen Tests at Technical University Dresden 63
4.2.2 Fatigue and Healing at University College Antwerp 63
4.2.3 Materials and Description of Equipment 64
4.2.3.1 Asphalt Mixtures 64
4.2.3.2 Manufacture of the composed binder: Binder II + RA 65
4.2.4 Definition and Composition of Mastic 65
4.2.5 Test Equipment 68

4.2.5.1 Dynamic Shear Rheometer 68
4.2.5.2 InfraRed Spectrofotometer 70
4.2.5.3 Selection of Ageing Indicator 71
4.2.6 Experimental Program 72
4.2.6.1 Binder Extraction and Recovery 72
4.2.6.2 Binder Ageing 72
4.2.6.3 Linear Visco-elastic Region and Master Curves 72
4.2.7 Fatigue and Healing Criteria for Binders and Mastic 73
4.2.8 Preliminary Fatigue and Healing Tests 74
4.2.9 Binder Testing 76
4.2.10 Mastic Testing 77

5 Results of Laboratory Performance Tests 78
5.1 Laboratory Performance Tests on bituminous Asphalt Mixes..... 78
5.1.1 Repeated Load Triaxial Tests at Technical University Dresden 78
5.1.1.1 Cyclic Compression Tests 78
5.1.1.2 Permanent Deformation Tests 91
5.1.2 Tension and Compression Tests at University of Nottingham 98
5.1.2.1 Constant strain tests at UNOTT 98
5.1.2.2 Creep & Recovery Tests 99
5.1.3 Indirect tensile tests 101
5.1.3.1 Comparison of the E-Modulus values 101
5.1.3.2 Fatigue Tests at Technical University Dresden 102
5.1.3.3 Fatigue Tests at University College Dublin 103
5.1.3.4 Healing Tests at University College Dublin 104
5.2 Laboratory Performance Tests on bituminous Binders..... 105
5.2.1 Binder Characterization at University of Nottingham 105
5.2.2 Binder Characterization at Technical University Dresden 108
5.2.3 Binder Characterization at University College Antwerp 110
5.2.3.1 Master Curves of Binders 110
5.2.3.2 Binder Fatigue tests 110
5.2.3.3 Binder Healing Tests 111
5.2.3.4 Mastic Fatigue and Healing Tests 114
5.2.3.5 Infrared Measurements 116
5.2.3.6 Conclusion 117

6 Model Development at TU Dresden..... 119
6.1 Introduction..... 119
6.2 Visco-elastic Model..... 119
6.2.1 Conventional and Fractional Rheological Models 120
6.2.1.1 Model Characteristics 121
6.2.2 Theoretical characterisation 124
6.2.3 Experiments 127
6.2.3.1 Experimental Set-Up 127
6.2.3.2 Results 130

6.2.4 Modeling 132
6.2.4.1 Cyclic Behavior 132
6.2.4.2 Base model 132
6.2.4.3 The Influence of Aged Material Components 142
6.2.4.4 Determination of model parameters 142
6.2.4.5 Conclusion 145
6.3 Plastic Model 146

7 Model Development at University of Nottingham 149
7.1 Dissipation energy based 3D constitutive model 149
7.1.1 Theoretical background 149
7.1.1.1 Multiplicative decomposition 150
7.1.1.2 Hyper-elasticity 151
7.1.2 The proposed model: Elasto-visco-Perzyna formulation 151
7.1.2.1 Local dissipation 152
7.2 Mechanistic procedure for parameter determination 155
7.2.1 Parameters determination - Hyper-elastic spring 156
7.2.2 Parameters determination - spring of Maxwell component 158
7.2.3 Parameters determination - dashpot of Maxwell component 161
7.2.4 Parameters determination - Perzyna component 162
7.3 Model Calibration..... 163
7.3.1 Failure stress levels 163
7.3.2 Creep & Recovery tests 164
7.3.3 Calibration procedures 166
7.3.3.1 Input parameters calculation 168

8 Model Validation 171
8.1 Circular Wheel Tracking Tests at UC Dublin 171
8.1.1 Light Detection and Ranging (LiDAR) 173
8.1.1.1 LiDAR evaluation 173
8.1.2 Test Methodology 174
8.1.2.1 Specimen manufacture 174
8.1.2.2 Test set-up 174
8.1.2.3 Test procedure 175
8.1.3 LiDAR Data Analysis 178
8.1.4 Measurement of Permanent Deformation 182
8.1.4.1 Using LiDAR scanning 182
8.1.4.2 Using manual measurement 182
8.2 Hamburg Wheel Tracking Tests at TU Dresden..... 184
8.2.1 Test Parameter 184
8.2.2 HWTT results 185
8.3 Model Validation at TU Dresden..... 187
8.3.1 Numerical Calculation of the Rut Depth 187
8.3.3 Input values for the FE calculation 188
8.3.4 Results of the FE calculation 189

8.4 Model Validation at University of Nottingham 193

9 Pavement Design Life Calculations conducted at TU Dresden 200
9.1 Input Values for the Calculation 201
9.2 Analysis of the Calculation Results 203

10 Numerical Tool developed at TU Dresden 205
10.1 Numerical tool to determine the Elastic Model Parameters 205
10.2 FE Code used 208
10.3 Numerical Tool to predict Plastic Deformations 209

11 Conclusions 211

12 Suggestions for implementation 212
12.1 Research needs identified 212
12.2 Implementations of the research 213

13 References 214

14 Acknowledgements 219

15 Appendix 220

Tables

Table 1-1 Partners involved in WP5 28
Table 2-1 Binder content of the asphalt mixes investigated 31
Table 4-1 Dynamic RLTTs – Test Conditions 40
Table 4-2 Specimen properties from procedures A and B 50
Table 4-3 Details density and air voids for optimisation 53
Table 4-4 Repeatability study: gyratory compaction results of 150 x 150 specimens 53
Table 4-5 cyclic ITTs – Test Conditions 58
Table 4-6 Parameters for fatigue and healing test programme 62
Table 4-7 Properties of the binders investigated 63
Table 4-8 DSR Test Parameter 63
Table 4-9 List of materials used for binder tests 64
Table 4-10 Rheological Data Binder Material I after extraction and recovering (source: TU Dresden) 64
Table 4-11 Rheological Data Binder Material III after extraction and recovering (source: TU Dresden) 65
Table 4-12 Binder mixture composition for Binder II + RA 65
Table 4-13 Summary aggregate coating Material I 66
Table 4-14 Summary aggregate coating Material III 67
Table 4-15 Mastic design values 68
Table 4-16 Summary of the specifications of RTFOT, PAV and RCAT ageing tests 69
Table 4-17 Selected binders for Infrared Measurements 70
Table 4-18 Test settings for frequency sweeps 73
Table 4-19 Healing test types 74
Table 4-20 Output data Healing Test before correction (part: Constant Stress Loading) 75
Table 4-21 Output data Healing Test after correction (part: Constant Stress Loading) 75
Table 4-22 Summary binder fatigue and healing test scheme [I] 76
Table 4-23 Summary binder fatigue and healing test scheme [II] 76
Table 4-24 Summary binder fatigue and healing test scheme 77

Table 5-1 Realized repeated load triaxial tests 78

Table 5-2 Parameter of the surface function of ε_1 (stress dependent approach) 81

Table 5-3 Parameter of the surface function of ε_1 (stress independent approach) 82

Table 5-4 Absolute modulus $|E_1|$ in dependency of σ_{23} for stress dependent approach 83

Table 5-5 Absolute modulus $|E_1|$ for stress independent approach 85

Table 5-6 Parameters of the regression function of $|E_1|$ in dependency of σ_{23} 86

Table 5-7 Parameters of the regression functions of the master curves for Material I, II and III 87

Table 5-8 Parameters of the plots of phase lag vs. absolute modulus for Material I, II and III 89

Table 5-9 Realized long-term multistage triaxial tests 92

Table 5-10 Input and output of Constant Strain rate tests at 25°C 99

Table 5-11 Input and output of Creep and Recovery test at 25°C 101

Table 5-12 Empirical properties of the recovered binders 105

Table 5-13 Viscosity measurements of the recovered binders 105

Table 5-14 Test settings of the Dynamic mechanical Analysis 105

Table 6-1 Exponents and coefficients of the base model 133

Table 6-2 Parameters of the “2S3P”-element 144

Table 6-3 Parameter of plastic model for the materials tested 148

Table 7-1 Material I: calibration procedure 167

Table 7-2 Material II: calibration procedure 167

Table 7-3 Material III: calibration procedure 168

Table 7-4 Model’s Input parameters of Material I 169

Table 7-5 Model’s Input parameters of Material II 169

Table 7-6 Model’s Input parameters of Material III 170

Table 8-1 Scanning schedule for LiDAR measurements 176

Table 8-2 Average permanent deformation calculated using LiDAR 182

Table 8-3 Average permanent deformations using manual measurements 182

Table 8-4 HWTT parameter 184

Table 8-5 Material parameter for the FE model 188

Figures

Figure 2-1 Materials composition diagram 29

Figure 2-2 Grading curves of the asphalt mixes investigated: material I – virgin mixture (0% RA); material II (15% RA); material III (30% RA) 31

Figure 3-1 Phase lag 33

Figure 3-2 Absolute modulus in complex plane 34

Figure 3-3 theoretic Cole-Cole-Plot with storage and loss modulus (Oeser, 2009) 34

Figure 3-4 Master curve (Oeser, 2009)..... 35

Figure 3-5 Theoretic figure of the deformation curve obtained from a permanent deformation test..... 36

Figure 3-6 Theoretic figure of a fatigue curve obtained from a fatigue test.... 37

Figure 4-1 Schematic illustration of the triaxial apparatus (Grohs, 2005) 40

Figure 4-2 Preparation of hot rolled asphalt test samples (Zeißler, 2012) 42

Figure 4-3 Typical output of a multistage repeated load tri-axial test..... 46

Figure 4-4 transformation of a multistage test into a single stage test 46

Figure 4-5 X-ray CT equipment (a) Configuration of scanned specimen in stack (b) X-ray Image of HRA..... 48

Figure 4-6 Specimen A: Air voids distribution for (a) Material I (0%RA) (b) Material III (30%RA) 51

Figure 4-7 Cores & rings analyses of compacted Material III specimen (30% RA) 51

Figure 4-8 Schematic showing the specimen manufacturing process to get the homogeneous distribution of air voids from the 150 mm diameter, 150 mm height gyratory compacted specimen 52

Figure 4-9 Relationships of the target air voids content for 100/100 specimen and the density to be set during compaction for 150/150 specimen 54

Figure 4-10 Air voids distribution within the cored section of 100/100 after optimisation for Material I (0% RA) and Material III (30% RA) with the air voids content, 2.6%..... 54

Figure 4-11 RCAT device at RERS-Antwerp (external and internal view) 69

Figure 4-12 RCAT device at RERS-Antwerp (internal view right)..... 70

Figure 4-13 Definition of fatigue life 73

Figure 5-1 Stress path and level of stresses for the realized repeated load triaxial tests..... 78

Figure 5-2 Realized repeated load triaxial tests 79

Figure 5-3 ε_1 vs. σ_1 for f=1 Hz and T=25 °C for a constant amplitude of σ_{23} .. 80

Figure 5-4 ε_1 vs. σ_{23} for f=1 Hz and T=25 °C for a constant amplitude of σ_1 .. 80

Figure 5-5 Surface plot of axial strain as a function of axial stress and horizontal stress for f=1 Hz and T=25°C 81

Figure 5-6 Surface plot of axial strain as a function of axial stress and horizontal stress for f=1 Hz and T=25°C 82

Figure 5-7 $|E_1|$ as a function of frequency and horizontal stress for T=25°C for stress dependent approach 84

Figure 5-8 $|E_1|$ as a function of frequency and horizontal stress for T=-10°C for stress dependent approach 84

Figure 5-9 $|E_1|$ as a function of frequency for stress independent approach .. 85

Figure 5-10 Master curves of $|E_1|$ for T_R=20 °C and six different σ_{23} 86

Figure 5-11 Master curve of the absolute modulus $|E_1|$ for T_R=20°C for Material I 87

Figure 5-12 Shift factor α_T as a function of temperature 87

Figure 5-13 Master curves of the absolute modulus $|E_1|$ for T_R=20°C for Material I, II and III 88

Figure 5-14 absolute modulus $|E_1|$ as a function of temperature for f=1 Hz ... 88

Figure 5-15 phase lag vs. absolute modulus for Material I 89

Figure 5-16 phase lag vs. absolute modulus for Material I, II and III 90

Figure 5-17 Cole-Cole Plots for Material I 91

Figure 5-18 Cole-Cole Plots for Material I, II and III 91

Figure 5-19 realized staged repeated load triaxial test (permanent deformation) 92

Figure 5-20 results of realized staged repeated load tri-axial tests (permanent deformation, 10000 LC) 93

Figure 5-21 extrapolated plastic strains of a multistage test of Material II at 25 °C and σ_{23} =0.13 N/mm^2 94

Figure 5-22 Long term triaxial test: 1000 cycles regression and measured ε_1 94

Figure 5-23 Long term triaxial test: 1000 cycle regression error 95

Figure 5-24 variation of permanent strain with number of load cycles 95

Figure 5-25 Correlation between permanent strain rate and resilient strain .. 96

Figure 5-26 Correlation between permanent strain rate and stress invariants 97

Figure 5-27 Compression CSR tests at 0.0005 s-1 (60 micr/sec): typical Loading curve (left), and Strain-Stress plots (right)..... 98

Figure 5-28 Overall results of the CSR tests 99

Figure 5-29 Typical loading curve of a Creep & recovery tests in compression 100

Figure 5-30 Absolute modulus values at 20 °C and 1 Hz frequency determined using the results of ITT and Triaxial tests 102

Figure 5-31 Fatigue relations obtained for the asphalt mixes 102

Figure 5-32 Influence of RA content on fatigue life at a vertical stress of 2.5 MPa 103

Figure 5-33 Black diagram of the recovered binders 106

Figure 5-34 Complex modulus master curve at 25ºC of the recovered binders 107

Figure 5-35 Phase angle master curve at 25 ºC of the recovered binders .. 107

Figure 5-36 Complex shear modulus versus temperature for the bitumen investigated 108

Figure 5-37 Relative change of the G* due to aging process 109

Figure 5-38 Phase angle versus temperature for the bitumen investigated . 109

Figure 5-39 Master curves for G* and phase for Binder I series..... 110

Figure 5-40 Fatigue curves of binders 111

Figure 5-41 Fatigue and healing curve for binder I (tests at 10°C and 10 Hz) 112

Figure 5-42 Fatigue and healing curve for binder II+RA (tests at 10 °C and 10 Hz) 112

Figure 5-43 Fatigue and Healing curve of long term aged binders 113

Figure 5-44 First cycles of healing test of binder II+RA 114

Figure 5-45 Mastic Fatigue and Healing results 115

Figure 5-46 Infrared graphs of virgin and aged binders 116

Figure 5-47 Infrared graphs of virgin and aged binders (2000 – 500 cm^{-1}).. 116

Figure 6-1 Standard and Generalized Elements..... 121

Figure 6-2 Fractional viscoelastic analogical models used for bituminous materials 122

Figure 6-3 Cole-Cole plot 123
Figure 6-4 Black diagram 124
Figure 6-5 Aging 125
Figure 6-6 Creep-curves 126
Figure 6-7 Visco-analyzer 128
Figure 6-8 Cole-Cole plot, virgin binder 130
Figure 6-9 Cole-Cole plot, aged binder 131
Figure 6-10 Cole-Cole plot, mixed binder, 50-50 131
Figure 6-11 Base model (“3S6P”-element) 134
Figure 6-12 Coefficients and exponents of various fractional rheological elements 135
Figure 6-13 Cole-Cole-curves 137
Figure 6-14 Model (“2S3P”-element) 138
Figure 6-15 Cole-Cole plot, virgin and aged binder 142
Figure 6-16 Cole-Cole Plots and Master Curves for Material I, II and III (Model fit) 143
Figure 6-17 Determination of the plastic strain rate 147
Figure 6-18 Correlation between permanent strain rate and resilient strain 147
Figure 6-19 Correlation between permanent strain rate and stresses 148
Figure 7-1 Multiplicative decomposition of the deformation gradient 150
Figure 7-2 Schematic of (a) the Elasto-visco-Perzyna constitutive model, (b) Multiplicative decomposition 151
Figure 7-3 Schematic of (a) the developed constitutive model, (b) test specimen and principal stretch directions 155
Figure 7-4 Schematic of the contribution of the Hyperelastic spring on the rheological behaviour of asphaltic material under Creep & Recovery tests . 157
Figure 7-5 Schematic of the contribution of the Maxwell spring on the rheological behaviour of asphaltic material under Creep & Recovery tests . 158
Figure 7-6 Schematic of the contribution of the Maxwell dashpot on the rheological behaviour of asphaltic material under Creep & Recovery tests . 161
Figure 7-7 Schematic of the contribution of the Perzyna component on the rheological behaviour of asphaltic material under Creep & Recovery tests . 162
Figure 7-8 Failure stresses in compression CSR tests 163

Figure 7-9 Material I: Plot of the vertical strain of the Creep & Recovery tests in compression 164

Figure 7-10 Material II: Plot of the vertical strain of the Creep & Recovery tests in compression 165

Figure 7-11 Material III: Plot of the vertical strain of the Creep & Recovery tests in compression 165

Figure 7-12 Calibration procedures: instants to be identified 166

Figure 8-1 UCD circular wheel tracker - original layout 171

Figure 8-2 Slab specimen coordinate system 178

Figure 8-3 LiDAR scans for the Material I after (a) 0 wheel passes (b) 20,000 wheel passes, (c) 90,000 wheel passes and (d) 150,000 wheel passes 179

Figure 8-4 LiDAR scans for the Material II after (a) 0 wheel passes (b) 20,000 wheel passes, (c) 90,000 wheel passes and (d) 150,000 wheel passes 180

Figure 8-5 LiDAR scans for the Material III after (a) 0 wheel passes (b) 20,000 wheel passes, (c) 90,000 wheel passes and (d) 150,000 wheel passes 181

Figure 8-6 HWTT results for Material I, Material II and Material III 185

Figure 8-7 FE mesh of the HWTT - Quarter of the total system in its initial configuration 187

Figure 8-8 FE mesh of the sample - geometry and loaded area 188

Figure 8-9 FE deformed configurations (a) hydrostatic stresses (b) deviatoric stresses 189

Figure 8-10 Hydrostatic stresses in the loading axis 190

Figure 8-11 Deviatoric stresses in the loading axis 190

Figure 8-12 Vertical strains in the loading axis 191

Figure 8-13 Results obtained from the model (Equation (6-50)) and the HWTT at 40°C - calculated and measured 192

Figure 8-14 Results obtained from the model (Equation (6-50)) and the HWTT at 40°C - calculated and measured 192

Figure 8-15 Material I – 5% PS: Experimental curve vs model output 193

Figure 8-16 Material I – 10% PS: Experimental curve vs model output 194

Figure 8-17 Material I – 15% PS: Experimental curve vs model output 194

Figure 8-18 Material II – 5% PS: Experimental curve vs model output 195

Figure 8-19 Material II – 10% PS: Experimental curve vs model output 195

Figure 8-20 Material II – 15% PS: Experimental curve vs model output 196

Figure 8-21 Material II – 20% PS: Experimental curve vs model output 196
Figure 8-22 Material III – 5% PS: Experimental curve vs model output 197
Figure 8-23 Material III – 10% PS: Experimental curve vs model output 197
Figure 8-24 Material III – 13% PS: Experimental curve vs model output 198
Figure 8-25 Material III – 17% PS: Experimental curve vs model output 198
Figure 9-1 Fatigue relations obtained for the asphalt mixes 200
Figure 9-2 Pavement structure investigated (surface layer: 20 cm) 201
Figure 9-3 Relative frequency distribution of the axle load classes 202
Figure 9-4 Representative frequency distribution of the asphalt surface temperatures – temperature zone 3 according to RDO Asphalt 202
Figure 9-5 Fatigue status for the pavements investigated (20 cm asphalt surface layer) 203
Figure 9-6 Maximum number of axle load repetitions for the pavements investigated (20 cm asphalt surface layer) 203
Figure 9-7 Fatigue status for the pavements investigated (10 cm asphalt surface layer) 204
Figure 9-8 Maximum number of axle load repetitions for the pavements investigated (10 cm asphalt surface layer) 204
Figure 10-1 Screenshot of the cover page 206
Figure 10-2 Screenshot of the data regression procedure 207
Figure 10-3 Screenshot of the Cole-Cole plots 207
Figure 10-4 Screenshot of the master curve plots 208
Figure 10-5 Screenshot of the determination of the plastic model parameter 209
Figure 10-6 Screenshot of the prediction of the plastic deformation - rutting in dependence on the number of load cycles 210
Figure 12-1 Volumetric composition of binders before and after aging 212

Pictures

Picture 2-1 Filling and stocking of buckets with asphalt material 30

Picture 2-2 Cross section of asphalt mixes: (a) Material I, (b) Material II, (c) Material III 32

Picture 4-1 Repeated load triaxial test maschine with a triaxial pressure cell at TU Dresden 39

Picture 4-2 Triaxial pressure cell and specimens covered by a rubber membrane 39

Picture 4-3 Position of the internal contact-less system for the measurement of the axial deformations (Grohs, 2005) 41

Picture 4-4 Position of the external LVDTs for the measurement of the radial or horizontal deformations (Grohs, 2005) 41

Picture 4-5 Stresses in a triaxial test 41

Picture 4-6 X-ray CT equipment 48

Picture 4-7 Mould and Volumetric of dog-bone specimens 55

Picture 4-8 Specimen installation for Compression tests (left) and Tension tests (right) 56

Picture 4-9 ITT testing device at TU Dresden 57

Picture 4-10 Heated material in steel mould 59

Picture 4-11 Samples placed in roller compactor (sheets of paper used to prevent material sticking to roller) 59

Picture 4-12 (a) Compacted specimen slab (b) Compacted specimen slab with steel mould removed 59

Picture 4-13 Coring of cylinders from specimen slab 60

Picture 4-14 (a) Cylinders cored from specimen slab (b) slicing of cylinders . 60

Picture 4-15 Specimen marked and with fixtures bonded to it 61

Picture 4-16 Cooper Technology Servo-Pneumatic Universal Testing Machine NU-10 testing apparatus in temperature controlled cabinet 61

Picture 4-17 MCR300 Dynamic Shear Rheometer 68

Picture 8-1 UCD circular wheel tracker - redesigned track 171

Picture 8-2 Specimen Holder – diagram 172

Picture 8-3 Specimen Holder - in use 172

Picture 8-4 LiDAR unit positioned above the test surfaces 173

Picture 8-5 Specimen secured in testing station 175

Picture 8-6 Wheel loaded by steel plates..... 175

Picture 8-7 Material I (a) before testing and (b) after 150,000 wheel passes; Material II (c) before testing and (d) after 150,000 wheel passes; Material III (e) before testing and (f) after 150,000 wheel passes..... 177

Picture 8-8 Hamburg Wheel Tracking Test Device in the Pavement Engineering Laboratory of TU Dresden 184

Picture 8-9 Contact patch measurements..... 185

List of abbreviations

CSR	Constant Strain rate tests
C&R	Creep & Recovery
DSO	Direct Strain Oscillation mode
DSR	Dynamic Shear Rheometer
FE	Finite Element
FTIR	Fourier Transformation InfraRed
HA UCA	Hogeschool Antwerpen, University College Antwerp
HWTT	Hamburg Wheel Tracking Test
ITT	Indirect Tensile tests
LiDAR	Light Detection and Ranging
LVDT	Linear Variable Differential Transformer
LVER	Linear Vicos-Elastic Region
Material I	Asphalt material with 0 % RA
Material II	Asphalt material with 15 % RA
Material III	Asphalt material with 30 % RA
PA	Open Porous Asphalt
PAV	Pressure Ageing Vessel
PmB	Polymer modified Binder
RAP	Reclaimed Asphalt Pavement
RCAT	Rotating Cylinder Ageing Test
RERS	Road Engineering Research Section of the Artesis University Colleges of Antwerp
RLTT	Repeated Load Triaxial Tests
RTFOT	Rotating Thin Film Oven Test
SMA	Stone Mastic Asphalt
TTSP	Time Temperature Superposition Principle
TUD	Technical University Dresden
UCA	University Colleges of Antwerp
UCD	University College Dublin

UNOTT	University of Nottingham
WP	Work Package
X-Ray CT	X-Ray Computer Tomography

A_C	Cross-sectional area
A_S	Surface area
a_1, a_2, a_3, a_4,	Function parameters
a, b, c, d	Material parameter
$\alpha_{i,j}$, $\beta_{i,j}$	Exponent
$\propto_T$	Shift factor
γ^*	Peak shear strain
d	Shear strain
E*	Complex Modulus
E’	Storage Modulus
E’’	Loss Modulus
|E*|	Absolute Modulus
E_{min}	Static modulus
E_{max}	Glassy modulus
ε	Strain
ε^*	Peak strain
$\varepsilon_{pl,axial}$	Permanent strain
ε_{el}, $\varepsilon_{el,anf}$	Initial elastic strain
$\varepsilon_{1;p;rate}$	Vertical plastic strain rate
$\varepsilon_{1;r}$	Vertical resilient strain
F	Force
F_∞	elastic component of deformation gradient of elasto-plastic element
F_p	plastic component of deformation gradient of elasto-plastic element
F_e	elastic component of deformation gradient of visco-elastic element

F_v	viscous component of deformation gradient of visco-elastic element
f	Frequency
f_{corr}	Corrected frequency
G*	Complex shear modulus
G'	Shear storage Modulus
G''	Shear loss Modulus
h	High
I, j	Complex number
K_1, K_2	Material parameter
m	Material parameter
N	Number of load cycles until macro-crack
η	Viscosity of the fluid
p	Hydrostatic stress
p_a	Reference stress
$p_{i,j}$	Coefficient
q	Deviator stress
σ	Stress
σ*	Peak stress
$\dot{\sigma}_j$	Stress ratio
σ_1	Major principal stress
σ_3	Minor principal stress (cell pressure)
σ_d	Deviator stress
σ_{hyd}	Hydrostatic stress
σ_1	Axial stress
σ_{23}	Horizontal stress (cell pressure)
t	Time
T	Temperature of interest
T_R	Reference temperature
T_S	Duration
τ	Shear stress

τ^*	Peak shear stress
δ	Phase lag
u	Vertical displacement
Ω	Angular frequency

1 Introduction

The combined effects of traffic loads and meteorological impact (climatic changes) in combination with the natural aging of the materials are the main reasons for pavement deterioration over time. When the damaged pavement cannot guarantee for a comfortable traffic anymore, rehabilitation works are needed. This can be done by surface maintenance or by removing entire layers of the damaged road and paving new ones.

Reconstruction with new material requires large budget and energy resources. Therefore, there is a trend towards using recycling technologies, in which the materials from the deteriorated pavement, known as reclaimed asphalt pavement (RAP), are partially reused in the new construction.

The purpose of recycling is to enhance the properties of reclaimed asphalt (RA), such that the whole mix (RA, fresh bitumen and new aggregates) performs as good as fresh mix.

Due to complex interactions between the new and recycled components of the mixture, its performance in the road is widely unknown and difficult to assess. Therefore, there is an increasing need in developing methods to predict the performance of asphalt mixes with RA.

A deeper insight into the mechanics of asphalts composed of recycled and new components were to be researched in the framework of work package 5 (WP5) „performance and modelling“ of the “Re-Road” project sponsored by the European Union. For this reason, a comprehensive material test program was conducted. The results obtained from this test program formed the basis for new and adapted models describing the constitutive characteristics of such asphalt materials.

1.1 Aim of the Research

The objective of WP5 was to evaluate the performance of two asphalt mixtures with RA and to compare the results with a virgin asphalt that is referred to in the report as reference mixture.

The aims of WP5 were to develop visco-elastic and plastic models that can be used to design pavements made of recycled materials, and to predict pavement life as well as their sensitivity to damage.

Within the research project, laboratory tests on selected RA mixes were conducted to investigate and understand the elastic, visco-plastic and visco-elastic deformation as well as the fatigue performance of asphalt mixes containing RA and to determine the input parameters required for the numerical simulations.

In addition, new and relevant healing factors of binders and asphalt mixes are determined. These factors can contribute to more accurate pavement design and pavement design life calculation. Healing factors of unaged and aged binders and

mastics were determined using appropriate testing methods. In this study a new healing model of University College of Antwerp has been verified.

In this report the major outcomes from the research within WP5 are presented.

1.2 Background

Recycling of asphalt has been practiced as early as 1915, however, its popularity has grown since 1980 (Hajj et al., 2007). Its use in road construction and rehabilitation has been widespread due to the advantages that it shows in comparison with constructions with virgin materials. Besides general savings in cost, recycling addresses the main criteria for a sustainable pavement (Harris et al., 2011):

- optimize the use of natural resources,
- reduce energy consumption,
- to be environmental friendly.

RA content between 10 % and 30 % is commonly used in hot recycled bituminous mixes. For these rates the recycled mixes performs similarly to conventional mixes (Kandhal et al., 1995)(Valdes et al., 1995).

However, due to environmental restrictions, the agencies around the world are now promoting the use of higher contents of RA.

It is believed that the existence of RA in the mix may improve the resistance of rutting, however, it could improve the resistance to fatigue (Hajj et al., 2007), (Dragon et al., 2011). To predict the real life behaviour of pavements, the laboratory fatigue life is multiplied with a factor called ‘shift factor’. This shift factor is composed by three partial factors: healing, test conditions and lateral wandering. In this study, the healing factor is selected to be investigated since in countries with a high amount of hot recycling of asphalt; such as the Netherlands, the value of the healing factor is reconsidered when RA is used in the mixture. There are different ways to investigate healing on asphalt mixes depending on material (binder and asphalt), test set-up, damage mechanics, definition of healing (ratio end of life, healing index. Each country or pavement design program has its own healing factor to take into account. The healing factor varies from 1 up to 100. These factors were determined decades ago on asphalt mixes with unaged materials only. At the moment, material characteristics are adjusted, hence, new healing factors are needed to have a good pavement design life calculation. In the Netherlands a study of Van den bergh (Van den bergh, 2011) has shown that the healing factor decreases significantly when RA is added. This means that the benefit in fatigue which occurs when RA is used can be counterbalanced.

There are some discrepancies regarding the effect of RA on the moisture susceptibility and its relation with the durability of the mix. Some authors (Hajj et al., 2007) indicate that moisture susceptibility of mixtures with RA is the main reason of its poor durability. Other sources such as those reported in (Kandhal et al., 1995) indicate that recycled mixtures withstand better the action of water than virgin

mixtures and they conclude that the durability of asphalt mixtures with RA is greater than that of traditional mixtures. Furthermore, the investigations reported in (Hajj et al., 2007) concluded that the RA has no influence, neither positive nor negative, on the moisture's susceptibility of the mixture. Based on these results it can be concluded that there is a need to gain further knowledge about the performance of asphalt mixes containing RA.

1.3 Organisation of WP5

WP5 was organised in two tasks: (A) Task 5.1: determine the input parameter from laboratory tests for a numerical tool and (B) Task 5.2: predict the pavement life as well as their sensitivity to damage of recycled materials. The following partners were involved in WP5:

Table 1-1 Partners involved in WP5

Participant short name	Participant name	Role within WP5
TUD	Technical University Dresden	Leader of work package 5 and Task leader of task 5.1 and task 5.2.
UNOTT	University of Nottingham	
HA UCA	Hogeschool Antwerpen, University College Antwerp, Vlaamse Autonome Hogeschool	
UCD	University College Dublin	

The major outcomes from the research within task 5.1 and task 5.2 are presented in this report.

2 Materials tested

2.1 Material Selection

The aim was to investigate and understand the elastic, visco-plastic and visco-elastic deformation as well as the fatigue performance of asphalt mixes containing RA. A prerequisite was to design and select representative RA mixes. Asphalt mixes with nearly identical grading and clearly different amounts of aged and unaged binders were taken into account in this investigation.

The choice of sort of material was carried out with the partners of all work packages. It was decided to work with Stone Mastic Asphalt (SMA). As reference material (Material I) SMA 11 S was chosen. For Material II and III reclaimed asphalt replacement levels of 20 M.-% and 40 M.-% were envisaged but had to be reduced to 15 M.-% and 30 M.-% due to problems during material production. The chosen reclaimed asphalt was open porous asphalt (PA) and provided and analysed by WP2. The reclaimed asphalt came from a building site close to Braunschweig (Germany). Virgin binder for all asphalt materials was PmB 25/55-55A. However, due to organisational issues Material I, II and III could not be produced at the same time. Consequently the added virgin binders are named differently although equal classified (Table 4-9). All virgin aggregates came from the same quarry close to Dresden (dolomite filler and greywacke aggregate). It was decided within WP5 to define the mix design of the three asphalt mixes investigated based on German guidelines. It was also decided to define the mix designs without adding rejuvenators.

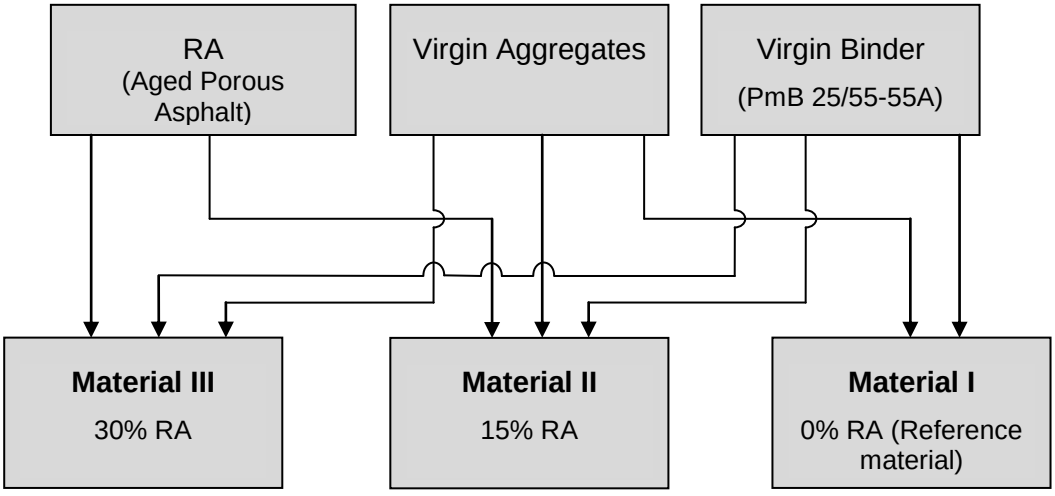

Figure 2-1 Materials composition diagram

2.1.1 Preliminary Analysis

Preliminary studies on different virgin binders and the binder from the provided RA have been conducted within WP2 (of the Re-Road project), at TU Dresden in the

scope of a Master's Thesis (Wulandari, 2009) and a Diploma Thesis (Malcherek, 2010) and at University College Antwerp in the Scope of a PhD Thesis (Van den bergh, 2011). Selected results of the preliminary studies are presented in section 5.2

Within the preliminary analysis at TUD it was studied amongst others which virgin binder should be added to the asphalt mixes incorporating RA. The three in Europe existing equations using Penetration value and/or Softening Point Ring and Ball have been used to calculate the virgin binder to be added. The results showed no significant differences. Consequently, it was decided to define the mix design of the three asphalt mixes investigated based on German guidelines.

2.2 Asphalt Production

A prerequisite was to design and produce representative asphalt mixes.

Picture 2-1 Filling and stocking of buckets with asphalt material

The three stone mastic asphalts (SMA 11 S) have been mixed in a German asphalt mixing plant under the supervision of TU Dresden and further sent to UNOTT, HA UCA and UCD. A total of 20 ton asphalt were produced and tested in WP5.

2.3 Mixes Properties

Due to technical restrictions and the inhomogeneity of the RA, it was not possible to receive three asphalt mixes produced in an asphalt mixing plant with identical grading and binder content. Figure 2-2 shows the grading curves of the three asphalt mixes investigated in WP5.

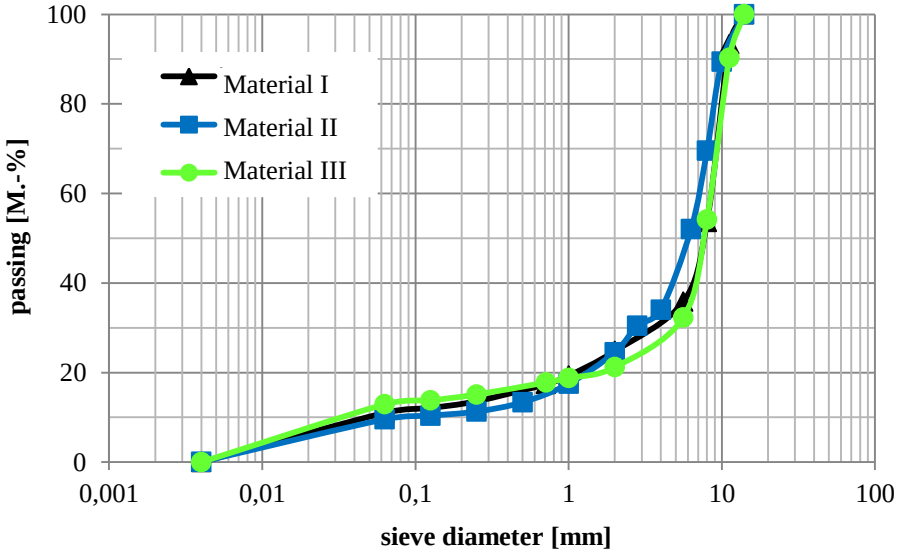

Figure 2-2 Grading curves of the asphalt mixes investigated: material I – virgin mixture (0% RA); material II (15% RA); material III (30% RA)

A table in Annex 1 show exemplary the volumetric characteristics of the reference material (Material I). The mix design of Material II and III was defined based on the volumetric characteristics of Material I, the characteristics of the provided RA and the available virgin components.

The binder contents are listed in Table 2-1 and the binder properties are summarized and discussed in section 5.2.

Table 2-1 Binder content of the asphalt mixes investigated

Asphalt mixture	Percentage of RA	Binder content
Material I	0 %	6.55 %
Material II	15 %	5.63 %
Material III	30 %	7.20 %

The components of each mix can be identified in the cross sections depicted in Picture 2-2.

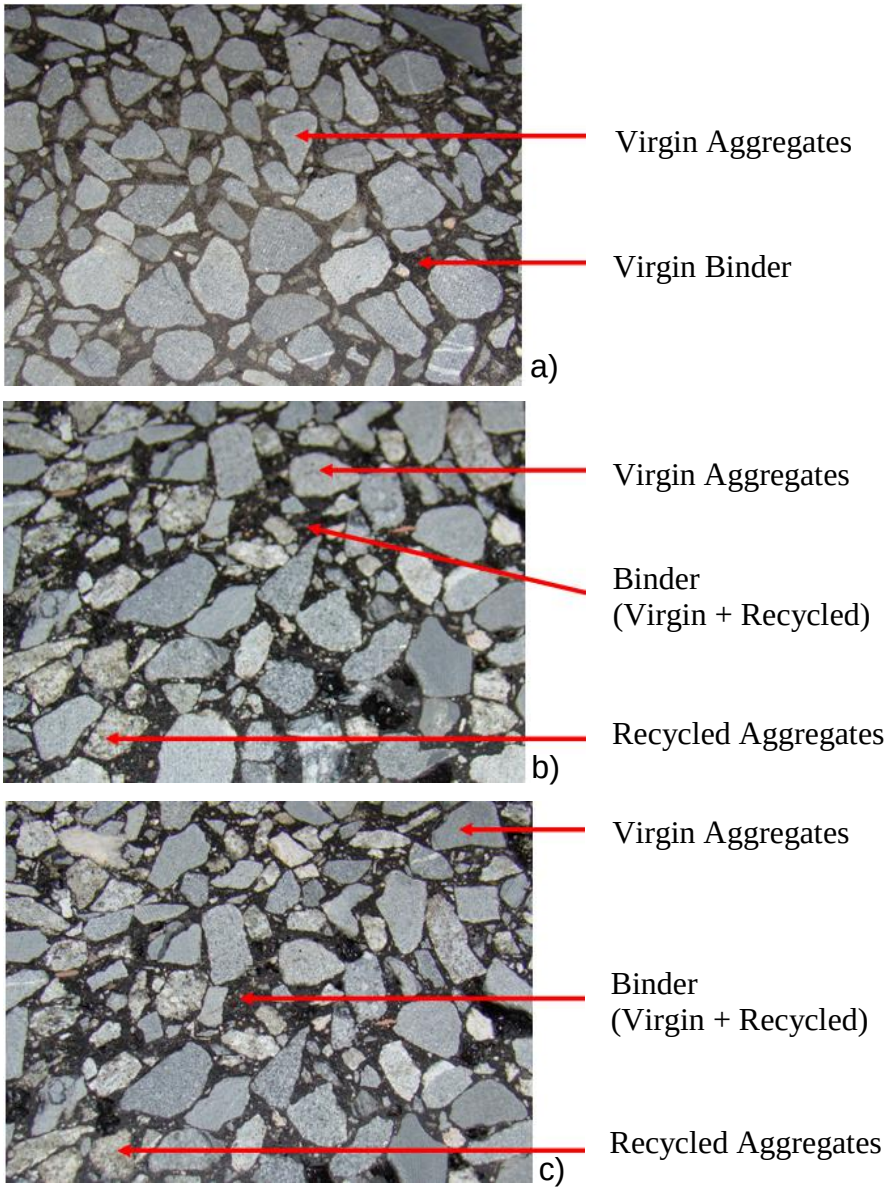

Picture 2-2 Cross section of asphalt mixes: (a) Material I, (b) Material II, (c) Material III

3 Characterisation of Bituminous Mixtures

In order to characterize the behaviour of bituminous mixes used in road construction the following aspect has to be considered (Kim, 2009):

- Stiffness and stiffness time-temperature dependency
- Permanent deformation and rut development
- Fatigue and degradation by fatigue
- Crack initiation and propagation (very important at low temperatures).

The first aspect corresponds to the elastic-viscoelastic material behaviour. The other three aspects are related to pavement distresses. Each aspect can be described by a range of different tests. The partners involved in WP5 conducted different laboratory tests on bituminous binders and asphalt mixtures. For the determination of the input parameters of the two visco-elastic models developed at TU Dresden and University of Nottingham both partners selected the required performance tests based on the theory of the models and the national state-of-the-art of science and technology.

Crack initiation and propagation was not a topic of the researches undertaken.

3.1 Complex Modulus

The complex modulus E^* is the representation of the stiffness of visco-elastic materials, such as asphalt mixtures, under the action of cyclic loads.

The complex modulus of asphalt materials is temperature and time dependent. The time dependency is evidenced in Figure 3-1 in which the strain lags behind the input stress. This lag is known as the phase lag (δ).

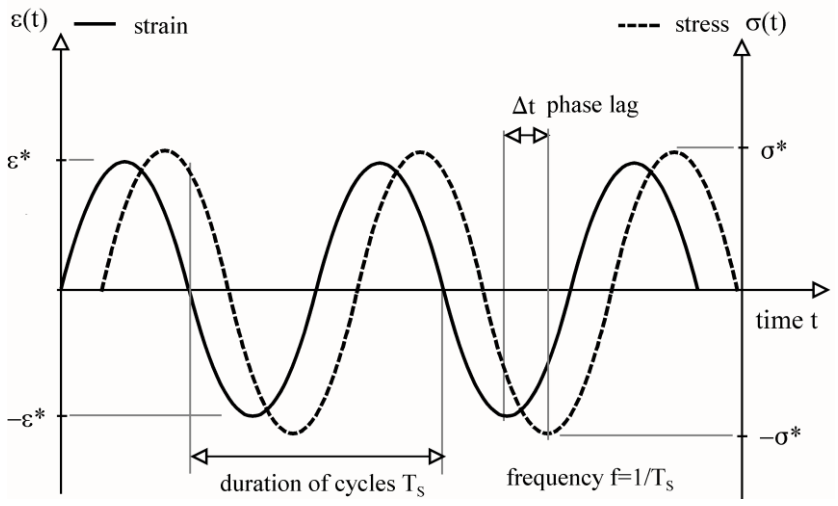

Figure 3-1 Phase lag

E* is a complex number comprising a real and an imaginary part as indicated in Equation (3-1).

$$E^* = E' + iE'' \tag{3-1}$$

with

$$= \sqrt{-1} \tag{3-2}$$

$$E_1' = |E_1| \cos \partial_1 \tag{3-3}$$

$$E_1'' = |E_1| \sin \partial_1 \tag{3-4}$$

The real part represents the storage modulus E' that characterises the elastic portion (measures the stored energy) and the imaginary part represent the loss modulus E'' that symbolizes the viscous portion (measures of the energy dissipated as heat).

In Figure 3-2, the complex modulus and its relationship with the phase lag is illustrated. The complex modulus E* in vector representation is known as absolute modulus |E*|.

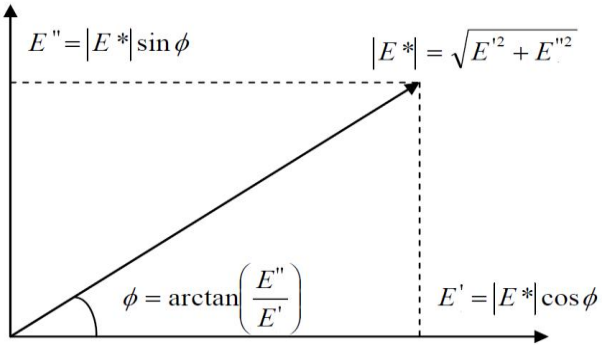

Figure 3-2 Absolute modulus in complex plane

3.1.1 Complex Modulus Representation

Cole-Cole complex plane:

The complex modulus can be plotted in the complex plane where E'' is represented as a function of E'.

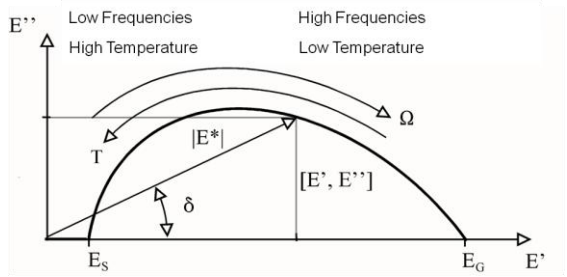

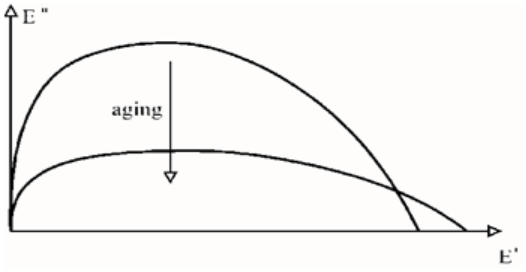

Figure 3-3 theoretic Cole-Cole-Plot with storage and loss modulus (Oeser, 2009)

Figure 3-3 shows a typical asphalt Cole-Cole plot determined at different frequencies and temperatures. It can be seen that at high temperatures and low frequencies the behaviour of the material is mainly viscous and at high frequencies and low temperatures the asphalt behaves as an elastic solid.

Master curve:

If the absolute modulus follows a single curve in the Cole-Cole plane then the time temperature superposition principle (TTSP) applies and a master curve can be constructed. The TTSP states that the same |E*| can be found for different frequency- temperature combinations.

When the TTSP applies, |E*| values at different temperatures (isochrones of |E*|) can be translated by applying a multiplier (shift factor) to the frequency at which the measurement is taken so that they are combined to form a single curve of frequency versus stiffness, this curve is known as master curve.

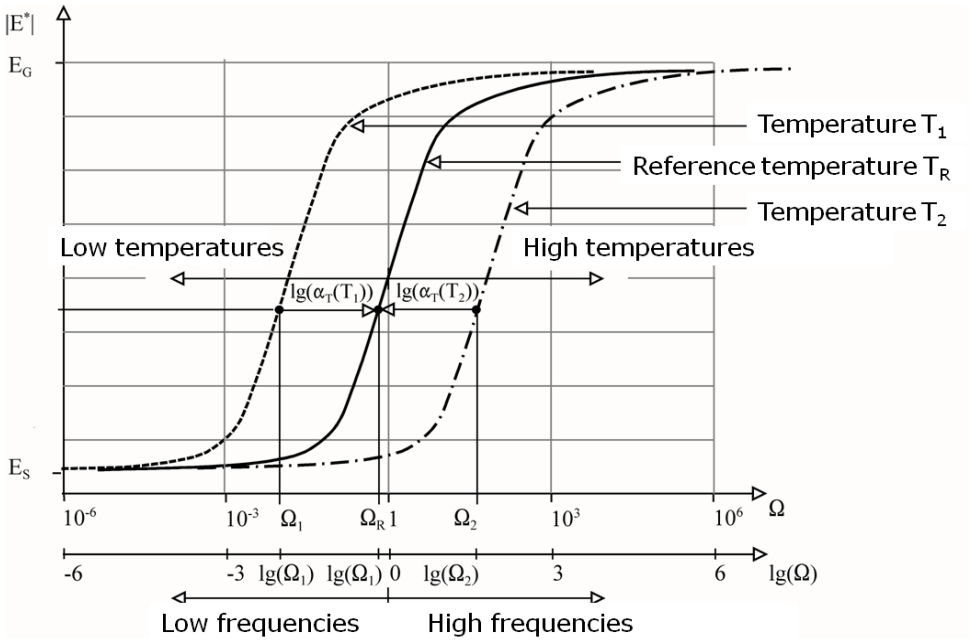

Figure 3-4 Master curve (Oeser, 2009)

For the construction of the master curve the following steps are to follow:

- Calculation of the isochrones of elastic modulus at various temperatures as input for the construction of the master curve. The isochrones can be determined with the data obtained from triaxial tests on different frequencies, load amplitudes and temperatures.

- Calculation of the shift factor and representation of the master curve in a functional form.

Figure 3-4 shows an absolute modulus master curve and its temperature-frequency relationship.

Phase lag δ vs. absolute modulus $|E_1|$

One way to represent the asphalt mixture rheology is to plot the phase lag against the absolut modulus. Unlike the master curves, this diagram does not require any shifting, thus it is temperature independent.

The phase angle vs. absolute modulus is represented in functional form with the regression function indicated in Equation (3-5).

$$\delta_{\varepsilon_1} = f\left(log_{10}(|E_1|)\right) = a_1\, e^{a_2\,(a_3 + log_{10}(|E_1|))^2} + a_4 \qquad (3\text{-}5)$$

with

a_1, a_2, a_3, a_4 function parameters [-]

e = 2.718281

3.2 Permanent Deformation

A test used for the determination of the permanent deformation should involve the conduct of a large number of loading cycles with a single level of stress at any one time.

The result of such a test is the amount of permanent strain ($\varepsilon_{pl,axial}$) versus load cycles as depicted in Figure 3-5.

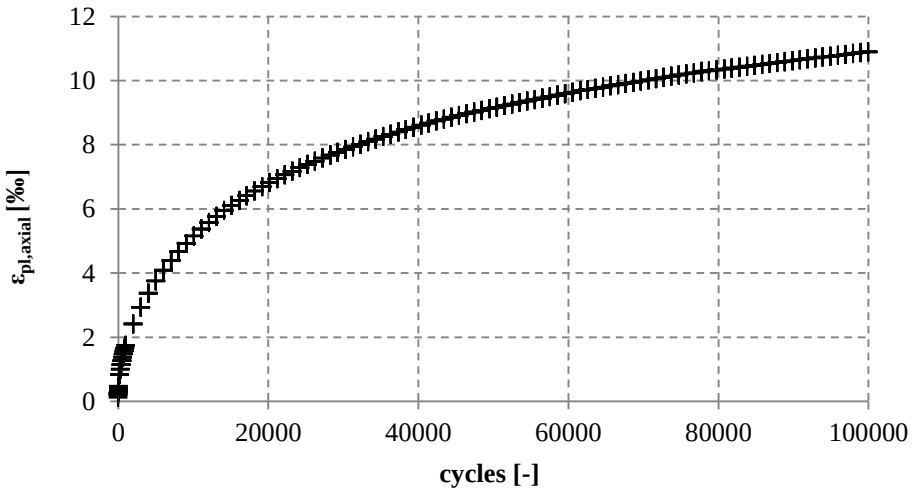

Figure 3-5 Theoretic figure of the deformation curve obtained from a permanent deformation test

3.3 Fatigue

There are different test methods to obtain the fatigue properties of asphalt mixes. Material specific fatigue curves can be determined using Equation (3-6)

$$N = K_1 \cdot \epsilon_{el}^{K_2} \tag{3-6}$$

where ε_{el} = initial elastic strain; N = number of load cycles until macro-crack; and K_1, K_2 = material parameter. The result of fatigue test is the number of load cycles N versus initial elastic strains $\varepsilon_{el,anf}$ as depicted in Figure 3-6.

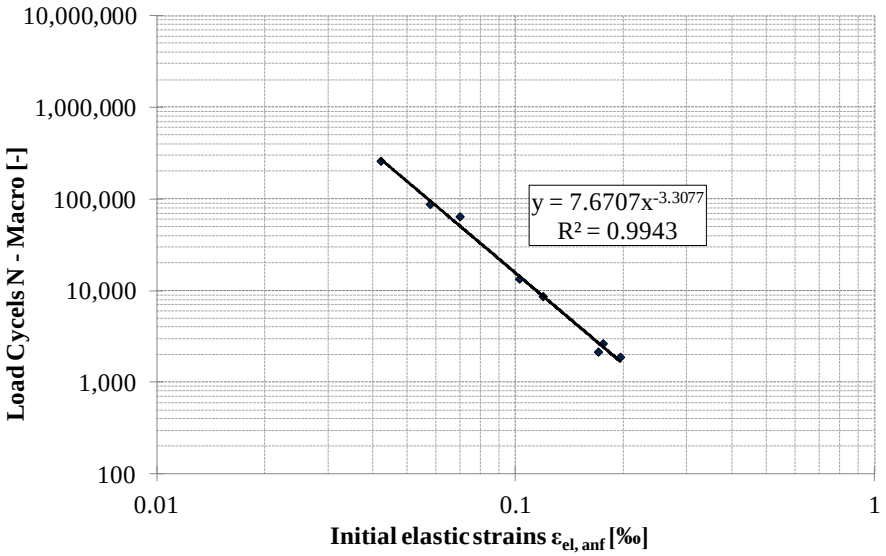

Figure 3-6 Theoretic figure of a fatigue curve obtained from a fatigue test

4 Laboratory Performance Tests

One aim of WP5 was to conduct laboratory tests on selected RA mixes to investigate and understand the elastic, visco-plastic and visco-elastic deformation as well as the fatigue performance of asphalt mixes containing RA and to determine the input parameters required for numerical simulations and pavement design life calculations.

The comprehensive material characterisation was conducted by all partners involved in WP5 (TUD, UNOTT, HA UCA and UCD.). Each partner conducted different laboratory tests on bituminous binders and asphalt mixtures and selected the most qualified sampling for his laboratory tests. Different test set-ups normally require different sample preparation. Following in section 4.1 the different sample preparations are shortly described for each conducted performance test on asphalt mixtures. The sample preparation of the binder samples is included in section 4.2.

Model development and pavement design life calculation (see chapter 6, 7 and 9)) had to be done independent from each other by the partners TUD and UNOTT. Two different models, both using different input parameters, have been developed.

4.1 Laboratory Performance Tests on bituminous Asphalt Mixes

For the pavement design life calculation and numerical simulations input parameters like fatigue curves, master curves and Cole Cole Plots for the asphalt mixtures are required for TUD model, while constant strain-rate tests and Creep & Recovery curves are required for UNOTT model. These parameters can be determined using the results of performance laboratory tests on asphalt mixes (e.g. RLT tests and fatigue tests). Hence, the mechanical properties and the performance characteristics of three asphalt mixes were determined within the research by using appropriate testing methodologies.

4.1.1 Repeated Load Triaxial Tests at Technical University Dresden

For the determination of the input parameters for the pavement design life calculation and the numerical simulations a testing machine (see Picture 4-1) with a triaxial pressure cell designed for cylindrical specimen of a diameter of 150 mm and a height of 300 mm was used.

The apparatus is able to apply a static load of up to ± 100 kN and a dynamic load of up to -70 / +40 kN on the specimen with a maximum frequency of 10 Hz. In addition, the apparatus is able to apply a confining stress of up to 1.5 N/mm² on the specimen.

The specimens are covered by a rubber membrane of 2-3 mm thickness (see Picture 4-2). Using this testing apparatus the ratio between the vertical and horizontal stress can be chosen independently.

Hence, any stress condition occurring in the real pavement can be simulated in laboratory tests (temperature range –10 °C and +50 °C). A maximum test temperature of 35 °C was chosen. The performed test conditions are summarised in Table 4-1.

The vertical elastic and permanent deformations of the specimen were measured at different locations. External LVDTs (Picture 4-3) and an internal contact-less system (Picture 4-4) were used to measure the axial deformations.

Picture 4-1 Repeated load triaxial test maschine with a triaxial pressure cell at TU Dresden

Picture 4-2 Triaxial pressure cell and specimens covered by a rubber membrane

The external system can be used to measure the permanent deformations over the sample height and to define the termination criteria of the test. The internal system

uses poled magnets and coils. This measurement system uses six magnets that have to be placed in the specimen. Small holes are drilled into the specimen. Afterwards, magnets are glued into the specimen using bitumen. This system allows measuring the vertical elastic and permanent deformations in the mid height of the specimen. The system to measure the radial or horizontal deformations consists of nine LVDTs. The LVDTs are placed at three heights (75, 150 and 225 mm) in the triaxial cell.

Table 4-1 Dynamic RLTTs – Test Conditions

Parameter	Performed test condition
Wave	sinusoidal stress
Frequency f [Hz]	1, 5, 10
Duration of Loading [s]	1/f
Rest period [s]	none
Test Temperature [°C]	-10, +35
Lower Stress – vertical [N/mm²]	0.2
Upper Stress – vertical [N/mm²]	1.0, 2.0
Lower Stress – horizontal [N/mm²]	0.02
Upper Stress – horizontal [N/mm²]	0.3, 0.6, 0.9

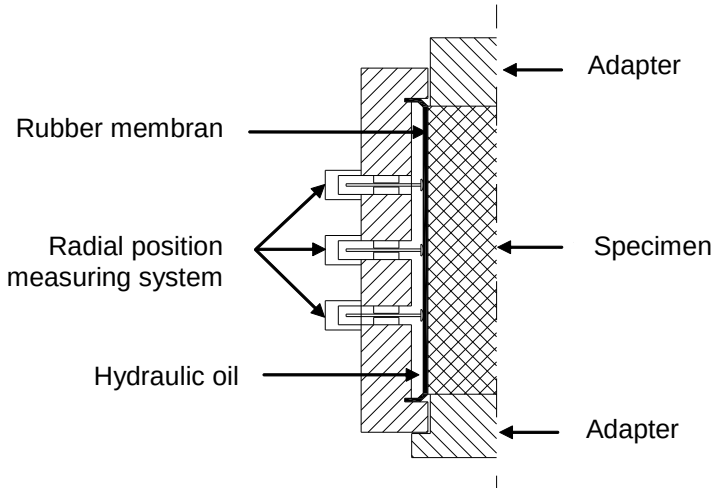

Figure 4-1 Schematic illustration of the triaxial apparatus (Grohs, 2005)

Laboratory repeated load triaxial tests can simulate traffic loads by subjecting a cylindrical specimen to a cyclic vertical stress and a cyclic confining stress. Picture 4-5 shows schematically the stresses on a specimen in a triaxial test.

In order to characterize the elastic-viscoelastic properties as well as the plastic behaviour of the selected asphalt mixtures, two types of repeated load triaxial tests were conducted.

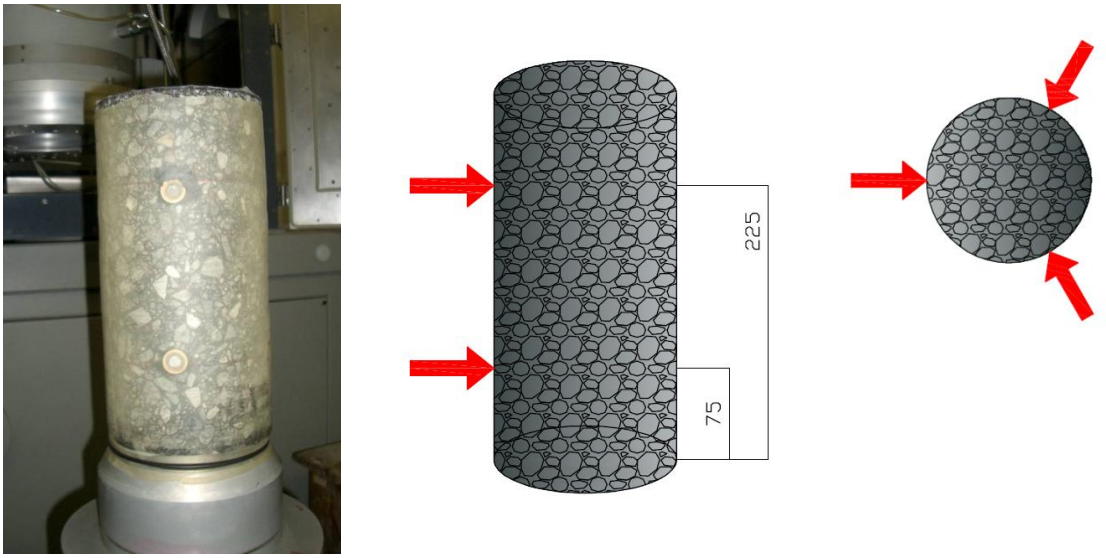

Picture 4-3 Position of the internal contact-less system for the measurement of the axial deformations (Grohs, 2005)

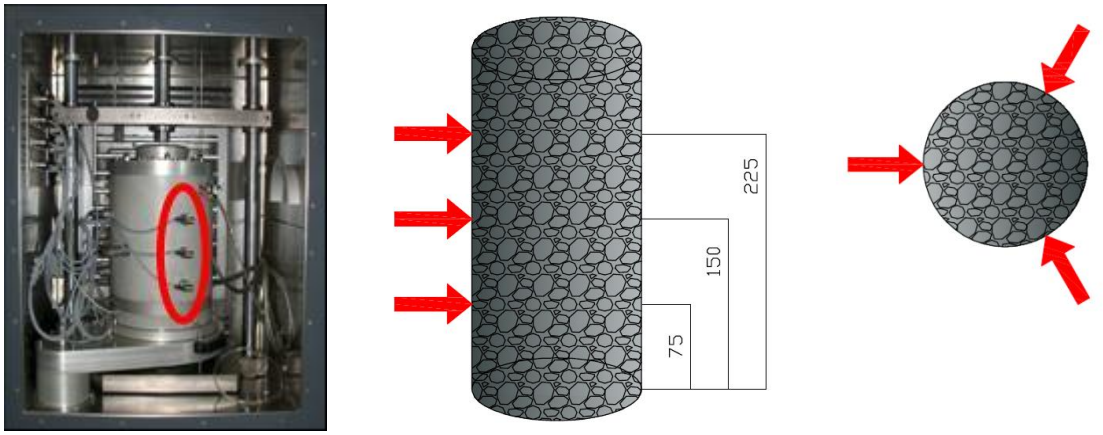

Picture 4-4 Position of the external LVDTs for the measurement of the radial or horizontal deformations (Grohs, 2005)

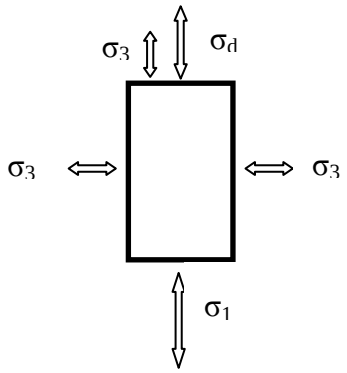

with:

σ_1: major principal stress [N/mm^2]

σ_3: minor principal stress (cell pressure) [N/mm^2]

σ_d: deviator stress [N/mm^2]

σ_1: $\sigma_d + \sigma_3$

Picture 4-5 Stresses in a triaxial test

4.1.1.1 Asphalt Sample Preparation

For the preparation of the asphalt test samples in laboratory, a Roller Sector Compactor was used. In a first step, an asphalt slab was prepared. The compaction load is applied vertically. During the compaction process, the mineral particles mainly orientate horizontally (see Figure 4-2). Thus, the behaviour of asphalt can be assumed to be anisotropic. The anisotropic material behaviour of asphalt was not investigated in this research.

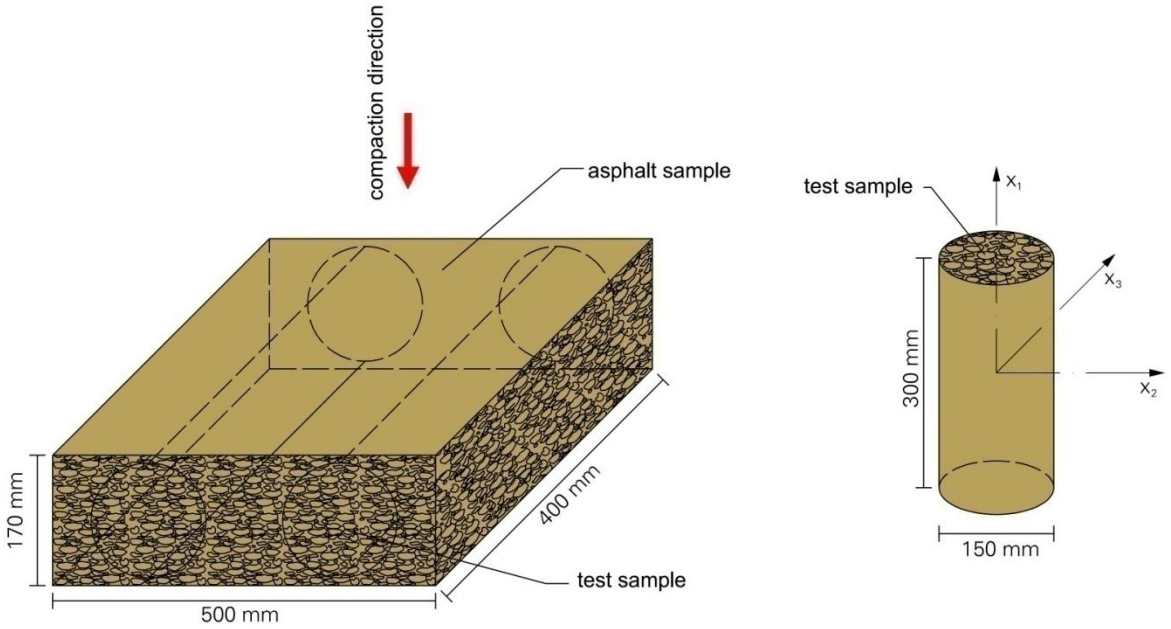

Figure 4-2 Preparation of hot rolled asphalt test samples (Zeißler, 2012)

In a second step, cylindrical test samples of 150 mm diameter were taken by drilling them from the asphalt slabs and then sawed to the appropriate height of 300 mm.

4.1.1.2 Cyclic Compression Tests

The cyclic compression test was used to determine the elastic modulus and Poisson's ratio of the specimens under the action of cyclic stresses. This test provides the material properties needed for the model parameter identification of the elastic-visco elastic model developed at TUD (see chapter 6).

Determination of absolute modulus $|E_1|$

Before explaining the approach used to estimate the stiffness values of the selected asphalt mixtures, a brief introduction to the equations governing the material behaviour is given.

As result of the preparation process of the test samples the asphalt behaviour is anisotropic (Zeißler, 2012). For anisotropic materials the axial strain as related to the stress components is given by Equation (4-1).

$$\varepsilon_1 = \frac{\sigma_1}{|E_1|} - \mu_{12}\frac{\sigma_2}{|E_2|} - \mu_{13}\frac{\sigma_3}{|E_3|} \quad (4\text{-}1)$$

However, for the interpretation of the test results, a simplification is made and the material is considered transverse isotropic (i.e. with one axis of symmetry). With this assumption Equation (4-1) is reduced to

$$\varepsilon_1 = \frac{\sigma_1}{|E_1|} - 2\,\mu_1\frac{\sigma_{23}}{|E_{23}|} \quad (4\text{-}2)$$

The absolute elastic modulus $|E_1|$ is determined with a new approach in the interpretation of the RLT test results. The basic idea of this approach is that if the functional relationship between axial strain as related to the axial and horizontal stresses is known then the absolute modulus can be calculated via the derivative of this function with respect to the axial stress (σ_1) (Zeißler, 2012).

The triaxial test results show that if the amplitude of one of the stress components (σ_1 or σ_{23}) is constant then the trend of the strain function in dependence of vertical and horizontal stresses is linear (see Figure 5-3 and Figure 5-4). This linear trend is used to derivate a functional relationship between ε_1 as related to σ_1 and σ_{23}. For this purpose the following surface function is used:

$$\varepsilon_1 = f(\sigma_1, \sigma_{23}) = a_1\sigma_1 + a_2\sigma_{23} + a_3\sigma_1\sigma_{23} \quad (4\text{-}3)$$

with

a_1, a_2, a_3 [-]	surface function parameters dependent on temperature and frequency
σ_1 [N/mm²]	axial stress
σ_{23} [N/mm²]	horizontal stress (cell pressure)

The last term of Equation (4-3) represents the dependency of $|E_1|$ on σ_{23} (Zeißler, 2012). For stress independent simplification, the surface function is reduced to

$$\varepsilon_1 = f(\sigma_1, \sigma_{23}) = a_1\sigma_1 + a_2\sigma_{23} \quad (4\text{-}4)$$

The basic condition for the application of Equation (4-3) or Equation (4-4) is that for σ_1=0 and σ_{23} = 0 also ε_1 equals 0.

Finally, the absolute modulus is determined from the derivative of the surface function with respect to σ_1 related to the derivative of Equation (4-2) with respect to σ_1, as follows:

$$\frac{d\varepsilon_1}{d\sigma_1} = a_1 + a_3\sigma_{23} = \frac{1}{|E_1|} \xrightarrow{yields} |E_1| = \frac{1}{a_1 + a_3\sigma_{23}} \quad (4\text{-}5)$$

Analogous, the absolute modulus can be calculated for the stress independent approach as follows:

$$\frac{d\varepsilon_1}{d\sigma_1} = a_1 = \frac{1}{|E_1|} \xrightarrow{yields} |E_1| = \frac{1}{a_1} \qquad (4\text{-}6)$$

Summarizing, the steps to determine $|E_1|$ are:

- Collect the data from several triaxial tests at different load conditions, temperatures and frequencies. Enough data is needed for an accurate approximation of the surface function of axial strain (Equation (4-3) or Equation (4-4)).

- Determine the axial strain (ε_1) of each loading case and temperature-frequency combination.

- Estimate the parameters a_1, a_2 and a_3 of the surface function of axial strain (Equation (4-3)). For the stress independent approach the applicable equation is Equation (4-4) and the parameters are only a_1 and a_2.

- Finally, the absolute modulus |E1| is calculated with Equation (4-5) (or with Equation (4-6) in case of stress independent simplification).

Master curve of the absolute modulus $|E_1|$

Within the mechanistic empirical pavement design the master curves are used to characterize the stiffness of asphalt mixtures.

The asphalt absolute modulus $|E_1|$ is a function of frequency as well as a function of temperature. This dual relation can be described by using a frequency-temperature superposition which is the basic idea behind the master curve (see section 3.1).

Construction procedure: For the construction of the master curve the isotherms of $|E_1|$ are shifted by applying a multiplier (shift factor α_T) to the frequency at which the measurement is taken so that the individual isotherms are combined to form a single smooth curve of frequency versus stiffness.

The shift factor is determined with the Arrhenius function indicated in Equation (4-7).

$$\propto_T = \frac{1}{e^{-m\left(\frac{1}{T+273}-\frac{1}{T_R+273}\right)}} \qquad (4\text{-}7)$$

$\propto_T$ [-] shift factor

m [-] material parameter,

for the selected asphalt mixture m=28000 can be used

T [°C] temperature of interest

T_R [°C] reference temperature, T_R=20°C was used

Using a corrected frequency defined by Equation (4-8).

$$f_{corr} = f \ \propto_T \tag{4-8}$$

with

f_{corr} [Hz] corrected frequency

f [Hz] frequency of interest

$\propto_T$ [-] shift factor

the master curve can be represented in a functional form with the sigmoidal function indicated in Equation (4-9).

$$|E_1| = f(\log_{10}(f_{corr})) = E_{\min} + \frac{E_{\max} - E_{\min}}{1 + e^{-\frac{\log_{10}(f_{corr}) - a_1}{a_2}}} \tag{4-9}$$

with

E_{min} [N/mm^2] static modulus

E_{max} [N/mm^2] glassy modulus

f_{corr} [Hz] corrected frequency

a_1, a_2 [-] parameters

The parameters a_1 and a_2 are determined with the least square method assuming a glassy modulus (E_{max}) of 40000 N/mm^2 and a static modulus (E_{min}) of 250 N/mm^2.

4.1.1.3 Permanent Deformation Tests

Rutting caused by permanent deformation in the asphalt layer of flexible pavements is a common pavement distress. In despite of this, there is not a well established method to determine the permanent deformation of asphalt mixes and to predict its contribution to the total rutting in the pavement. In order to understand the real performance of new materials there is a strong need to introduce a suitable mechanical performance test to characterize the resistance to permanent deformation of asphalt mixes.

Traditionally, the permanent deformation of asphalt materials is characterized using the results of repeated load triaxial tests in which a large number of loading cycles with a single level of stress are applied. However, for research purposes this type of test procedure is impractical and expensive – due to the amount of different tests required to cover a representative number of stress combinations. To overcome this limitation, a multistage test procedure, in which the same specimen is subjected to several repeated loading steps at different stress levels, was carried out.

Exemplary in Figure 4-3 the output of a multistage repeated load triaxial test is depicted.

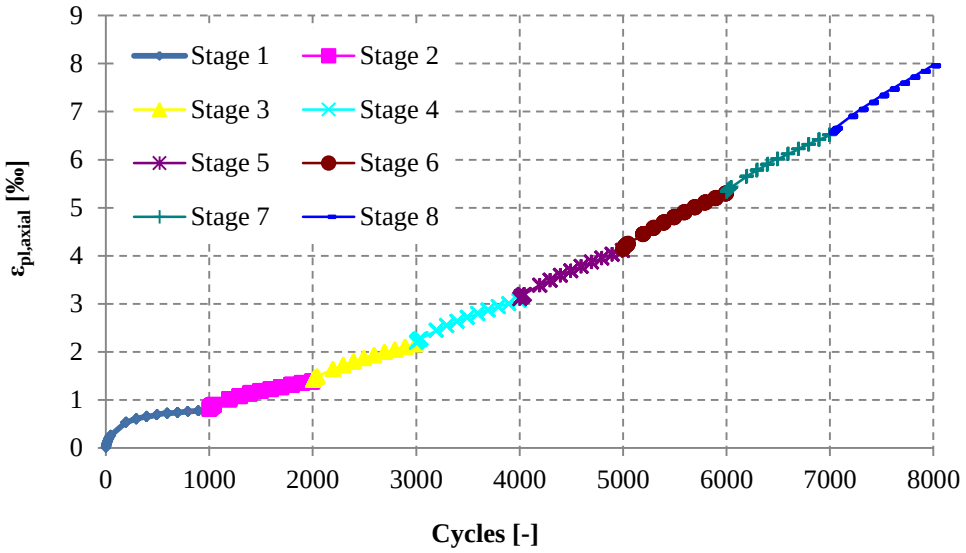

Figure 4-3 Typical output of a multistage repeated load tri-axial test

The test results are extrapolated to transform the multistage data to one test per stress stage using a power law function (Equation (4-10)). With this it is assumed that each new loading stage starts at nil deformation as if it was a single stage test.

$$\varepsilon_{pl,axial} = a\, N^{b} \tag{4-10}$$

The transformation of a multistage test into a single stage is illustrated in Figure 4-4 .

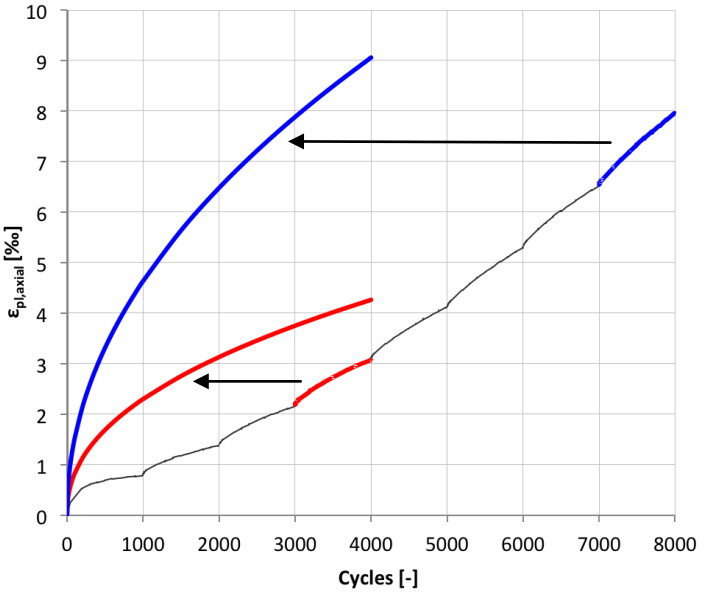

Figure 4-4 transformation of a multistage test into a single stage test

4.1.2 Experimental Programme at University of Nottingham

Before beginning the experimental programme the Materials I, II and III were analysed, as received. This has been done in order to ensure eventual discrepancies on further mechanical tests' results. First binder have been extracted and characterised (section 5.2.1), then aggregates were sieved to obtain the grading curve (Figure 2-2).

Results from the aggregates sieving confirmed the similarities amongst the three materials. Binders were characterised through conventional empirical test and a dynamic mechanical analysis, by means of a Dynamic Shear Rheometer, over a wide range o frequencies and the whole range of service temperature. An overall analysis of the tests' results on the binder indicates a substantial agreement amongst the different binder characterisations. Results highlights similarities between Binder I and Binder II, while shows overall better properties for binder III. This clarify the reasons of the higher efforts required during the specimens' compaction for Material III and provide fundamental information to be considered for further comparisons of mechanical properties of the mixes.

4.1.2.1 Experimental Settings

The experimental programme involved four different types of tests in both tension and compression at 25 ºC and at several level of loading. Preliminary investigations have been performed to optimise the production of specimens for testing purposes (section 4.1.2.1). After optimisation, 120 cylindrical specimens (compression) and 60 dog-bone specimens (tension) have been manufactured, placed in a temperature-controlled cabinet and, according to the following programme, tested in compression and tension. This was done with an Instron 1332 hydraulic loading frame with a maximum load capacity of ±100 kN, equipped with four loading ranges of 10, 20, 50 and 100 kN (more details in section 4.1.2.2):

- Constant strain tests: (strain rates: +0.0005, +0.001, +0.005)
- Creep & Recovery tests: (load levels: 5%, 10%, 15% and 20% of the peak stresses found in the Constant Strain Rate tests).

4.1.2.2 Specimen Manufacture - Compression Tests

A manufacturing process aiming at obtaining test specimens for estimating the fundamental mechanical properties of asphalts mixes for further model calibration, should be quick, reliable, repeatable and possibly it should allow using a limited amount of material. Gyratory compactor is definitely a convenient piece of equipment which allows controlling to a certain extent the specimen geometry, density and it requires a limited amount of material and manufacturing efforts. Based on this assumptions, within Re-Road UNOTT has conducted a study aiming at providing a protocol allows to confidently using gyratory compaction for the production of reclaimed asphalt test specimens to manufacture homogenous test specimen for a reliable evaluation of fundamental mechanical properties of reclaimed asphalts mixes.

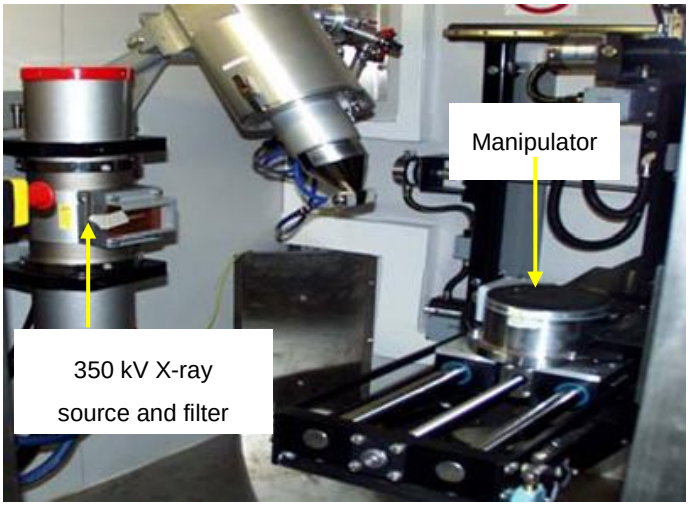

Picture 4-6 X-ray CT equipment

The study uses high profile technologies, as X-Ray CT (Picture 4-6) and image analysis technique (Figure 4-5), to have a better understanding of the compaction process, but it was tailored to finally provide a protocol involving only common laboratory techniques, as trimming procedures and buoyancy test (BS EN 12697-6:2003).

The imaging software package *ImageJ* was used to process and analyse the images provided from the CT scans. The images were opened in a stack for cropping and rescaling from pixels to the actual dimensions. Thresholding and segmentation tools were used to extract the air voids from the background image. Preliminary treatment such as intensity adjustment was carried out prior segmentation to improve the quality of the original image.

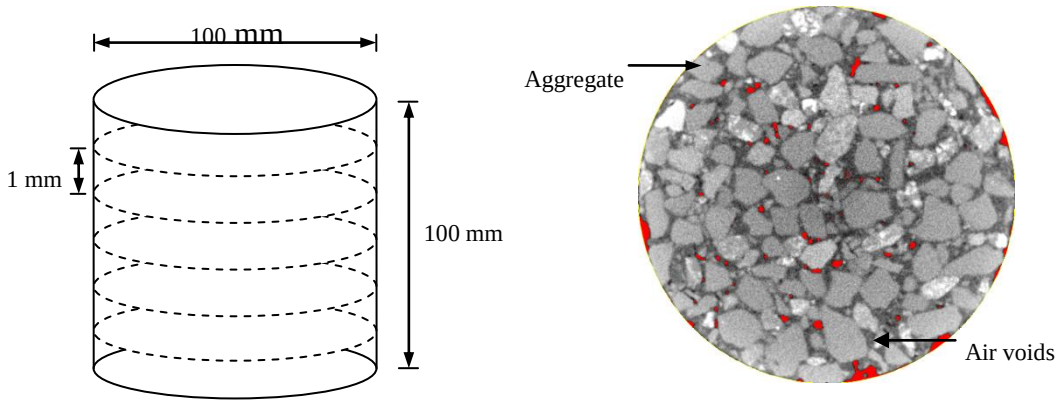

Figure 4-5 X-ray CT equipment (a) Configuration of scanned specimen in stack (b) X-ray Image of HRA

The volume fraction was calculated directly as the percentage of voids area measured on the two-dimensional images. The air void content was quantified based on the area fraction which was calculated by taking the ratio of the total air voids area within an image to the total image area (Equation (4-11)). The total void content from the images was compared to the total void content measured from the laboratory determined using sealed specimens method (BS EN 12697-6:2003).

$$Area\ fraction = \frac{Air\ voids\ area\ (mm^2)}{Total\ image\ area\ (mm^2)} \times 100 \qquad (4\text{-}11)$$

Furthermore, in this study, the same concept was applied to evaluate the radial distribution of the air voids distribution within the specimen. This operation has been called „Cores and Ring analysis“ and it consisted in a virtual cut in the radial direction of the specimen followed by sectorial image analysis.

First, cores of increasing radius (25 mm step) were analysed from the centre to outer ring. Then also rings of increasing radius (25 mm step) from the outer part to the core, have been analysed. Results of the Core & Rings analyses allowed to find the average air void content of the analysed cores and rings.

Gyratory compaction procedure

The gyratory compaction was conducted according to EN 12697-31:2007 and based on a procedure detailed in section 4.1.2 (De Visscher et al., 2010). The gyratory specimens were prepared to achieve the reference density and air void content that was obtained using a previous Marshall mix design procedure (Table 4-2). In order to establish an optimised procedure, the effect of height/diameter ratio (H/D) has been investigated (1.0 and 1.5) by compacting specimens with different combination of height and diameter (100mm and 150 mm). The compaction was conducted at 145 °C (±5 °C) with a vertical pressure of 600 kPa, internal angle, 0.82 ° and the speed of rotation, 30 gyrations/min.

The study aimed at producing homogenous cylindrical test specimens, of Material I (0%) and Material III (30%), with 100 mm diameter and H/D ratio at least equal to 1. Despite it is usually suggested to produce tests specimen with a H/D ratio of at least 2, previous studies (Erkens, 2002) have shown that it is possible to obtain reliable results also by testing specimen with H/D=1. Nevertheless, in this case is mandatory ensuring an efficient friction reduction system while testing.

The study has involved two complementary phases:

I. Establishing a procedure to obtain specimens with homogenous distribution of air voids

II. Achieving homogeneous specimen with a fixed air void content (target density)

Phase I: Manufacturing homogenous reclaimed asphalt test specimen

Under this investigation, a set of procedures consisting of two methods of gyratory compaction have been conducted for obtaining a targeted test specimen of 100 mm x 100 mm with homogeneous air voids distribution. The methods are summarised as follows:

Procedure A: directly compacting 100 mm x 100 mm specimen (H/D:100/100),
Procedure B: coring and trimming the 100 mm x 100 mm specimen from 150 mm x 150 mm specimen (H/D:150/150).

The specimens were then X-rayed for internal structure images and laboratory tested for air voids content (Buoyancy test EN 12697-6:2003). Table 4-2 summarises the specimen properties as a result of undertaking the three compaction procedures.

Looking at Table 4-2 and Figure 4-6, both virgin and RA specimens prepared with procedure Specimen obtained with procedure A, has higher air voids content at the top and bottom sections compared to the middle section indicating non-uniformity in the air voids distribution throughout the specimens. A final trimming (at least 15 mm) is needed at both ends of the specimens due to uneven surfaces caused by the pre-set angle (0.82 °) during compaction. This will provide a homogenous specimen but with a H/D ratio much lower than 1 which is not as targeted.

Table 4-2 Specimen properties from procedures A and B

Type	Specimen size (mm) (Height/ Diameter)	GYRO Air voids (%)	Buoyancy test Air voids (%)
Procedure A			
Material I	100/100	2.49	2.95
Material III	100/100	2.80	3.83
	Core 100/100	-	4.65
Procedure B			
Material I	150/150	2.83	1.83
	Core 100/100	-	0.2
Material III	150/150	2.82	2.00
	Core 100/100	-	0.7

Procedure B, aimed to obtain 100 x 100 test specimen by coring and trimming gyratory compacted specimen produced with a mould of 150 mm diameter and with H/D ratio of 1. Gyratory compaction results (Table 4-2) show a similar trend to the procedure A, but procedure B required higher compaction efforts, i.e. higher numbers of gyrations. Image analysis results show that specimens B, as already seen with procedure A, has a uniform distribution of air voids in the middle section, while having higher values towards both end surfaces (Figure 4-7). This of course

happens because bigger dimension of the specimen reduces the effects of the mould confinement.

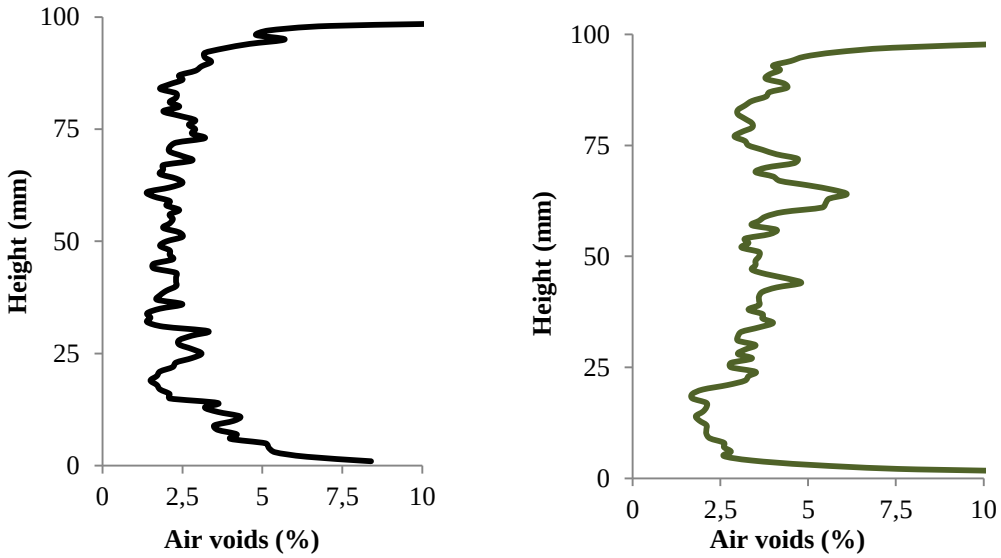

Figure 4-6 Specimen A: Air voids distribution for (a) Material I (0%RA) (b) Material III (30%RA)

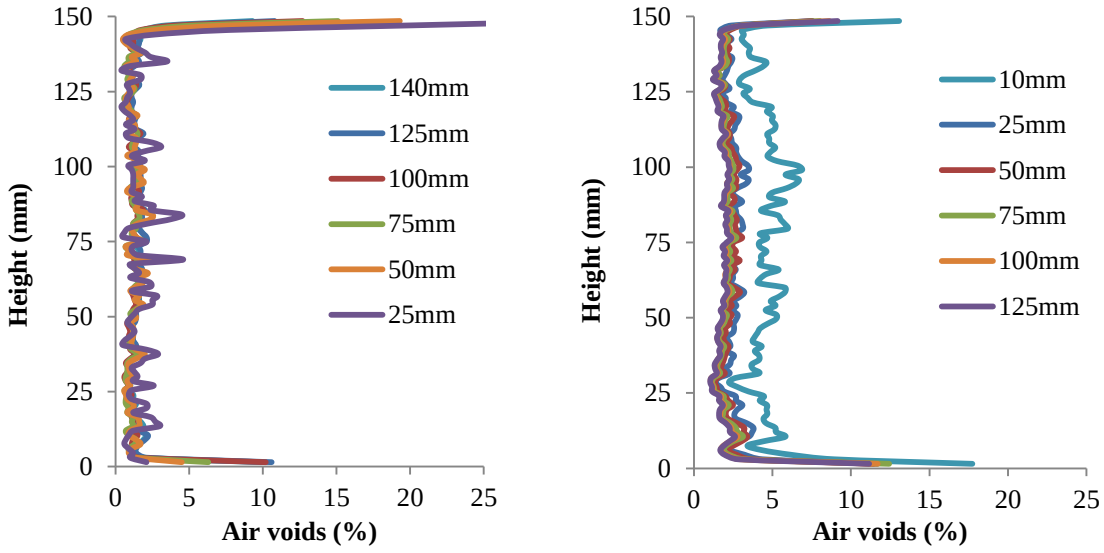

Figure 4-7 Cores & rings analyses of compacted Material III specimen (30% RA)

Finally, results show that Procedure B leads to a 100 mm x 100 mm specimen with homogenous distribution of the air voids, but with a much lower air void content than the desired on, especially when 30% of RA is incorporated into the mix. Although the

compaction allowed achieving the target density, after trimming and coring procedures (Table 4-2) the air void content was found much lower than the desired 2.6%. From an overall analysis of the procedures it can be summarised that the Material III (30% RA) was much harder to compact. In fact, the number of gyrations needed to achieve the target density were significantly higher as well as the difference between the theoretical density and air voids indicated by the compactor and those measured by buoyancy tests. With regard to the compaction procedures, procedures A and C provide a wide region with homogeneous air voids distribution throughout the specimen. Procedure C (Figure 4-8) was then selected to produce the homogeneous test specimens for the second part of the study.

Phase II: Optimisation Study to Achieve the Target Air Voids Content

The Phase II was performed to obtain 100 mm x 100 mm homogenous specimen at the designed air voids content, by using Procedure B (Figure 4-9) a preliminary investigation was carried out by compacting a number of 150mm x 150mm specimens at different densities for optimisation (100 %, 95 % and 90 % from the original target density at 2.6 % target air voids content). Three replicates were prepared for each target density.

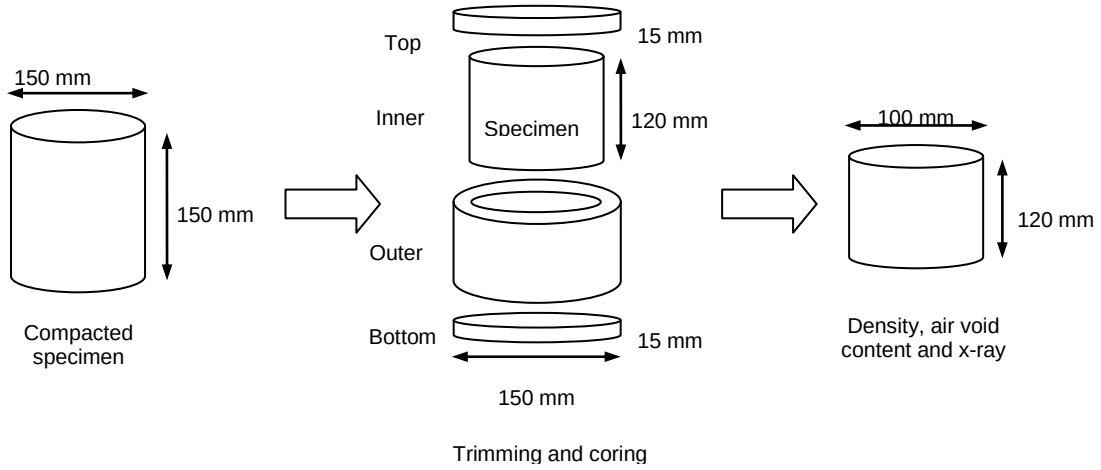

Figure 4-8 Schematic showing the specimen manufacturing process to get the homogeneous distribution of air voids from the 150 mm diameter, 150 mm height gyratory compacted specimen

Table 4-3 summarises the average values of resulting densities and air voids contents of specimen C before and after the coring work. The idea was to obtain a relationship between the measured air voids content of the cores (100 mm x 100 mm), and the target density to be set on the gyratory compactor for manufacturing the 150 mm x 150 mm specimens. The target density for compacting 150 mm x 150 mm specimen to obtain a core (100 mm x 100 mm) with homogenous air voids content of 2.6 % was then estimated from the linear relationships in Table 4-4 with the R-squared (R^2) values close to 1.

Table 4-3 Details density and air voids for optimisation

Type	Max. density [kg/m^3]	Gyratory compacted specimen (150/150)		After coring (lab. determined density of 100/100)
		Target density [kg/m^3]	Target air voids [%]	Av. air voids [%]
Material I	100%	2391	2.6	0.15
	95%	2271	7.5	2.6
	90%	2151	12.3	4.9
Material II	100%	2429	2.6	2.75
	95%	2308	7.5	4.4
	90%	2186	12.3	7.85
Material III	100%	2420	2.6	0.7
	95%	2298	7.5	4.6
	90%	2177	12.4	7.95

Table 4-4 Repeatability study: gyratory compaction results of 150 x 150 specimens

Type	N° gyrat. (avg)	final height (mm)	GYRO density (kg/m^3)	GYRO Air voids (%)	Buoyancy density (kg/m^3)	Buoyancy Air voids (%)
Material I	165	99.95	2393.6	2.59	2384	2.95
Material II	1401	101.87	2374.65	4.38	2365	4.36
Material III	1380	100.22	2420.3	2.60	2390	3.83

From the plot in Figure 4-9, the estimated target densities for all mixture types are as follows:

Material I: m_1 = 2267 kg/m^3, (95% of the original target)
Material II: m_2 = 2422 kg/m^3, (100% of the original target)
Material III: m_3 = 2355 kg/m^3, (97 % of the original target)

Once compaction laws have been defined a wider compaction campaign, 24 replicates per each mixture, has been performed for all the three mixes in order to ensure repeatability of the process. Buoyancy tests, X-ray CT and image analysis techniques were used to have a double confirmation of the achievement of the fixed air void content and to check that air voids were actually homogeneously distributed all over the 100 x 100 cores.

shows results of the gyratory compactions: all the mixes achieve consistently the targeted densities, air void content and final height. Nevertheless, Material III shows a significantly higher variability of the needed number of gyrations for the compaction process.

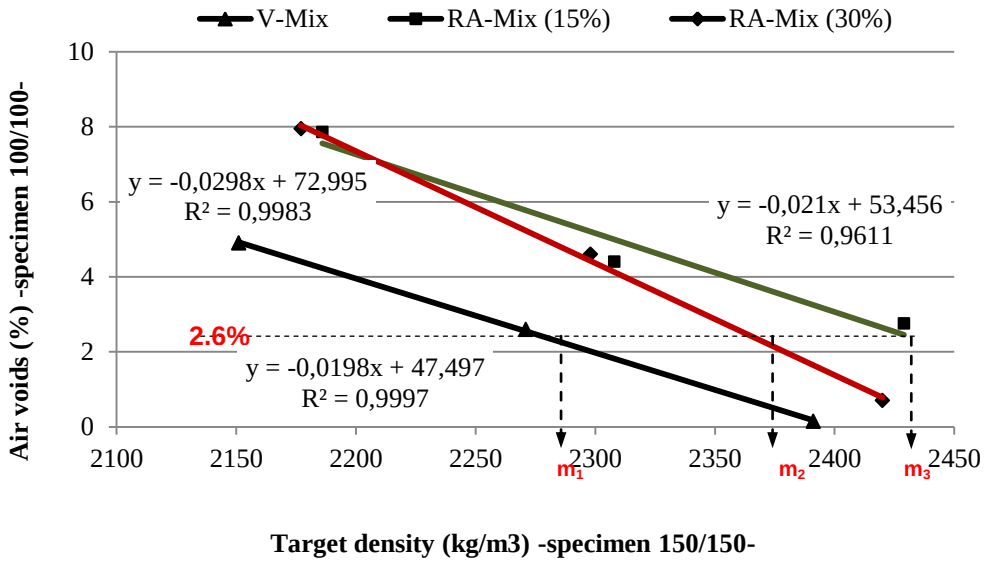

Figure 4-9 Relationships of the target air voids content for 100/100 specimen and the density to be set during compaction for 150/150 specimen

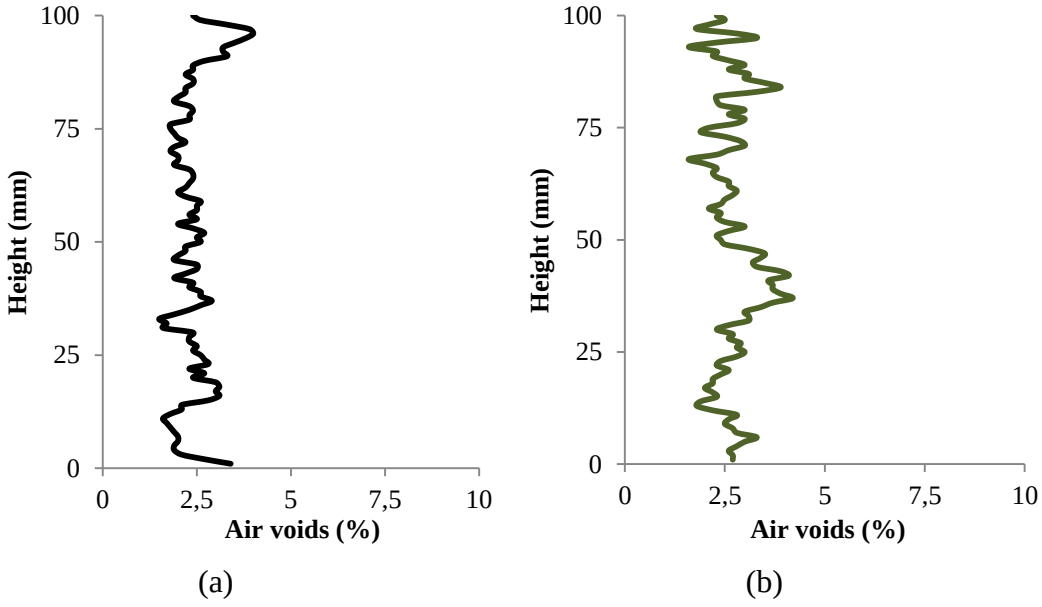

Figure 4-10 Air voids distribution within the cored section of 100/100 after optimisation for Material I (0% RA) and Material III (30% RA) with the air voids content, 2.6%

Buoyancy tests and image analyses show that the adopted procedure allows obtaining homogenous test specimens with an average air void content which differs of + 0.5% from the desired one (2.6%) but with a very low standard deviation which indicates a good repeatability.

As a result, Figure 4-9 and Figure 4-10 shows how incorporating high percentage of RA does not create any particular issues on the optimisation of specimen manufacturing.

4.1.2.3 Specimen Manufacture - Tension Tests

Dog bone specimens were used for the tension tests to ensure failure occurs at or near to the centre. The specimens are produced using a dog bone shaped mould with the dimensions shown in Picture 4-7. The required mass of material dictated by the desired density was added to the mould and was compacted using a vibratory hammer.

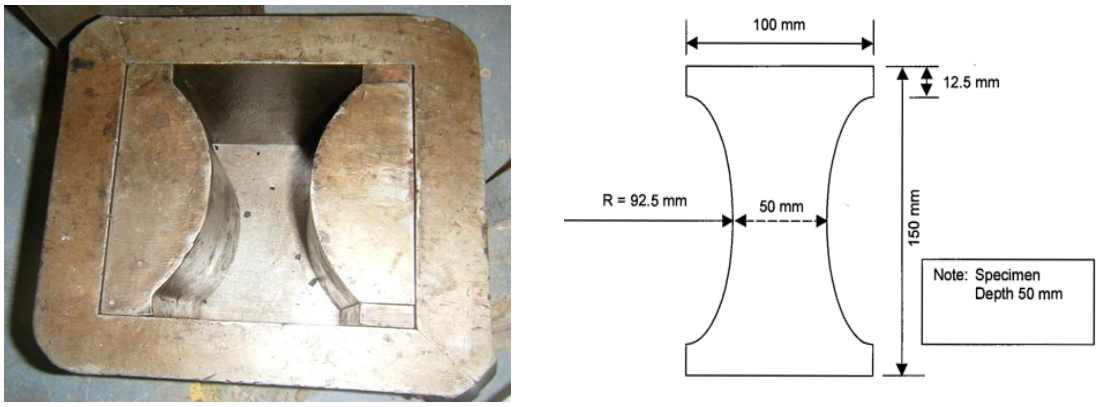

Picture 4-7 Mould and Volumetric of dog-bone specimens

The material was compacted until the specimens achieved the required depth and therefore the desired density and air void content. The compaction procedure was optimised for the virgin specimens and 4.1 % air voids content was obtained as optimum target to achieve a trimmed specimen with the desired 2.6 % air void content.

It was more difficult to compact the reclaimed asphalt mixes and to achieve the desired void ratio. The reclaimed asphalt mix was found to be more resistant to compaction and 2.8 % – 3.2 % was the lowest air void content achieved.

4.1.2.4 Specimen Manufacture - Compression Tests

Specimens were placed between two round metal plates. A sandwich of two plastic disks (used for the gyratory compactor) and soap was placed between the sample and the round plates. This is necessary to drastically reduce frictional effects which can cause overestimation of peak strength (Picture 4-8).

Strain gauges (LVDTs) were placed on the top of the specimens to measure the vertical displacement for the whole height of the specimen (120 mm) which represents the strain gauge used for calculations. A ring equipped with an LVDT calibrated to measure radial displacement was placed around the specimen to measure radial strain. Once all of the instruments have been attached, the specimen must remain in the closed cabinet for at least 2 hours before the testing is started. The temperature inside the cabinet was set to 25 ºC; defined as room temperature and was kept constant as the behaviour of the asphalt also varies with temperature.

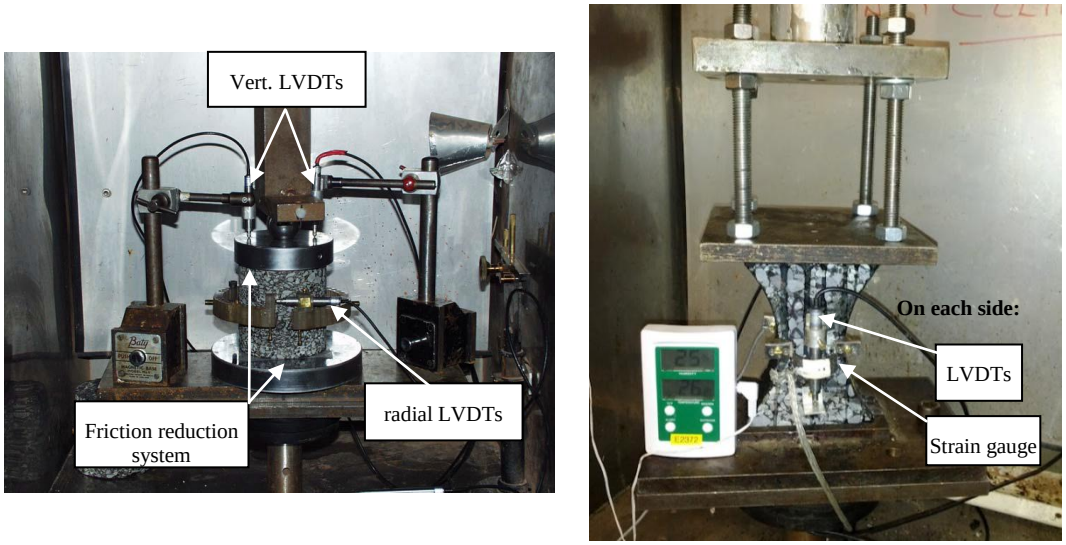

Picture 4-8 Specimen installation for Compression tests (left) and Tension tests (right)

4.1.2.5 Specimen Manufacture - Tension tests

Once the specimens had been produced, each specimen was marked in order to determine the centres of the specimen both vertically and horizontally. Following this, two horizontal lines are drawn at a distance of 30 mm above and below the centre line. This process is repeated on each side of the specimen. The 60 mm distance between these two lines indicates the area of the specimen where the behaviour was considered homogeneous. This length was therefore used as strain gauge for post calculations. Araldite 2 component glue was then used to rigidly fix the specimen to the platens, allowing the specimens to be attached to the testing equipment. Once the glue was applied, the sample and the plates were held by a jig to ensure that the platens and the specimen remained parallel for the 24 hours while the glue set. Each sample was removed from a temperature controlled environment and placed into the equipment.

Once the bottom platen was attached to the bottom platform of the testing machine, it was raised to allow the top platen to join with the top plate of the testing machine (Picture 4-8). This was done using nuts and bolts in each corner. LVDTs and omega strain gauges were attached to the front and back of the specimens allowing

measurements of displacement vertically and horizontally. The average front and back displacements were used to calculate the horizontal and vertical strain. The samples for tension tests undergo the same temperature control as the specimens subjected to compression.

4.1.3 Indirect Tensile Tests at Technical University Dresden

Different repeated load test methods have been established worldwide to investigate the stiffness and fatigue characteristics of asphalt mixes. The results of the fatigue tests can be used as input parameters for a mechanistic-empirical pavement design procedure. For the pavement design procedure the stiffness and the fatigue resistance of the asphalt mixes should be known in order to estimate the appropriate lifetime of the pavement structures. These characteristics can be obtained by various fatigue tests like bending, direct and indirect tensile tests. Fatigue parameters of asphalt mixes are commonly determined using the results of repeated load tensile tests. These parameters and the E-Modulus-temperature-function are required for the pavement design process. Different repeated load tests have been established in Germany and worldwide to determine the fatigue behaviour of asphalt mixes.

Within WP5 indirect tensile tests were carried out to determine the required parameters for the pavement design process. Due to technical problems at the participating institute of the University College Dublin the scheduled indirect tensile tests on the three asphalt mixtures had not yet been completed when conducting the pavement design life calculation (see chapter 9). To ensure the pavement design life calculation TU Dresden conducted additional indirect tensile tests to obtain the stiffness and fatigue properties of the selected asphalt mixes. Picture 4-9 shows the testing device used at TU Dresden.

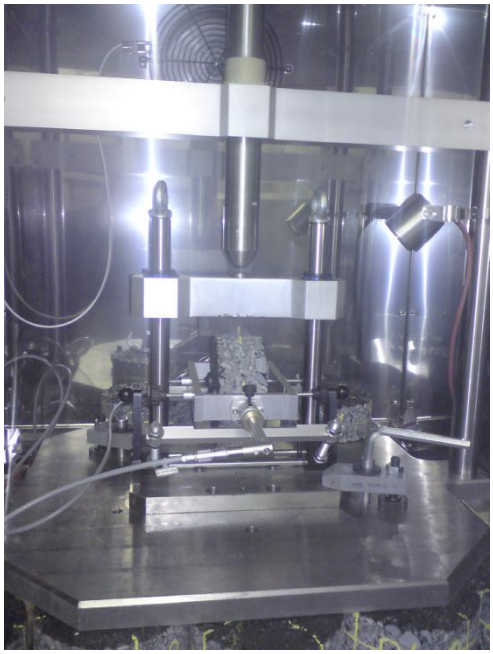

Picture 4-9 ITT testing device at TU Dresden

During testing, the resultant horizontal deformations are measured for a cylindrical specimen, which is loaded by two diametrically arranged compressive forces applied via curved load distribution bars. During the ITT a repeated load is applied to the specimen up to a defined criterion for test termination (fatigue crack). The ITTs were run in force-controlled mode. The horizontal displacement of the sample was measured using two Linear Variable Differential Transformers (LVDTs).

The test specimens had a diameter of 100 ± 3 mm and a height of 40 mm. Table 4-5 shows the test conditions for the ITTs.

Table 4-5 cyclic ITTs – Test Conditions

Parameter	Performed test condition
Wave	sinusoidal stress, without cycling through zero
Frequency f [Hz]	10
Duration of Loading [s]	1/f
Rest period [s]	none
Test Temperature [°C]	+20
Lower Stress	contact stress
Upper Stress	triple variation

The contact stress or lower stress level was 0.035 N/mm². The maximum stress level (upper stress level) for each test was determined in dependency of the aspired initial elastic strain values of 0.05, 0.10 and 0.15 ‰.

4.1.3.1 Asphalt Sample Preparation

Cylindrical test samples of 100 mm diameter were drilled from asphalt slabs in x-direction (see Figure 4-2). The asphalt slabs of a size of 320 mm x 260 mm x 40 mm were also compacted with a Roller Sector Compactor.

4.1.4 Indirect Tensile Tests at University College Dublin

To determine the fatigue properties of the bituminous mixtures, a series of tests were employed based on the standard fatigue test as described in EN 12697 Part 24. This involved testing cylindrical samples in indirect tension.

4.1.4.1 Compaction

To manufacture the appropriate test samples, the following steps were employed:

1. The premixed SMA material was heated in an oven at 160 °C for 5 hours. The required mass of material was then weighted and transferred into a preheated steel mould of dimensions 400 mm x 305 mm x 100 mm, as shown below in Picture 4-10.

2. The bulk density of each of the mixes was 2391 kg/m3. This resulted in the design mass of the specimens being 29.170 kg. The heated material in the mould was then compacted using a Cooper Technology Roller Compactor, shown below in Picture 4-11 .
3. The steel roller compactor head was preheated to 145 °C to minimise heat losses during compaction. The temperature of the mix in the mould prior the compaction was in excess of 140 °C and in excess of 100 °C subsequent to compaction. After the mould and specimen had been allowed to cool for 30 minutes, the mould was removed and the specimen was allowed to cool further to ambient temperature as shown in Picture 4-12.

Picture 4-10 Heated material in steel mould

Picture 4-11 Samples placed in roller compactor (sheets of paper used to prevent material sticking to roller)

Picture 4-12 (a) Compacted specimen slab (b) Compacted specimen slab with steel mould removed

4.1.4.2 Coring

After allowing the compacted specimen slabs to cool to ambient temperature for 24 hours, six cylinders of nominal 100 mm diameter were cored from the slab. The coring operation is shown in Picture 4-13.

After the cylinders were cored from the slab, a test specimen of nominal thickness 40 mm was sliced from the middle of the cylinders using a circular saw. This is shown in Picture 4-14.

Picture 4-13 Coring of cylinders from specimen slab

Picture 4-14 (a) Cylinders cored from specimen slab (b) slicing of cylinders

4.1.4.3 Specimen Preparation

The mass of each individual specimen was then recorded. The mean of four measurements of both the diameter and the thickness of the specimen was also recorded.

The faces of the specimens were then marked with two diametrically opposed centrelines, representing the vertical and horizontal plane. The horizontal deformation of the specimen was measured on both faces of the specimen using LDVTs. The deformation over the centre 40 mm portion of the specimen was recorded. Fixtures and brackets to secure the LDVTs in place during the test were bonded to the specimen using adhesive. This is shown in Picture 4-15.

The specimens were stored in a temperature controlled cabinet, which also contained the testing apparatus, at the test temperature of 10°C.

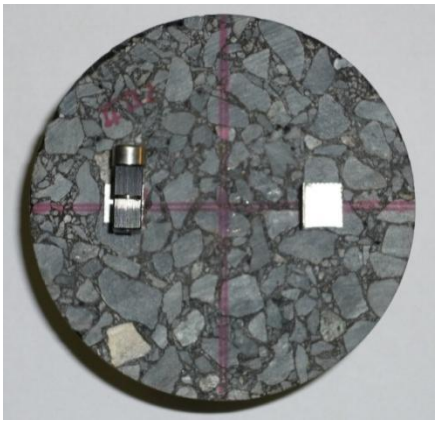

Picture 4-15 Specimen marked and with fixtures bonded to it

4.1.4.4 Specimen Testing

The indirect tensile fatigue and healing tests were conducted using a Cooper Technology Servo-Pneumatic Universal Testing Machine NU-10 apparatus, shown in Picture 4-16 (left).

Picture 4-16 Cooper Technology Servo-Pneumatic Universal Testing Machine NU-10 testing apparatus in temperature controlled cabinet

The specimen was placed in a holding rig with loading strips in the vertical plane as shown in Picture 4-16 (right). A load was applied to the specimen in the vertical axis, while deformation was measured in the horizontal axis over the centre 40mm of the specimen. The testing apparatus was controlled using the Cooper Technology Universal Software. This allowed customised fatigue testing profiles to be used. Two types of testing profiles were used; one with a rest period of 0.1 seconds between each loading pulse and one with no rest period between the loading pulses.

The three mixes were tested at three different vertical stress levels, with three replicates for each stress level. These tests were conducted with both of the test profiles with rest periods and without rest periods between the loading pulses. A summary of the test conditions is given in Table 4-6 parameters for fatigue and healing program. When initially designing the testing programme the intention was to test the samples at vertical stress levels of 0.2, 0.4 and 0.6 MPa as these would be representative of the typical pavement loading encountered in service. It was however found that the reference mixtures were extremely resilient and significantly higher stresses were required so as to obtain a pavement failure in a reasonable time frame.

Table 4-6 Parameters for fatigue and healing test programme

Parameter	Description
Waveform	Haversine
Frequency [Hz]	10
Duration of Loading [s]	0.1
Rest period [s]	0 or 0.1
Test Temperature [°C]	10
Lower Stress	Holding load
Peak stress [vertical, MPa]	1.5; 2.0; 2.5

4.2 Laboratory Performance Tests on bituminous Binders

4.2.1 Bitumen Tests at Technical University Dresden

In a first step the values needle penetration and ring and ball were determined of the binder reclaimed from the asphalt mixtures (Table 4-7). Due to the in-homogeneity of the RA the final binder content of the asphalt mixes was varying.

The needle penetration value as well as the SP R & B shows that with an increasing RA content the binder is getting stiffer.

Table 4-7 Properties of the binders investigated

Properties	Material I	Material II	Material III
RA content	0 M.-%	15 M.-%	30 M.-%
Binder content	6.55 M.-%	5.63 M.-%	7.20 M.-%
Needle penetration value [1/10 mm]	34	32	20.5
SP Ring and Ball [°C]	63.3	66.2	69.6

Table 4-8 DSR Test Parameter

Parameter	Value
Test mode	Strain controlled
Temperature	30 °C to 90 °C at intervals of 5 k
Frequency	10 rad/second
Spindle Geometry	25 mm ø, distance 1 mm

In a second step, Dynamic Shear Rheometer (DSR) tests were undertaken on the same binder in order to investigate the rheological properties (complex shear modulus (G*) and the phase angle (δ)) of the materials (Table 4-8).

The visco-elastic parameters being measured by the DSR apparatus are specimen's complex shear modulus (G*) and phase angle (δ). Complex shear modulus is defined as the ratio of maximum (shear) stress to maximum strain and provides a measure of the total resistance to deformation when the binder is subjected to shear repeated loading.

The results of the bitumen tests undertaken at TU Dresden are summarised in section 5.2.2.

4.2.2 Fatigue and Healing at University College Antwerp

The main task of RERS is to investigate the healing and fatigue characteristics of binders and mastics in their both virgin and aged condition. For rheological tests, a Dynamic Shear Rheometer (DSR) was used in its standard and modified settings.

These results can then be evaluated with fatigue and healing properties of asphalt mixtures, provided by other partners.

4.2.3 Materials and Description of Equipment

For binder and mastic testing, the following binders, mastics and mixtures are considered:

Table 4-9 List of materials used for binder tests

Material	Description
Material I	Asphalt mixture I, containing 0% RA, the reference material
Material III	Asphalt mixture III, containing 30 %RA
RA	Reclaimed Asphalt Aggregate, origin : porous asphalt
Binder I	Virgin binder, used as binder in Material I, PmB 25/55-55A (PmB 45A)
Binder II	Virgin binder, used as partial new binder in Material II and III
Binder RA	Extracted and Recovered binder from RA
Binder II+RA	Mixture of binder Binder II and Binder RA
Binder Material I	Extracted and recovered binder from Material I
Binder Material III	Extracted and recovered binder from Material III
Binder I RCAT	Binder I after Long Term Ageing RCAT
Binder II+RA RCAT	Binder BII + RA after Long Term Aging RCAT

4.2.3.1 Asphalt Mixtures

Material I is used as reference mixture and contains 0% RA. The binder properties after extraction and recovering are given in Table 4-10.

Table 4-10 Rheological Data Binder Material I after extraction and recovering (source: TU Dresden)

I.D.	PmB 25/55-55A (PmB45A)
Penetration [dmm]	34
Softening Point [°C]	62.4 – 64.2
Viscosity (Rot. 135°C) [Pa.s] Viscosity (Rot. 150°C) [Pa.s]	1.74 0.63

Material II, containing 15% RA, is not taken into account for binder nor mastic tests.

This analysed mixture is manufactured containing 30% RA. The binder properties after extraction and recovering are given in Table 4-11. The mixture is composed by adding 30% RA to virgin aggregates and new binder II.

Table 4-11 Rheological Data Binder Material III after extraction and recovering (source: TU Dresden)

Properties	Binder Material III
Penetration [dmm]	20- 21
Softening Point [°C]	70.8 - 68.4
Viscosity (Rot. 135°C) [Pa.s] Viscosity (Rot. 150°C) [Pa.s]	2.71 1.06

4.2.3.2 Manufacture of the composed binder: Binder II + RA

Binder II+RA was manufactured as a mixture of binder II and binder RA. It was aimed to a mixed binder, which composition was equal as applied in the asphalt production of Material III. For the estimated ratio in Material III, the calculation is explained in Table 4-12.

Table 4-12 Binder mixture composition for Binder II + RA

Material	Dry composition Material III	Binder Content [%]	Binder "on" [%]	Partial Binder	Binder comp. [%mix]	Ratio Binder [%binder]
RA	30% RA aggregates	8.14	8.87	2.66 Binder RA	2.44	34
New Materials	70% New Aggregates	-		5.1 Binder II	4.76	66
B II+ RA				7.76		
Material III	100% dry Material	7.2	7.76	7.76	7.2	100

The binder mixture was manufactured after heating both binders (max. 80 °C above softening point) and mixing during approximately 10 minutes.

4.2.4 Definition and Composition of Mastic

For the mastic design, the assumptions described by Van den bergh (2011) were considered: The mastic is composed by a part of the total binder volume and all the aggregates smaller than 0.125 mm. In order to define the binder content of the mastic, the following assumptions were proposed:

- all aggregates and filler particles are coated with a thin binder film of about 5 µm. A part of this binder is absorbed. In this work, the dry mastic mix is composed by aggregates with dimensions smaller than 0.125 mm and the filler. In this case, the binder volume which coats the aggregates with dimensions larger than 0.125 mm must be subtracted from the total binder content;

- the binder volume which is not part of the volume for wetting and absorption is taken into account as 'free binder'. This volume is the total volume of binder decreased with the binder volume that coats the aggregates;
- mastic glues the coated aggregates, equal and larger than 0.125 mm, together.

The mastic composition is defined as the bituminous mixture of the dry aggregate passing the sieve of 0.125 mm (a_{125}), the filler (f) and the reduced bitumen content (b_R). The reduced bitumen content is defined as the total bitumen volume in the mixture minus the bitumen that coats the aggregates with dimensions larger than 0.125 mm.

$$Mastic = a_{125} + f + b_R \tag{4-12}$$

The binder volume used as coating is calculated as 5 µm thickness on all surfaces of filler and aggregates. The specific surfaces are estimated by using the method developed by Hveem-Edwards (Hveem, 1974 and Roberts et al., 1996). For Material I, the summary is given in Table 4-13.

Table 4-13 Summary aggregate coating Material I

Surface Factor	Sieve [mm]	Passing [%]	Surface Area [m²/kg]
0.410	14.000	100	0.41
	9.500		
0.410	4.750	32	0.13
0.820	2.360	26	0.21
1.640	1.180	20	0.33
2.870	0.600	16	0.46
6.140	0.300	14	0.86
12.290	0.150	12	1.47
32.770	0.075	11	3.54
		sum	7.42
		Coating 0.125 mm	4.52
		Coating 0.500 mm	6.18

For wetting 1000 g aggregates with 5 µm binder, 38.03 g binder is needed (7.42 m² * 5 µm * 1025 kg/m³). In this case, 1.48 % of the total binder quantity (6.95 %) is used for coating the aggregates, which have dimensions larger than 0.125 mm; 3.8 % is free binder, and 2.32 % is for coating the aggregates smaller than 0.125 mm.

Some first mastic tests were done on the mixture of Material-composition together with binder BII+RA: the results are labelled Mastic II+RA. In this case, the effect of binder used for Material III can be directly compared to Binder I (=binder Material I), or in other words, the effect of using RA-binder instead of virgin binder.

Table 4-14 Summary aggregate coating Material III

Surface Factor	Sieve [mm]	Passing [%]	Surface Area [m²/kg]
0.410	14.000	100	0.41
	9.500	73	0
0.410	4.750	30	0.12
0.820	2.360	22	0.18
1.640	1.180	20	0.33
2.870	0.600	17	0.49
6.140	0.300	15	0.92
12.290	0.150	14	1.72
32.770	0.075	13	4.26
		sum	8.43
		Coating 0.125 mm	5.41
		Coating 0.500 mm	7.23

For Material III, the summary is given in Table 4-13. For wetting 1000 g aggregates with 5 µm binder, 43.2 g binder is needed (8.43 m² * 5µm * 1025 kg/m³). In this case, 1.55 % of the total binder quantity (7.76 %) is for coating the aggregates with dimensions larger than 0.125 mm; 3.44 % is free binder, and 2.77% is for coating the aggregates smaller than 0.125mm. As previously defined, the mastic is composed with free binder and binder coating aggregates smaller than 0.125 mm. For the mastic of mixture I and III, the design values are given in Table 4-15. Given for Material III, no distinction can be made in filler and other fines, these parts are added together in one value.

The mastic tests (master curves, fatigue and healing tests) will be done using the DSR in plate-plate configuration (8 mm plates and 2 mm gap). In a second step, the mastic tests will be performed using cylindrical test samples (diameter 5 mm and height 10mm). These samples have metal rings (diameter 7mm and height 8mm) on which special clamps, attached on the DSR shaft which will provide torsion. The samples are prepared using a special mould.

Table 4-15 Mastic design values

Component	Material I		Material III	
	[m/m%]	[v/v%]	[m/m%]	[v/v%]
a_{125}	21	13	69	45
f	47	31		
b_R	32	56	31	55

4.2.5 Test Equipment

4.2.5.1 Dynamic Shear Rheometer

For rheological tests, a dynamic shear rheometer (DSR) has been used in its standard and modified settings. In Picture 4-17, the MCR300 workstation at Artesis University Colleges is shown.

Picture 4-17 MCR300 Dynamic Shear Rheometer

For binders, the standard plate-plate configuration (EN14770) is used with plates 8mm (≤ 25°C) and 25mm (≥ 25°C). For the fatigue and healing tests on binders and mastics, the 8 mm plate is selected.

For the laboratory-ageing of binders, a number of tests and ageing devices are developed during the last decades. These tests can be classified into three groups: i) tests using heat flow by means of an oven, ii) tests using heat and pressure and iii) tests in combination with UV. Considering the ageing time scale, mostly a short term and long term ageing process is performed.

In Belgium, three types of ageing tests are used: RTFOT, PAV and RCAT. In Table 4-16, the specifications for these tests are given. RTFOT is developed to simulate the hardening of the binder during mixing, transport and compaction of the asphalt mixture. RCAT and PAV are used for simulating the long term ageing of binders. References for these tests can be found in the respective standards and in the Bitval-report.

The RCAT test and its device is developed for ageing binders and mastics in the laboratory. 500 to 550g of binder or mastic is conditioned in a stainless steel testing cylinder which rotates during the test. In this cylinder also a solid bar is introduced which makes a gravity rotating movement. This roller will press and distributes the binder (mastic) in the cylinder. The cylinder has a central opening on the front which allows the sampling of small specimens during ageing tests.

Table 4-16 Summary of the specifications of RTFOT, PAV and RCAT ageing tests

Method	Short Term Ageing STA		Long Term Ageing LTA		
	RTFOT	RCAT163ST	PAV100	RCAT85LT	RCAT90LT
Standard	EN 12607-1 ASTM D2872	EN15323	EN 14769 AASHTO PP1-98		EN 15323
Test type	Dynamic		Static	Dynamic	
Quantity	8 * 35g	500–550 ml	10 * 50g	500- 550 ml	
Duration	75 min	235 min	20h	240h	140-144h
Gas	Air	air	air	Oxygen	
Gas flow (l/min)	4		-	0.075	
Temperature	163		100	85	90
Pressure (MPa)	0.1		2.1	0.1	
Approx. film thickness (mm)	1.25	2.5	3.2	2.5	

Short term ageing is performed at 163°C using a continuous flow of air (4.0l/min) during 235 minutes. For the long term ageing the binder or mastic is conditioned at 90°C during 140-144 hours by means of a flow of oxygen (0.075 l/min).

Figure 4-11 RCAT device at RERS-Antwerp (external and internal view)

Since in this ageing device both binder as mastic samples can be aged in a large quantity, this test is selected.

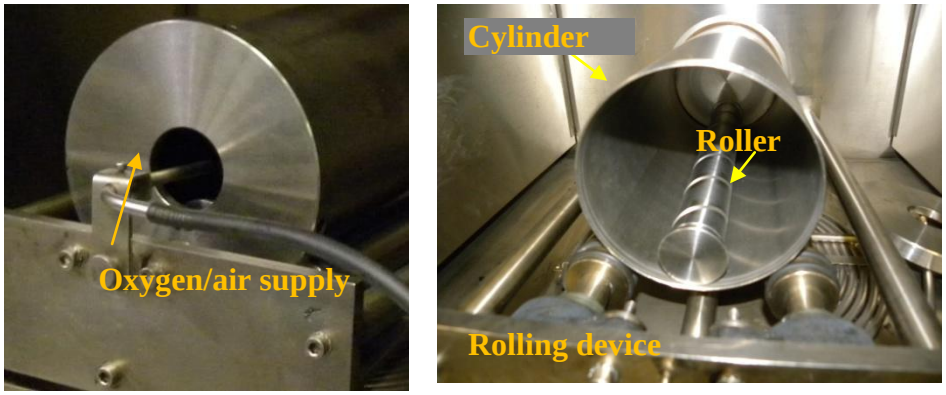

Figure 4-12 RCAT device at RERS-Antwerp (internal view right)

4.2.5.2 InfraRed Spectrofotometer

The ATR/FTIR spectrometer Thermo Scientific Nicolet iS10 of UCA, is equipped with a special Smart Orbit Sampling Accessory, which allows squeezing the sample up to a constant height. The crystal which is used is a diamond, permitting spectra between 30000 and 200 cm^{-1}. For testing bituminous binders, a diamond crystal is the best choice considering the broad spectra range, its durability and chemical inertness. Before each sample was tested, a background scan check was performed.

Table 4-17 Selected binders for Infrared Measurements

Binder	Binder state
Binder I	Virgin
Binder I ST	Binder I after Short Term ageing RCAT
Binder I_24	Binder I after Short Term ageing RCAT + 24 hours Long Term Ageing
Binder I_96	Binder I after Short Term ageing RCAT + 96 hours Long Term Ageing
Binder I RCAT	Binder I after Short Term ageing RCAT + 144 hours Long Term Ageing
Binder II + RA	Mixture of binder II and RA-binder
Binder II + RA RCAT	Mixture of binder II and RA-binder after Long Term ageing

This background check is done to avoid disturbances related to the apparatus and environment occurrences and consists of one or more scans of the system without a sample on the crystal. In that case, only the crystal and atmosphere are detected. The sample is heated in order to homogenize the sample and to be able to take a small quantity (one drop) with a spatula. The sample is cooled down to ambient

temperature and after cooling, placed on the base plate and squeezed between the spindle and the base plate with the crystal.

Next, the sample is scanned with an infrared beam. In this apparatus, only one reflection is performed. Increasing the number of scans reduces noise. The background scan check and sample scans were performed with 32 consecutive scans, with a resolution of 4 cm^{-1}. The scanning of each specimen was conducted in the Middle Infrared Region (400 – 4000cm-1).

The software OMNIC was used to process the interferogram into an absorption diagram ('spectrum') by Fourier transformation for further analysis. After the measurement was completed, the plate was cleaned with trichloroethylene and acetone. Seven binders were selected for Infrared analysis, given in Table 4-17.

4.2.5.3 Selection of Ageing Indicator

Selection of Ageing Indicator: Rheology and Infrared Measurements

Two binders and one mastic are aged by RCAT:

- Binder I RCAT: Binder I, short and long term aged conform EN 15323
- Binder II+RA RCAT: Binder II+RA (composed binder), short and long term aged conform EN 15323
- Mastic I RCAT conform EN 15323
- Mastic II+RA RCAT conform EN 15323

The EN15323 describes the ageing test, given in Table 4-16, as a short term ageing procedure followed with a long term ageing procedure for 140-144 hours. In this project, the binder ageing of binder I is tracked with rheological and chemical ageing indices in order to evaluate the ageing after 144 hours.

Ageing of bitumen has an effect on the chemical composition of the material; this can be studied with FTIR –although on a semi-qualitative way for C=O and S=O. The chemical changes in the binder will have consequences on the mechanical behavior and the fatigue life. The latter is investigated by the DSR, ageing will result in a lower penetration value - and thus a higher G* since these can be correlated on a logarithmic scale. Ageing will make the material (binder and mixture) more viscous/brittle and the surface tension will rise. This makes it acceptable that an aged binder can have different healing capacities compared to his virgin version. To express the ageing level of a binder several indexes can be calculated. Comparing indexes before and after ageing will give an ageing grade.

Chemical parameters:

$$ICO = \frac{Area \quad 1700cm^{-1}}{Area \;\; 1460cm^{-1} + Area \;\; 1375cm^{-1}} \tag{4-13}$$

$$ISO = \frac{Area\ 1030cm^{-1}}{Area\ 1460cm^{-1} + Area\ 1375cm^{-1}} \quad (4\text{-}14)$$

Where the area around 1700 cm^{-1} represents the C=O oxidation and the area around 1030cm-1 the S=O oxidation. Since the area and peak height measured by the FTIR cannot be measured quantitatively, the areas have to be compared to other ones in the material that are assumed to be present in all binders and not affected by neither ageing nor bitumen origin.

Rheological parameters:

$$AG_{pen} = \frac{penetration_{beforeageing}}{penetration_{after\ ageing}} \quad (4\text{-}15)$$

$$AG_{G^*0.4Hz,25°C} = \frac{G^*_{after\ ageing}}{G^*_{before\ ageing}} \quad (4\text{-}16)$$

4.2.6 Experimental Program

4.2.6.1 Binder Extraction and Recovery

Binder from RA, binder from Material I and binder from Material III were extracted and recovered conform resp. EN 12697-1 (Centrifuge) and EN12697-3 (Rota-evapory). Trichloorethene C_2HCl_3 was used as solvent. Binder RA was used for the mixture Binder II+RA and Binder II+RA RCAT.

4.2.6.2 Binder Ageing

Binder I was aged conform EN15323 (short + long term ageing). Rheological and chemical ageing indices are calculated.

Binder II+RA was aged conform EN15323 (short + long term ageing). Rheological and chemical ageing indices are calculated.

4.2.6.3 Linear Visco-elastic Region and Master Curves

Stress Sweeps were performed on the binders in order to determine the Linear Visco-elastic region.

Fatigue and Healing tests were done beyond the LVER; frequency Sweeps (at constant strain) were performed inside the LVER.

Frequency sweeps were performed in order to generate master curves. At each temperature, LVER-tests were performed in order to confirm the measurements within LVER for each frequency-sweep.

Table 4-18 Test settings for frequency sweeps

Test Type	Frequency Range [Hz]	Temperatures [°C]	Spindles
Frequency Sweep	0.1 - 20 Hz	55, 45, 35, 25, 15 15, 5, -5, -15	25 mm 8 mm

LVER –tests and Master Curves (reference temperature 15°C) were generated for the binders.

4.2.7 Fatigue and Healing Criteria for Binders and Mastic

In literature several fatigue life and healing criteria are defined. It is important to use always the same definition in each assessment.

For binder fatigue constant stress cyclic tests were selected. The fatigue life criterion is defined as the top in the G*x number of cycles plot as shown in Figure 4-13.

Since it is not feasible to perform healing tests with the DSR such as for asphalt mixtures with a hydraulic device (1 cycle loading and x cycles rest), an alternative procedure was defined. For the healing test, which is known as a long lasting test, three different healing procedures were selected.

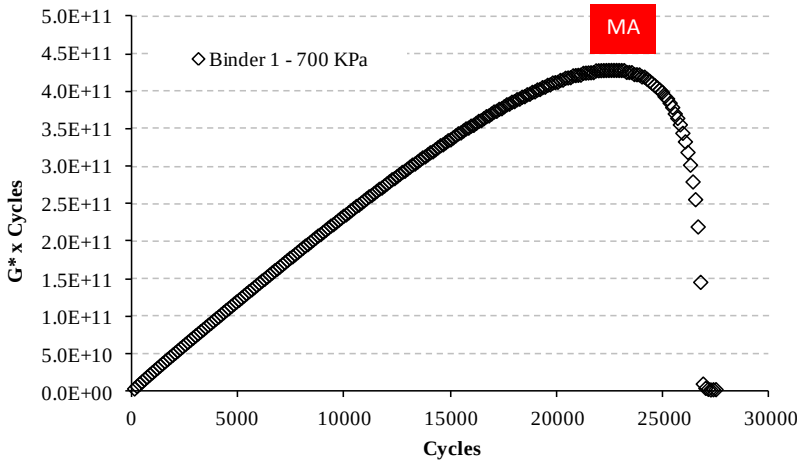

Figure 4-13 Definition of fatigue life

The first procedure was taken as standard. The healing test is performed as a discontinuous fatigue test. This procedure contains two steps in a loop until the maximum value for G* x number of cycles is reached, similar as for the fatigue test. For the fatigue life criterion under healing conditions, the number of loadings is taken. A second healing test was performed on aged binders: a two-step loop of 30 cycles of loading was followed by 70 cycles of rest. A third healing test was performed as 10 cycles of loading during 1 minute followed by rest of 30 minutes; followed by a fatigue test until failure. This test is only done for mastic and selected to investigate healing during longer rest periods.

An interim evaluation of healing tests revealed that the software script did not allow a correct loading signal. This problem was solved after an extensive secondary research (mainly software adaptations), but this problem led to an unfinished healing test program- at the time this report was written. This 'wrong' healing procedure is although taken into account as Healing test 4: in this case, the dissipated energy can be used.

Table 4-19 Healing test types

Healing test 1	3 seconds loading (1 single loading level) , 9 seconds rest
Healing test 2	3 seconds loading (1 single loading level) , 7 seconds rest
Healing test 3	3 seconds loading (multiple loading levels), 9 seconds rest
Healing test 4	10 x (1 minute loading, 3 minutes rest), fatigue until failure

As this report is written, mastic tests are on-going. For the mastic tests, the plate-plate configuration as the cylindrical samples are used. The results will be available after finishing the full test program, as annex or publication.

4.2.8 Preliminary Fatigue and Healing Tests

After a first series of healing tests, some problems occurred for strain and stress loading. Fatigue and healing are commonly expressed as a function of number of cycles and duration of rest periods. An exact calculation of the number of cycles and an accurate control of the specific loading settings are essential in order to evaluate fatigue and healing performance. For an oscillation test, the software of the MCR300 provides two options: stress or strain controlled oscillation tests. For the strain-controlled tests, a specific Direct Strain Oscillation mode (DSO) can be selected. First tests unveiled that for bituminous binders, which are high viscous at 10°C, this DSO cannot function properly and results into a too high strain level. A disturbed strain level during fatigue leads to difficulties for fatigue interpretation. The cause of this malfunctioning for viscous materials can be found in the loading method: in se, the DSR is stress-controlled. The hardware will perform stepwise small changes in stress in order to obtain the input strain; however, for bitumen its performance is too complex and retarded for a correct and real-time adaption. Therefore, stress controlled tests should be more easy to program and perform.

For fatigue tests, the first stress controlled tests showed a correct and continuous shear stress, at low and high stress levels. The stress controlled tests will be selected for fatigue tests.

In order to evaluate the functioning of stress controlled tests during healing tests (discontinuous tests), a series of healing tests with different loading times and stress levels was completed. It was found that a minimum of 10 cycles is needed for obtaining valuable results, e.g. G*. For tracking the fatigue performance during a healing test, it was chosen to select 3 seconds of loading (30 cycles). During these 3 seconds, another problem occurred: after 10 cycles, the stress level increased strongly. According to the supplier, this was also a hardware problem and not easy

to solve. Since, also for these tests, a steady stress level is essential, several software manipulations were tried. The problem was solved with an extra step in the software: the fatigue part was performed as a stepwise stress sweep instead of constant. An example is given below for the first part of the healing test: the fatigue step.

Before correction:

Table 4-20 Output data Healing Test before correction (part: Constant Stress Loading)

Meas. Pts.	Time [s]	Complex Modulus G* [Pa]	Phase Angle Delta [°]	Tempera-ture [°C]	Shear Stress [Pa]	Strain [%]
1	1212.5	2.83E+7	37.7	9.99	919.000	3.24
2	1213.1	2.19E+7	44.1	10	1.55E+6	7.08
3	1213.7	2.22E+7	43.3	9.99	1.16E+6	5.24
4	1214.3	2.26E+7	42.4	10	988.000	4.37
5	1214.9	2.28E+7	42.1	10	912.000	4

In Table 4-21 it is observed that the shear stress, directly related to the applied torque, is not constant during the first part of the healing procedure. The stress should be constant during 3 seconds at approximately 1.0 MPa. The peak stresses at point 2 and 3 will lead to a too high fatigue than expected. This makes the evaluation of the fatigue part during the healing test too complex. After correction in the software, the output is right, as shown in Table 4-21. For this new procedure, the peak stress is similar to the required and more important: constant during the loading period.

Table 4-21 Output data Healing Test after correction (part: Constant Stress Loading)

Meas. Pts.	Time [s]	Complex Modulus G* [Pa]	Phase Angle Delta [°]	Tempera-ture [°C]	Shear Stress [Pa]	Strain [%]
1	1500.8	2.88E+7	34.2	9.99	963.000	3.35
2	1501.5	2.75E+7	35.2	10	1.01E+6	3.65
3	1502.3	2.68E+7	36.1	10	1.01E+6	3.76
4	1503	2.60E+7	36.7	10	1.01E+6	3.89

The importance of this correction, and even as a reminder for data interpretation of future DSR-tests, is high. Without a detailed view on the data and many measurement points, it is not possible to detect larger stresses and strains than defined in the software. For instance, when only the last measurement was plot, this error could not been observed with the standard data setting.

4.2.9 Binder Testing

In Table 4-22, a summary is given for the binder fatigue and healing tests.

Table 4-22 Summary binder fatigue and healing test scheme [I]

Binder	Test	Conditions	
Binder I	Mastercurve	15°C	f-sweeps
	Fatigue	Cyclic single constant stress (603 – 904 kPa)	n = 14
	Healing	Cyclic single constant stress with rest periods Procedure 1	n = 7
Binder BII+RA	Fatigue	Cyclic single constant stress (603 – 964 kPa)	n = 9
	Healing	Cyclic single constant stress with rest periods Procedure 1	n = 6
	Healing	Variable stress Procedure 3	n=7
Binder Material III	Mastercurve	15°C	f-sweeps
	Fatigue	Cyclic single constant stress (804 – 1100 kPa)	n=4

Table 4-23 Summary binder fatigue and healing test scheme [II]

Binder	Test	Conditions	
Binder BII+RA+RCAT	Fatigue	Cyclic single constant stress (1140-1190)	n=8
	Healing	Cyclic single constant stress with rest periods Procedure 1	n=2
	Healing	Variable stress Procedure 3	n=3
Binder I + RCAT	Fatigue	Cyclic single constant stress (1140-1190)	n=5
	Healing	Cyclic single constant stress with rest periods Procedure 1	n = 2
	Healing	Procedure 2	n = 5
Binder Material I	Master Curve	15°C	f-sweeps
	Fatigue	Cyclic single constant stress (667-696 kPa)	n=2

4.2.10 Mastic Testing

In Table 4-24, a summary is given for the mastic fatigue and healing tests.

Table 4-24 Summary binder fatigue and healing test scheme

Binder	Test	Conditions	
Mastic I	Mastercurve	15°C	To be done
	Fatigue	Cyclic single constant stress (1194 – 1507 kPa)	n = 13
	Healing	Cyclic single constant stress with rest periods Procedure 1	n = 4
Mastic BII+RA	Fatigue	Cyclic single constant stress (1507 kPa)	n = 3
	Healing	Cyclic single constant stress with rest periods Procedure 1	To be done

5 Results of Laboratory Performance Tests

5.1 Laboratory Performance Tests on bituminous Asphalt Mixes

5.1.1 Repeated Load Triaxial Tests at Technical University Dresden

5.1.1.1 Cyclic Compression Tests

The compressive dynamic test was used to determine the elastic modulus and Poisson's ratio of the specimen under the action of cyclic stresses. The test provides the material properties needed for the parameter model identification of the elastic-visco-elastic model developed at TU Dresden (see chapter 6).

The realized tests are indicated in Table 5-1.

Table 5-1 Realized repeated load triaxial tests

Material	Temperature [°C]	Frequency [Hz]	σ_1 [N/mm^2]	σ_{23} [N/mm^2]
Material I	-10	1	-0.2; -0.5;	0.0; -0.2
Material II	0	5	-0.7; -1.0;	-0.5; -0.7
Material III	15	10	-1.2; -1.7	-1.0; -1.2
	25		-2.0	
	35			

Determination of absolute modulus $|E_1|$

Step 1: Repeated load triaxial test

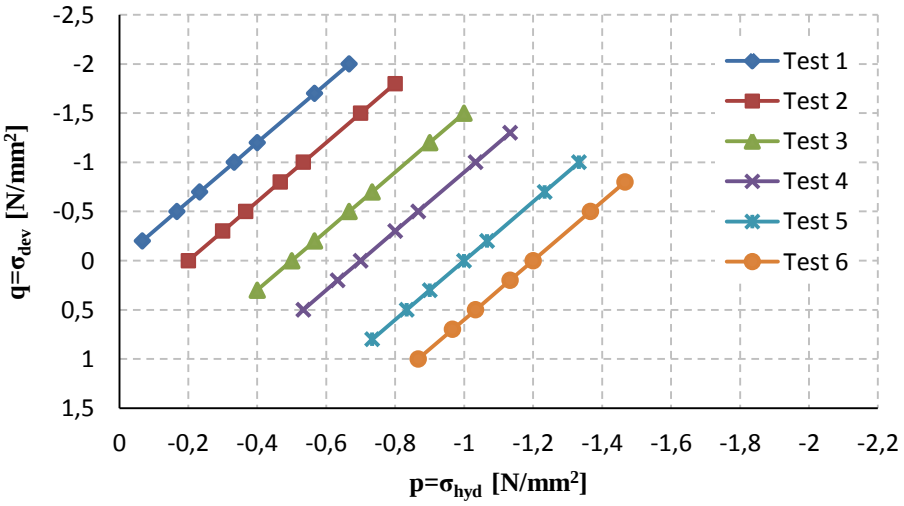

Figure 5-1 Stress path and level of stresses for the realized repeated load triaxial tests

For the characterization of the absolute modulus $|E_1|$ of each material repeated load triaxial tests with seven load cases each at several temperature-frequency combinations were conducted.

The stress path and the level of stress applied on each test are indicated in Figure 5-1.The effective stress path (in the p-q plane) is a straight line with slope equal to 3.

Exemplary Figure 5-2 shows the loading patterns for a test at 0 °C and 1 Hz with seven load cases of ten cycles per case. It can be seen that for each load case the vertical load increases and the cell pressure remains constant.

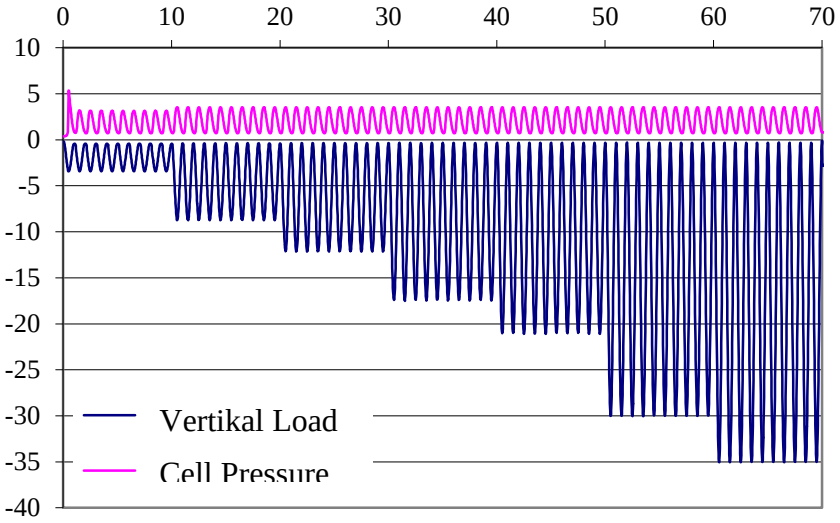

Figure 5-2 Realized repeated load triaxial tests

For high temperatures, a rest period between loading stages was applied to allow transient strains to recover and to prevent the specimen from heating. In our case heating is not a concern because the number of cycles per loading stage is limited to 20.

Step 2: Axial strain

The axial strain was determined with the aid of an Excel spreadsheet developed at the institute of pavement engineering of TU Dresden that extrapolates the test measurements. The axial strains and the linear trend of the strain function in dependence of vertical and horizontal stresses for a test temperature of 25 °C and a frequency of 1 Hz are exemplary shown in Figure 5-3 and Figure 5-4.

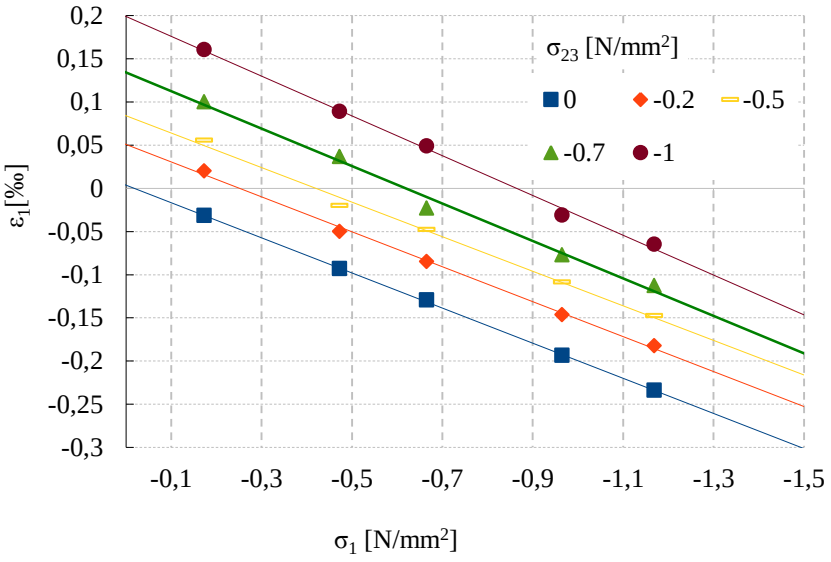

Figure 5-3 ε_1 vs. σ_1 for f=1 Hz and T=25 °C for a constant amplitude of σ_{23}

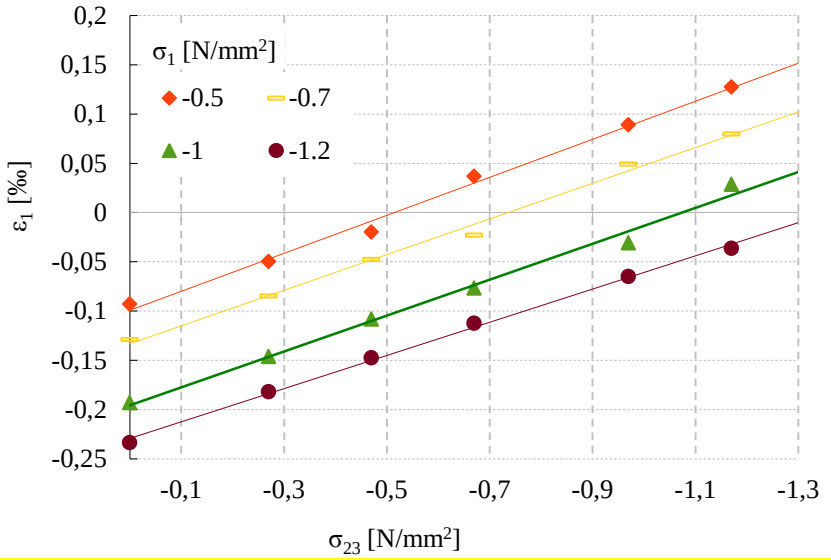

Figure 5-4 ε_1 vs. σ_{23} for f=1 Hz and T=25 °C for a constant amplitude of σ_1

Step3: Surface function

Stress dependent approach

The parameters of the surface function of the axial strain (Equation (4-3)) are indicated in Table 5-2. These parameters are calculated with the method of least squares.

Table 5-2 Parameter of the surface function of ε_1 (stress dependent approach)

Temperature [°C]	Frequency [Hz]	Parameters of the surface function of ε1		
		a_1	a_2	a_3
-10	1	0.0483	-0.0343	-0.0011
	5	0.0339	-0.0231	-0.0007
	10	0.0324	-0.0216	0.0004
0	1	0.0427	-0.0292	-0.0036
	5	0.0407	-0.0296	-0.0056
	10	0.0394	-0.0290	-0.0038
15	1	0.1325	-0.0852	-0.0034
	5	0.0987	-0.0624	0.0013
	10	0.0881	-0.0559	0.0003
25	1	0.2014	-0.1908	-0.0204
	5	0.1454	-0.1309	-0.0094
	10	0.1256	-0.1040	-0.0024

In Figure 5-5 the surface plot of the axial strain (ε_1) at f=1 and T=25°C is exemplary shown. We could see that the surface function fits very well the measurement points.

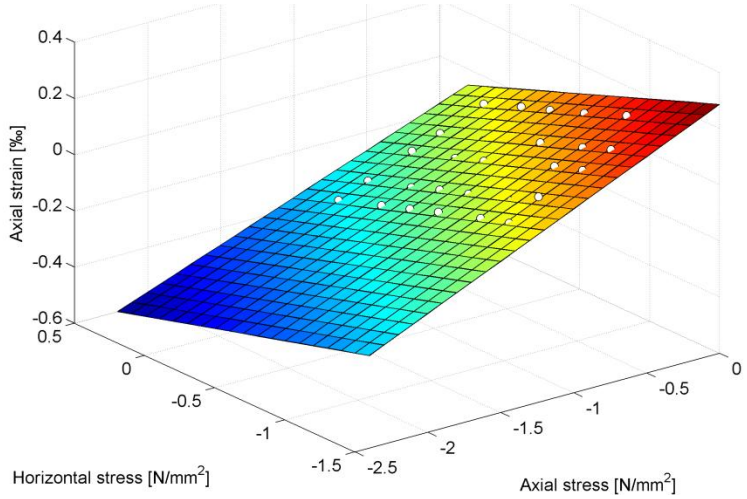

Figure 5-5 Surface plot of axial strain as a function of axial stress and horizontal stress for f=1 Hz and T=25°C

Stress independent approach

The parameters of the surface function of the axial strain (Equation (4-4)) are indicated in Table 5-3. These parameters are calculated with the method of least squares.

Table 5-3 Parameter of the surface function of ε_1 (stress independent approach)

Temperature [°C]	Frequency [Hz]	parameters of the surface function of ε_1	
		a_1	a_2
-10	1	0.0487	-0.0337
	5	0.0341	-0.0226
	10	0.0323	-0.0219
0	1	0.0439	-0.0268
	5	0.0424	-0.0258
	10	0.0402	-0.0258
15	1	0.1336	-0.0830
	5	0.0983	-0.0632
	10	0.0881	-0.0561
25	1	0.2064	-0.1797
	5	0.1472	-0.1254
	10	0.1260	-0.1024

In Figure 5-6, the surface plot of ε_1 for the RLT test at 1 Hz and 25 °C is exemplary shown.

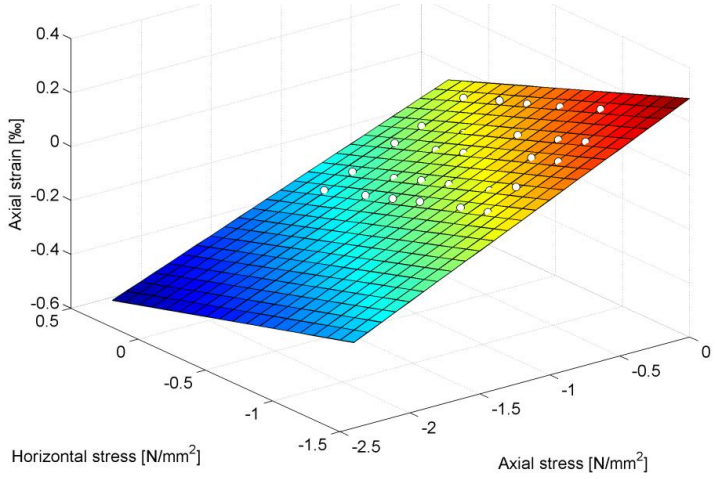

Figure 5-6 Surface plot of axial strain as a function of axial stress and horizontal stress for f=1 Hz and T=25°C

Step 4: Absolute modulus $|E_1|$

Stress dependent approach

The absolute modulus $|E_1|$ is calculated for six different horizontal stresses using Equation (4-5). The resulted stiffness for all temperature, frequency and σ_{23} combinations are indicated in Table 5-4.

Table 5-4 Absolute modulus $|E_1|$ in dependency of σ_{23} for stress dependent approach

T	f	absolute modulus $\|E_1\|$ [N/mm^2]					
[°C]	[Hz]	σ_{23}=0	σ_{23}=0.2	σ_{23}=0.5	σ_{23}=0.7	σ_{23}=1	σ_{23}=1.2
-10	*1*	*20712*	*20622*	*20489*	*20401*	*20270*	*20184*
-10	5	29485	29362	29181	29061	28884	28766
-10	10	30862	30937	31049	31125	31238	31315
0	1	23417	23025	22462	22101	21581	21248
0	5	24557	23894	22965	22385	21568	21055
0	10	25412	24933	24247	23810	23184	22785
15	1	7548	7510	7453	7416	7360	7324
15	5	10136	10162	10203	10230	10272	10299
15	10	11346	11353	11365	11372	11384	11391
25	1	4965	4866	4725	4636	4508	4427
25	5	6878	6790	6662	6579	6459	6381
25	10	7960	7931	7886	7857	7813	7784

It is noted that the absolute modulus at f=1 Hz and T=-10 °C is very low and it does not follows the expected trend. This could be due to an error in the test measurements. For this reason, the results at 1 Hz and -10 °C were not considered in the construction of the master curve.

Figure 5-7 and Figure 5-8 illustrates the trend of $|E_1|$ for the highest and the lowest test temperatures (25°C and -10°C, respectively) for three different frequencies in dependency of horizontal stress σ_{23}.

In Figure 5-8 it can be seen that for low temperatures the asphalt behavior is almost independent of the applied pressure σ_{23}. On the other hand, Figure 5-7 shows a small stress dependency. However, this dependency is not very high as evidenced by the small slope of the curves.

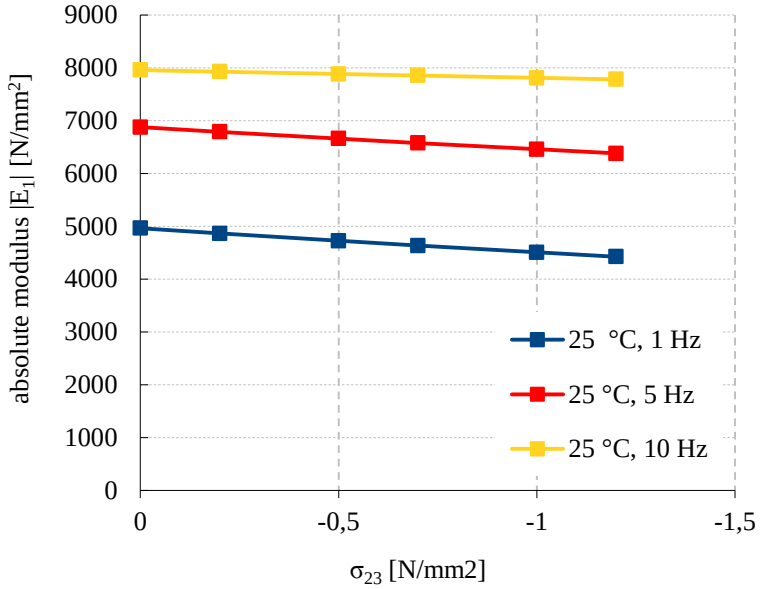

Figure 5-7 $|E_1|$ as a function of frequency and horizontal stress for T=25°C for stress dependent approach

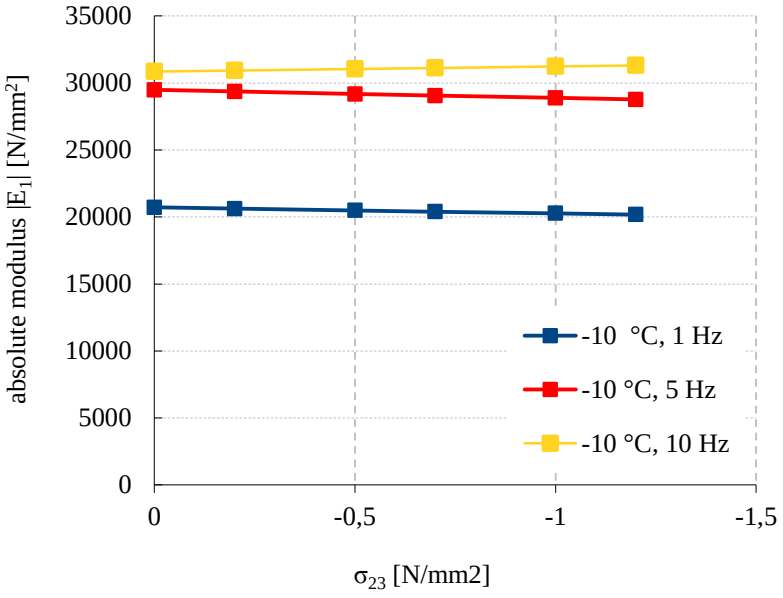

Figure 5-8 $|E_1|$ as a function of frequency and horizontal stress for T=-10°C for stress dependent approach

Stress independent approach

The absolute modulus $|E_1|$ is calculated with Equation (4-6) and the parameters of Table 5-3. The values of $|E_1|$ are listed in Table 5-5.

Table 5-5 Absolute modulus $|E_1|$ for stress independent approach

Temperature [°C]	Frequency [Hz]	absolute modulus $|E_1|$ [N/mm^2]
-10	*1*	*20551*
-10	5	29312
-10	10	30957
0	1	22797
0	5	23603
0	10	24904
15	1	7486
15	5	10175
15	10	11355
25	1	4845
25	5	6794
25	10	7939

Figure 5-9 shows the four isotherms of absolute modulus resulted from the data of Table 5-5.

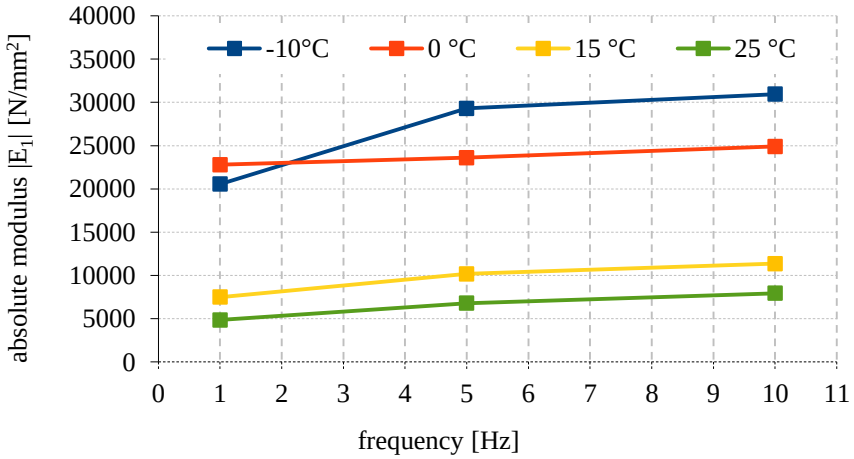

Figure 5-9 $|E_1|$ as a function of frequency for stress independent approach

The absolute modulus $|E_1|$ at 1 Hz and -10 °C was expected to be higher than the modulus at 0 °C. However, the results show the opposite. This discrepancy is evidenced in the trend of the isochrone at -10 °C (Figure 5-9).

Mastercurve of the absolute modulus $|E_1|$

Within the mechanistic empirical pavement design the master curves are used to characterize the stiffness of asphalt mixtures. Asphalt absolute modulus $|E_1|$ is a function of frequency as well as a function of temperature. This dual relation can be described by using a frequency-temperature superposition which is the basic idea behind the master curve.

Stress dependent approach

The parameters a_1, a_2 and a_3 of the regression function of $|E_1|$ (Equation (4-3)) are calculated for six different combinations of σ_{23}. The results are listed in Table 5-6.

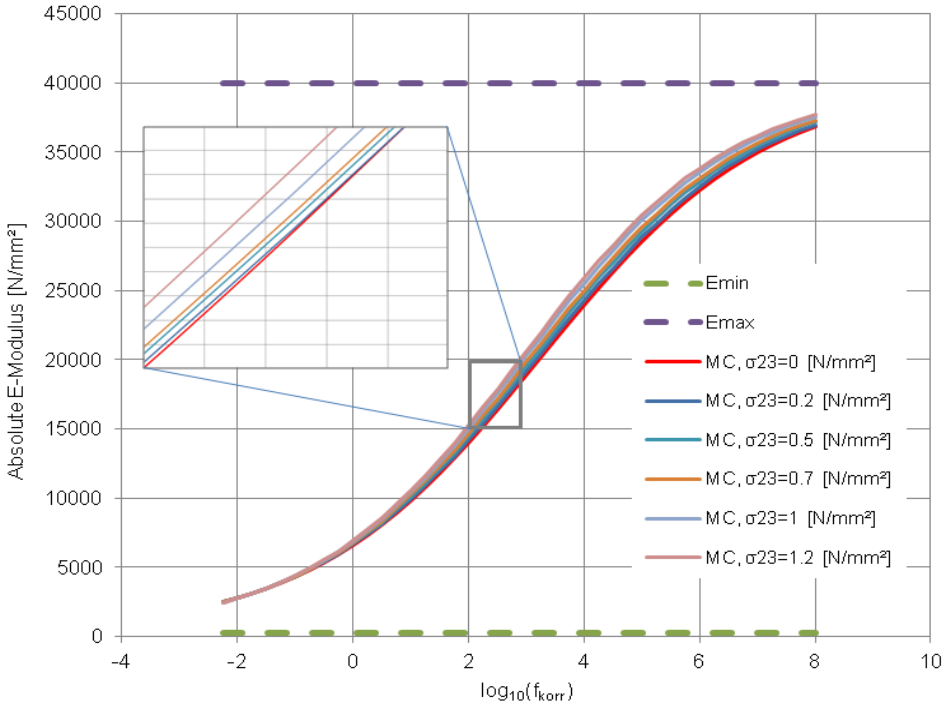

Figure 5-10 Master curves of $|E_1|$ for T_R=20 °C and six different σ_{23}

Table 5-6 Parameters of the regression function of $|E_1|$ in dependency of σ_{23}

σ_{23} [N/mm²]	T_R [°C]	m [-]	E_{min} [N/mm²]	E_{max} [N/mm²]	a_1 [-]	a_2 [-]
0	20	28000	250	40000	3.2380	1.9444
0.2					3.1889	1.9284
0.5					3.1120	1.9013
0.7					3.0583	1.8807
1					2.9739	1.8458
1.2					2.9151	1.8193

Stress independent approach

Analogous, the parameters a_1 and a_2 of Equation (4-4) are indicated in Table 5-5 for the three asphalt mixtures.

Table 5-7 Parameters of the regression functions of the master curves for Material I, II and III

Material	T_R [°C]	m [-]	E_{min} [N/mm²]	E_{max} [N/mm²]	a_1 [-]	a_2 [-]
I	20	29920.2	215	35135	3.1314	1.7845
II	20	28000	250	40000	3.3030	1.9650
III	20	28000	250	40000	4.036	2.479

Figure 5-11 shows exemplarily the regression of the master curve of the absolute modulus $|E_1|$ for T_R=20°C for Material I as well as the corresponding experimental data. The fitting of the experimental data and the interpolated curve is satisfying.

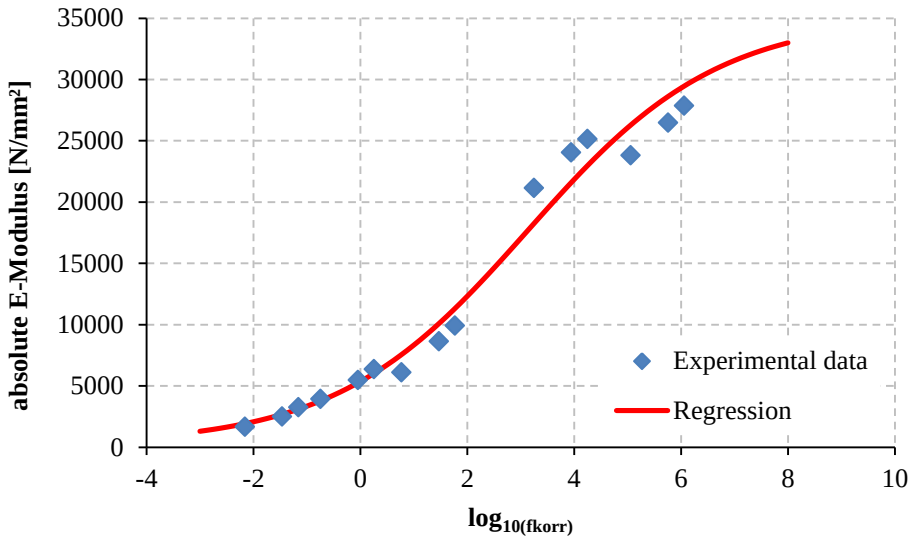

Figure 5-11 Master curve of the absolute modulus $|E_1|$ for T_R=20°C for Material I

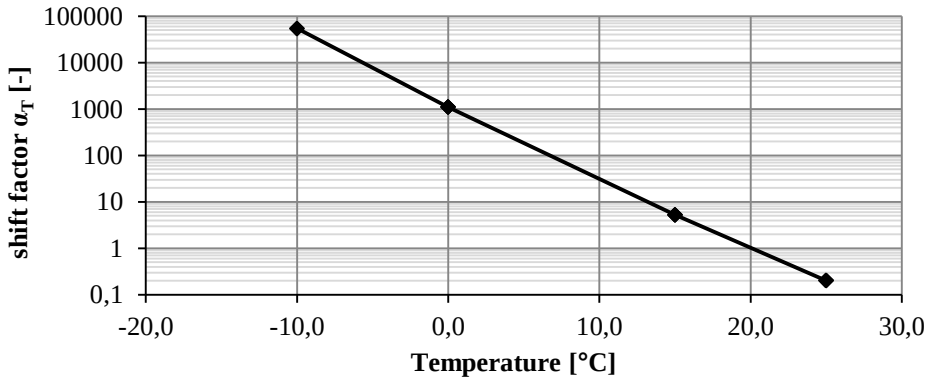

Figure 5-12 Shift factor α_T as a function of temperature

Figure 5-11 shows the master curves of the absolute modulus $|E_1|$ for T_R=20°C for Material I, II and III.

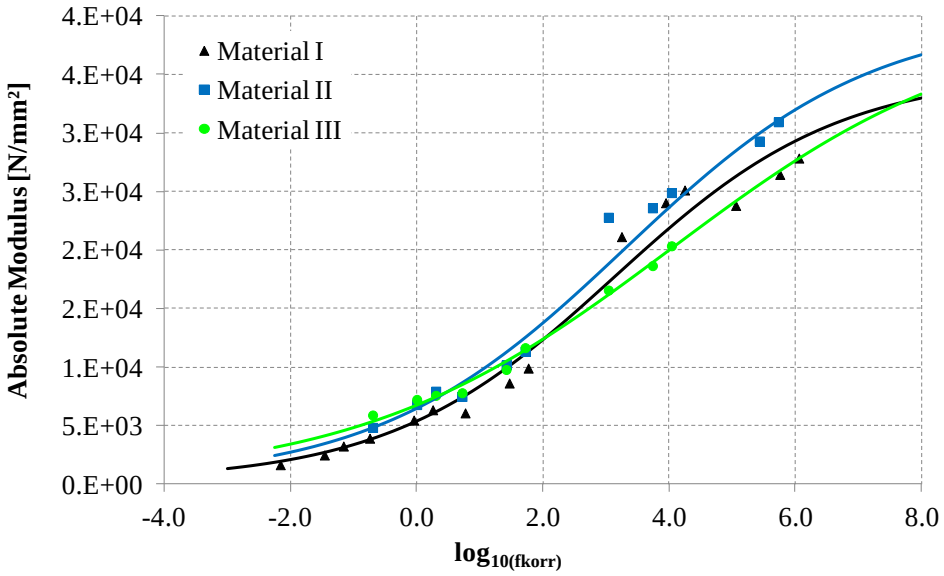

Figure 5-13 Master curves of the absolute modulus $|E_1|$ for T_R=20°C for Material I, II and III

From the comparison of the three master curves it can be concluded, that at high temperatures and low frequencies (i.e. left part of the curve) the stiffness of the two asphalt mixes with RA (Material II and Material III) is higher compared with the stiffness of the virgin mixture (Material I) as expected.

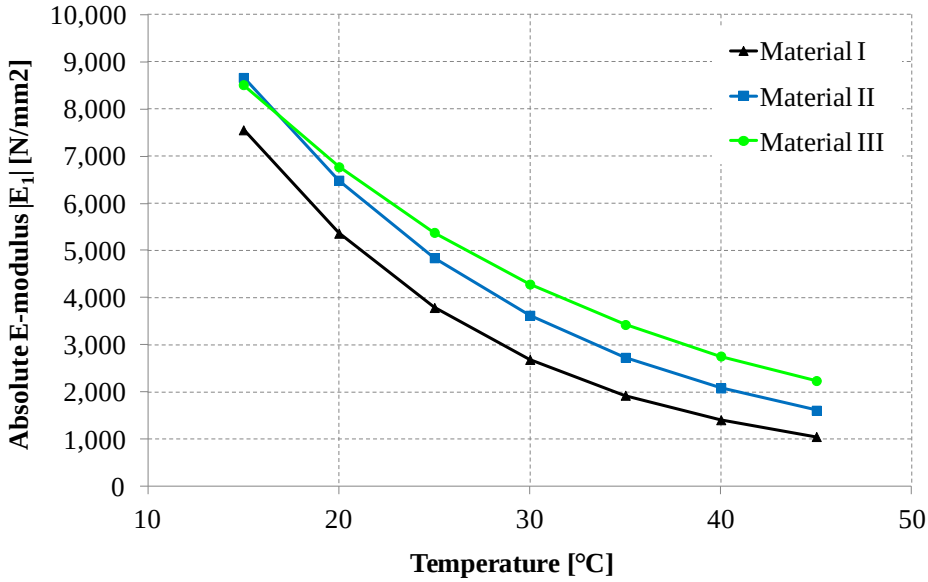

Figure 5-14 absolute modulus $|E_1|$ as a function of temperature for f=1 Hz

This can also be seen in Figure 5-14 where the temperature dependency of the absolute modulus is plotted for a frequency of 1Hz.

Through the use of the master curve and shift factor relationships it is possible to interpolate stiffness at an expanded range of frequencies and temperatures compared with those at which the data was collected.

Phase lag δ vs. absolute modulus $|E_1|$

One way to represent the asphalt mixture rheology is to plot the phase lag against the absolute modulus. Unlike the master curves, this diagram does not require any shifting, thus it is temperature independent.

The parameters a_1, a_2, a_3 and a_4 of Equation 5-1 are indicated in Table 5-8 for the three asphalt mixtures.

Table 5-8 Parameters of the plots of phase lag vs. absolute modulus for Material I, II and III

Material	a_1 [-]	a_2 [-]	a_3 [-]	a_4 [-]
I	0.8582	-0.7525	-3.4381	-0.3410
II	0.8508	-0.8307	-3.4586	-0.3000
III	0.4928	-1.9147	-3.5257	-0.0507

Figure 5-15 shows exemplarily the plots of phase lag vs. absolute modulus over all test temperatures and frequencies for Material I as well as the corresponding experimental data. The fitting of the experimental data and the interpolated curve is satisfying.

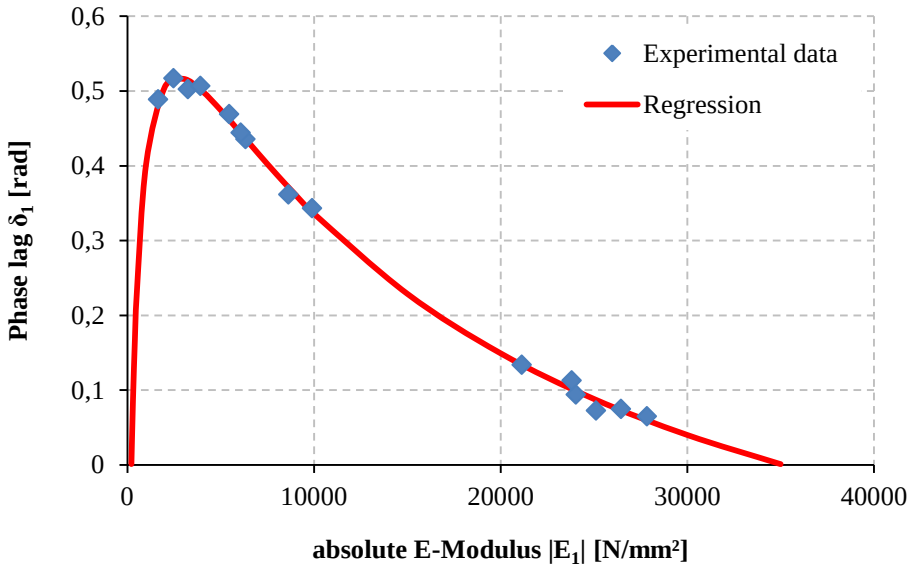

Figure 5-15 phase lag vs. absolute modulus for Material I

In Figure 5-16 the plots of phase lag vs. absolute modulus over all test temperatures and frequencies are indicated for the materials investigated.

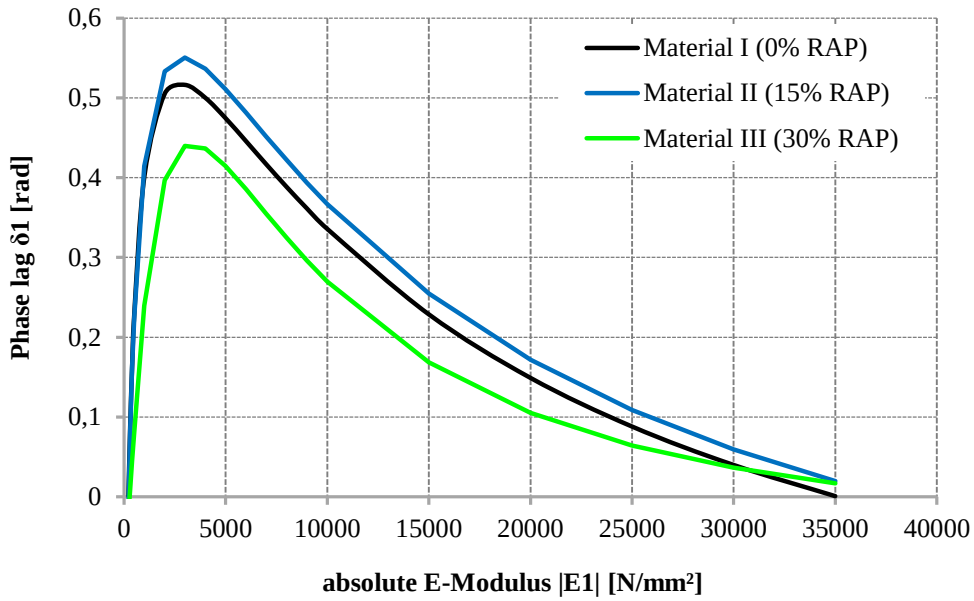

Figure 5-16 phase lag vs. absolute modulus for Material I, II and III

Figure 5-16 shows how Material III appears to be more elastic by having a smaller phase lag compared with Material II with 15% RA and Material I, the virgin mixture. It can be seen that the phase angle increases as the complex modulus decreases. The phase angle reaches a peak at the point where the elastic behavior of the aggregates becomes significant as compare with the visco-elastic behaviour of the binder (Doucet, 2010).

Cole-Cole plot

An alternative diagram that represents the asphalt mixture rheology is the so called Cole-Cole plot. This diagram is the results of plotting the storage modulus E' vs. the loss modulus E''. Figure 5-17 shows exemplarily the Cole-Cole plot for Material I as well as the corresponding experimental data. The fitting of the experimental data and the interpolated curve is satisfying.

In Figure 5-18 the Cole-Cole plots are indicated for the materials investigated.

Material III behaves more elastic than the other two materials. At low temperatures and high frequencies the visco-elastic behavior of Material III differs from the trend observed on Materials I and II but conforms to the theory. The behavior of Material II could base on the significant lower binder content due to the inhomogeneity of the provided RA.

The master curves and the Cole-Cole Plots of the asphalt mixtures investigated are required for the determination of the parameters of the visco-elastic model developed at TU Dresden (see chapter 6).

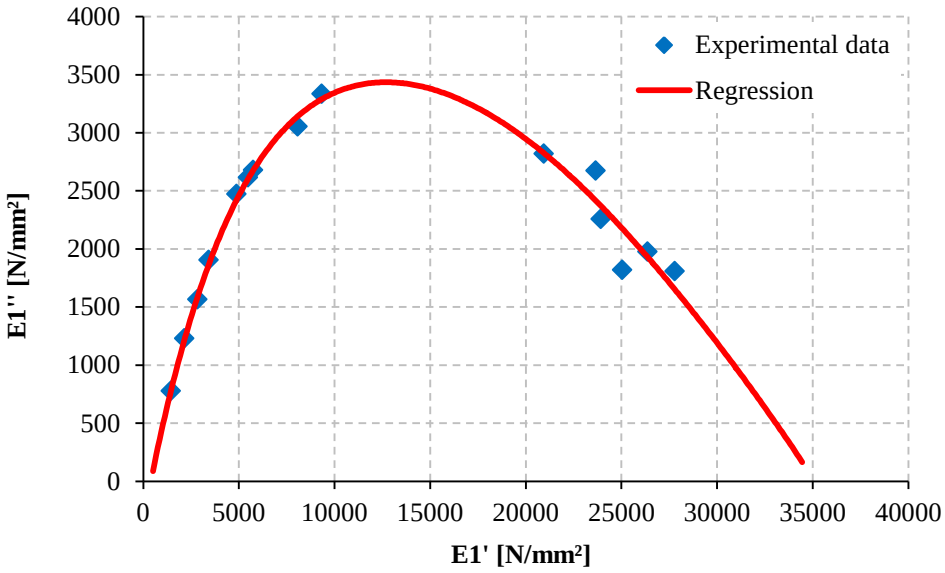

Figure 5-17 Cole-Cole Plots for Material I

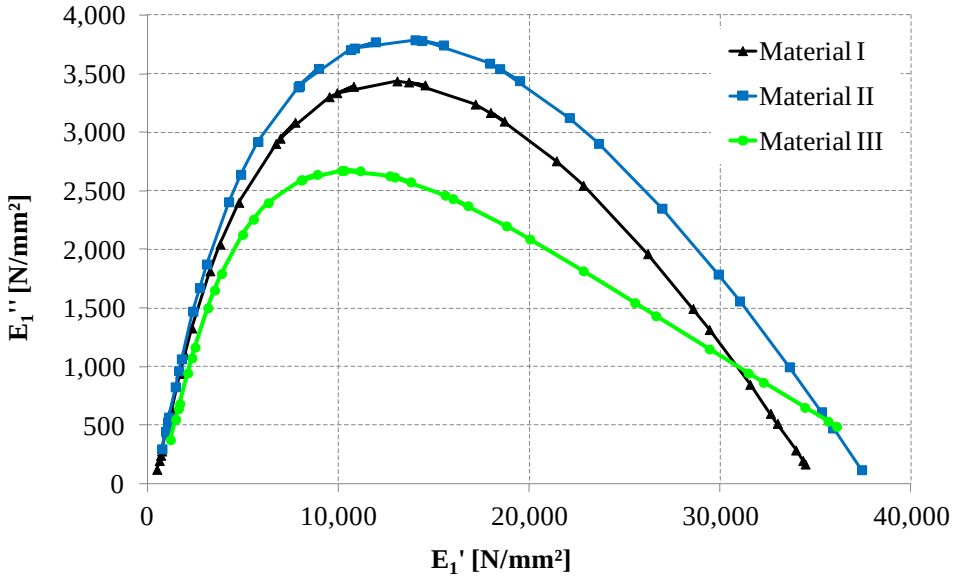

Figure 5-18 Cole-Cole Plots for Material I, II and III

5.1.1.2 Permanent Deformation Tests

Several long-term repeated load triaxial tests were performed to characterize the plastic behaviour of each material. The test results were used to determine the input parameters of the permanent deformation model.

As explained earlier, a multistage test procedure, in which the same specimen is subjected to several repeated loading steps at different stress levels, was developed.

Initial attempt

A first attempt to characterize the permanent performance of the materials was carried out at the early stage of the project. In this phase, each material was subjected to six multistage repeated load tri-axial tests at three different cell pressures and two different temperatures. One thousand cycles at 1 Hz were applied to each stress state.

Table 5-9 Realized long-term multistage triaxial tests

Material	Temperature [°C]	Frequency [Hz]	Cell pressure σ_{23} [N/mm^2]	Axial stress σ_1 [N/mm^2]
Material I	25	1	0.13	0.18; 0.28; 0.38;
Material II	40		0.43	0.48; 0.58; 0.68;
Material III			0.63	0.78; 0.88, 0.98;
				1.08, 1.18; 1.28;
				1.38; 1.48; 1.58;
				1.68

The chosen stress paths and stress levels are indicated in Table 5-9 and Figure 5-19. The test results in terms of plastic strains vs. load cycles are depicted in Figure 5-20. The stress path and the level of stress applied on each test are indicated in Figure 5-19.

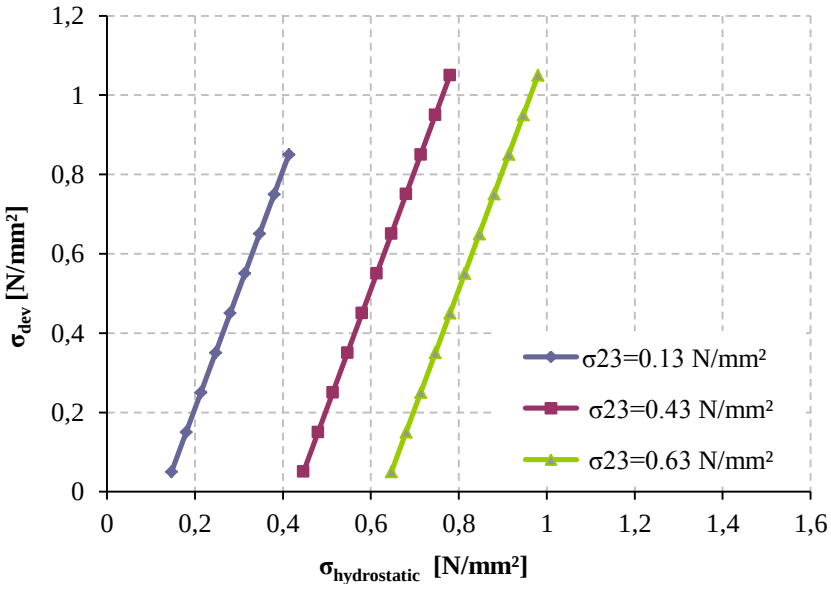

Figure 5-19 realized staged repeated load triaxial test (permanent deformation)

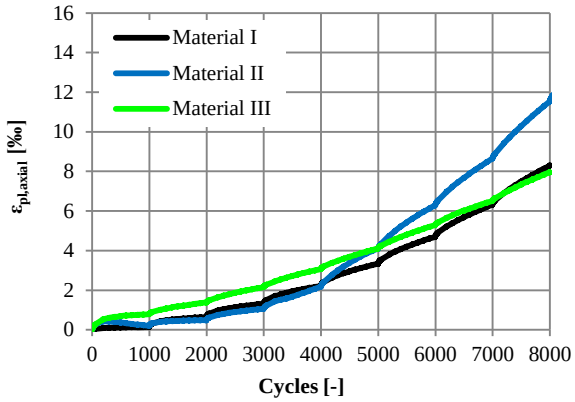

25°C, 1Hz and σ_{23}=0.13 N/mm^2

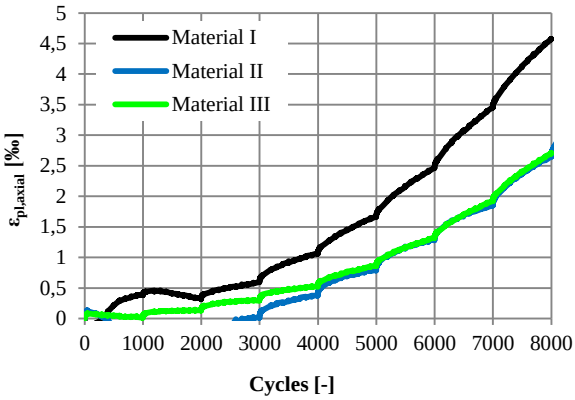

25°C, 1Hz and σ_{23}=0.43 N/mm^2

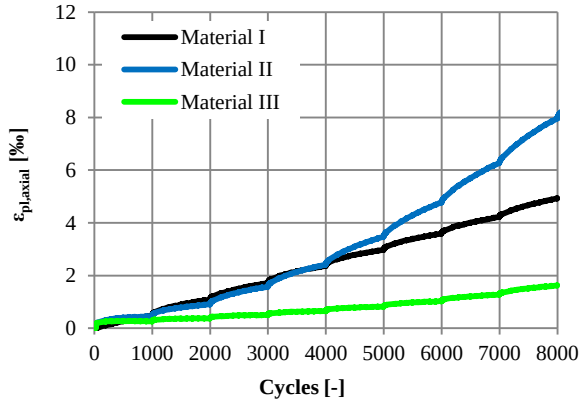

25°C, 1Hz and σ_{23}=0.63 N/mm^2

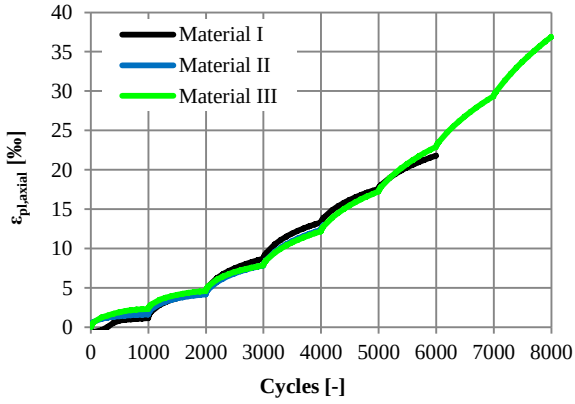

40°C, 1Hz and σ_{23}=0.13 N/mm^2

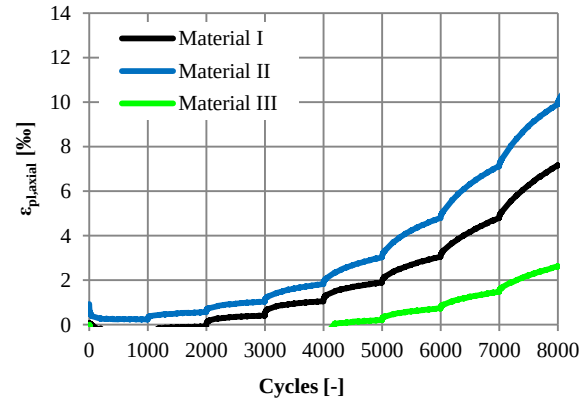

40°C, 1Hz and σ_{23}=0.43 N/mm^2

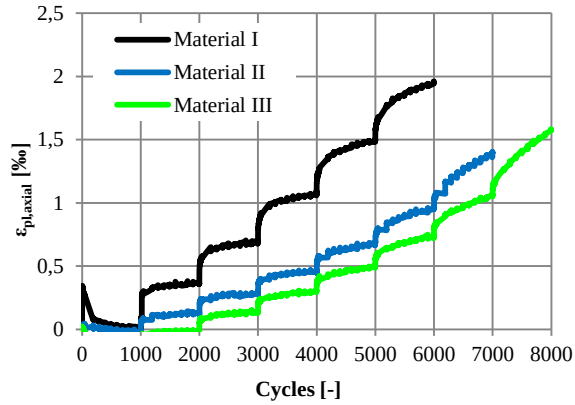

40°C, 1Hz and σ_{23}=0.63 N/mm^2

Figure 5-20 results of realized staged repeated load tri-axial tests (permanent deformation, 10000 LC)

Transformation of multistage data to single stage

The multistage tests are transformed into single stage with the power regression function of Equation (5-2). Exemplary Figure 5-21 shows the extrapolated plastic strains corresponding to the multistage test of Material II at T=25°C and σ_{23} =0.13 N/mm^2.

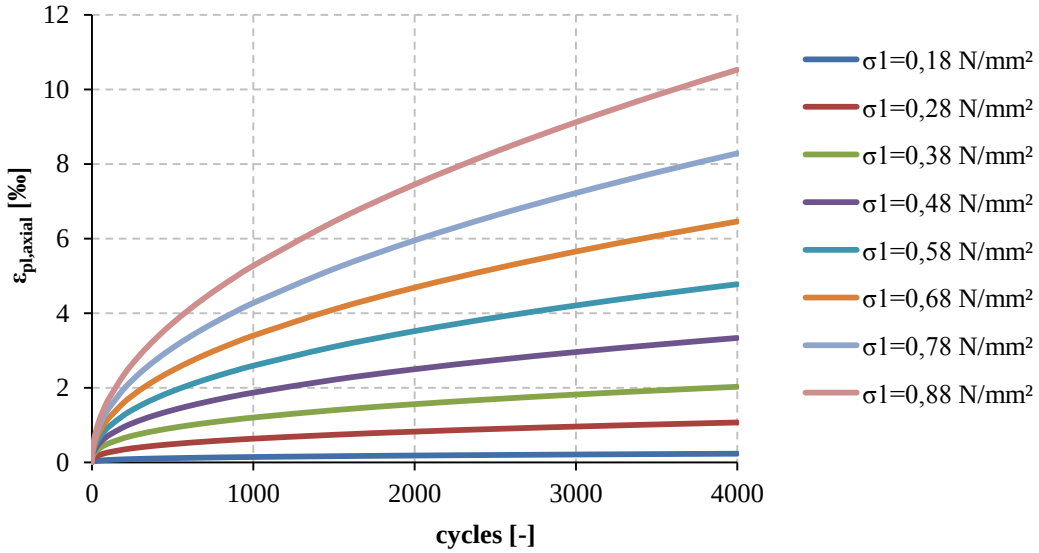

Figure 5-21 extrapolated plastic strains of a multistage test of Material II at 25 °C and σ_{23} =0.13 N/mm^2

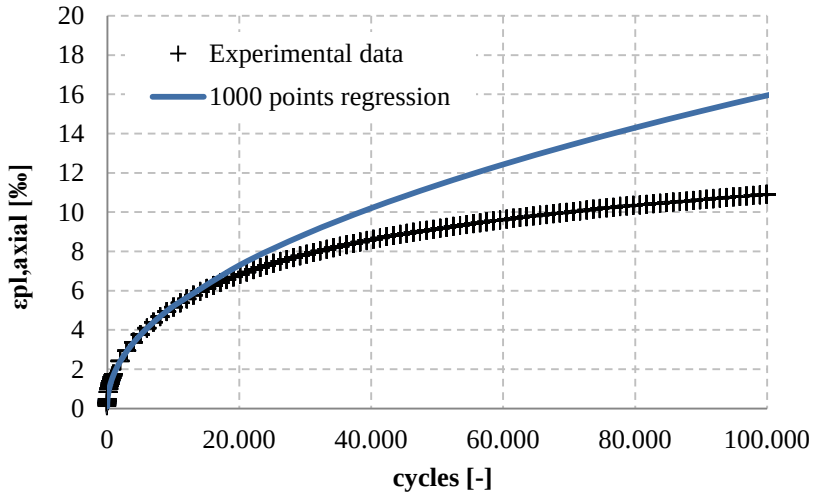

Figure 5-22 Long term triaxial test: 1000 cycles regression and measured ε_1

Examination of the test data indicates that thousand load cycles are not enough to capture properly the shape of the plastic deformation curve. To illustrate this fact, a long term repeated load triaxial test (frequency =1Hz, axial stress = 0.58 N/mm^2, cell pressure = 0.13 N/mm^2, temperature = 25 °C) with 100,000 load cycles was carried out with a test sample made of material III (30 M.-% RA). The measured plastic

strains were extrapolated with the first thousand load cycles and the regression error was estimated. The results, indicated in Figure 5-22 and Figure 5-23, showed an error of more than 40% at the end of the curve.

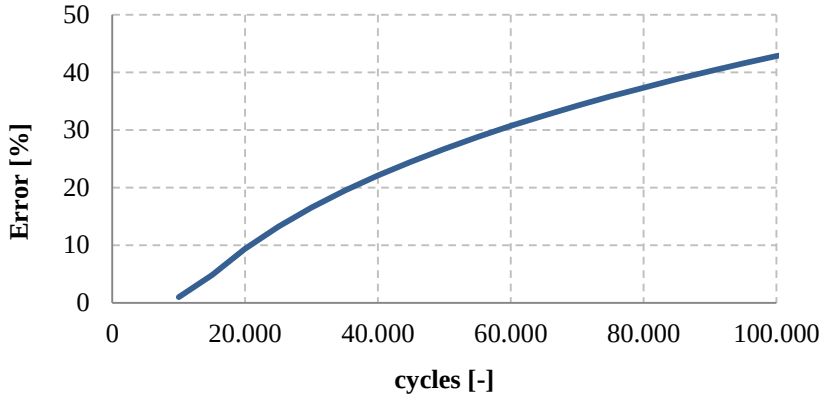

Figure 5-23 Long term triaxial test: 1000 cycle regression error

Final test sequence

Based on the experience acquired during the first lot of permanent deformation tests, a second multistage triaxial test program was developed. Thus, five series of long sinus shaped loading steps of 40,000 load cycles at 1 Hz and 40 °C were applied to each material. The cell pressure (σ_3) was kept constant at 100 kPa and the shear stress ratio (σ_{dev}/σ_3) was varied from 0.6 to 4.6.

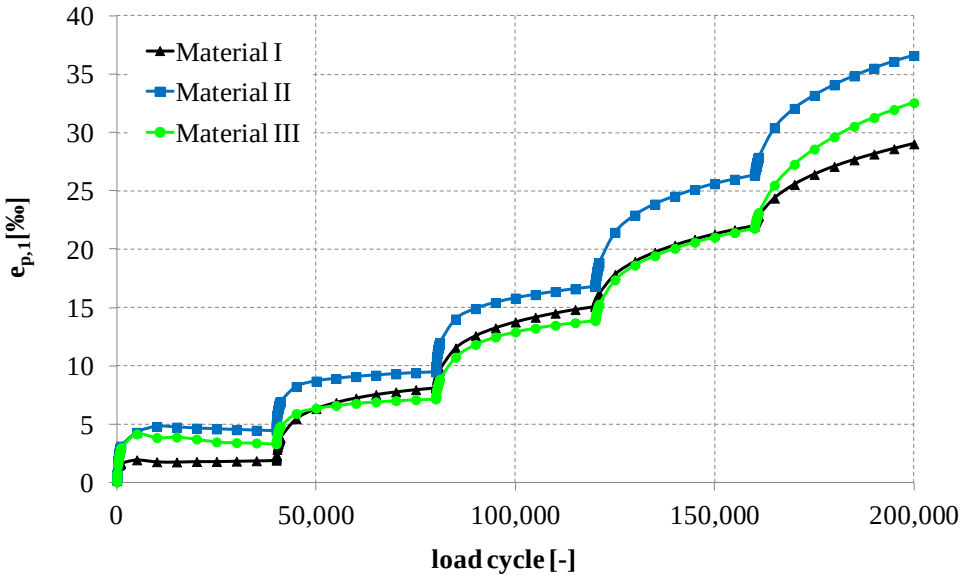

Figure 5-24 variation of permanent strain with number of load cycles

Figure 5-24 shows the variation of permanent axial strain with number of load cycles obtained from the multistage tests. It is observed that the permanent deformation increases rapidly during the first hundreds of load cycles, and then tends to stabilize – especially at low stress levels (first three load series). For high shear stress ratios,

the permanent deformations continue to increase leading to a potential failure of the material. This progressive increase of accumulation of permanent deformations at high stress ratio is more evidenced in the asphalt mixes containing RA.

Correlation between resilient strain and plastic strain rate

A correlation between resilient strain and plastic strain rate was used to compare the development of permanent deformation of the three materials. The model is build on an exponential law (Equation 5-2) that links the vertical plastic strain rate $\varepsilon_{1;p;rate}$ to the vertical resilient strain $\varepsilon_{1;r}$.

$$\varepsilon_{1,p,rate} = a \cdot \left(e^{b \cdot \varepsilon_{1,r}} - 1\right) \tag{5-2}$$

where

$\varepsilon_{1;p;rate}$	[10^{-3}/cycle]	vertical plastic strain rate
$\varepsilon_{1;r}$	[10^{-3}]	vertical resilient strain
a, b	[-]	material parameters

The plastic strain rates were determined from the permanent strain curves using the secant rate of permanent strain between 25,000 and 40,000 load cycles. The results, indicated in Figure 5-25, show a different plastic behaviour between the virgin material (Material I) and the two asphalt mixes with RA (Materials II and III).

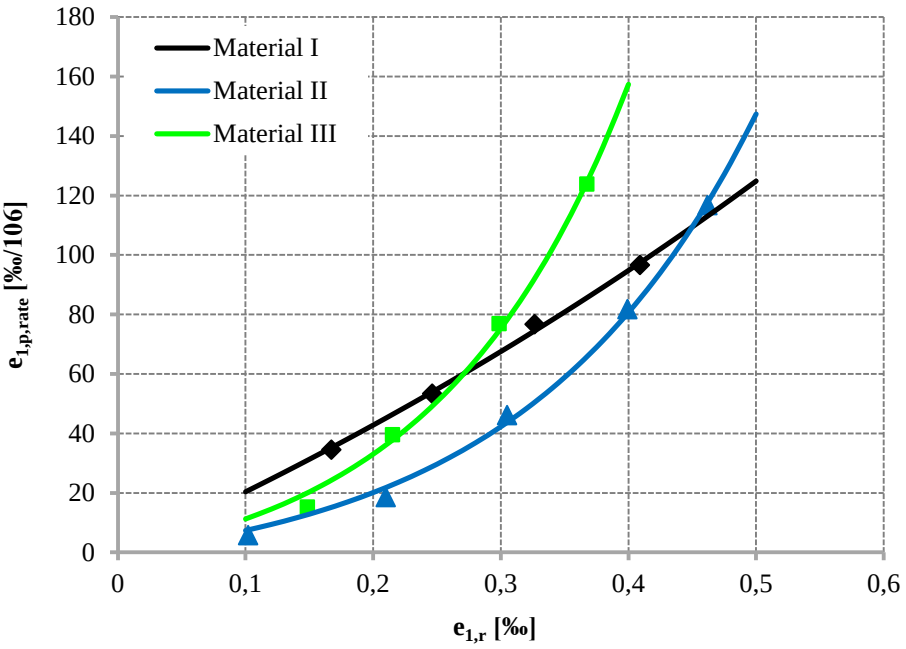

Figure 5-25 Correlation between permanent strain rate and resilient strain

The plot show that the permanent deformation performance of the two asphalt mixes with RA is hindered severely at large shear stress ratios where the resilient strains are also large.

Correlation between stress invariants and plastic strain rate

An alternative model, based on stress invariants, was also developed. For this case a correlation between deviator and hydrostatic stresses and plastic strain rate was used. The model is build on the basis of Equation (5-3).

$$\frac{\varepsilon_{1,p,rate}}{(L/p_a)} = c \cdot \left(e^{d \cdot \frac{q}{p}} - 1 \right) \qquad (5\text{-}3)$$

where

$\varepsilon_{1;p;rate}$	[10^{-3}/cycle]	vertical plastic strain rate
q	[kPa]	deviatoric stress
p	[kPa]	hydrostatic stress
L	[kPa]	$L=(p^2+q^2)^{0.5}$
p_a	[kPa]	reference stress = 100 kPa
c, d	[-]	material parameters

The results obtained with the stress approach are presented in Figure 5-26.

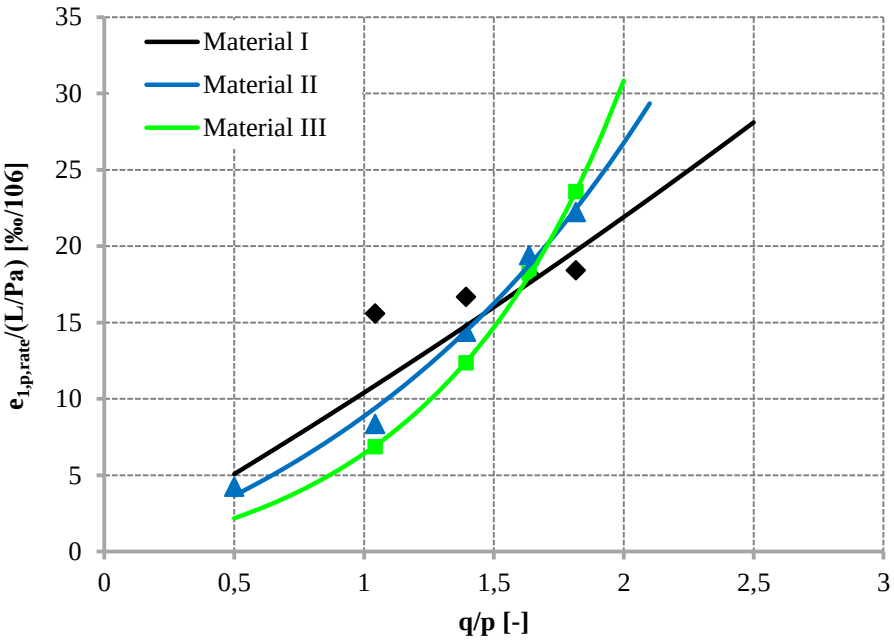

Figure 5-26 Correlation between permanent strain rate and stress invariants

The results, indicated in Figure 5-25 and Figure 5-26 show a different plastic behavior between the virgin material (Material I) and the two asphalt mixes with RA (Materials II and III). From the plots it is clear, that the permanent deformation performance of the two asphalt mixes with RA is hindered severely at large shear stress ratios where the resilient strains are also large.

More test results would be necessary to confirm this trend. Based on the very limited number of tests that have been carried out in the framework of the project, it seems impossible to find a plausible explanation to this phenomenon.

5.1.2 Tension and Compression Tests at University of Nottingham

5.1.2.1 Constant strain tests at UNOTT

Constant strain rate (CSR) tests were performed in order to establish the stress and strain level at which failure occurs. This has been done in order to have mechanical references for each material and at different loading speeds, in order to calibrate further tests.

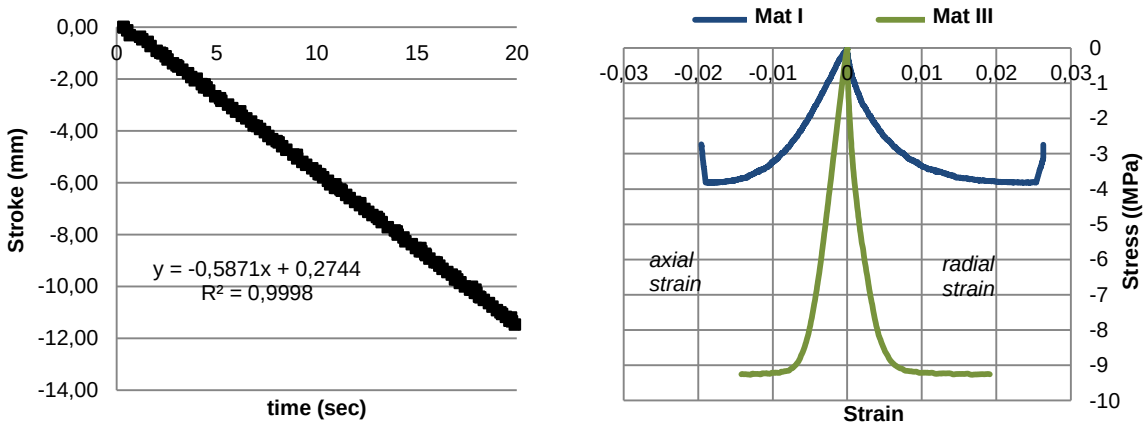

Figure 5-27 Compression CSR tests at 0.0005 s-1 (60 micr/sec): typical Loading curve (left), and Strain-Stress plots (right)

CSR tests have been done at 3 different strain rates: $0.005s^{-1}$, $0.001s^{-1}$ and $0.0005s^{-1}$. All constant rate compression tests have to be carried in displacement control.

After initial set-up of a cylindrical specimen, a compressive pre-load of 0.3kN was applied to avoid actuator hitting the specimen during the load application and to firmly hold the specimen. This last operation was not necessary for tension tests.

After starting the testing at the required strain rate, LVDT data, actuator displacement data and axial load data were logged with a RUBICON data acquisition system throughout the test. Each test was carried out until the specimen fails, which is indicated by a reversal of stress in the plot of strain versus stress (Figure 5-27 right). The peak stress obtained from each constant strain rate test, in both compression and tension, are shown in Table 5-10 and Figure 5-28.

Table 5-10 Input and output of Constant Strain rate tests at 25°C

		Compression test		Tension test	
mix type	strain rate	applied displacement rate [micron/sec]	Peak stress [MPa]	applied displacement rate [micron/sec]	Peak stress [MPa]
Material I	0.0005	60	-4.03	30	+0.85
	0.001	120	-4.70	60	+1.00
	0.005	600	-6.30	300	+2.30
Material II	0.0005	60	-5.49	30	+1.45
	0.001	120	-7.15	60	+1.85
	0.001	120	-9.24	60	+2.54
Material III	0.0005	60	-6.25	30	+2.14
	0.001	120	-8.22	60	+2.90
	0.005	600	-9.28	300	+3.09

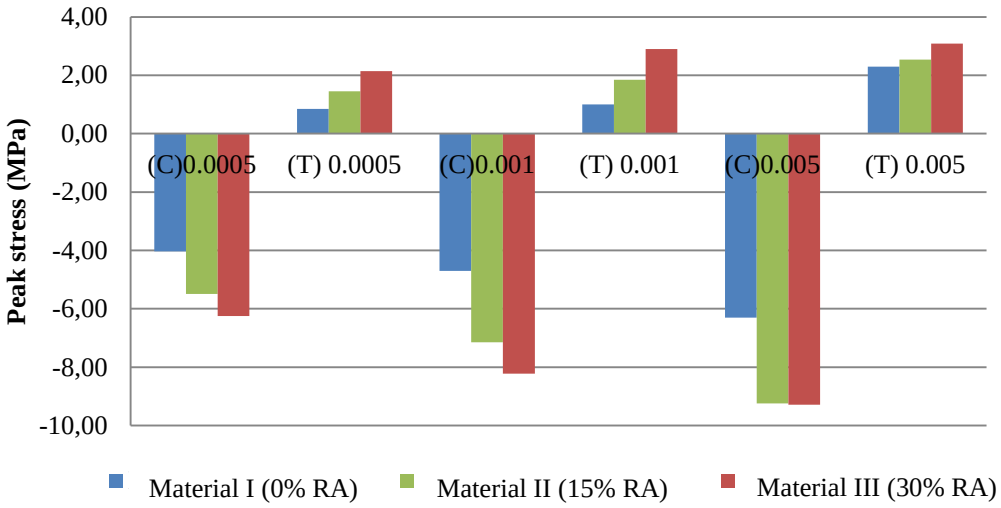

Figure 5-28 Overall results of the CSR tests

Results show that increasing the content of RA increases the peak stress of the mixes. The same trend is seen by increasing the loading speed.

5.1.2.2 Creep & Recovery Tests

Single creep recovery tests were performed to study the effect of damage accumulation on the recovery behavior of the reference material (Material I) and the mixes containing RA (Material II and Material III). In a single creep recovery test after preparation, instrumentation and preloading of the specimen, as explained in Section

4.1.2.2, the target load was quickly applied to the specimen and held constant for a certain time. This time was such that the total axial strain in the specimen was in the secondary creep region, i.e. when strain rate reaches a constant value (less than 5% difference in strain rate values in the last quarter of the loading period).These tests were carried out as the recovery curves generated from the secondary creep region of the test allows the elastic, delayed elastic and viscous strain components to be separated.

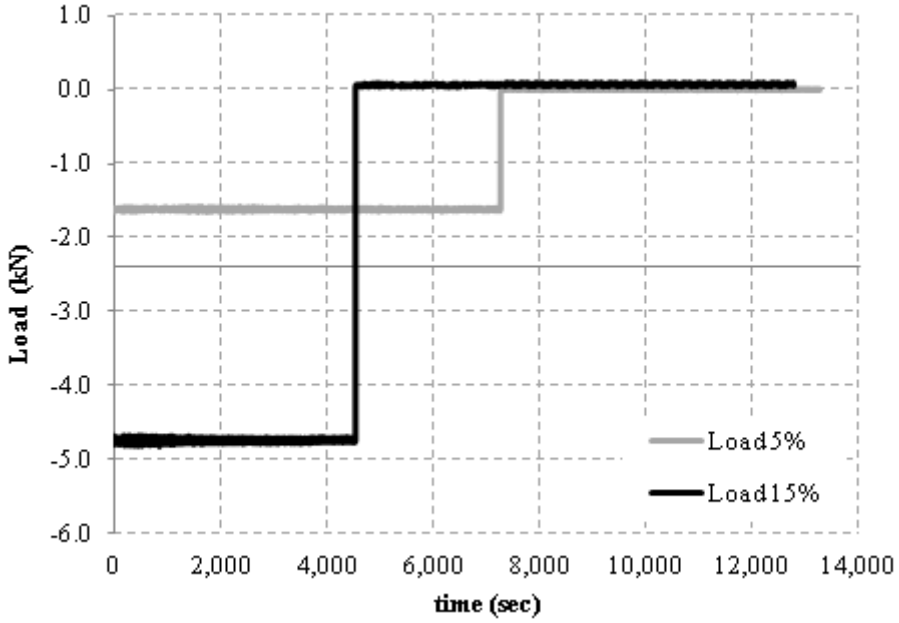

Figure 5-29 Typical loading curve of a Creep & recovery tests in compression

In the present study Creep Recovery tests were conducted at four different stress levels below the 20% of the failure peak stresses previously obtained in the constant strain rate tests at the 0.0005 strain level.

These load levels have been chosen in order to ensure the materials were tested far from their failure state. Creep Recovery tests needed more accurate stress control and smaller loading levels, for these reason the 10 kN load range was used to perform the tests. Figure 7-9, Figure 7-10 and Figure 7-11 shows the loading curves and the Strain-time plots of Material I, II and III in compression. Table 5-11instead shows a summary of the comparison between the two ”extreme” situations: 0% and 30% RA.

As a result, when the load is applied, an instantaneous (time-independent) strain develops in the specimen followed by gradually increasing (time-dependent) strains. When the load is removed, there is an instantaneous recovery (elastic strain) followed by time-dependent elastic strain (delayed elastic strain) recovery. The irrecoverable strain remains in the specimen as permanent strain, which is comprised of the plastic and viscous components.

As can be seen comparing the figures and from Table 5-11, during the compression tests, the mixes have very similar elastic recovery but the Material III in percentage deforms less and shows to accumulate a lower permanent strain. Furthermore, both control and RA mixes show that within the range of the utilised test conditions, independent of the applied axial stress level, the recovered strain decreases with increasing the loading levels. The outcomes of tension tests show a different trend. The Material III shows a very high recovery which leads to small permanent strains. On the other hand, the Material III shows a higher elastic strain but overall a smaller recovery.

Table 5-11 Input and output of Creep and Recovery test at 25°C

		Compression test			Tension test		
mix type	Load level [% of Peak stress]	Applied load [kN]	Perman. strain [%peak strain]	Elastic strain [%peak strain]	Applied load [kN]	Perman. strain	Elastic strain [%peak strain]
Material I	5%	-1.55	78%	0.045%	0.11	-	-
	10%	-3.1	75%	0.031%	0.21	30%	0.040%
	15%	-4.7	80%	0.054%	0.32	27%	0.040%
	20%	-6.3	86%	0.147%	0.43	58%	0.076%
Material III	5%	-2.4	61%	0.078%	0.27	-	-
	10%	-4.9	63%	0.083%	0.54	80%	0.094%
	15%	-7.3	71%	0.055%	0.80	83%	0.122%
	20%	-9.8	76%	0.138%	1.07	58%	0.158%

It seems that these results are dependent from the different rheological behaviour of the mixes but results are misleading due to the experimental set-up. In the tension test, the unloading phase still involves a link between the specimen and the testing equipment. This affects the recovery of the materials resulting in misleading outcomes in the visco-elastic properties of the tested materials.

5.1.3 Indirect tensile tests

Different repeated load tests have been established in Germany and worldwide to investigate the stiffness and fatigue characteristics of asphalt mixes. Within WP5 indirect tensile tests were carried out to determine the required parameters for the pavement design process.

5.1.3.1 Comparison of the E-Modulus values

Repeated load tests are necessary to obtain the stiffness characteristics of asphalt mixes in dependence on the loading time and temperature. However, a direct comparison of the E-Modulus values using the temperature frequency equivalence

was not possible because the tests were conducted at selected temperature and frequency values.

The difference between the E-Modulus values determined using ITT and RLTT can be explained by the different stress conditions during testing (ITT tensile stress conditions and RLTT compressive stress conditions).

Figure 5-30 shows the absolute modulus values at 20 °C and 1 Hz frequency determined using the results of ITT and triaxial tests conducted at TU Dresden.

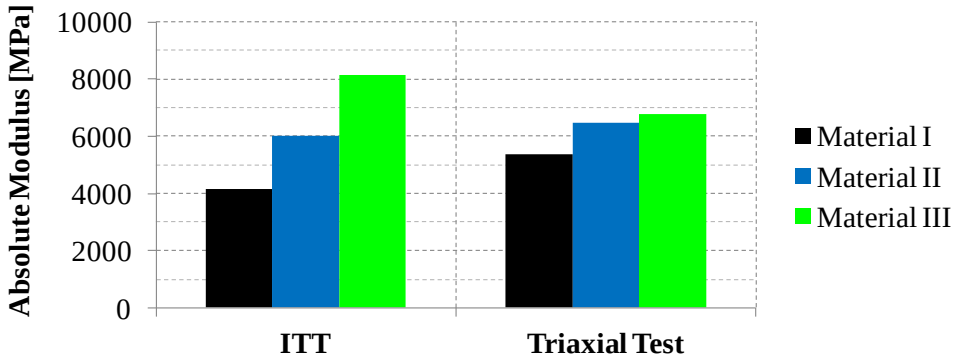

Figure 5-30 Absolute modulus values at 20 °C and 1 Hz frequency determined using the results of ITT and Triaxial tests

5.1.3.2 Fatigue Tests at Technical University Dresden

Repeated load tests are required as well to obtain the fatigue properties of asphalt mixes. In particular the content of RA influences the fatigue properties. This is shown in Figure 5-31 where results of the three asphalt mixes are presented.

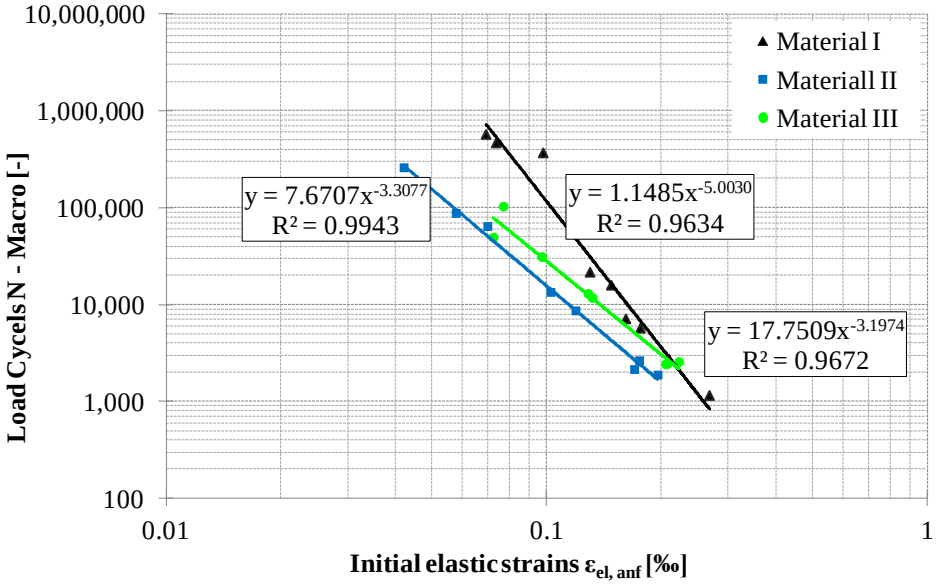

Figure 5-31 Fatigue relations obtained for the asphalt mixes

From this diagram it becomes quite clear that intercept value K_2 of the fatigue relation is changing significantly due to the RA content of the asphalt. Overall it can be seen that the resistance against fatigue is decreasing by adding RA.

The number of load cycles to fatigue failure in-situ (in a real pavement) cannot be estimated directly from the results of laboratory fatigue tests. For this reason fatigue models that utilise the results of fatigue tests are needed to estimate the number of load cycles to fatigue failure. Different factors like lateral wander, duration of rest periods between loadings, crack propagation etc. are held responsible for the fact that the number of load cycles to fatigue failure in the pavement are always greater than the number of load cycles to fatigue determined in the laboratory.

5.1.3.3 Fatigue Tests at University College Dublin

The testing programme was implemented so as to follow the parameters described in Table 4-6. The results of the testing programme are presented in Figure 5-32 and it can be seen that in all cases, the weakest performing material was Material I, whose fatigue life was typically ~40% of that of Material II and ~15% of that observed in Material III. It was noted that Material III was an extremely resilient material and persistently displayed a fatigue life far above that observed in the other mixtures, highlighting the benefits of adding high quantities of RA.

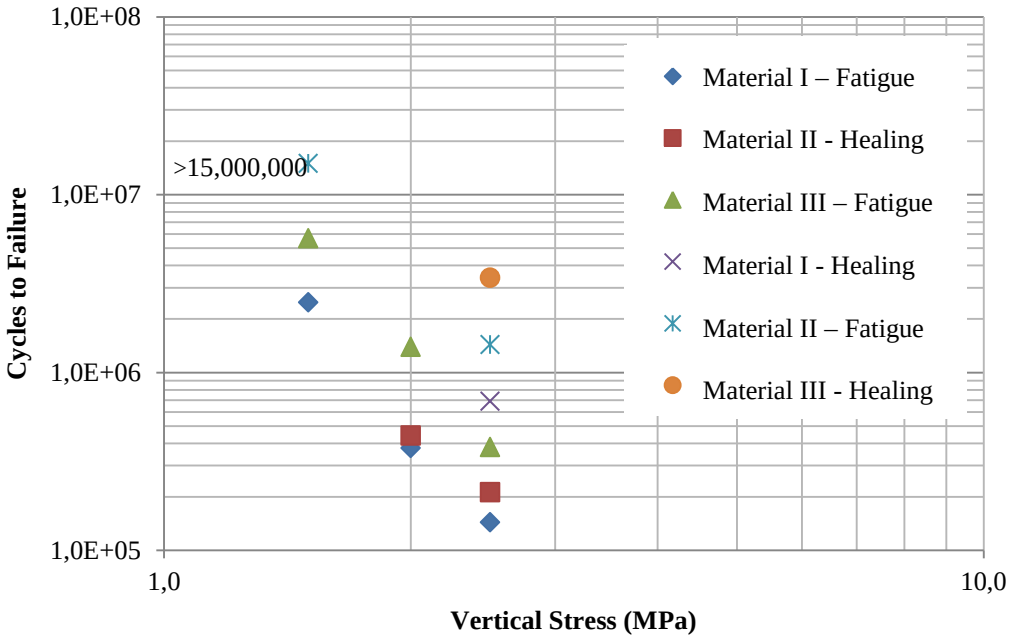

Figure 5-32 Influence of RA content on fatigue life at a vertical stress of 2.5 MPa

As it was discussed in the sections above, it should be noted that stresses required to induce a fatigue failure within a reasonable time frame were very high. EN 12697 Part 24 recommends that fatigue tests should commence with a 'reasonable' stress

level and suggests 250 kPa as a typical starting point. For this particular testing programme it was found that such a stress was not having any impact on the samples as the quality of the reference mixtures was very high. To illustrate this point, one may consider the performance of the materials in tests conducted at a vertical stress of 1.5 MPa. It can be seen that Material I failed within 3 days, but 7 days were required before failure was observed in Material II. The test for Material III was ultimately stopped after 19 days, with no sign of distress on the material. It is considered that the use of a weaker reference material would have been more appropriate for this testing programme.

However despite these difficulties, the benefits of using RA are clear. It can be seen that significant increases obtained in fatigue resistance are obtained with increasing RA content. This however is not in agreement with the results presented in Figure 5.34, where a decrease in fatigue resistance was associated with increasing RA content. The reasoning for this is unclear as the test configurations are very different. These include different stress states, temperature and loading frequency.

5.1.3.4 Healing Tests at University College Dublin

The results of the healing tests are also included in Figure 5-32 and show that rest periods have a significant effect on the fatigue life of the reference mixtures. Due to the high resistance of the reference mixtures, it was only feasible to conduct these tests at very high vertical stress levels (2.5 MPa). These tests have however shown a significant increase in fatigue life, as can be seen in Figure 5-32. For Material I, an increase of 48% was observed, while for Material II and Material III, increases of 81% and >100% were observed. It should however be noted, that these increases are obtained at stress levels that will never be encountered by most pavements in service. Unfortunately it is not possible to obtain such data at lower stress levels as each individual test would require a significant amount of time. For example, it is estimated that to test Material III under these conditions would require 1-2 months per individual test specimen. However despite this shortcoming, the significant impact of rest periods on the fatigue life is demonstrated.

5.2 Laboratory Performance Tests on bituminous Binders

The comprehensive characterisation of binder and mastic was conducted by the partners TUD, UNOTT and HA UCA. Each partner conducted different laboratory tests on bituminous binders.

5.2.1 Binder Characterization at University of Nottingham

In order to have a better understanding of the outcomes of the mechanical characterisation of the mixes, a particular attention was paid for the characterisation of the binders recovered (EN 13074) from the three materials (Binder I, II and III).

Firstly, Penetration and Softening point have been assessed to characterise the binder through standard empirical test (Table 5-12). Furthermore, rotational viscosity tests at 100 ºC and 150 ºC have been performed to assess the temperature at which the binders are fluid enough to be properly mixed with and to coat aggregate (Table 5-13).

Table 5-12 Empirical properties of the recovered binders

Property Tested	Binder I (0% RA)	Binder II (15% RA)	Binder III (30% RA)
Penetration 25°C (mm/10) - EN 1426	34	32	20.5
Softening Point (°C) - EN 1427	63.3	66.2	69.6

Table 5-13 Viscosity measurements of the recovered binders

Property Tested	Binder I (0% RA)	Binder II (15% RA)	Binder III (30% RA)
Viscosity at 135°C, (Pa s) - EN 13302	1.74	1.80	2.71
Viscosity at 150°C, (Pa s) - EN 13302	0.63	0.64	1.06

Table 5-14 Test settings of the Dynamic mechanical Analysis

Mode of loading	controlled-strain
Temperatures	0 ºC to 80 ºC at 5 ºC intervals
Frequencies	0.10, 0.16, 0.25, 0.40, 0.63, 1, 1.6, 2.5, 4, 6.3 and 10 Hz
Spindle geometries	8 mm ϕ and 2 mm gap (5-40 ºC), 25 mm ϕ and 1 mm gap (35-70 ºC)
Strain amplitude	0.5 % (within LVE response dependent on G*)

As a result, empirical properties and viscosity data provide similar information: Binder I and II are comparable, while Binder III results harder, with higher softening point and indicates that Material III could require more efforts to be compacted when placed on site.

The extracted binder have been characterised also by performing a Dynamic Mechanical Analysis (DMA) with a Dynamic Mechanical Analysis by means of Dynamic Shear Rheometer (DSR). DSR allows the assessment of the binder's rheology within the whole range of service temperatures and frequencies.

The binders' rheological properties were measured in terms of their complex (shear) modulus, G*, which gives an idea of the stiffness, and the phase angle (visco-elastic balance of rheological behavior). The tests were performed under the conditions shown in Table 5-14.

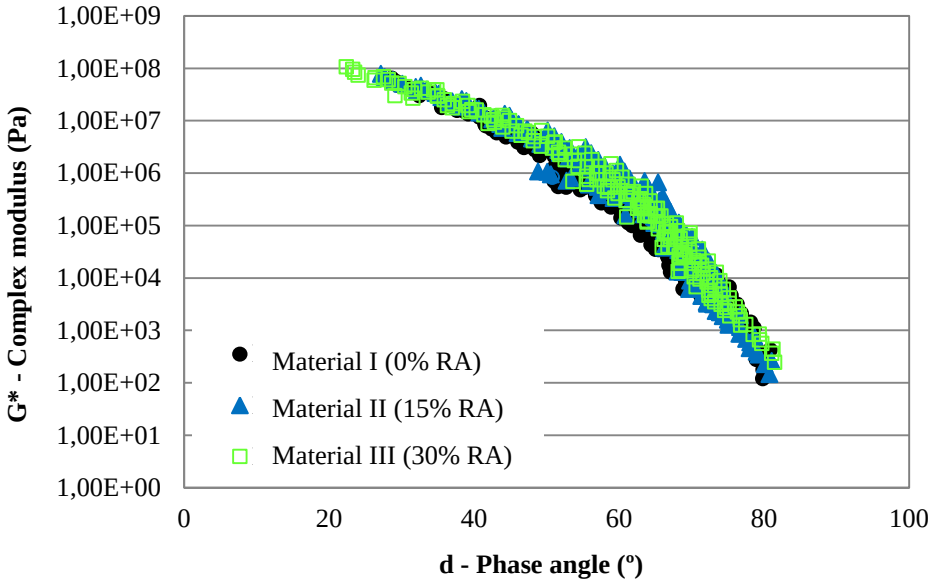

Figure 5-33 Black diagram of the recovered binders

Once measured, the data were used together with the time temperature superposition principle and shift factors to produce master curves at 25°C. Black diagrams (Figure 5-33) and Master curves (Figure 5-34, Figure 5-35) have been used as the basis of all the rheological analysis. As a results, Black diagram show that fingerprint of binders can be considered similar, but looking at the master curves, Binder III shows to differ from the others: It results to be stiffer over the whole range of temperatures (frequencies) and show also to have a slightly better elastic behavior (lower phase angle values), Binder I and Binder II shows again very similar characteristics.

An overall analysis of the results indicates a substantial agreement amongst the different binder characterisations. Results clarify the reasons of the higher efforts required during the specimens' compaction for Material III and provide fundamental information to be considered for further comparisons of mechanical properties of the mixes.

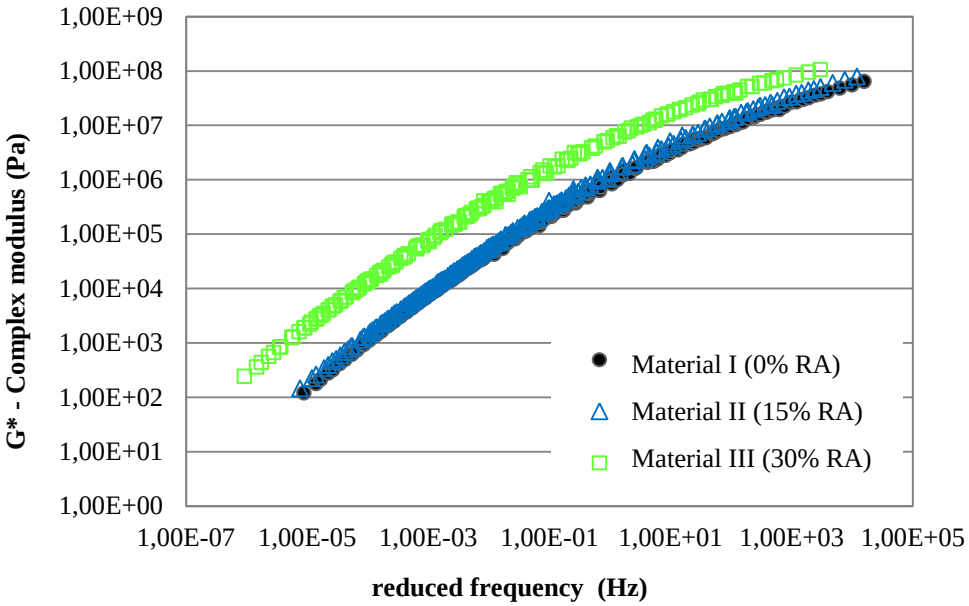

Figure 5-34 Complex modulus master curve at 25ºC of the recovered binders

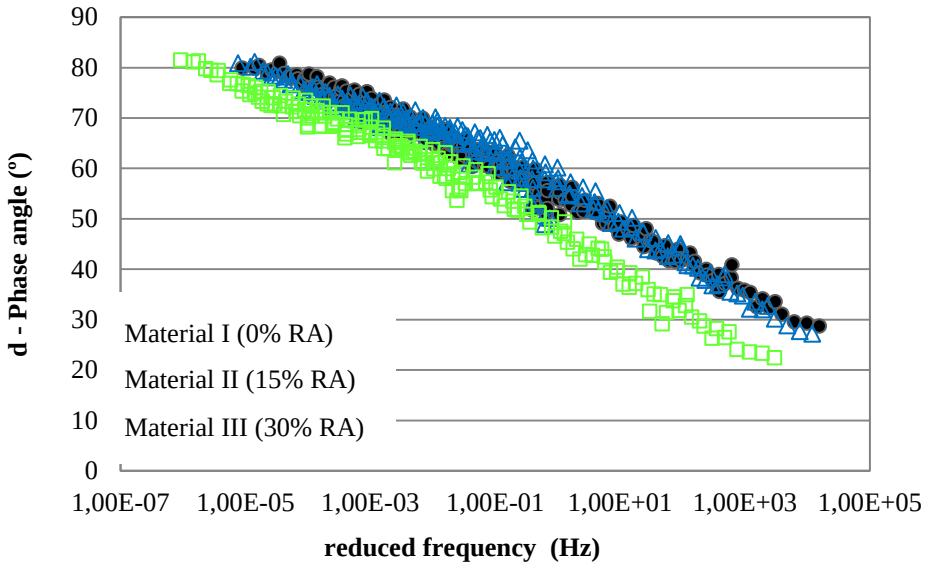

Figure 5-35 Phase angle master curve at 25 ºC of the recovered binders

5.2.2 Binder Characterization at Technical University Dresden

In a first step the values needle penetration and ring and ball were determined of the binder reclaimed from the asphalt mixtures (Table 4-7). Due to the in-homogeneity of the RA and due to problems during material production the final binder content of the asphalt mixes was varying.

The needle penetration value as well as the SP R & B shows that with an increasing RA content the binder is getting stiffer.

In a second step, Dynamic Shear Rheometer (DSR) tests were undertaken on the same binder in order to investigate the rheological properties (complex shear modulus (G*) and the phase angle (δ)) of the materials (Table 4-8).

The visco-elastic parameters being measured by the DSR apparatus are specimen's complex shear modulus (G*) and phase angle (δ). Complex shear modulus is defined as the ratio of maximum (shear) stress to maximum strain and provides a measure of the total resistance to deformation when the binder is subjected to shear repeated loading.

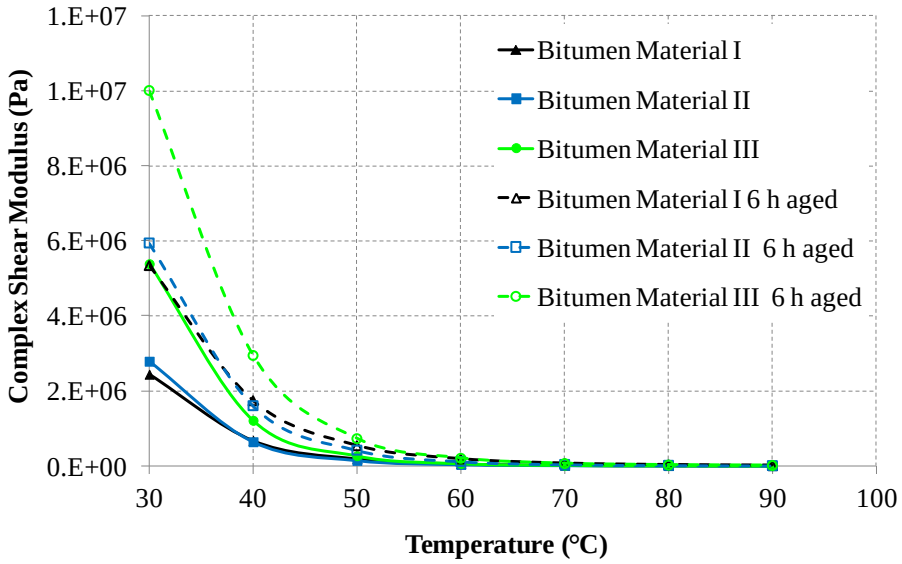

Figure 5-36 Complex shear modulus versus temperature for the bitumen investigated

In order to gain knowledge of the bitumen aging process, the bitumen was artificially aged using the Rolling Thin Film Oven Test (RTFOT). After the RTFOT aging process, the rheological properties of the three bitumen samples were assessed and compared with the base bitumen. The results of the DSR tests on the unaged and aged bitumen are presented in Figure 5-36 and Figure 5-37.

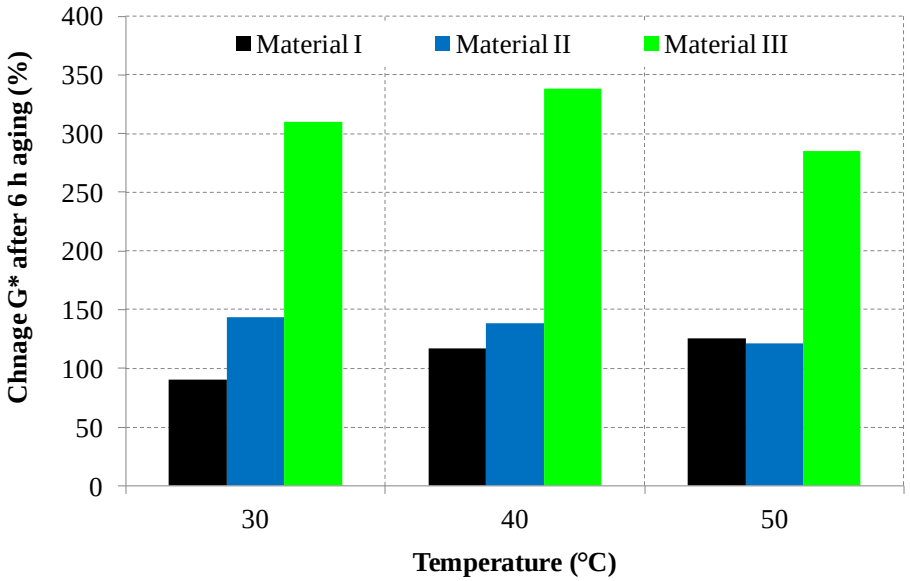

Figure 5-37 Relative change of the G* due to aging process

As expected the bitumen of material I (fresh bitumen) shows the lowest stiffness followed by the bitumen of material II and III. In addition the bitumen of material III shows a significant increase in shear modulus values compared to the bitumen of material I and II due to the accelerated aging process.

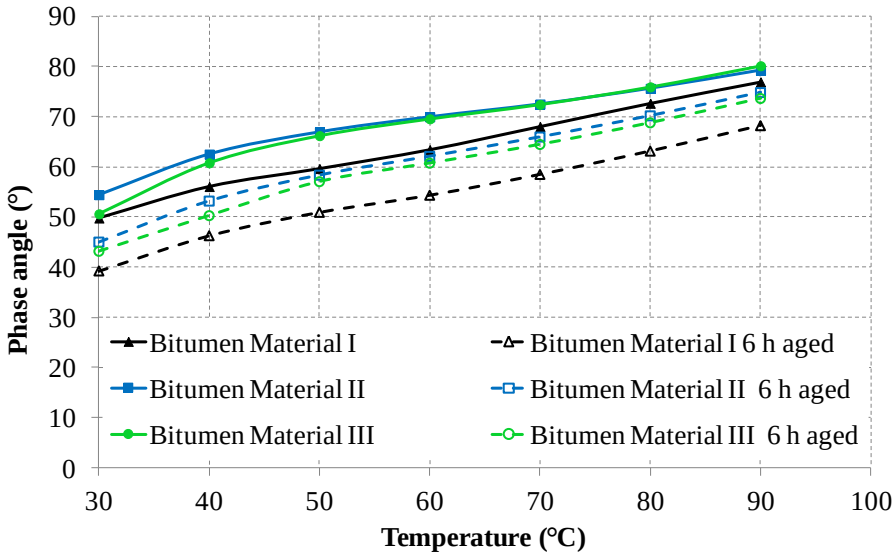

Figure 5-38 Phase angle versus temperature for the bitumen investigated

Figure 3 presents the change of the phase angle due to the aging of the bitumen. The aging process leads to a decrease of the phase angle which is related to a decrease of the bitumen viscosity.

5.2.3 Binder Characterization at University College Antwerp

5.2.3.1 Master Curves of Binders

In Figure 5-39, Master curves for G* and phase of binder I series are plotted.

These curves show that binder I is a modified binder, but when this binder is aged (manufacturing of Material I), the binder is harder and the phase curve becomes more straight. There is also a clear difference observed between the recovered binders of Material I and Material III. This means that probably the mixture Material III contains a harder binder mixture (Binder II + RA Binder).

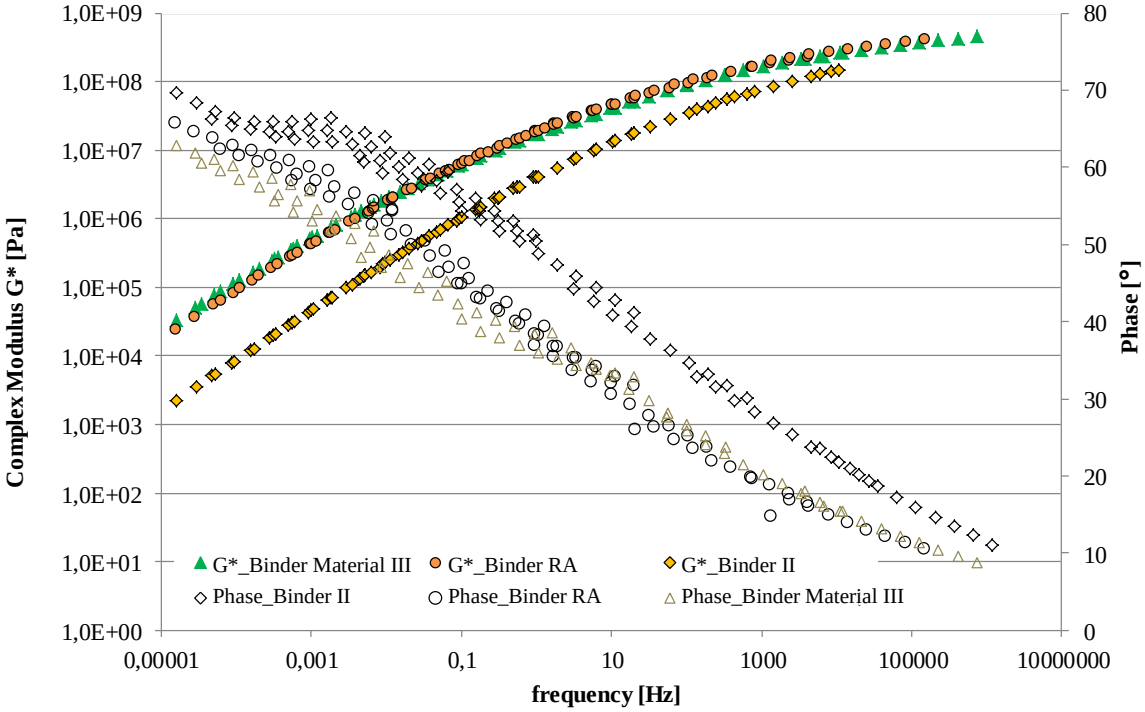

Figure 5-39 Master curves for G* and phase for Binder I series

5.2.3.2 Binder Fatigue tests

In order to evaluate the binder fatigue and healing performance and the influence of extraction and recovery after mixture production, fatigue curves are given as a function of sample stress, as shown in Figure 5-40. The curves show that:

- For a certain sample stress, the fatigue life of binder BII+RA is smaller than for binder I,
- When binder BII+RA is long-term aged, its fatigue properties improve,
    - Fatigue properties of binder BII+RA and binder Material III (recovered binder) are not similar, this is also found in the different G*-values: the G* values of binder Material III are larger.

- For binder Material I, two points are considered; the fatigue is situated between binder BII+RA and binder I.

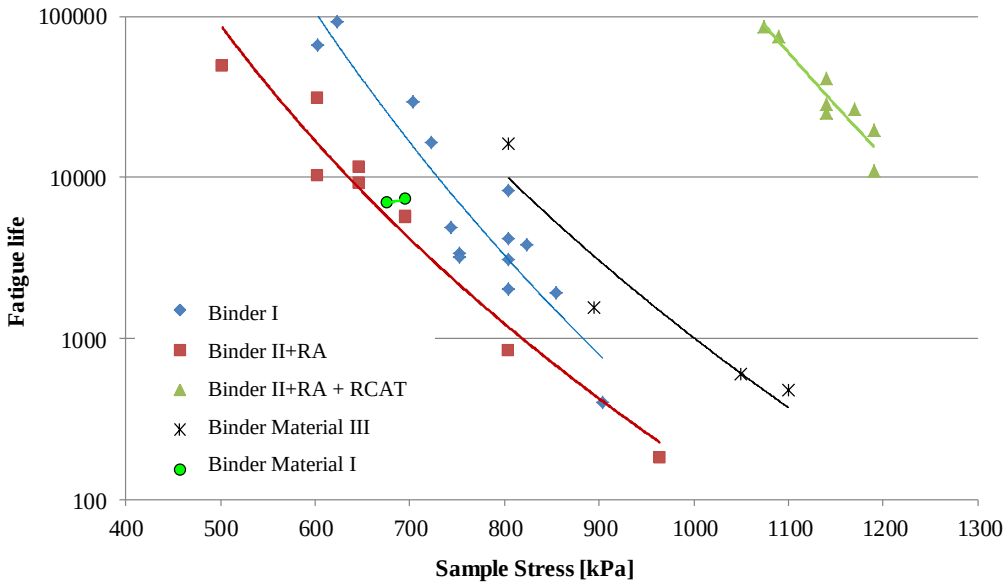

Figure 5-40 Fatigue curves of binders

5.2.3.3 Binder Healing Tests

Study on the effect of rest periods during fatigue

The effect of rest periods during a fatigue test (also called “Healing potential”) was studied for Binder I. The results are given in Figure 5-41, where the results for Binder I are given for Fatigue mode (Binder I FAT) and for Healing mode (Binder I HEA). It is clear that rest periods between a number of fatigue cycles (30 fatigue cycles followed by 90 cycles of rest) have a positive effect on the absolute fatigue life. This factor is very high. Since there is no common applied sample stress, the factor cannot be quantified in function of sample stress. A quantification can be made as follows: for an equal fatigue life (1000 and 10000) the implementation of rest periods allows to increase the sample stress with 230 kPa.

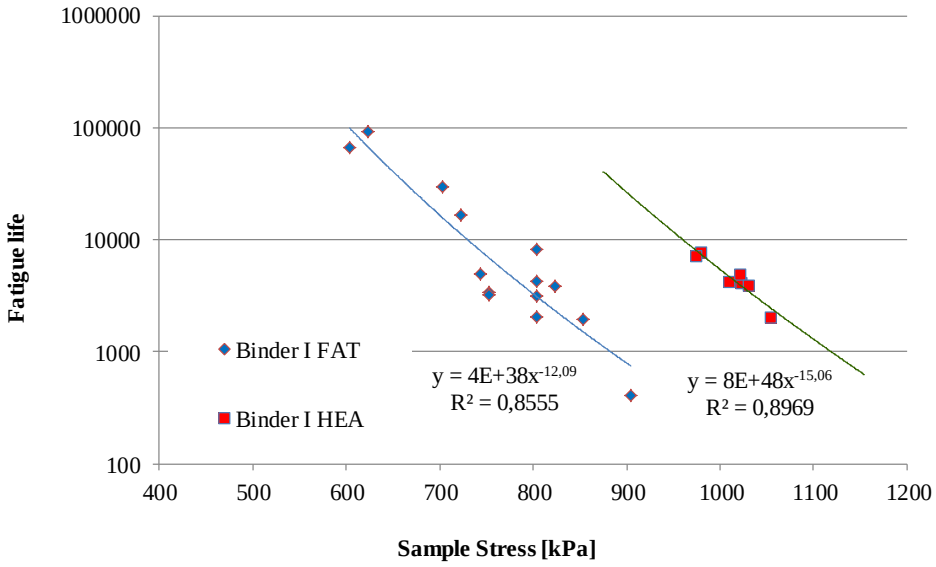

Figure 5-41 Fatigue and healing curve for binder I (tests at 10°C and 10 Hz)

It is recommended, in future projects, to perform a healing test which is less long-lasting and with an equal sample stress.

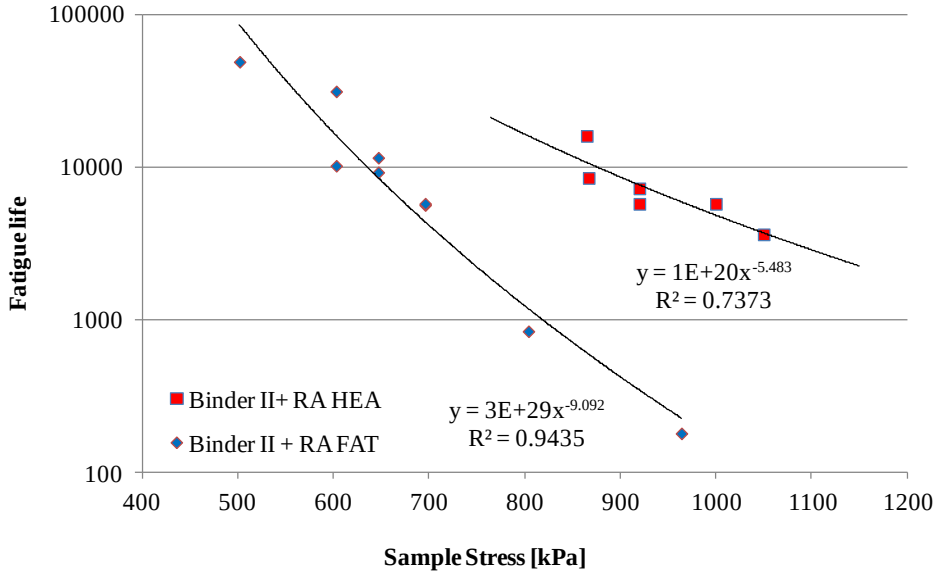

Figure 5-42 Fatigue and healing curve for binder II+RA (tests at 10 °C and 10 Hz)

As for binder I, rest periods have a positive effect on the fatigue life for binder II+RA. For an equal fatigue life of 10000 cycles, the rest periods allow an increase of 245 kPa (in extrapolation for 4000 cycles 320 kPa). The effect of rest periods between

both binders is different: the healing curve of Binder II+RA tends to more effect of rest periods in the higher stress zone.

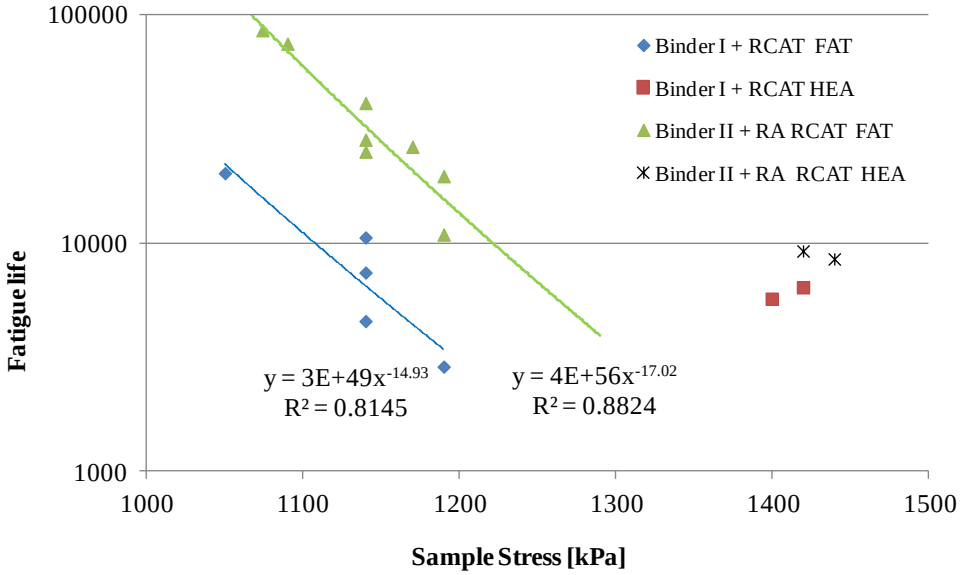

Figure 5-43 Fatigue and Healing curve of long term aged binders

When the long term aged binders of the reference binder and the mixed binder are considered, the mixed binder (Binder II + RA after RCAT long term), shows a better fatigue at a similar sample stress. Introducing rest periods has a positive effect on the fatigue life of both binders. Considering 10000 cycles, Binder II + RA RCAT shows a higher increase for sample stress (200 kPa) compared to Binder I after long term ageing (260 kPa). This is a different result regarding the unaged binders; however it should be mentioned that for the aged binders only two points of the healing curve are achieved.

Analysis of healing curves

For most healing tests, several measurements points are taken during loading and un-loading steps. These data can be used as a parameter in asphalt models in order to predict the effect of a rest period on regaining specific visco-elastic (e.g. complex modulus and phase angle) and fatigue properties.

In Figure 5-44, an example is given of output data during a fatigue test of 3 seconds (30 cycles) loading and 9 seconds rest. Only G* is plot. The results show that during loading cycles the G* value decreases and during unloading cycles G* increases. The graph also shows specific limitations of the DSR: a data point for G* is a calculated mean value of ratios of applied (maximum) stress and measured (maximum) strain during a time period of several cycles. If this time period is too short, errors occur in the calculation, as shown in healing period 1 and 3. In Healing period 2, less measurement points improve the data output.

This graph demonstrates the recovery of the complex modulus during rest periods. The healing curves, given in a previous chapter demonstrated that the

implementation of rest periods between intervals of loading cycles benefits the total fatigue life of the binder.

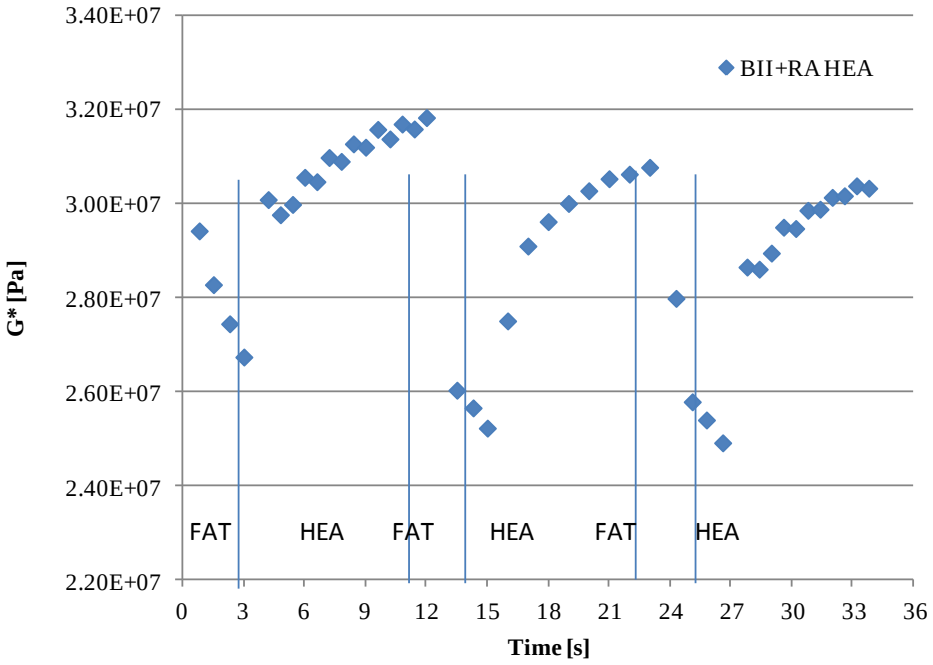

Figure 5-44 First cycles of healing test of binder II+RA

5.2.3.4 Mastic Fatigue and Healing Tests

Fatigue and healing tests for mastic I (manufactured with binder I) and mastic II+RA (manufactured with binder II and RA-binder) were performed.

The effect of rest periods during a healing test (also called “Healing potential”) was studied for mastic. The results are given in Figure 5-45. It is clear that rest periods between a number of fatigue cycles (30 fatigue cycles followed by 90 cycles of rest) have a positive effect on the absolute fatigue life. This is similar as for the binders. The factor is 4.3 – 6.0 for mastic I and 7.4 for mastic II+RA. It must be emphasized that only few data points are gathered for the healing tests since these tests are long-lasting and only at the highest stress level healing results possible for a reasonable test period (< 10 hours). The mastics are very stiff and in the plate-plate mode the maximum torque of the DSR is required. It is recommended to execute these healing and fatigue tests, in the future, at higher temperature, e.g. 15°C, for accelerating the test. Nevertheless, the effect of rest is measured, and the effect is different. As for the binders, the mastic containing RA shows more effect of the rest periods.

One can also express the effect of rest periods as follows: for an equal fatigue life (20000 cycles) the implementation of rest periods allows to increase the sample stress with 220 kPa for mastic I.

The fatigue curve of Mastic II+RA shows, for an equal sample stress, a slight increased fatigue life. For 65000 cycles, the sample stress may increase 120 kPa due to the rest periods. A comparison at 20000 cycles is not possible due to the torque limitations of the equipment.

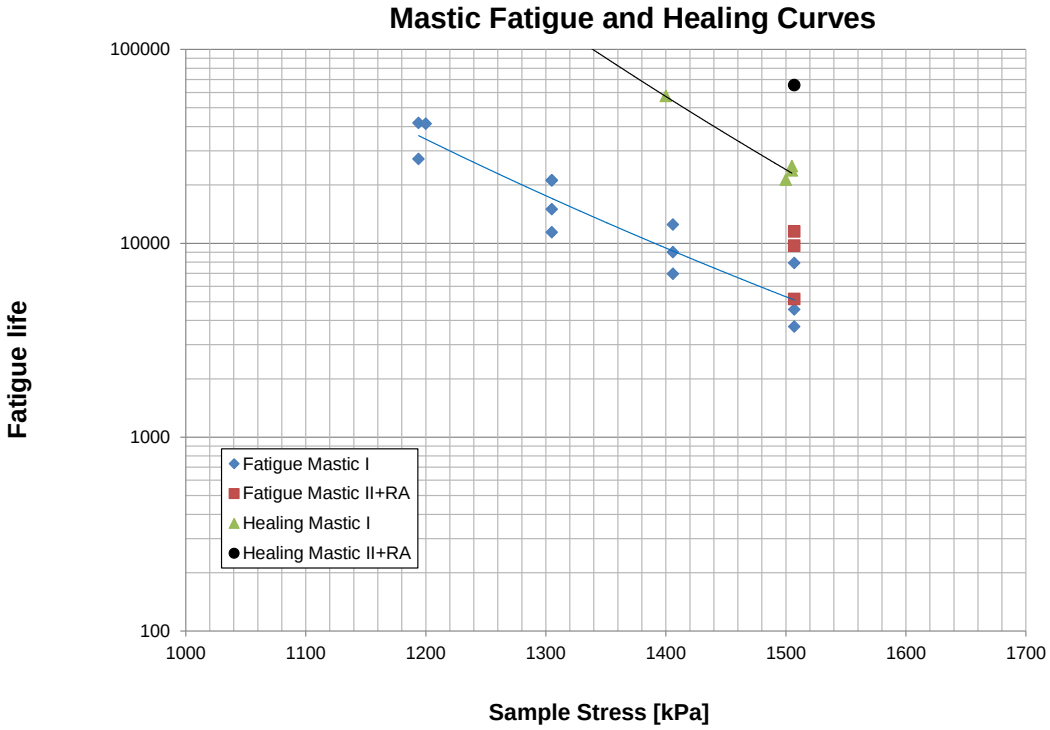

Figure 5-45 Mastic Fatigue and Healing results

5.2.3.5 Infrared Measurements

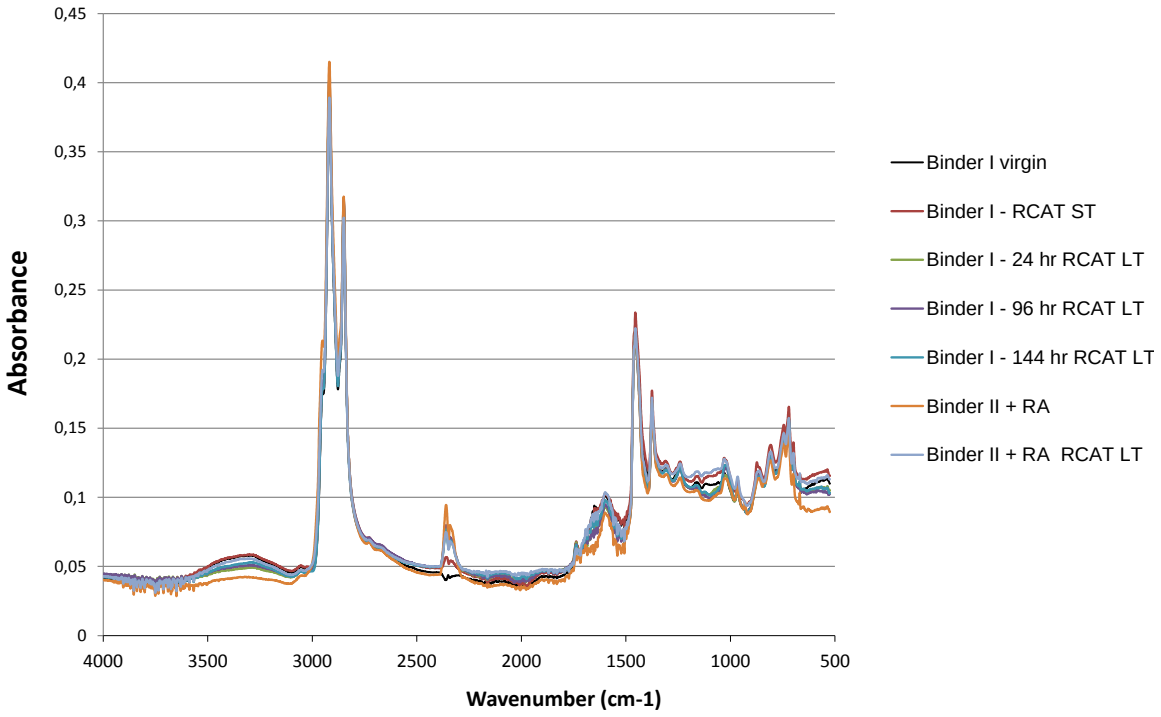

Figure 5-46 Infrared graphs of virgin and aged binders

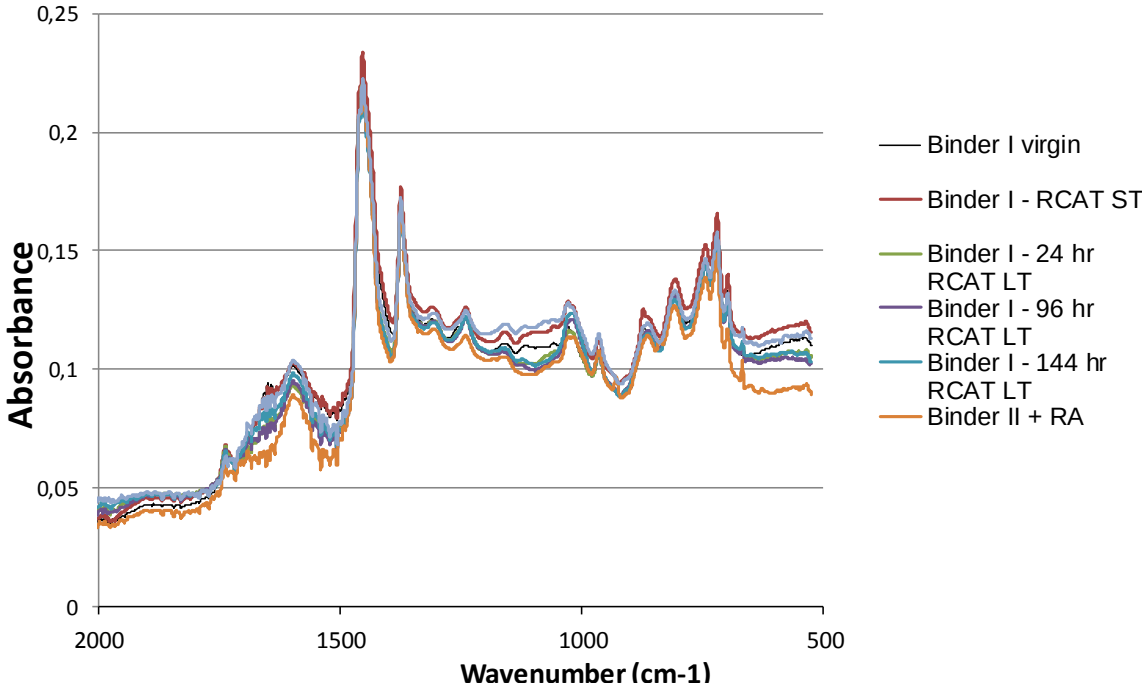

Figure 5-47 Infrared graphs of virgin and aged binders (2000 – 500 cm^{-1})

Seven binders were selected for InfraRed measurements between 4000 cm^{-1} and 500 cm^{-1}. Figure 5-46 shows the results for these binders. For further ageing evaluation, the range 500 – 2000 cm^{-1} can be taken.

5.2.3.6 Conclusion

The comprehensive research on binder and mastic demonstrates that:

- Fatigue and healing tests on bituminous binders are feasible using a DSR (in its plate-plate configuration);
- Stress-controlled tests are preferable since the DSR is in se a stress-controlled device;
- For a healing test program definition, it is recommended that one should first analyse the output values of the selected parameter (strain/stress) during the first cycles: a too high value will lead to a too high and unwanted damage in the sample;
- For binder I, binder II+RA and their respective long term aged conditioned binders, fatigue curves were completed. The mixed binder (Binder II+RA) shows a better fatigue life than binder I at equal stress level. Binder ageing enhances the fatigue property for both binder.
- The implementation of rest periods after a loading interval will lead to an extended fatigue life and, during the rest periods an increase of G* is demonstrated. A DSR allows to record this process, although correct settings of the software is required. It is possible to monitor the healing process during the individual rest periods as during the whole test.
- The healing shift factor is very high for all binders. Since there is no common applied sample stress between fatigue and healing curve, the factor cannot be quantified in function of sample stress. A quantification can be made as follows: for Binder I at an equal fatigue life (1000 and 10000) the implementation of rest periods allows to increase the sample stress with 230 kPa.
- As for binder I, rest periods have a positive effect on the fatigue life for binder II+RA. For an equal fatigue life of 10000 cycles, the rest periods allow an increase of 245 kPa (in extrapolation for 4000 cycles 320 kPa). The effect of rest periods between both binders is different: the healing curve of Binder II+RA tends to more effect of rest periods in the higher stress zone. For the respective aged binders, 4 healing tests were performed. Considering 10000 cycles, Binder II + RA RCAT shows a higher increase for sample stress (200 kPa) compared to Binder I after long term ageing (260 kPa). This is a different result regarding the unaged binders; however it should be mentioned that for the aged binders only two points of the healing curve of each binder were achieved.

- For Mastic I, rest periods have a positive effect on fatigue life (factor 4). When using the binder II+RA, a slight increased fatigue life is noticed however more tests must be done for verification.
- Since another partner is performing fatigue and healing tests on asphalt mixtures, it is strongly recommended to compare the binder-mastic results with the asphalt results.
- It is recommended to use the DSR for fatigue and healing tests on binder and mastic when is it possible to adjust the software in order to perform the correct stress or strain.

6 Model Development at TU Dresden

6.1 Introduction

Model development and pavement design life calculations had to be done independent from each other by the partners TUD and UNOTT (see chapter 7). Two different models, both using different input parameters, have been developed.

In the Re-Road project WP5 wanted to pursuit two different approaches:

The first approached, chosen by TU Dresden, aimed to develop two decoupled visco-elastic and plastic models. While the visco-elastic model was meant to determine the stresses and visco-elastic strains at all relevant points in the pavement considering influencing factors such as temperature and frequency etc., the (very empirical) plastic model would use this stresses and strains to estimate the accumulation of permanent strain. Both models, the visco-elastic and the plastic one, may be not very scientifically sophisticated, but very practical. With these two models at hand, even pavement engineers that are too familiar with constitutive modelling techniques of pavement materials can estimate the performance of pavements with recycled asphalt material. In addition, the computational time demand – associated with this first approach chosen by TU Dresden – is very low.

The second approach – chosen by University of Nottingham – founds upon a fully coupled visco-elastic-plastic model which was developed in collaboration with the group of structural mechanics at TU Delft. From a scientific point of view, this model is more sophisticated than the models developed by TU Dresden and a higher accuracy of the results produces with this model can be expected. This model provides a platform more suitable for scientists/researchers and its application requires a background of computational mechanics, programming and constitutive modelling.

The two different models proposed have been therefore developed to satisfy practical needs as well as scientists/researchers requirements.

6.2 Visco-elastic Model

In recent years, there has been vast development of visco-elastic models in pavement engineering for both asphalt binders and mixtures. At the same time, computational concepts have been developed to the point that complex pavement problems can now be solved through the implementation of Multi-Layer Theory (MLT), the Finite Element Method (FEM), the Fourier Series Aided Finite Element Method (FSAFEM), the Finite Difference Method (FDM) or the Boundary Element Method (BEM). In addition, significant effort is being made to develop a simple method for implementing commonly used visco-elastic models into these computational concepts through the theory of rheology. In this chapter, a

computational framework is presented for deriving the most commonly used rheological models from a single base-model, including the derivation of a new visco-elastic model.

6.2.1 Conventional and Fractional Rheological Models

In general, visco-elastic material exhibit both creep and relaxation type of processes when loaded and unloaded. A complete presentation of the theory of linear visco-elasticity can be found in Ferry (1980). The simplest model that predicts both the creep and stress relaxation of visco-elastic solids is the Standard Solid element that has a linear spring and a Kelvin element in series (see Figure 6-1). The Standard Zener element consists of a spring and a Maxwell element in parallel arrangement. The Standard Solid element and the Standard Zener element are rheologically identical, since they represent the same visco-elastic behaviour (Oeser et al., 2008). By adding a dashpot in series, the solid elements can be transformed into elements that represent fluids such as the Burgers element and the Roths element. The Burgers and the Roths elements are also known to be rheologically equivalent. These formulations can be expanded to the Generalized Discrete Solid, Zener, Burgers and Roths elements comprising of a spring, a dashpot (if applicable) and n number of Kelvin and Maxwell elements respectively (see Figure 6-1). Despite the fact that the generalized Maxwell and Kelvin model has been successful in simulating asphalt behaviour, increasing the number of elements in the constructed model can blur the conceptual meaning of each component and increase computational effort in the analysis procedure. Thus, new strands of models known as fractional visco-elastic models have been developed.

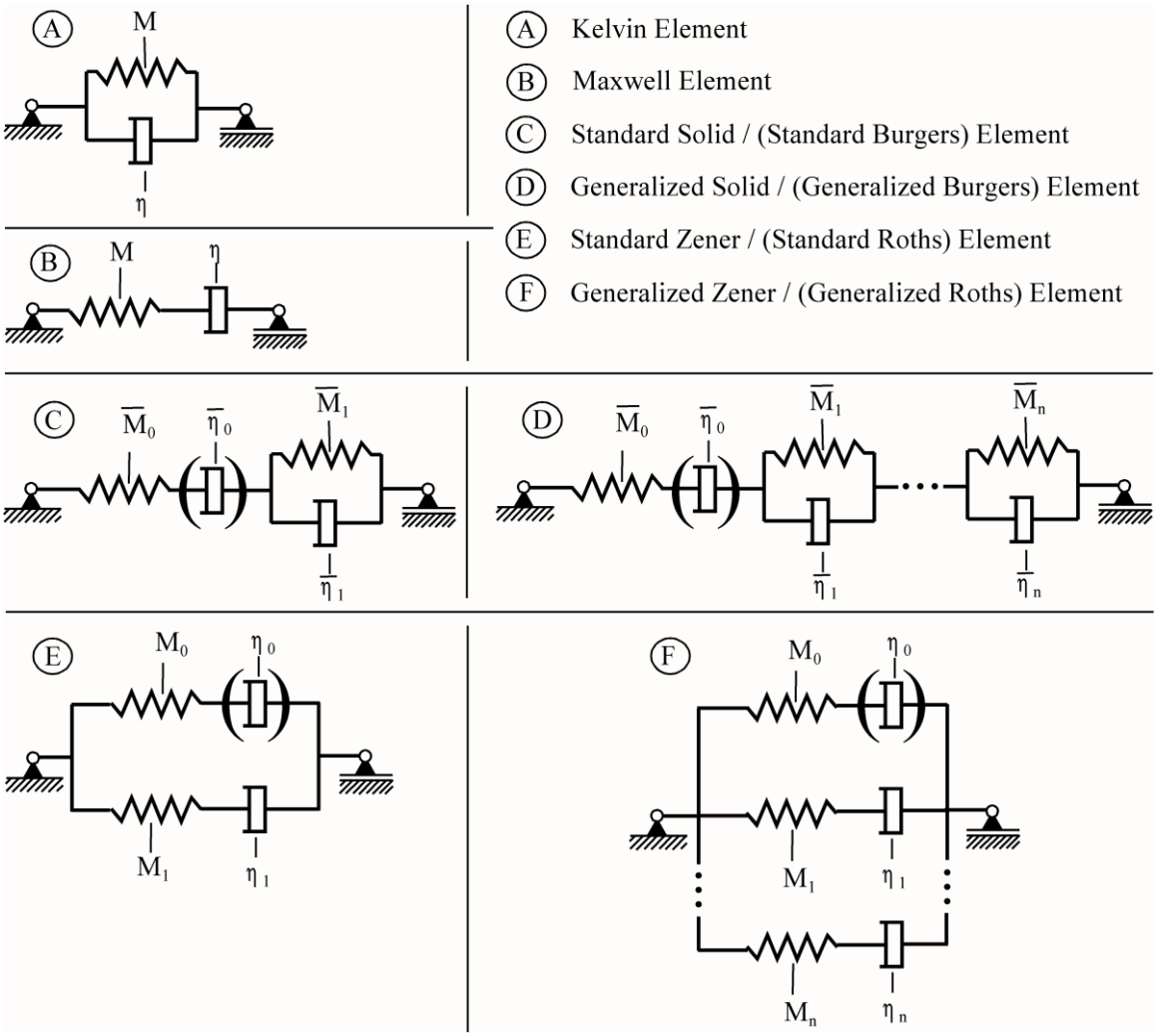

Figure 6-1 Standard and Generalized Elements

In Figure 6-1 the symbols M, M_0, M_1, ..., M_n, $\bar{M}_0$, $\bar{M}_1$, ..., $\bar{M}_n$ represent the modules of the rheological elements and η, η_0, η_1, ..., η_n, $\bar{\eta}_0$, $\bar{\eta}_1$, ..., $\bar{\eta}_n$ are the viscosities.

6.2.1.1 Model Characteristics

Fractional models have the advantage of having a small number of parameters associated to some physical properties of the material. Apart from this, the main advantage associated with the fractional concept is due to the fact that it allows for the establishment of a new component called a fractional dashpot (or fractional Newton element). This component interpolates between the pure elastic behaviour, which is usually modelled by a spring, and the viscous behaviour, modelled by a conventional dashpot (or Newton element). Unlike the conventional differential equations that use integer order differentiation, the fractional dashpot is achieved by using real order of differentiation. Based on Olard & di Benedetto (2003), the first

fractional models developed for bituminous materials were the Huet model, published in 1963, and the Huet-Sayegh model, published in 1965. These models had “parabolic creep” elements, which can be modelled as fractional dashpots combined with elastic springs (see Figure 6-2). A recent development is the 2S2P1D model established by Olard and di Benedetto (2003), which overcomes some problems encountered with these older models.

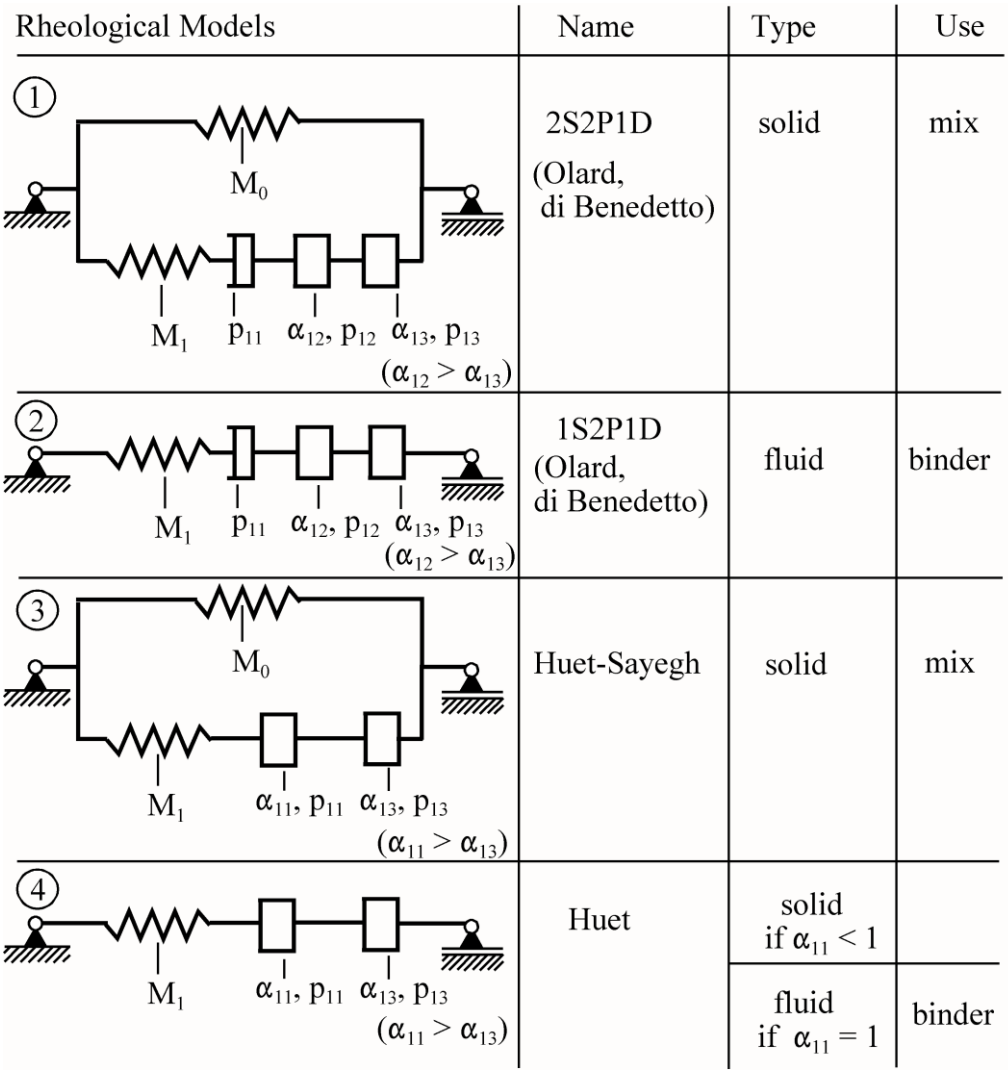

Figure 6-2 Fractional viscoelastic analogical models used for bituminous materials

In Figure 6-2 the symbols M_0 and M_1 represent the modules of the rheological elements, α_{11}, α_{12}, α_{13} denote the order of fractional differentiation and p_{11}, p_{12}, p_{13} may be obtained from the viscosity of the material as will be explained later.

Cole-Cole Plot and Black Diagram

Based on Powels (1993), K.S. Cole and R.H. Cole, who were working in electrical engineering, introduced the analytical Cole and Cole Plots in 1941, in which the imaginary part of complex permittivity, $\varepsilon''(\omega)$, is plotted as a function of the real part, $\varepsilon'(\omega)$, with ω, the angular frequency as a parameter. The Cole-Cole plot is an Argand diagram (complex plane presentation) for the complex dielectric constant. For visco-elastic materials, the Cole-Cole plots are often used to study the energy-storage and energy-loss characteristics of these materials when subjected to harmonic loading (see Figure 6-3). The Cole-Cole plots also provide a practical method of identifying parts of the parameters of the rheological models shown in Figure 6-2. The Cole-Cole plot comprises of a point-by-point graph of loss modulus, M'', versus storage modulus, M' (see Jones, 2001). The slope of the graph at the left intersection point (between the graph itself and M'-axis) is represented by parameter, α_{11}, and the slope at the right intersection point by parameter, α_{13}. The distance between the intersection points is, M_1, and the distance between the origin of the Cole-Cole diagram and the left intersection point is modelled by parameter, M_0. M_0, represents the modulus of the material that is approached when the loading frequencies are very low and/or the temperatures are very high, and is often referred to as the static modulus. The glassy modulus, M_0+M_1, represents the modulus of the viscous material at very high frequencies and/or very low temperatures.

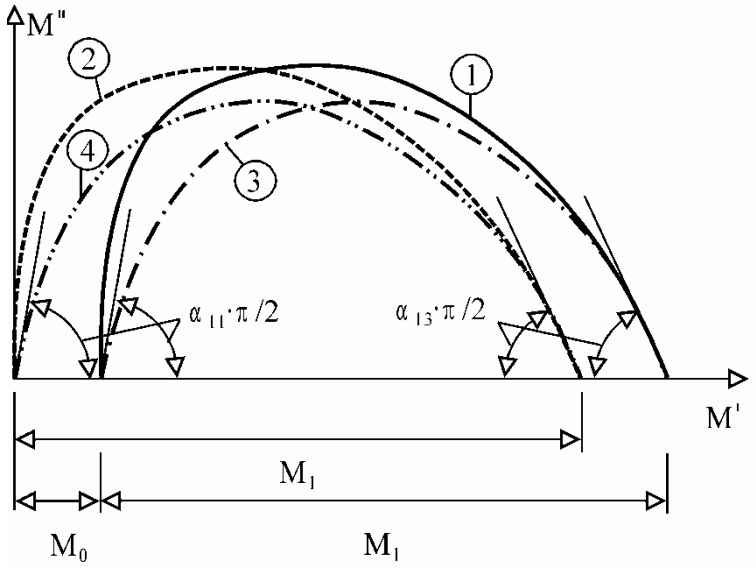

Figure 6-3 Cole-Cole plot

Similarly for the bituminous materials, a plot of phase angle, δ, vs. log modulus, $|M^*|$, has been used for presenting the visco-elastic material response to harmonic loading. The representation of the material behaviour, shown in Figure 6-4, is called the Black Diagram, which may also be used to determine some of the parameters of the rheological elements shown in Figure 6-3.

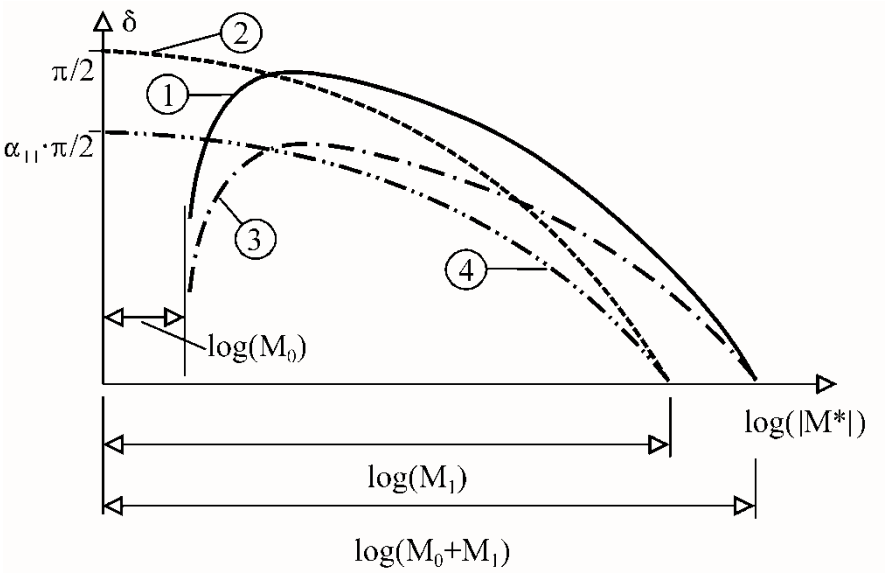

Figure 6-4 Black diagram

Visco-Elastic Soilds vs. Visco-Elastic Liquids

Generally, models that are used for asphalt binders are referred to as visco-elastic liquids, while the visco-elastic solid models are used for the mixtures. By definition, the visco-elastic liquids will accumulate permanent viscous strain by having irrecoverable deformations, while the visco-elastic solids will recover deformations with time. Another difference between visco-elastic solids and liquids can be seen in the Black Diagram (Figure 6-4), where the visco-elastic fluid model no. 2 will approach a phase lag of 90 degrees or $\pi/2$, while the visco-elastic solid models no. 1 and no. 3 will approach a phase lag of zero degrees. All visco-elastic models that only include springs and fractional dashpots (as, for example, model no. 4) will fully recover the strain but do not produce true solid like behaviour since they approach phase lags of, $\alpha_{11} \cdot \pi/2$. True solid like visco-elastic behaviour can only be created when a spring is either coupled in parallel to a conventional or to a fractional dashpot. Single conventional dashpots exhibit liquid behaviour and produce irrecoverable viscous strain. As the Huet model does not have conventional dashpots, it cannot model asphalt binders properly. To solve this problem Olard and di Benedetto (2003) added a linear dashpot to the Huet model (compare model no. 4 with model no. 2 in Figure 6-2).

6.2.2 Theoretical characterisation

Asphalt pavements age after several years in service. The aging is mainly caused by a change in the chemical composition on the binder. Binder consists of solid components as well as viscous components. Both components are constituted by molecular substances of different structure. These substances mainly consist of carbon, hydrogen, nitrogen oxygen and sulphur. Due to oxidation and distillation processes the molecular structure of these substances changes. This change generally leads to a transformation of viscous components into solid components,

which in turn causes the binder to behave more solid-like with time. A graphical representation of this process is given in Figure 6-5.

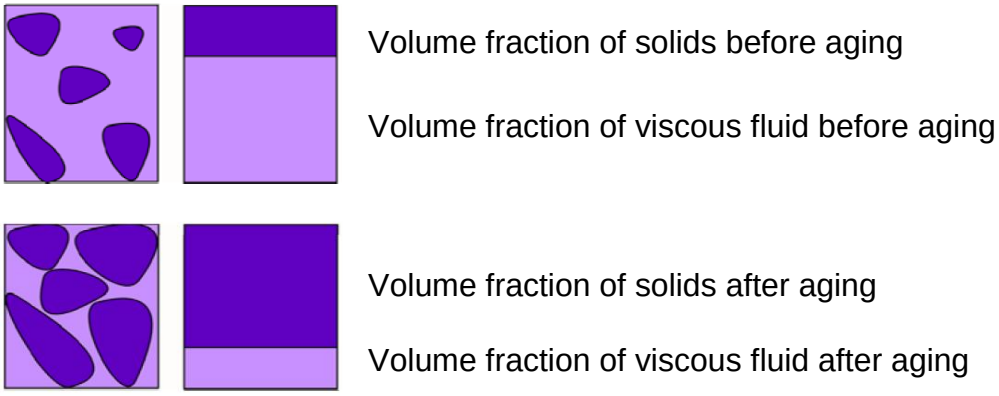

Figure 6-5 Aging

6.2.2.1 Preliminary remarks

The rheological behaviour of ideal viscous fluids may be modelled by means of a dashpot. Dashpots rely on a differential time equation of first order, (see Equation (6-1).

$$\sigma = \frac{d}{dt}\varepsilon(t)\cdot\eta \tag{6-1}$$

In Equation (6-1) σ represents the stresses, ε represents the strain, t denotes the time and η is the viscosity of the fluid. Solving Equation (6-1) for constant stresses Δσ yields the creep-function of the dashpot, which is given by Equation (6-2).

$$\varepsilon(t) = \frac{t}{\eta}\cdot\Delta\sigma \tag{6-2}$$

The graph of the creep function is shown in Figure 6-6 (curve 1). During the loading phase, the dashpot creeps linearly with time. When the load is removed, the strains remain constant. Hence, the dashpot does not recover any strains built up during the loading phase. For comparison, Figure 6-6 also shows the strain curve of a linear elastic spring (curve 2). In the spring the strains are being built up immediately after loading, remain constant throughout the loading phase (since the stresses are constant) and are being fully and instantly recovered when the load is removed. Since binder contains of solid-like as well as fluid-like components a creep behavior between those of dashpots and springs is to be expected. This can be modelled by a fractional differential time equation. A very simple example for such a fraction differential time equation is given with Equation (6-3).

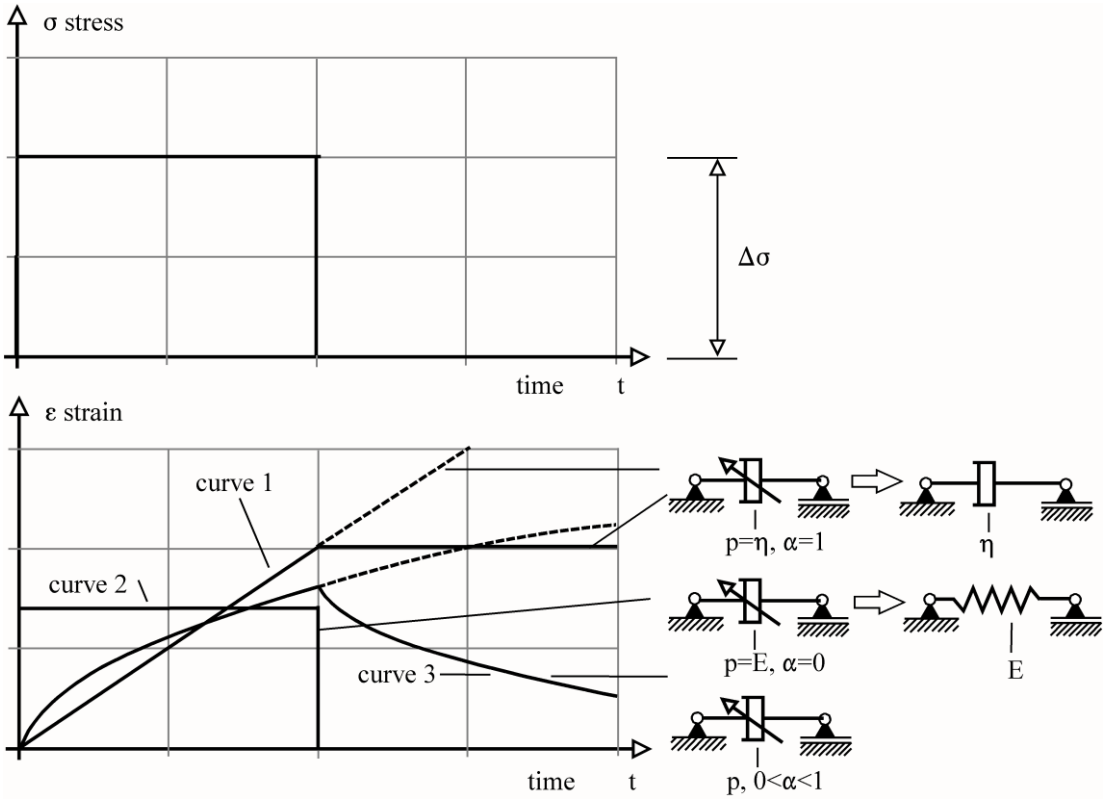

Figure 6-6 Creep-curves

$$\sigma = p \cdot \frac{d^{\alpha}}{dt^{\alpha}} \varepsilon \tag{6-3}$$

Fractional differential equations rely on differential operators of real order. In Equation (6-3) this differential operator is represented by the expression d^{α}/dt^{α}, wherein, α, denotes the order of the differential equation, t, is the time and, p, is the coefficient of the equation for which the following definition may be chosen;

$$p = E \cdot \left(\frac{\eta}{E} \right)^{\alpha} \tag{6-4}$$

If α equals 0 Equation (6-3) loses its differential character and turns into an ordinary equation. In this case p becomes E.

$$\sigma = E \cdot \left(\frac{\eta}{E} \right)^{0} \cdot \frac{d^{0}}{dt^{0}} \varepsilon = E \cdot \varepsilon \tag{6-5}$$

Equation (6-5) represents the stress-strain-behavior of linear elastic solids. If α equals 1 Equation (6-3) and Equation (6-1) become identical. In this case Equation (6-3) describes the stress-strain-behavior of ideal viscous fluids. If α takes on values

between 0 and 1 the corresponding creep function must be determined by fractional integration of Equation (6-3). Fractional integration techniques have been developed roughly 100 year ago. First applications to engineering problems were discussed by Caputo et al. (1971). Fractional time integration of Equation (6-3) yields the fractional creep function,

$$\varepsilon(t) = \frac{t^{\alpha}}{p \cdot \Gamma(\alpha+1)} \cdot \Delta\sigma \tag{6-6}$$

wherein Γ denotes the gamma-function. The graph of the fractional creep-function (6-6) is also shown in Figure 6-6 (see, curve (3)). From Figure 6-6 it can be seen that a fractional dashpot exhibits nonlinear creep behavior during the loading phase and has the ability of gradually recovering strains after unloading. It may be speculated that the α-value represents the volumetric fraction of solids and fluids in the binder. In other words, α-values closed to 0 may represent binders with high contents of solid-like and low contents of fluid-like particles while binders with low contents of solid-like and high contents of fluid-like particles may be represented by α-values closed to 1. Since the fraction of solid-like and fluid-like particles changes with time due to aging, α may also be used to characterize the state of aging of bitumen. However, this speculation must be further discussed considering different loading scenarios, and experimental evidence ought to be found before it can be adopted in the modeling process of the visco-elastic behavior of binders composed of virgin and aged components.

6.2.3 Experiments

6.2.3.1 Experimental Set-Up

To study the rheological behavior of binders under angular shear and tension-compression, rheometric devices such as the visco-analyzer [1] may be used. Such devices can be operated in shear and tension-compression mode. If the visco-analyzer is operated in shear mode a ring-shaped binder probe must be placed between a hollow steel cylinder and a solid steel piston. The cylinder is connected to a base plate and is therefore stationary while the piston moves up and down following a harmonic function of frequency, f, (see Figure 6-7a). The force needed to move the piston is measured by a load cell and recorded throughout the experiment.

Using the device in the tension-compression mode requires a cylindrical bitumen probe to be placed between a stationary base plate and a solid steel piston, (see Figure 6-7b). Similarly to the shear mode, the piston moves up and down harmonically and the force needed for this movement is measured.

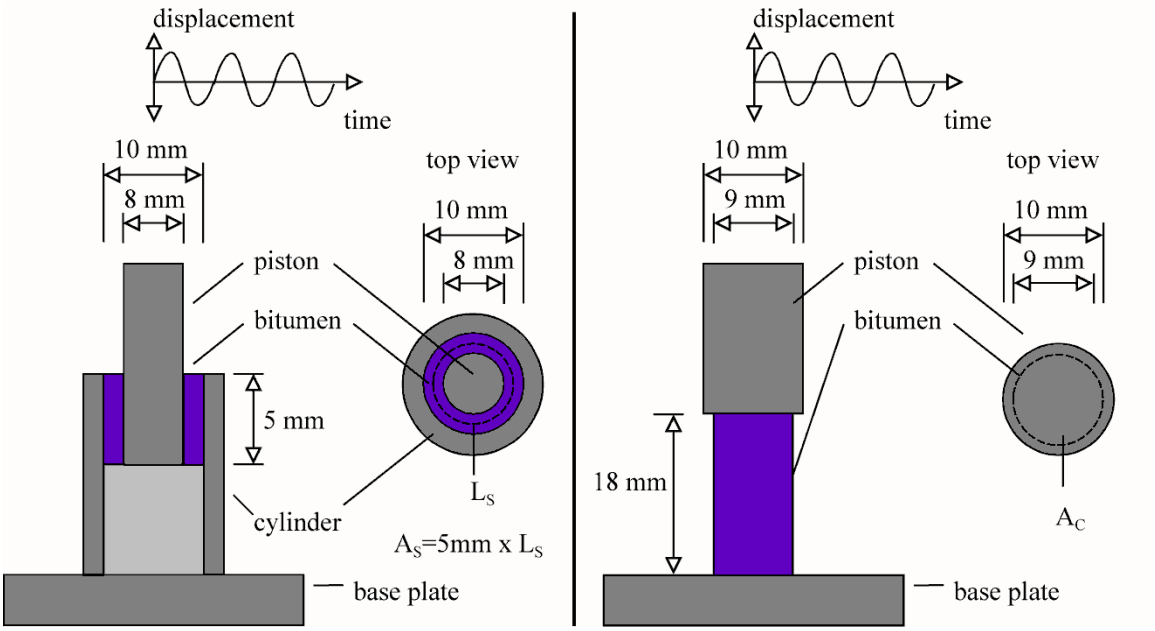

(a) (b)

Figure 6-7 Visco-analyzer

In addition to the force, the visco-analyzer also measures the time lag between the peak displacement and the peak force (phase lag). From the vertical displacement of the piston, u, and the thickness of the ring-shaped binder probe, d, the shear strain in the binder, γ, may be back-calculated using Equation (6-7).

$$\gamma = \frac{u}{d} \tag{6-7}$$

In tension-compression mode the strain in the binder, ε, may be determined from the height of the probe, h, and the vertical displacement of the piston, u, using Equation (6-8).

$$\varepsilon = \frac{u}{h} \tag{6-8}$$

Equations (6-7) and (6-8) only hold for small displacement-thickness-ratios and small displacements-height-ratios respectively. The experiment can be carried out under controlled temperature conditions. The devices usually allow for temperature ranges between -50 and +100 °C and frequencies ranging between 8 and 250 Hz.

The shear stresses in the binder, τ, may be determined with Equation (6-9) wherein, F, represents the force needed for the movement of the piston and, A_S, is the mean surface area of the bitumen.

$$\tau = \frac{F}{A_S} \tag{6-9}$$

In the compression-tension mode the normal stress in the binder, σ, can be determined from the force, F, and the cross-sectional area, A_C, of the bitumen probe.

$$\sigma = \frac{F}{A_C} \tag{6-10}$$

Figure 3-1 shows a typical plot of strains and stresses recorded during an experiment.

From the time lag, Δt, between the occurrence of the peak strain, ε^*, and the peak stress, σ^*, and from the duration, T_S, of a full harmonic cycle, the phase lag, δ, may be determined.

$$\delta = \frac{\Delta t}{T_S} \cdot 2\pi \tag{6-11}$$

Knowing the phase lag, δ, and the peak strain, ε^* ($-\varepsilon^*$), as well as the peak stress, σ^* ($-\sigma^*$), the loss-modulus, E'', and the storage-modulus, E', can be calculated.

$$E' = \frac{\sigma^*}{\varepsilon^*} \cdot \cos(\delta) \tag{6-12}$$

$$E'' = \frac{\sigma^*}{\varepsilon^*} \cdot \sin(\delta) \tag{6-13}$$

Similar calculations may be carried out when the experiment is run in shear mode. In this case the shear-storage-modulus, G', and the shear-loss-modulus, G'', can be calculated from the peak shear strain, γ^*, and the peak shear stress, τ^*.

$$G' = \frac{\tau^*}{\gamma^*} \cdot \cos(\delta) \tag{6-14}$$

$$G'' = \frac{\tau^*}{\gamma^*} \cdot \sin(\delta) \tag{6-15}$$

A more general formulation of Equation (6-12), (6-13), (6-14) and (6-15) is given by Equation (6-16) and (6-17), where the following definitions are made: $M' = E', G'$; $M'' = E'', G''$; $\theta = \sigma, \tau$; $\zeta = \varepsilon, \gamma$.

$$M' = \frac{\theta_0}{\zeta_0} \cdot \cos(\delta) \tag{6-16}$$

$$M'' = \frac{\theta_0}{\zeta_0} \cdot \sin(\delta) \tag{6-17}$$

Based on the findings by Chailleux et al. (2006) it is assumed that shear-moduli can be converted into tension-compression-moduli using a Poison's ratio equal to 0.5. In order to identify the visco-elastic properties of the virgin and aged binder the visco-analyzer was operated in it's two loading modes depending on the test temperatures. For low temperatures [-30 to 10 °C] the tension-compression mode was applied, while for high temperatures [20 to 50 °C] the visco-analyzer was operated in shear mode.

6.2.3.2 Results

Figure 6-8 shows a plot of the storage moduli vs. loss moduli obtained from the test results (small symbols) and the results obtained from the model (large symbols) for virgin binder. Figure 6-9 contains the experimental and theoretical results obtained for aged binder.

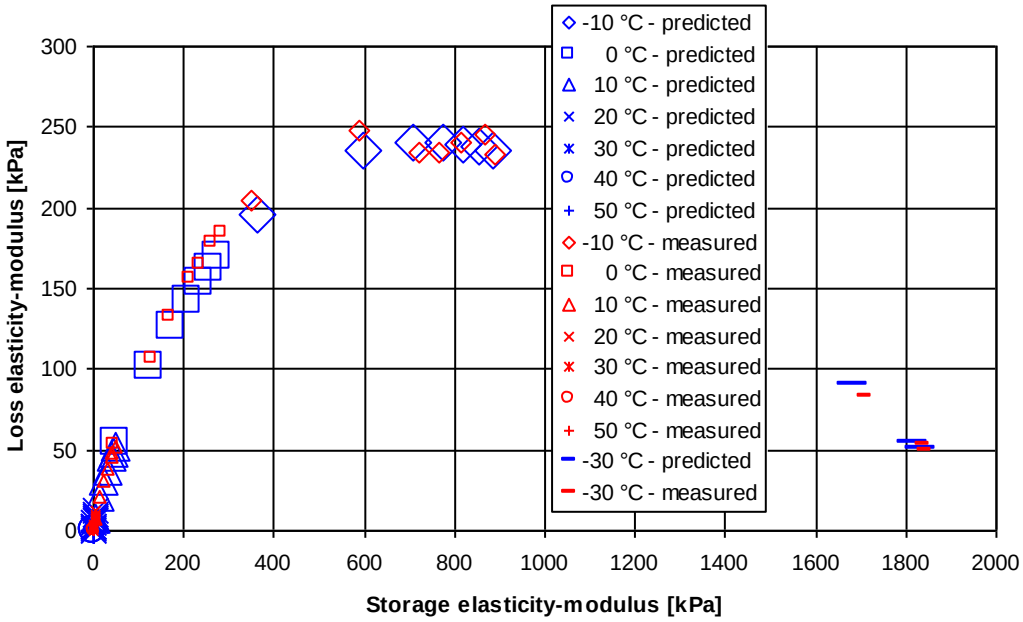

Figure 6-8 Cole-Cole plot, virgin binder

The viscous behavior of bitumen mixes composed of virgin and aged bitumen were also investigated in this study using the same experimental set-up as described above.

Figure 6-10 shows the loss moduli vs. the storage moduli obtained for a bitumen mix consisting of 50% virgin and 50% aged bitumen (small symbols) as well as the model predictions (large symbols).

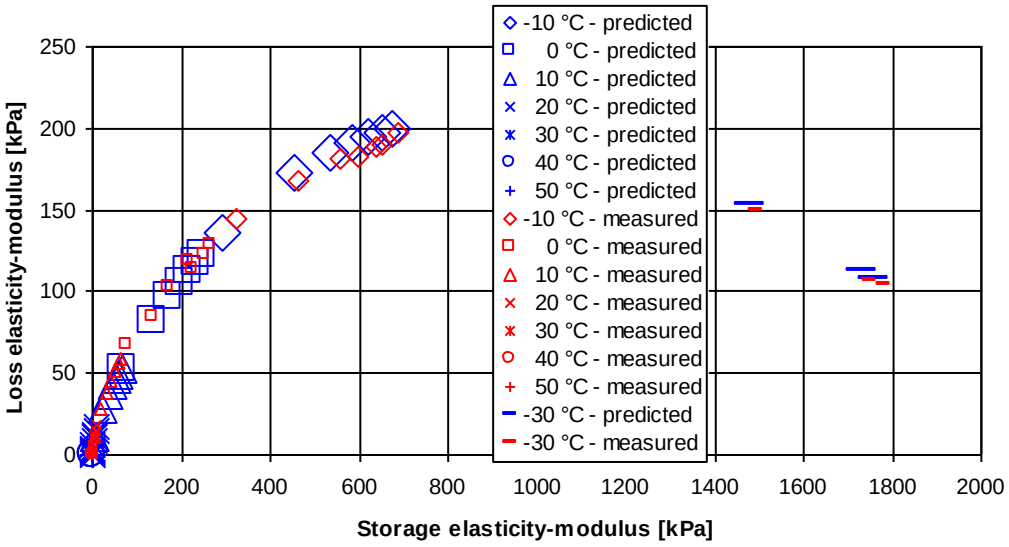

Figure 6-9 Cole-Cole plot, aged binder

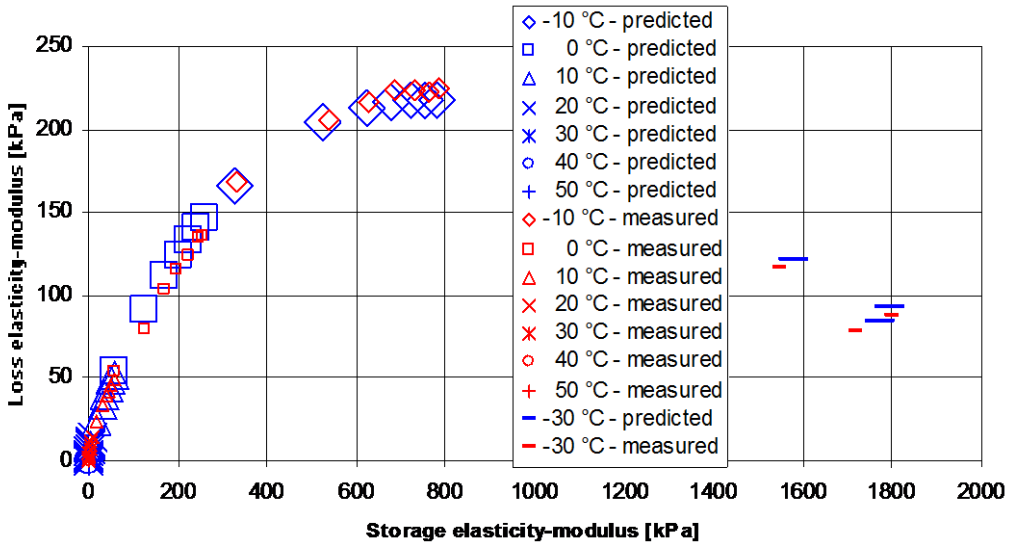

Figure 6-10 Cole-Cole plot, mixed binder, 50-50

The visco-elastic behavior of bitumen mixes composed of virgin and aged bitumen were also investigated in this study using the same experimental set-up as described above.

Figure 6-10 shows the loss moduli vs. the storage moduli obtained for a bitumen mix consisting of 50 % virgin and 50 % aged bitumen.

6.2.4 Modeling

6.2.4.1 Cyclic Behavior

To identify suitable rheological models that can represent the material behavior of bitumen, it may be helpful to study the loss and storage characteristics of different combinations of springs and fractional dashpots. This may be achieved by solving the fractional differential equation of these spring-dashpot-combinations for harmonic loading, such as represented by Equation (6-18).

$$\sigma(t) = \sigma^* \cdot \exp(i \cdot \Omega \cdot t) \tag{6-18}$$

In Equation (6-18), i, denotes a complex number with $i_2 = -1$, Ω, represents the angular frequency with $\Omega = 2\pi f$, and, t, is the time. The strain response, $\varepsilon(t)$, to the harmonic loading may be calculated from Equation (6-19).

$$\varepsilon(t) = \varepsilon^* \cdot \exp(i \cdot \Omega \cdot t) \cdot \exp(-i \cdot \delta) \tag{6-19}$$

The fractional time derivatives of Equation (6-18) and (6-19) are given by Equation (6-20) and (6-21).

$$\frac{d^\alpha}{dt^\alpha}\sigma(t) = \sigma^* \cdot \exp(i \cdot \Omega \cdot t) \cdot \exp(i \cdot \alpha \cdot \frac{\pi}{2}) \cdot \Omega^\alpha \tag{6-20}$$

$$\frac{d^\alpha}{dt^\alpha}\varepsilon(t) = \varepsilon^* \cdot \exp(i \cdot \Omega \cdot t) \cdot \exp(i \cdot \alpha \cdot \frac{\pi}{2}) \cdot \Omega^\alpha \cdot \exp(-i \cdot \delta) \tag{6-21}$$

6.2.4.2 Base model

Fractional time derivatives for various combinations of springs and dashpots may be derived from Equation (6-22) in combination with the tables and figures provided in the Appendix.

$$\sum_{i=1}^{16} b_i \cdot \frac{d^{\beta_i}}{dt^{\beta_i}}\sigma = \sum_{i=1}^{16} c_i \cdot \frac{d^{\beta_i}}{dt^{\beta_i}}\varepsilon \tag{6-22}$$

Equation (6-22) represents the fractional differential equation of the rheological model displayed in Figure 6-11. The coefficients of this model, b_i, and c_i, with i = 1,2,…,16, are given in

Table 6-1. A physical explanation for this model will be provided later. In the context of this section, the model will serve only as a base model from which a number of simpler spring-dashpot-combination can be easily derived.

Table 6-1 Exponents and coefficients of the base model

Exponents	Stress-coefficients	Strain-coefficients
$\beta_1 = \alpha_{11} + \alpha_{12} + \alpha_{21} + \alpha_{22}$	$b_1 = E_1 \cdot E_2 / (p_{13} \cdot p_{23})$	$c_1 = E_1 \cdot E_2 \cdot E_\infty / (p_{13} \cdot p_{23})$
$\beta_2 = \alpha_{11} + \alpha_{12} + \alpha_{21} + \alpha_{23}$	$b_2 = E_1 \cdot E_2 / (p_{13} \cdot p_{22})$	$c_2 = E_1 \cdot E_2 \cdot E_\infty / (p_{13} \cdot p_{22})$
$\beta_3 = \alpha_{11} + \alpha_{12} + \alpha_{22} + \alpha_{23}$	$b_3 = E_1 \cdot E_2 / (p_{13} \cdot p_{21})$	$c_3 = E_1 \cdot E_2 \cdot E_\infty / (p_{13} \cdot p_{21})$
$\beta_4 = \alpha_{11} + \alpha_{13} + \alpha_{21} + \alpha_{22}$	$b_4 = E_1 \cdot E_2 / (p_{12} \cdot p_{23})$	$c_4 = E_1 \cdot E_2 \cdot E_\infty / (p_{12} \cdot p_{23})$
$\beta_5 = \alpha_{11} + \alpha_{13} + \alpha_{21} + \alpha_{23}$	$b_5 = E_1 \cdot E_2 / (p_{12} \cdot p_{22})$	$c_5 = E_1 \cdot E_2 \cdot E_\infty / (p_{12} \cdot p_{22})$
$\beta_6 = \alpha_{11} + \alpha_{13} + \alpha_{22} + \alpha_{23}$	$b_6 = E_1 \cdot E_2 / (p_{12} \cdot p_{21})$	$c_6 = E_1 \cdot E_2 \cdot E_\infty / (p_{12} \cdot p_{21})$
$\beta_7 = \alpha_{12} + \alpha_{13} + \alpha_{21} + \alpha_{22}$	$b_7 = E_1 \cdot E_2 / (p_{11} \cdot p_{23})$	$c_7 = E_1 \cdot E_2 \cdot E_\infty / (p_{11} \cdot p_{23})$
$\beta_8 = \alpha_{12} + \alpha_{13} + \alpha_{21} + \alpha_{23}$	$b_8 = E_1 \cdot E_2 / (p_{11} \cdot p_{22})$	$c_8 = E_1 \cdot E_2 \cdot E_\infty / (p_{11} \cdot p_{22})$
$\beta_9 = \alpha_{12} + \alpha_{13} + \alpha_{22} + \alpha_{23}$	$b_9 = E_1 \cdot E_2 / (p_{11} \cdot p_{21})$	$c_9 = E_1 \cdot E_2 \cdot E_\infty / (p_{11} \cdot p_{21})$
$\beta_{10} = \alpha_{11} + \alpha_{12} + \alpha_{13} + \alpha_{21} + \alpha_{22}$	$b_{10} = E_2 / p_{23}$	$c_{10} = (E_1 \cdot E_2 + E_2 \cdot E_\infty) / p_{23}$
$\beta_{11} = \alpha_{11} + \alpha_{12} + \alpha_{13} + \alpha_{21} + \alpha_{23}$	$b_{11} = E_2 / p_{22}$	$c_{11} = (E_1 \cdot E_2 + E_2 \cdot E_\infty) / p_{22}$
$\beta_{12} = \alpha_{11} + \alpha_{12} + \alpha_{13} + \alpha_{22} + \alpha_{23}$	$b_{12} = E_2 / p_{21}$	$c_1 = (E_1 \cdot E_2 + E_2 \cdot E_\infty) / p_{21}$
$\beta_{13} = \alpha_{11} + \alpha_{12} + \alpha_{21} + \alpha_{22} + \alpha_{23}$	$b_{13} = E_1 / p_{13}$	$c_{13} = (E_1 \cdot E_2 + E_1 \cdot E_\infty) / p_{13}$
$\beta_{14} = \alpha_{11} + \alpha_{13} + \alpha_{21} + \alpha_{22} + \alpha_{23}$	$b_{14} = E_1 / p_{12}$	$c_{14} = (E_1 \cdot E_2 + E_1 \cdot E_\infty) / p_{12}$
$\beta_{15} = \alpha_{12} + \alpha_{13} + \alpha_{21} + \alpha_{22} + \alpha_{23}$	$b_{15} = E_1 / p_{11}$	$c_{15} = (E_1 \cdot E_2 + E_1 \cdot E_\infty) / p_{11}$
$\beta_{16} = \alpha_{11} + \alpha_{12} + \alpha_{13} + \alpha_{21} + \alpha_{22} + \alpha_{23}$	$b_{16} = 1$	$c_{16} = E_1 + E_2 + E_\infty$

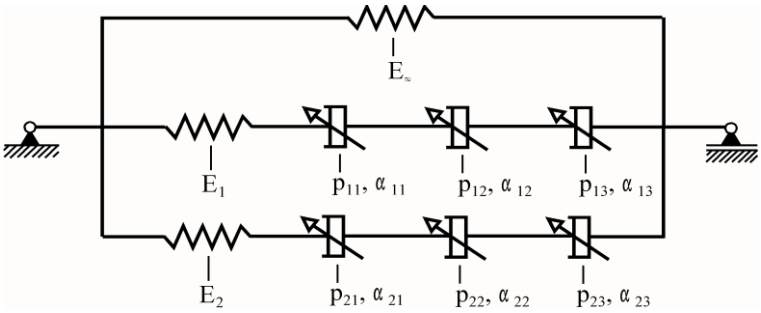

Figure 6-11 Base model ("3S6P"-element)

To derive simpler combinations of springs and dashpots the flow chart given in Figure 6-12 must be used. As an example, we will derive the fractional differential equation of the single fractional dashpot introduced in section 1. To obtain this equation we need to carry out the mathematical operations specified in Figure 6-12. Firstly, E_∞ is to be set to zero, which results in zero values for the coefficients b_1 to b_9 and c_1 to c_9. Secondly, we must set E_2, α_{12}, α_{13}, α_{21}, α_{22} and α_{23} to zero and then let p_{22} and p_{23} approach infinity. After doing this, b_{15}, b_{16} and c_{16} will become the only coefficients to be different from zero. Thirdly, we divide these coefficients by E_1 and let E_1 approach infinity, which yields

$$b_{15} = 1/p_{11}\,,\quad b_{16} = 0\,,\quad c_{16} = 1 \quad \text{and} \quad \beta_{15} = 0\,,\quad \beta_{16} = \alpha_{11} \tag{6-23}$$

Using Equation (6-24) in combination with the coefficients (6-23), we obtain

$$\sigma = p_{11} \cdot \frac{d^{\alpha_{11}}}{dt^{\alpha_{11}}} \varepsilon \tag{6-24}$$

which is equivalent to Equation (6-3). Similar operations can be carried out for the other rheological elements given in Figure 6-12. Hence, Equation (6-22), Figure 6-11, Table 6-1 and the flow chart in Figure 6-12 constitute a general approach to derive differential equations for the most common rheological elements used in modeling of asphalt binders and asphaltic materials.

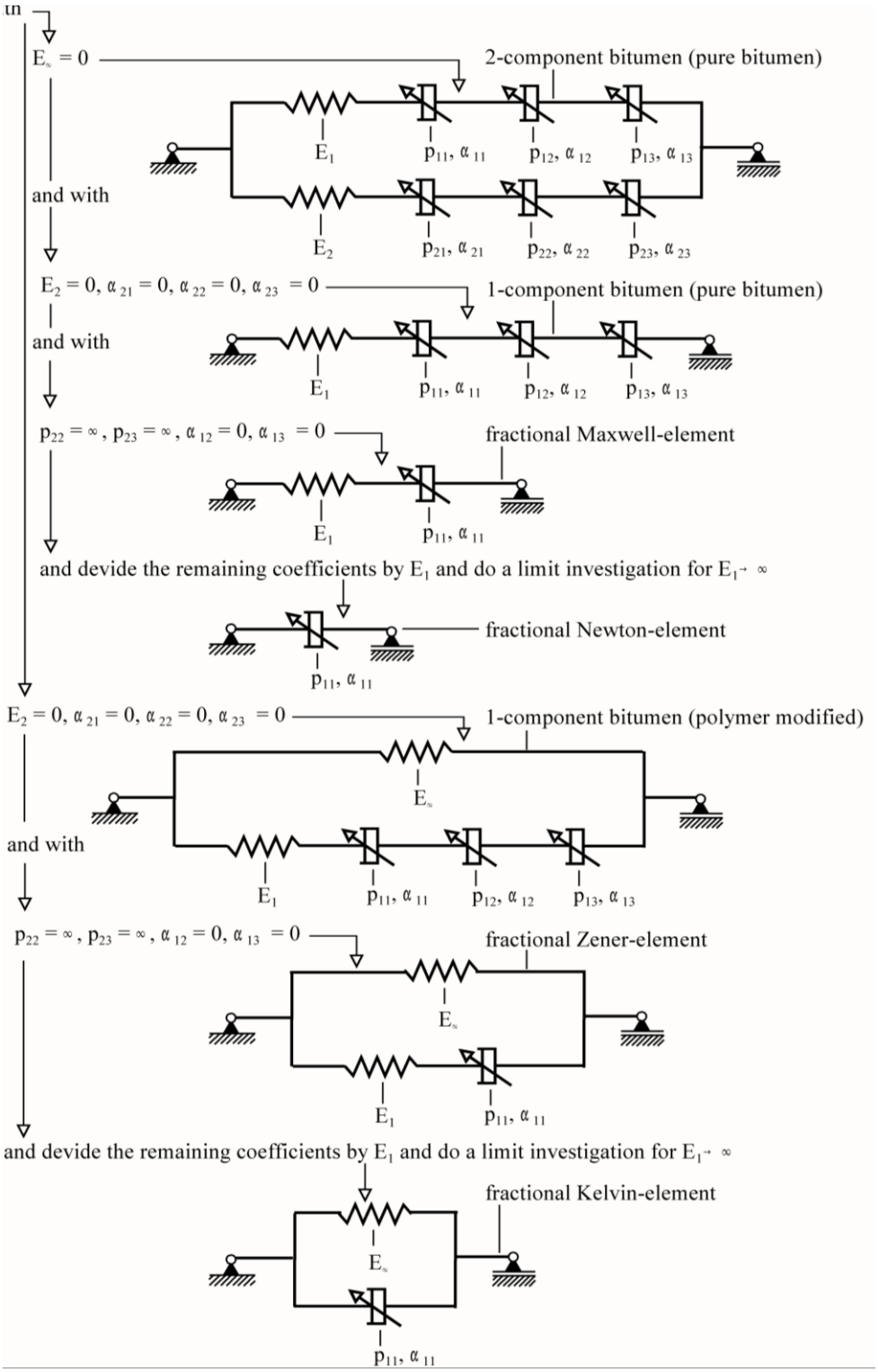

Figure 6-12 Coefficients and exponents of various fractional rheological elements

For harmonic loading, Equation (6-22) can be solved when replacing the fractional differential operators d^{β_i}/dt^{β_i} by Equations (6-20) and (6-21).

$$\sigma^* \cdot \sum_{i=1}^{16} \left(b_i \cdot \exp(i \cdot \beta_i \cdot \frac{\pi}{2}) \cdot \Omega^{\beta_i} \right) = \varepsilon^* \cdot \sum_{i=1}^{16} \left(c_i \cdot \exp(i \cdot \beta_i \cdot \frac{\pi}{2}) \cdot \Omega^{\beta_i} \right) \cdot \exp(-i \cdot \delta) \tag{6-25}$$

Rearranging Equation (6-25) with respect to the stress-strain-quotient, σ^*/ε^*, yields the complex modulus, E^*.

$$\frac{\sigma^*}{\varepsilon^*} = E^* \cdot \exp(-i \cdot \delta) \quad \text{with} \quad E^* = \frac{\sum_{i=1}^{16} \left(c_i \cdot \exp(i \cdot \beta_i \cdot \frac{\pi}{2}) \cdot \Omega^{\beta_i} \right)}{\sum_{i=1}^{16} \left(b_i \cdot \exp(i \cdot \beta_i \cdot \frac{\pi}{2}) \cdot \Omega^{\beta_i} \right)} \tag{6-26}$$

The exponential functions, $\exp(i \cdot \beta_i \cdot \pi/2)$, in Equation (6-26) may be replaced by

$$\exp(i \cdot \beta_i \cdot \frac{\pi}{2}) = \cos(\beta_i \cdot \frac{\pi}{2}) + i \cdot \sin(\beta_i \cdot \frac{\pi}{2}) \tag{6-27}$$

which yields to

$$E^* = \frac{a_1 + i \cdot a_2}{a_3 + i \cdot a_4} \tag{6-28}$$

with

$$\begin{aligned} a_1 &= \sum_{i=1}^{16} \left(c_i \cdot \cos(\beta_i \cdot \frac{\pi}{2}) \cdot \Omega^{\beta_i} \right) \\ a_2 &= \sum_{i=1}^{16} \left(c_i \cdot \sin(\beta_i \cdot \frac{\pi}{2}) \cdot \Omega^{\beta_i} \right) \\ a_3 &= \sum_{i=1}^{16} \left(b_i \cdot \cos(\beta_i \cdot \frac{\pi}{2}) \cdot \Omega^{\beta_i} \right) \\ a_4 &= \sum_{i=1}^{16} \left(b_i \cdot \sin(\beta_i \cdot \frac{\pi}{2}) \cdot \Omega^{\beta_i} \right) \end{aligned} \tag{6-29}$$

After rearrangement of Equation (6-28), we obtain

$$E^* = E' + i \cdot E'' \tag{6-30}$$

wherein, E', denotes the storage modulus

$$E' = \frac{a_1 \cdot a_3 + a_2 \cdot a_4}{(a_3)^2 + (a_4)^2} \tag{6-31}$$

and, E'', is the loss modulus

$$E'' = \frac{a_2 \cdot a_3 - a_1 \cdot a_4}{(a_3)^2 + (a_4)^2} \tag{6-32}$$

Having determined the relationships (6-31) and (6-32), it is now possible to study the loss and storage characteristics of the different rheological elements shown in Figure 6-11 and Figure 6-12.

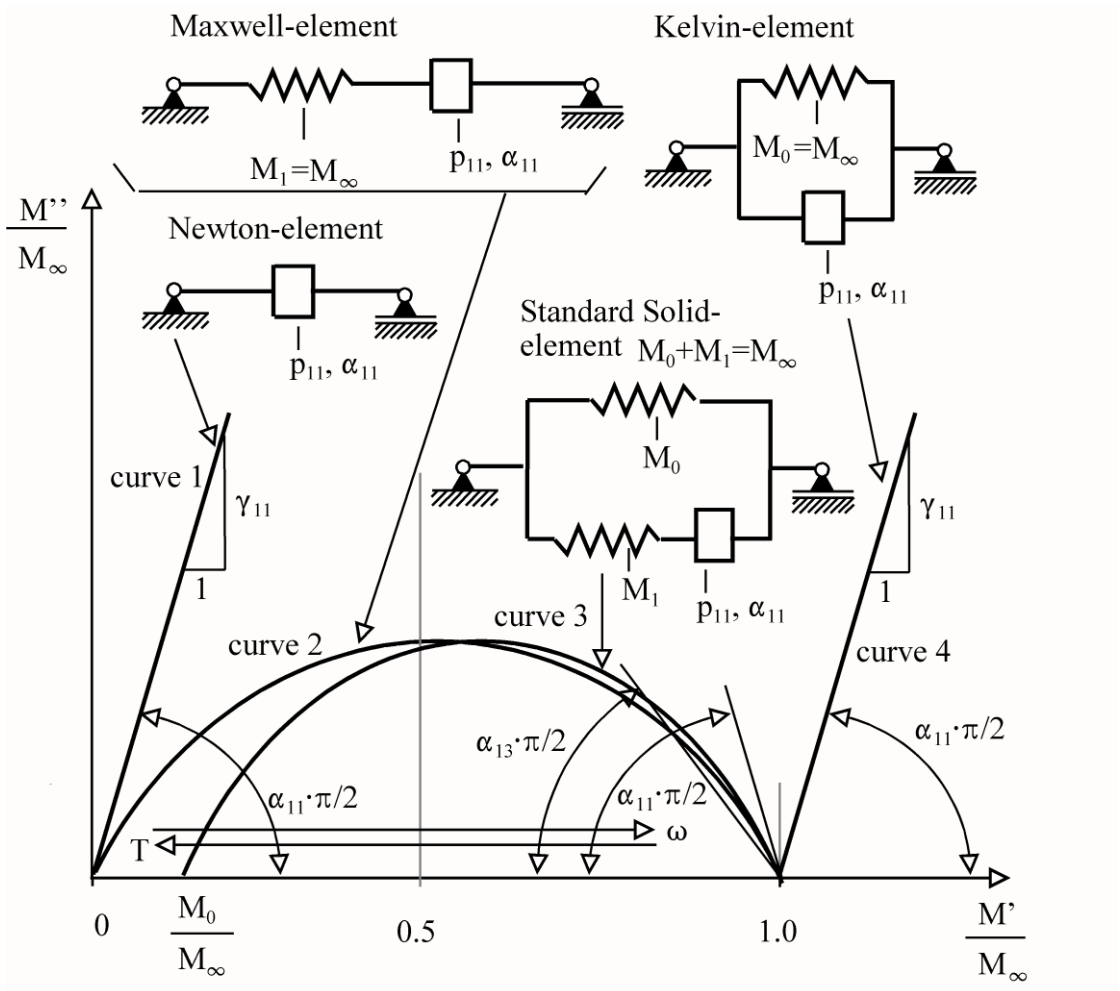

Figure 6-13 Cole-Cole-curves

The loss-storage-moduli-curve (Cole-Cole-curve) of the single fractional dashpot is a straight line of slope $\gamma_{11}/1$ (see Figure 6-13, curve 1). The slope may be calculated from the exponent, α_{11}.

$$\alpha_{11} = \frac{2}{\pi} \cdot \tan^{-1}(\gamma_{11}) \tag{6-33}$$

The Cole-Cole-curve of the fractional Maxwell-element is represented by curve 2 in Figure 6-13. This curve is a section of a circle intersecting with the axis of the storage modulus at angle, α_{11}, on both sides. The distance between the intersection points is, E_1. Curve 3 represents a rheological element consisting of one spring and three fractional dashpots connected in series. According to the nomenclature developed in Olard & di Benedetto (2003) we shall call this element "1S3P" meaning 1 spring, 3 parabolic elements. The expressions "parabolic elements" and "fractional dashpots" are identical in a sense that both of them refer to a dashpot-like element based on the fractional differential formulation given by Equation (6-3). The Cole-Cole-curve of the "1S3P"-element intersects with the axis of the storage-modulus at angles, α_{11}, and α_{13} if $\alpha_{11} < \alpha_{12} < \alpha_{13}$. This rheological element is best suited to model binders that exhibit pure liquid behavior for low frequencies and high temperature, i.e., binder that have a phase lag of almost 90° and no relaxation in the quasi-liquid state. If the phase lag in the quasi-liquid state is in fact 90°, the exponent α_{11} becomes 1. In this case the first fractional dashpot turns into a conventional dashpot. According to Olard & di Benedetto (2003) we call this element "1S2P1D", meaning 1 spring, 2 parabolic elements and 1 dashpot.

The relaxation behavior in the quasi-liquid state can be best studied by means of Black-curves. The black-curve of the "1S3P' element is shown in Figure 6-8. Figure 6-8 also contains the Black-curve on an element consisting of one spring coupled to another "1S3P" element in parallel. This new developed element is called "2S3P" element and shown in Figure 6-14.

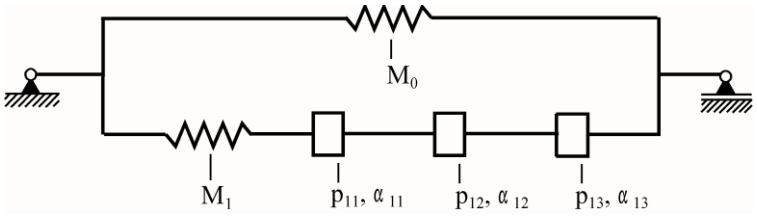

Figure 6-14 Model ("2S3P"-element)

Because of the (stiffness of the) parallel spring this element exhibits solid-like behavior for high temperatures and low frequencies. The "2S2P1D" element discussed in Olard & di Benedetto (2003) is a sub-case of the "2S3P" element obtained when the exponent of the first dashpot of the "2S3P" element is set to 1. "2S2P1D" and "2S3P" elements are suited to model the behavior of polymer modified bitumen. A physical explanation for this is that polymer modified bitumen possess special molecules that can form a solid-like skeleton within the bitumen.

This solid-like skeleton becomes active when the rest of the bitumen is in its quasi-liquid state. Cole-Cole-curves of other solid-like elements such as the fractional Zener-element and the fractional Kelvin-element are shown in Figure 6-13.

Creep Behavior

In order to study the creep behavior of rheological elements we need to solve Equation (6-22) for loading scenarios other than harmonic ones. A widely used approach is to split the non-harmonic load-time-curve into increments. Within each increment stresses are assumed to be constant. Under these conditions, the strain response, ε_k , of the single fractional dashpot may be obtained by convoluting creep-function (6-6) with respect to, t. The variable, τ, represents the convoluted time, t.

$$\varepsilon_k(t) = \int_0^t \left(\frac{(t-\tau)^{\alpha_{jk}}}{p_{jk} \cdot \Gamma(\alpha_{jk}+1)} \right) d\sigma_j(\tau) \quad \text{with } \varepsilon_k = \varepsilon \text{ and } \sigma_j = \sigma \text{ and with } j=1,\ k=1 \tag{6-34}$$

Equation (6-34) may also be defined in terms of stress ratios, $\dot{\sigma}_j$, rather that differential stresses, $d\sigma_j$.

$$\varepsilon_k(t) = \int_0^t \left(\frac{(t-\tau)^{\alpha_{jk}}}{p_{jk} \cdot \Gamma(\alpha_{jk}+1)} \cdot \dot{\sigma}_j(\tau) \right) d\tau \tag{6-35}$$

Equation (6-35) must now be evaluated for each increment, $[i]$, with $[i] = [1], \ldots, [m]$. The stress ratio, $\dot{\sigma}_j$, may be expressed by quotient, $\Delta\sigma_j^{[i]}/\Delta t^{[i]}$, wherein, $\Delta\sigma_j^{[i]}$, represents the stress increment, and, $\Delta t^{[i]}$, the duration of increment [i].

$$\varepsilon_k\left(t^{[m]}\right) = \varepsilon_k^{[m]} = \sum_{i=1}^{m} \left(\int_{t^{[i-1]}}^{t^{[i]}} \left(\frac{\left(t^{[m]}-\tau\right)^{\alpha_{11}}}{p_{jk} \cdot \Gamma(\alpha_{jk}+1)} \cdot \frac{\Delta\sigma_j^{[i]}}{\Delta t^{[i]}} \right) d\tau \right) \tag{6-36}$$

In Equation (6-36), $\varepsilon^{[m]}$, denotes the strain at the end of increment $[m]$. The point in time that corresponds to the end of increment $[m]$ is called, $t^{[m]}$. Evaluating the integrals in Equation (6-36) yields to

$$\varepsilon_k^{[m]} = \sum_{i=1}^{m} \left(\frac{\left(t^{[m]}-t^{[i-1]}\right)^{\alpha_{11}+1} - \left(t^{[m]}-t^{[i]}\right)^{\alpha_{11}+1}}{p_{11} \cdot \Gamma(\alpha_{11}+1) \cdot (\alpha_{11}+1)} \cdot \frac{\Delta\sigma^{[i]}}{\Delta t^{[i]}} \right) \tag{6-37}$$

The strain response, $\varepsilon_0^{[m]}$, of a single spring may be calculated from Equation (6-38).

$$\varepsilon_0^{[m]} = \sum_{i=1}^{m}\left(\frac{1}{E_j}\cdot\frac{\Delta\sigma_j^{[i]}}{\Delta t^{[i]}}\cdot\left(t^{[i]}-t^{[i-1]}\right)\right) \tag{6-38}$$

The strain response of an element consisting of a spring and three fractional dashpots connected in series ("1S3P" element) may be derived by adding Equations (6-37) and (6-38) as follows.

$$\varepsilon^{[m]} = \sum_{i=1}^{m}\left(\frac{1}{E_j}\cdot\frac{\Delta\sigma_j^{[i]}}{\Delta t^{[i]}}\cdot\left(t^{[i]}-t^{[i-1]}\right)\right)+\sum_{i=1}^{m}\left(\sum_{k=1}^{3}\left(\frac{\left(t^{[m]}-t^{[i-1]}\right)^{\alpha_{jk}+1}-\left(t^{[m]}-t^{[i]}\right)^{\alpha_{jk}+1}}{p_{jk}\cdot\Gamma(\alpha_{jk}+1)\cdot(\alpha_{jk}+1)}\right)\cdot\frac{\Delta\sigma_j^{[i]}}{\Delta t^{[i]}}\right) \tag{6-39}$$

To derive the strain response of the "2S3P" element we need to couple Equation (6-39) in parallel with the strain response of the single spring, E_∞, (see Figure 6-12). The strain response of the single spring, E_∞, is given by Equation (6-40).

$$\varepsilon^{[m]} = \sum_{i=1}^{m}\left(\frac{1}{E_\infty}\cdot\left(t^{[i]}-t^{[i-1]}\right)\cdot\frac{\Delta\sigma_\infty^{[i]}}{\Delta t^{[i]}}\right) \tag{6-40}$$

The coupling of Equations (6-39) and (6-40) may be realized by using Equation (6-41) that states that the stress increment in the spring, $\Delta\sigma_\infty^{[m]}$, must add up with the stress increment in the "1S3P" element, $\Delta\sigma_1^{[m]}$, to the total stress increment, $\Delta\sigma^{[m]}$.

$$\Delta\sigma^{[m]} = \begin{cases} \Delta\sigma_\infty^{[m]}+\Delta\sigma_1^{[m]} & \text{for the "2S3P" element} \\ \Delta\sigma_\infty^{[m]}+\sum_{j=1}^{2}\Delta\sigma_j^{[m]} & \text{for the "3S6P" element} \end{cases} \tag{6-41}$$

To use Equation (6-41) we must first isolate the stress increments, $\Delta\sigma_j^{[m]}$, and , $\Delta\sigma_\infty^{[m]}$, from the sum in Equation (6-39) and (6-40). Performing this on Equation (6-39) results in:

$$\varepsilon^{[m]} = A_j^{[m]}\cdot\frac{\Delta\sigma_j^{[m]}}{\Delta t^{[m]}}+\in_j^{[m-1]} \tag{6-42}$$

with

$$A_j^{[m]} = \frac{1}{E_j}\cdot\left(t^{[m]}-t^{[m-1]}\right)+\sum_{k=1}^{3}\left(\frac{\left(t^{[m]}-t^{[m-1]}\right)^{\alpha_{jk}+1}}{p_{jk}\cdot\Gamma(\alpha_{jk}+1)\cdot(\alpha_{jk}+1)}\right) \tag{6-43}$$

and with

$$\in_j^{[m-1]} = \sum_{i=1}^{m-1}\left(\frac{1}{E_j}\cdot\frac{\Delta\sigma_j^{[i]}}{\Delta t^{[i]}}\cdot\left(t^{[i]}-t^{[i-1]}\right)\right)+\sum_{i=1}^{m-1}\left(\sum_{k=1}^{3}\left(\frac{\left(t^{[m]}-t^{[i-1]}\right)^{\alpha_{jk}+1}-\left(t^{[m]}-t^{[i]}\right)^{\alpha_{jk}+1}}{p_{jk}\cdot\Gamma(\alpha_{jk}+1)\cdot(\alpha_{jk}+1)}\right)\cdot\frac{\Delta\sigma_j^{[i]}}{\Delta t^{[i]}}\right) \tag{6-44}$$

For Equation (6-40) we obtain:

$$\varepsilon^{[m]} = A_\infty^{[m]}\cdot\frac{\Delta\sigma_j^{[m]}}{\Delta t^{[m]}}+\varepsilon^{[m-1]} \tag{6-45}$$

with

$$A_\infty^{[m]} = \frac{1}{E_\infty}\cdot\left(t^{[m]}-t^{[m-1]}\right) \tag{6-46}$$

Equation (6-41), (6-42) and (6-45) constitute a system of equations for the stress increments, $\Delta\sigma_j^{[m]}$, and , $\Delta\sigma_\infty^{[m]}$.

$$\begin{bmatrix}1 & 1\\ -A_\infty^{[m]} & A_1^{[m]}\end{bmatrix}\cdot\begin{bmatrix}\Delta\sigma_\infty^{[m]}\\ \Delta\sigma_1^{[m]}\end{bmatrix}=\begin{bmatrix}\Delta\sigma^{[m]}\\ \varepsilon^{[m-1]}-\in_1^{[m-1]}\end{bmatrix} \tag{6-47}$$

$$\underline{\underline{A}}^{[m]}\cdot\Delta\dot{\sigma}^{[m]} = \underline{\in}^{[m-1]}$$

The stress increments can now be determined by:

$$\Delta\underline{\sigma}^{[m]} = \left(\underline{\underline{A}}^{[m]}\right)^{-1}\cdot\underline{\in}^{[m-1]} \tag{6-48}$$

For the “3S6P” element the population of the coefficient matrix, $\underline{\underline{A}}^{[m]}$, and the vectors, $\Delta\underline{\sigma}^{[m]}$, and, $\underline{\in}^{[m-1]}$, is given by Equation (6-49).

$$\begin{bmatrix}1 & 1 & 1\\ -A_\infty^{[m]} & A_1^{[m]} & 0\\ -A_\infty^{[m]} & 0 & A_2^{[m]}\end{bmatrix}\cdot\begin{bmatrix}\Delta\sigma_\infty^{[m]}\\ \Delta\sigma_1^{[m]}\\ \Delta\sigma_2^{[m]}\end{bmatrix}=\begin{bmatrix}\Delta\sigma^{[m]}\\ \varepsilon^{[m-1]}-\in_1^{[m-1]}\\ \varepsilon^{[m-1]}-\in_2^{[m-1]}\end{bmatrix} \tag{6-49}$$

$$\underline{\underline{A}}^{[m]}\cdot\Delta\underline{\sigma}^{[m]} = \underline{\in}^{[m-1]}$$

To determine the inner variable, $\in_j^{[m-1]}$, (see Equation (6-44)) knowledge of the entire stress history (i.e. knowledge of all previous stress increments) is required. This significantly restricts the applicability of fractional rheological elements for numerical analysis since the provision of all previous stress increments slows down the computation and requires extensive memory space. To avoid these problems, recursive artificial neural networks have been used, do determine, $\in_j^{[m-1]}$. Using

these networks may significantly reduce computational time need as well as memory demand without compromising the accuracy of computational results.

6.2.4.3 The Influence of Aged Material Components

The influence of aging on the energy-loss/energy storage characteristics of binder can be seen from Figure 6-15. Because of the lower content of viscous components in the binder after aging the energy dissipation ability of the material is significantly reduced. This phenomenon manifests itself in a flatter slope of the Cole-Cole curve at the left side and the right intersections well as in a lower position of the curve's apex. These effects can be easily captured by the model through reducing the parameters α_{11} and α_{13} accordingly. In addition to a flatter sloped and lower apex of the Cole-Cole curve, most binders and asphalts exhibit a higher modulus when aged or composed of aged components.

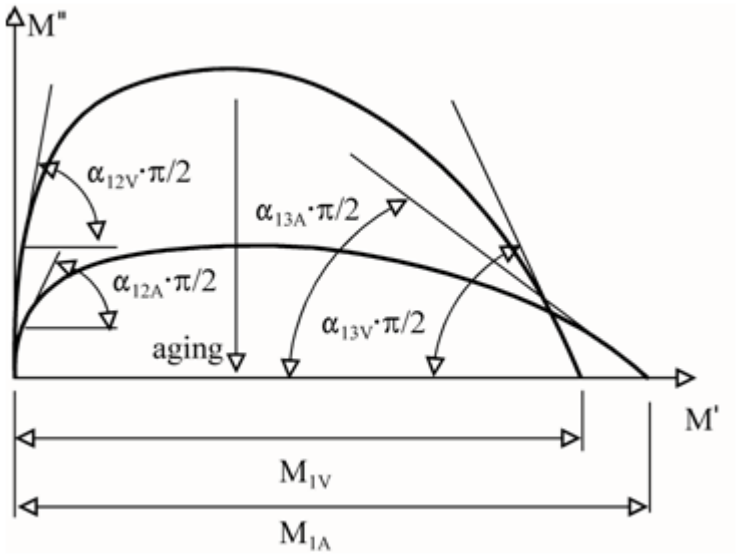

Figure 6-15 Cole-Cole plot, virgin and aged binder

In Figure 6-15, the index V represent the virgin material and the index A the aged.

6.2.4.4 Determination of model parameters

At TU Dresden repeated load triaxial tests (dynamic compression tests) were conducted to determine the material parameters of the visco-elastic model developed at TU Dresden. The Master Curves and the Cole-Cole Plots of the asphalt mixtures investigated are required for the determination of the parameters of the visco-elastic model. The development of the Master Curves and the Cole-Cole plots are explained in detail in chapter 3, section 4.1.1 and section 5.1.1. The parameters for the Cole-Cole plots and the master curves can be determined automaticly using the numerical tool **ReRoadToolTUD** developed at TU Dresden within the Re-Road project and described in chapter 10.

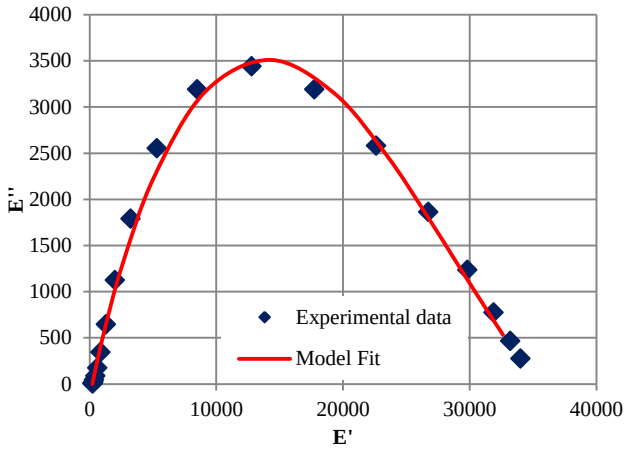

Cole-Cole plot Material I

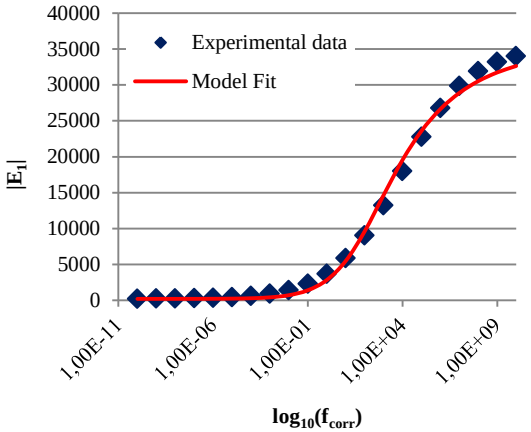

Master curve Material I

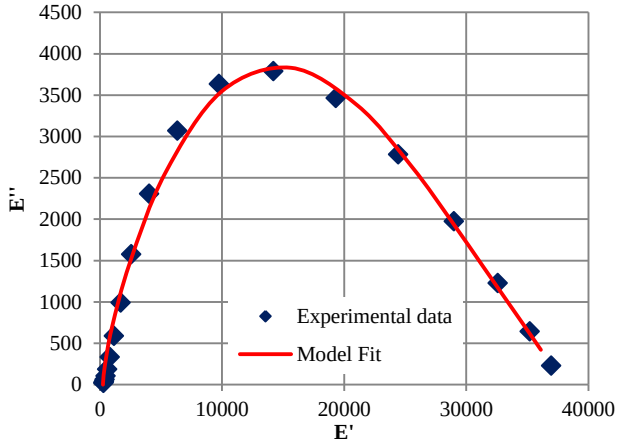

Cole-Cole plot Material II

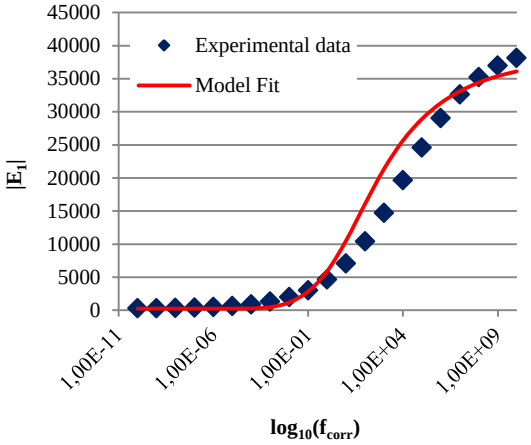

Master curve Material II

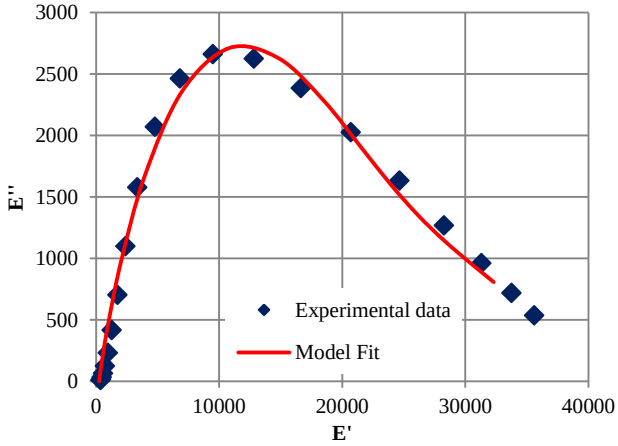

Cole-Cole plot Material III

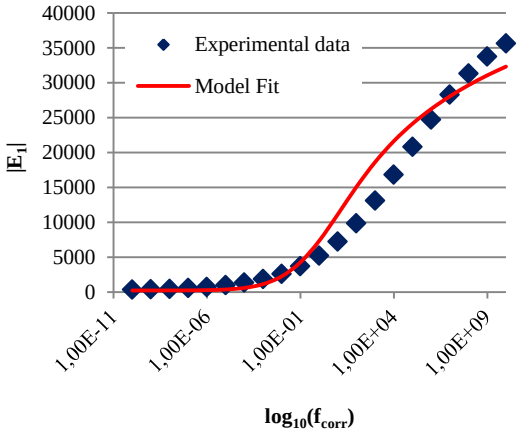

Master curve Material III

Figure 6-16 Cole-Cole Plots and Master Curves for Material I, II and III (Model fit)

The realized dynamic compression tests are indicated in Table 5-1. The regression functions of the master curves of the absolute modulus $|E_1|$ for T_R=20°C and the Cole-Cole plots for Material I, II and III are shown in Figure 5-11 and Figure 5-18 .

For the "2S3P"-element the parameters M_0, M_1, α_{11}, α_{12} α_{13}, p_{11} p_{12} and p_{13} can be determined using the equations and explications summarised in this chapter.

Figure 6-16 shows the curves obtained for the asphalt mixtures tested after fitting with the experimental data. The curve fitting was performed by the least square method. The determined parameters of the "2S3P"-element are listed in Table 6-2. The numerical tool ReRoadToolTUD developed at TU Dresden (see chapter 10) allows entering the model paramters to determine manually a satisfying set of parameters.

Table 6-2 Parameters of the "2S3P"-element

Parameter	Material I	Material II	Material III
M_0 [MPa]	215	250	250
M_1 [MPa]	34900	37750	40000
α_{11}	0.40	0.85	0.50
α_{12}	0.38	0.395	0.315
α_{13}	0.14	0.145	0.077
p_{11}	151500	184000	85500
p_{12}	3400	9000	14000
p_{13}	18100	25000	26900

It can be concluded from Figure 6-16 and the discussions in chapter 5 that for a satisfying set of parameters (satisfaying fitting) more laboratory tests at low temperatures are necessary. However, the fitting of the section with the highest relevance for road construction is satisfying.

6.2.4.5 Conclusion

Since the 2S3P element only comprises fractional dashpots and a spring is coupled in parallel to those dashpots, all strains will be fully recovered by the element after unloading. Hence, the 2S3P element, similar to the 2S2P1D element, represents the behaviour of visco-elastic solids. The difference between these two elements lies in that the Cole-Cole curve of the 2S2P1D element intersects with the axis of the storage modulus at 90 degrees for very low frequencies and very high temperatures (see Figure 6-1), while the 2S3P element has an intersection angle of 0 degrees at that temperature and frequency range. Although it is known that most of the asphalt mixes currently used in pavements may be modelled with 2S2P1D elements, it must be considered that if alternative binders, such as resins are used, the behaviour at high temperatures and low frequencies will be very different from conventional mixes. For such materials with new or alternative binders, the 2S3P element will provide a much more accurate representation of the actual rheological behaviour than the 2S2P1D element. As the cost for conventional binders have increased over the past years due to high demand and shrinking supply, the use of new or alternative binders for road pavements will become more common in the future.

New or alternative binders may be extracted from resin obtained from naturally occurring sources, such as trees or plants. In dependency on the molecular composition of these materials, their susceptibility to high temperatures and low frequencies may be very different from conventional binders. Most of the new or alternative binders that are currently researched and developed are much less temperature dependant that conventional binders. However, the rheological characteristics of these materials change during the curing process in that it turns from a viscous fluid into a viscous solid. Given the circumstances that resins may shrink by as much as 6% during curing (O'Brien at el., 2001), accurate modelling of the material behaviour will be crucial to prevent damages during the construction of pavements using such binders. The base model allows for these effects to be captured in an efficient and mathematically elegant manner.

The rheological formulation established in this report constitutes a physical representation of the viscous behavior of virgin and aged binders as well as binder mixes. The model is based on fractional differential equations that are independent of the boundary conditions used in the tests. As such, they can be solved for conditions allowing solutions for static, harmonic (cyclic) and any other loading scenarios to be determined. It has been shown in the paper that the rheological formulation is capable of modeling and predicting the viscous behavior of binders and binder mixes at reasonably good accuracy levels.

It can be concluded that the visco-ealstic model is used to determine the stresses and strains at the relevant point in the pavement. Based on theses stresses and strains the plastic model estimates the accumulated permanent deformation.

At TU Dresden repeated load triaxial tests (dynamic compression tests) were conducted to determine the material parameters of the visco-elastic model

developed at TU Dresden. The Master Curves and the Cole-Cole Plots of the asphalt mixtures investigated are required for the determination of the parameters of the visco-elastic model. The development of the Master Curves and the Cole-Cole plots are explained in detail in chapter 3, section 4.1.1 and section 5.1.1. The parameters for the Cole-Cole plots and the master curves can be determined automaticly using the numerical tool **ReRoadToolTUD** developed at TU Dresden within the Re-Road project (see chapter 10. The developed model can be implemented amongst others in a FE program.

6.3 Plastic Model

The plastic model developed during the project is based on the results of the cyclic triaxial tests. This model was validated using experimental data from the Hamburg Wheel Tracking Tests (HWTT) at 40°C. The rut depth was measured in the HWTT and the stresses were calculated with the FE program ReFEM. The HWTT were used for model validation in place of the Dublin wheel tracking test since in the HWTT the development of the plastic deformation was measured continuously in dependency on the number of wheel passes (see Figure 8-6).

The plastic model predicts the plastic deformation using a correlation between resilient and plastic strains and /or stresses and plastic strains. This simplified approach can be used to predict the plastic deformation in the loading axis. The model build on an exponential law that links the vertical plastic strain rate $\varepsilon_{1;p;rate}$ to the vertical resilient strain $\varepsilon_{1;r}$ and the stresses respectively.

$$\varepsilon_{1,p,rate} = a \cdot \left(e^{b \cdot \varepsilon_{1,r}} - 1\right) \tag{6-50}$$

$$\frac{\varepsilon_{1,p,rate}}{(L / p_a)} = c \cdot \left(e^{d \cdot \frac{q}{p}} - 1 \right) \tag{6-51}$$

where

$\varepsilon_{1;p;rate}$	[10^{-3}/cycle]	vertical plastic strain rate
$\varepsilon_{1;r}$	[10^{-3}]	vertical resilient strain
a, b, c, d	[-]	material parameters
q	[kPa]	deviatoric stress
p	[kPa]	hydrostatic stress
p_a	[kPa]	reference stress = 100 kPa
L	[kPa]	$\sqrt{p^2 + q^2}$

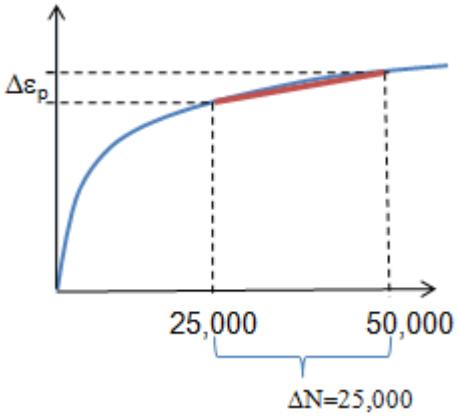

Figure 6-17 Determination of the plastic strain rate

The model is fitted with the results of long term repeated load triaxial tests in which stresses as well as resilient and permanent strain are recorded. The plastic strain rates, $\varepsilon_{1;p;rate}$, are determined from the permanent strain curve (permanent strains vs. load cycles) using the slope of the secant line between 25,000 and 50,000 cycles (Figure 6-17).

Figure 6-18 and Figure 6-19 show the curves obtained for the materials tested after fitting Equation 2.1 and 2.2 with experimental data. The rate of permanent strain was calculated in $‰$ per 1 million load cycles. Table 6-3 presents the parameter obtained after fitting the experimental data. The curve fitting was performed by the least square method.

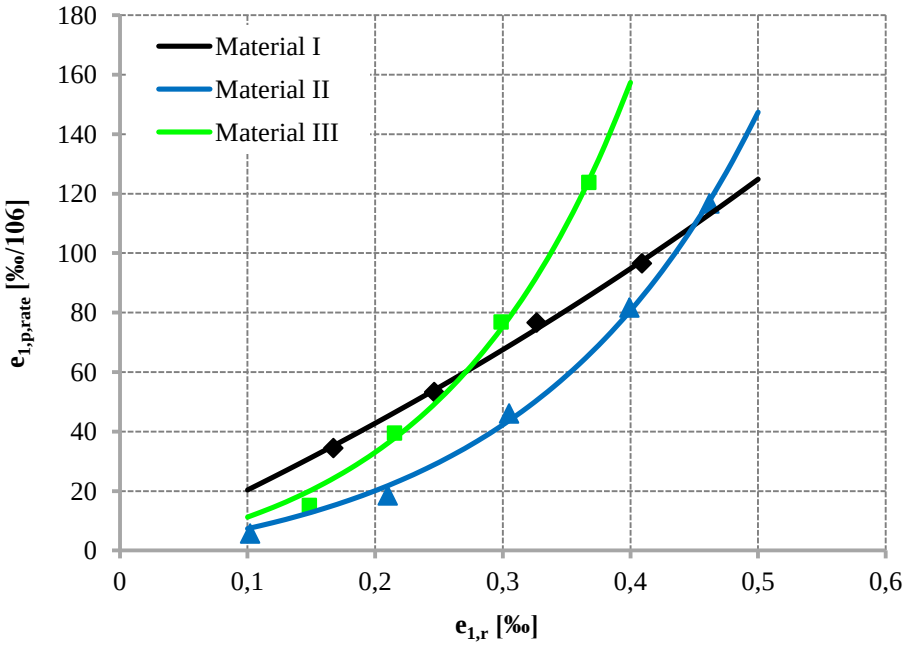

Figure 6-18 Correlation between permanent strain rate and resilient strain

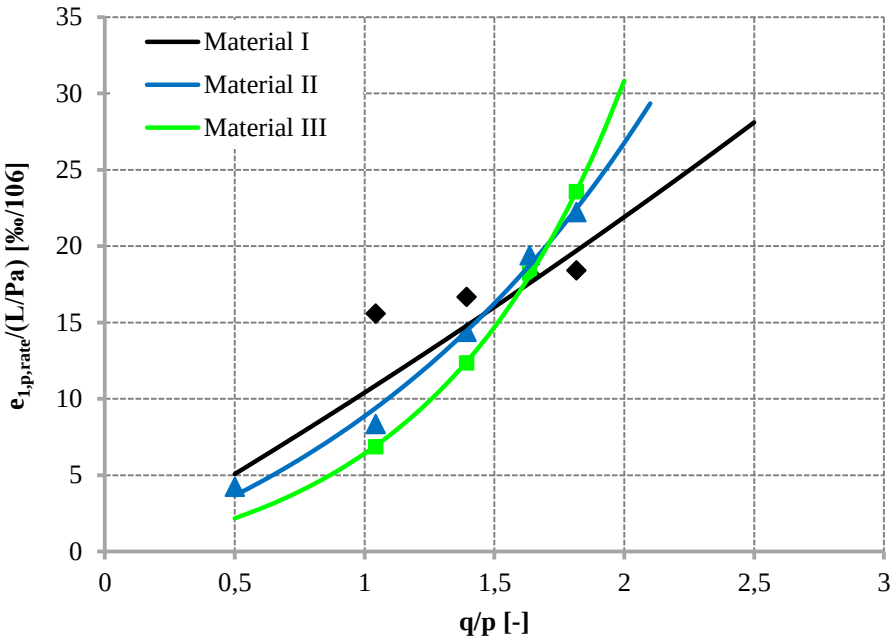

Figure 6-19 Correlation between permanent strain rate and stresses

Table 6-3 Parameter of plastic model for the materials tested

Plastic Model Parameter	Material I	Material II	Material III
a [-]	199	9.99	11.95
b [-]	0.97	5.91	6.62
c [-]	98.93	8.69	2.28
d [-]	0.1	0.7	1.34

The results, indicated in Figure 6-18 and Figure 6-19, show a different plastic behavior between the virgin material (Material I) and the two asphalt mixes with RA (Materials II and III). From the plots it is clear, that the permanent deformation performance of the two asphalt mixes with RA is hindered severely at large shear stress ratios where the resilient strains are also large.

More test results would be necessary to confirm this trend. Based on the very limited number of tests that have been carried out in the framework of the project, it seems impossible to find a plausible explanation to this phenomenon.

At the moment the empirical plastic model can only describe behaviour for 1 specific test condition (1 frequency, 1 temperature). However, this model can be easily extended when more experimental data become available.

7 Model Development at University of Nottingham

This chapter will present a new material constitutive model specifically calibrated for Re-Road reclaimed asphalt mixes and developed from collaboration between the University of Nottingham (UNOTT) and the Technical University of Delft (TU Delft).

In the first part of this section, details on the material constitutive model are presented via the description of the general constitutive framework and the description of the flow surfaces. In a second part the suitable constitutive model will be shown together with a description of the procedure used for obtaining the proper parameters for each element. The model will be then calibrated based on Creep & Recover tests performed on the Re-Road Materials I, II and III which contain respectively, 0%, 15% and 30% of RA.

Details of the calibration and validation of the model will be provided in Section 4.4 where experimental curves will be used for both the calibration and validation phases. In this study, the finite element (FE) system CAPA-3D (Erkens 2002) in the framework of large strain, energy based, and three dimensional constitutive model developed at the Section of Structural Mechanics of TU Delft has been utilised as the numerical platform. Nevertheless the algorithms and procedures, showed in the following sections, represent an open source that can be implemented in any FE code (e.g. Pavement Design Software) which allows the customisation of the constitutive laws of the materials.

7.1 Dissipation energy based 3D constitutive model

The constitutive model proposed has been formulated for the response prediction of asphaltic materials incorporating RA. It is based on a dissipation energy based elasto-visco-plastic obtained by coupling in-serie a visco-elastic component (”Zener” element) with a ”Perzyna” component to take into account the inelastic behaviour (Figure 7-3a). This constitutive model has been developed from a collaboration between the University of Nottingham and the Delft University of Technology.

7.1.1 Theoretical background

There is a great variety of engineering materials which, depending on strain rate and/or temperature, exhibit response characteristics varying anywhere between the elasto-plastic and the visco-elastic limits. Asphalt mixes concrete typical examples. Constitutive modelling of such types of materials can be implemented by combining the features of purely elasto-plastic and purely visco-elastic materials to create a more general category of constitutive models termed elasto-visco-plastic. The actual number of necessary components is decided on the basis of the available experimental evidence.

Depending on strain rate and temperature, the response of an asphalt mixture can vary anywhere between the elasto-plastic and the visco-elastic limits. Constitutive models for such types of materials can be developed by combining the features of

purely elastoplastic and purely visco-elastic materials to create a more general category of constitutive models termed elasto-visco-plastic.

7.1.1.1 Multiplicative decomposition

When applying the multiplicative decomposition, has been proposed by Lee et. al. (1967) and Lee (1969), the total deformation gradient could be divided into a residual deformation component (F_r) and a component signifying the elastic unloading (F_e) that the material must undergo from the configuration at time t to the residual configuration.

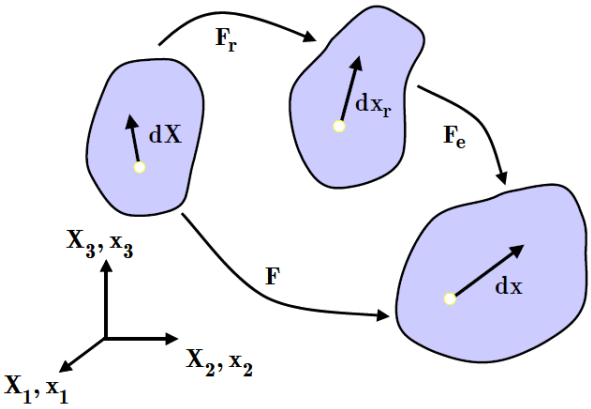

Figure 7-1 Multiplicative decomposition of the deformation gradient

Figure 7-1 shows the multiplicative decomposition of the deformation gradient of a material in which the elasto-plastic and the viscoelastic components act in parallel. It holds

$$\mathbf{F} = \mathbf{F}_\infty \mathbf{F}_p \quad ; \quad \mathbf{F} = \mathbf{F}_e \mathbf{F}_v \tag{7-1}$$

in which

F∞ = the *elastic* component of the deformation gradient of the *elasto-plastic* element
Fp = the *plastic* component of the deformation gradient of the *elasto-plastic* element
Fe = the *elastic* component of the deformation gradient of the *visco-elastic* element
Fv = the *viscous* component of the deformation gradient of the *visco-elastic* element

Furthermore the following definitions hold:

$$\mathbf{C}_\infty = \mathbf{F}_\infty^T \mathbf{F}_\infty \quad ; \quad \mathbf{C}_e = \mathbf{F}_e^T \mathbf{F}_e$$
$$\mathbf{C}_p = \mathbf{F}_p^T \mathbf{F}_p \quad ; \quad \mathbf{C}_v = \mathbf{F}_v^T \mathbf{F}_v \tag{7-2}$$

therefore:

$$\mathbf{C} = \mathbf{F}^T \mathbf{F} = \mathbf{F}_v^T \mathbf{C}_e \mathbf{F}_v$$
$$= \mathbf{F}_p^T \mathbf{C}_\infty \mathbf{F}_p \tag{7-3}$$

7.1.1.2 Hyper-elasticity

A so called hyperelastic material postulates the existence of a Helmholtz free energy function that can be defined as a function of the deformation gradient Ψ. For the purpose of this report, the strain energy function known as the compressible neo-Hookean l is considered:

$$\Psi(I_1, I_2, I_3) = \frac{\mu}{2}\left[(I_1 - 3) + \frac{1}{\alpha}\left(I_3^{-\alpha} - 1\right)\right] \qquad (7\text{-}4)$$

where I_1 and I_3 are respectively the first and third strain invariants and μ and α are model parameters.

7.1.2 The proposed model: Elasto-visco-Perzyna formulation

The new defined constitutive model is based on a dissipation energy based elastovisco-plastic obtained by coupling in serie a visco-elastic component (”Zener” element) with a ”Perzyna” component to take into account the inelastic behaviour.

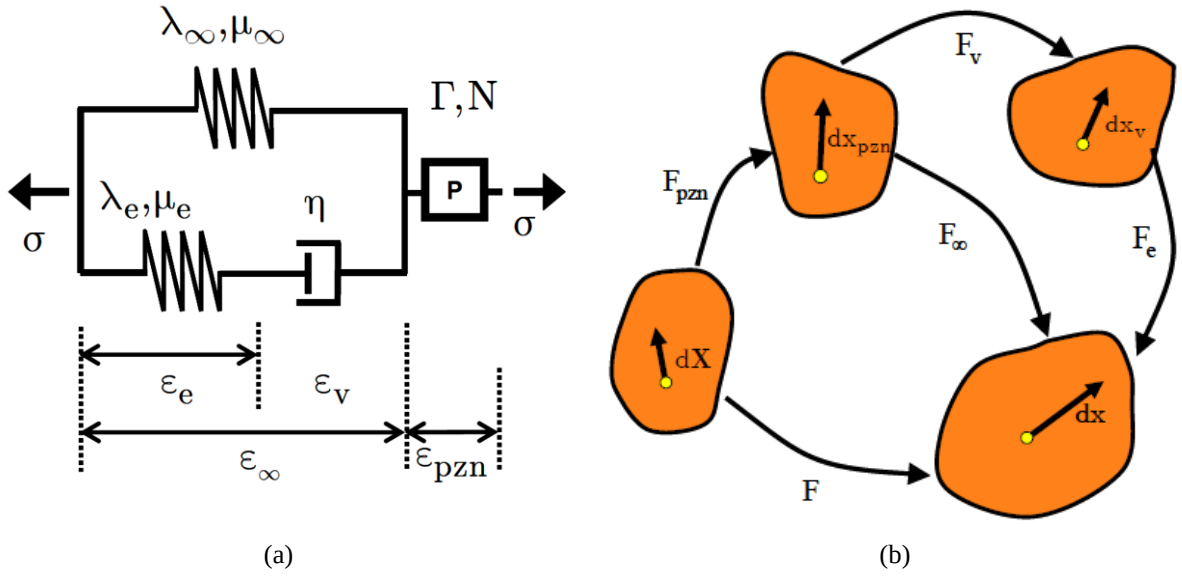

(a) (b)

Figure 7-2 Schematic of (a) the Elasto-visco-Perzyna constitutive model, (b) Multiplicative decomposition

Figure 7-2a shows a one-dimensional schematic of a material model. Figure 7-2b shows the corresponding multiplicative decomposition of the model which allows to divide the deformation gradient tensor F into elastic and plastic components. For the selected model, the gradient tensor F could be then divided into an elastic and an inelastic component, as it to F = F∞ Fpzn= F∞ Fp, or into elastic and viscous components F = Fe Fv .

On the basis of Figure 7-2b it holds

$$F = F_\infty F_p \tag{7-5}$$

and

$$dx_{pzn} = F_p \, dX \tag{7-6}$$

hence

$$dx = F_\infty \, dx_{pzn} = F_\infty F_p \, dX \tag{7-7}$$

The deformation of the Maxwell component can be multiplicatively decomposed as

$$dx = F_e \, dx_v \tag{7-8}$$

and

$$dx_v = F_v \, dx_p \tag{7-9}$$

hence

$$dx = F_e F_v \, dx_p \tag{7-10}$$

7.1.2.1 Local dissipation

For elasto-plastic deformation path strain energy is stored in the hyperelastic spring and in the hardening component of the inelastic component, hence

$$\Psi_p = \Psi_p \left(\mathbf{C}_\infty, \xi_p \right) \tag{7-11}$$

In the Maxwell element strain energy is stored only in the hyperelastic spring.

$$\Psi_v = \Psi_v \left(\mathbf{C}_e \right) \tag{7-12}$$

Hence

$$\Psi = \Psi_v \left(\mathbf{C}_e \right) + \Psi_p \left(\mathbf{C}_\infty, \xi_p \right) \tag{7-13}$$

The Clausius-Planck local dissipation inequality states

$$\mathbf{P} : \dot{\mathbf{F}} - 2\frac{\partial \Psi_e}{\partial \mathbf{C}_e} : \dot{\mathbf{C}}_e - 2\frac{\partial \Psi_\infty}{\partial \mathbf{C}_\infty} : \dot{\mathbf{C}}_\infty + \frac{\partial \Psi_\infty}{\partial \xi}\dot{\xi} \geq 0 \tag{7-14}$$

The following Equation can be obtained:

$$\left(\mathbf{P} - 2\mathbf{F}_e \frac{\partial \Psi}{\partial \mathbf{C}_e}\mathbf{F}_{vp}^{-T} - 2\mathbf{F}_\infty \frac{\partial \Psi_\infty}{\partial \mathbf{C}_\infty}\mathbf{F}_p^{-T} \right) : \dot{\mathbf{F}} + 2\mathbf{C}_\infty \frac{\partial \Psi_\infty}{\partial \mathbf{C}_\infty}\dot{\mathbf{F}}_p^{-T} : \mathbf{F}_p^{-1} + 2\mathbf{F}_e \frac{\partial \Psi}{\partial \mathbf{C}_e}\mathbf{F}\mathbf{F}_p^{-1}\dot{\mathbf{F}}_p\mathbf{F}_{vp}^{-1} + 2\mathbf{F}_e \frac{\partial \Psi}{\partial \mathbf{C}_e}\mathbf{F}\mathbf{F}_{vp}^{-1}\mathbf{l}_v + \frac{\partial \Psi_\infty}{\partial \xi}\dot{\xi} \geq 0 \tag{7-15}$$

the first Kirchoff-Piola tensor can be described also as:

$$\mathbf{P} = 2\mathbf{F}_e \frac{\partial \Psi}{\partial \mathbf{C}_e}\mathbf{F}_{vp}^{-T} + 2\mathbf{F}_\infty \frac{\partial \Psi_\infty}{\partial \mathbf{C}_\infty}\mathbf{F}_p^{-T} \tag{7-16}$$

$$2\mathbf{C}_\infty \frac{\partial \Psi_\infty}{\partial \mathbf{C}_\infty}\dot{\mathbf{F}}_p^{-T} : \mathbf{F}_p^{-1} + 2\mathbf{F}_e \frac{\partial \Psi}{\partial \mathbf{C}_e}\mathbf{F}\mathbf{F}_p^{-1}\dot{\mathbf{F}}_p\mathbf{F}_{vp}^{-1} + 2\mathbf{F}_e \frac{\partial \Psi}{\partial \mathbf{C}_e}\mathbf{F}\mathbf{F}_{vp}^{-1}\mathbf{l}_v + \frac{\partial \Psi_\infty}{\partial \xi}\dot{\xi} \geq 0 \tag{7-17}$$

The first term of Equation (7-17) can be rewritten as:

$$2\mathbf{C}_\infty \frac{\partial \Psi_\infty}{\partial \mathbf{C}_\infty}\dot{\mathbf{F}}_p^{-T} : \mathbf{F}_p^{-1} = 2\mathbf{C}_\infty \frac{\partial \Psi_\infty}{\partial \mathbf{C}_\infty} : \mathbf{l}_p = \mathbf{C}_\infty \mathbf{S}_\infty : \mathbf{l}_p \tag{7-18}$$

The second term of Equation (7-17) can be rewritten as:

$$2\mathbf{F}_e \frac{\partial \Psi}{\partial \mathbf{C}_e}\mathbf{F}\mathbf{F}_p^{-1}\dot{\mathbf{F}}_p\mathbf{F}_{vp}^{-1} = 2\mathbf{F}\mathbf{F}_p^{-1}\mathbf{F}_v^{-1}\frac{\partial \Psi}{\partial \mathbf{C}_e}\mathbf{F}_v^{-T}\mathbf{F}_v^{T} : \mathbf{F}\mathbf{F}_p^{-1}\dot{\mathbf{F}}_p\mathbf{F}_{vp}^{-1} = \mathbf{F}\mathbf{F}_p^{-1}\mathbf{S}_{ev} : \mathbf{F}\mathbf{F}_p^{-1}\dot{\mathbf{F}}_p\mathbf{F}_p^{-1} = \mathbf{F}\mathbf{F}_p^{-1}\mathbf{S}_{ev} : \mathbf{F}\mathbf{F}_p^{-1}\mathbf{l}_p = \mathbf{C}_\infty \mathbf{S}_{ev} : \mathbf{l}_p \tag{7-19}$$

The third term of Equation (7-17) can be rewritten as:

$$
\begin{aligned}
&2\mathbf{F}_e \frac{\partial \Psi}{\partial \mathbf{C}_e} \mathbf{F}\mathbf{F}_{vp}^{-1}\mathbf{l}_v = \\
&2\mathbf{F}\mathbf{F}_p^{-1}\mathbf{F}_v^{-1} \frac{\partial \Psi}{\partial \mathbf{C}_e} \mathbf{F}_v^{-T}\mathbf{F}_v^{T} : \mathbf{F}\mathbf{F}_p^{-1}\mathbf{F}_v^{-1}\mathbf{l}_v = \\
&\mathbf{F}\mathbf{F}_p^{-1}\mathbf{S}_{ev}\mathbf{F}_v^{T} : \mathbf{F}_e\dot{\mathbf{F}}_v^{-1}\mathbf{F}_v^{-1} = \\
&\mathbf{F}_e^{T}\mathbf{F}_e\mathbf{F}_v\mathbf{S}_{ev} : \dot{\mathbf{F}}_v\dot{\mathbf{F}}_v^{-1}\mathbf{F}_v \\
&\mathbf{F}_v^{-T}\mathbf{F}_v^{T}\mathbf{C}_e\mathbf{F}_v\mathbf{S}_{ev} : \dot{\mathbf{F}}_v \\
&\mathbf{C}_\infty\mathbf{S}_{ev} : \mathbf{F}_v^{-1}\dot{\mathbf{F}}_v \\
&\mathbf{C}_\infty\mathbf{S}_{ev} : \mathbf{F}_v^{-1}\dot{\mathbf{F}}_v \\
&\mathbf{C}_\infty\mathbf{F}_v^{-1}\mathbf{S}_e : \mathbf{F}_v^{-1}\dot{\mathbf{F}}_v\mathbf{F}_v^{-1} \\
&\mathbf{F}_v^{-T}\mathbf{C}_\infty\mathbf{F}_v^{-1}\mathbf{S}_e : \mathbf{F}_v^{-1}\dot{\mathbf{F}}_v \\
&\mathbf{C}_e\mathbf{S}_e : \mathbf{l}_v
\end{aligned}
\tag{7-20}
$$

Substituting Equations (7-18), (7-19) and (7-20) and in Equation (7-14), the expression can be rewritten as:

$$
\mathbf{C}_\infty\bar{\mathbf{S}} : \mathbf{I}_p + \mathbf{C}_\infty\mathbf{S}_{ev} : \mathbf{F}_v^{-1}\dot{\mathbf{F}}_v + \frac{\partial \Psi_\infty}{\partial \xi}\dot{\xi} \geq 0 \tag{7-21}
$$

Defining the Mandel tensor as:

$$
\bar{\Sigma} = \mathbf{C}_\infty\bar{\mathbf{S}} \tag{7-22}
$$

Considering that:

$$\bar{\mathbf{S}} = \mathbf{S}_{ev} + \mathbf{S}_{\infty} = 2\mathbf{F}_v^{-1}\frac{\partial \Psi}{\partial \mathbf{C}_e}\mathbf{F}_v^{-T} + 2\frac{\partial \Psi}{\partial \mathbf{C}_{\infty}} = \left(\mu\mathbf{I} - \mu I_3^{-\alpha}\mathbf{C}_{\infty}^{-1}\right) + \mathbf{F}_v^{-1}\left(\mu\mathbf{I} - \mu I_3^{-\alpha}\mathbf{C}_e^{-1}\right)\mathbf{F}_v^{-T}$$

$$\begin{aligned}
\bar{\boldsymbol{\Sigma}} &= \mathbf{C}_{\infty}\mathbf{S}_{ev} + \mathbf{C}_{\infty}\mathbf{S}_{\infty} = \mathbf{C}_{\infty}\mathbf{S}_{\infty} + \mathbf{C}_{\infty}\mathbf{F}_v^{-1}\mathbf{S}_e\mathbf{F}_v^{-T} \\
&= \mathbf{C}_{\infty}\mathbf{S}_{\infty} + \left(\mathbf{F}_{\infty}^{T}\mathbf{F}_{\infty}\right)\mathbf{F}_v^{-1}\mathbf{S}_e\mathbf{F}_v^{-T} = \mathbf{C}_{\infty}\mathbf{S}_{\infty} + \left(\left(\mathbf{F}_e\mathbf{F}_v\right)^{T}\left(\mathbf{F}_e\mathbf{F}_v\right)\right)\mathbf{F}_v^{-1}\mathbf{S}_e\mathbf{F}_v^{-T} = \\
&= \mathbf{C}_{\infty}\mathbf{S}_{\infty} + \left(\mathbf{F}_v^{T}\mathbf{F}_e^{T}\mathbf{F}_e\mathbf{F}_v\right)\mathbf{F}_v^{-1}\mathbf{S}_e\mathbf{F}_v^{-T} = \\
&= \mathbf{C}_{\infty}\mathbf{S}_{\infty} + \mathbf{F}_v^{T}\mathbf{C}_e\mathbf{S}_e\mathbf{F}_v^{-T} = \\
&= \mathbf{C}_{\infty}\mathbf{S}_{\infty} + \mathbf{F}_v^{T}\boldsymbol{\Sigma}_e\mathbf{F}_v^{-T}
\end{aligned} \tag{7-23}$$

Equation (7-21) can be rewritten in the compacted form:

$$\bar{\Sigma} : \mathbf{I}_p + \Sigma_e : \mathbf{I}_v + \frac{\partial \Psi_{\infty}}{\partial \xi}\dot{\xi} \geq 0 \tag{7-24}$$

7.2 Mechanistic procedure for parameter determination

This section explains the parameter determination procedure to extrapolate the input parameters from each component of the model that will be able to predict performance and end of life of RA mixes.

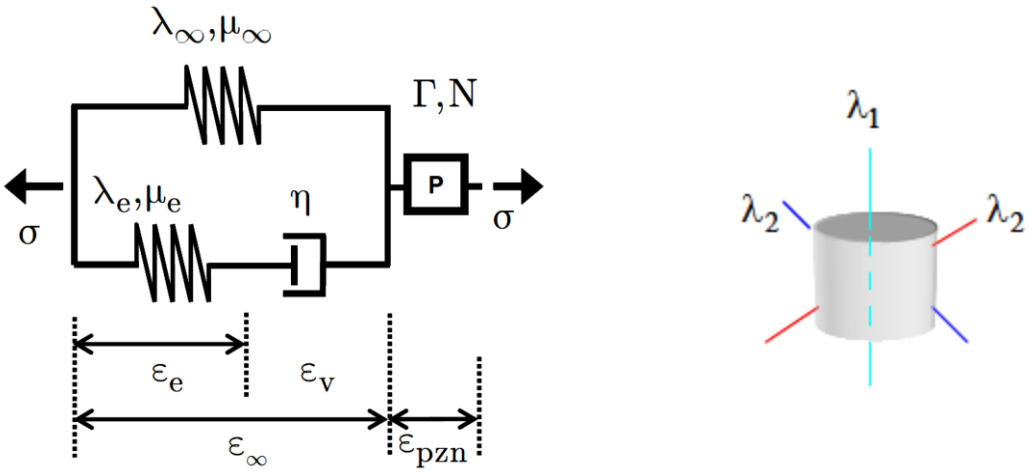

(a) (b)

Figure 7-3 Schematic of (a) the developed constitutive model, (b) test specimen and principal stretch directions

As mentioned before, the new defined constitutive model is obtained by coupling in parallel a visco-elastic component (”Zener” element) and an elasto-plastic components, with the in-serie addition of a ”Perzyna” component to take into account the inelastic behaviour, Figure 7-3a. Cylindrical specimens were utilized the laboratory tests. The principal stretch directions are indicated in Figure 7-3b.

The corresponding deformation tensor is:

$$\mathbf{F} = \begin{bmatrix} \lambda_1 & 0 & 0 \\ 0 & \lambda_2 & 0 \\ 0 & 0 & \lambda_2 \end{bmatrix} \tag{7-25}$$

The first Piola-Kirchhoff stress as a function λ1 can be obtained:

$$P_i = \frac{\partial \Psi}{\partial \lambda_i} = \frac{\partial \Psi}{\partial \lambda_j^2} \frac{\partial \lambda_j^2}{\partial \lambda_i} = 2 \frac{\partial \Psi}{\partial \lambda_i^2} \lambda_i \tag{7-26}$$

For the model of Figure 7-3a it holds:

$${}_{\infty}P = {}_{\infty}P_e \quad \text{and} \quad {}_{M}P = {}_{M}P_e = {}_{M}P_v \tag{7-27}$$

$$\lambda = {}_{\infty}\lambda = {}_{M}\lambda \tag{7-28}$$

in which the subscript M refers to the Maxwell component and ∞ to the Infinite elastic Spring. On the basis of the multiplicative decomposition the following expressions can be considered:

$${}_{\infty}\lambda = {}_{\infty}\lambda_e \quad ; \quad {}_{M}\lambda = {}_{M}\lambda_e \, {}_{M}\lambda_v \tag{7-29}$$

In the following, on the basis of these notions of specimen response and by exploiting particular aspects of the measured experimental response, the characteristics of the individual model components are determined.

7.2.1 Parameters determination - Hyper-elastic spring

Considering that immediately before unloading the response of the material is due to the infinite spring and the Perzyna, the elastic parameters of the infinite spring can be calculated.

As discussed already in section 7.1 the stress-strain behaviour of a spring can been modelled by invariant based continuum mechanics theory considering Neo-Hookean

hyperelasticity. As it is shown in section 7.2, Equations (7-4) and (7-28) can be rewritten:

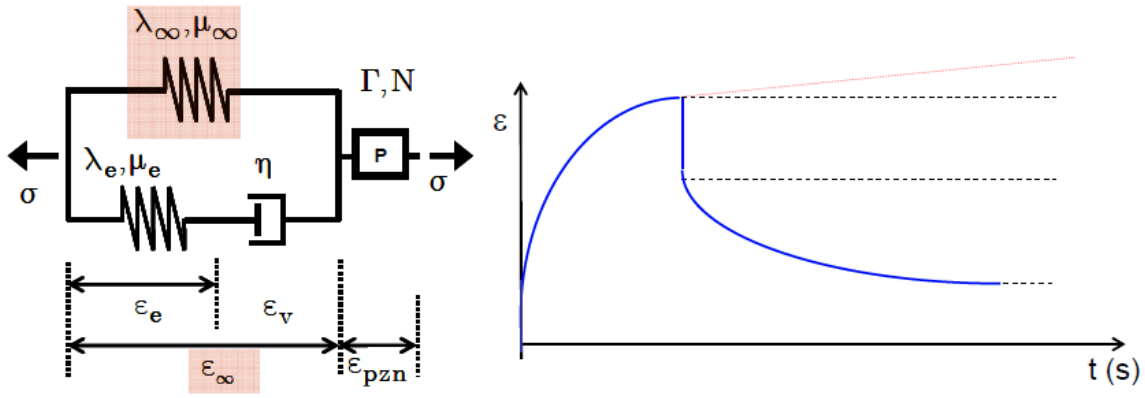

Figure 7-4 Schematic of the contribution of the Hyperelastic spring on the rheological behaviour of asphaltic material under Creep & Recovery tests

$$P_{11\infty} = \lambda_1 \mu_\infty \left[1 - \frac{1}{\lambda_1^2 \left(\lambda_1^2 \lambda_2^4 \right)^{\alpha}} \right] \tag{7-30}$$

$$P_{22\infty} = \lambda_2 \mu_\infty \left[1 - \frac{1}{\lambda_2^2 \left(\lambda_1^2 \lambda_2^4 \right)^{\alpha_\infty}} \right] \tag{7-31}$$

The parameters μ and α can be calculated via Equations (7-31) and (7-35) respectively obtained from Equations (7-30) and (7-31).

$$\alpha_\infty = -\ln \left(\frac{\lambda_{1\infty}\lambda_{2\infty}\left(\lambda_{2\infty} P_{11\infty} - \lambda_{1\infty} P_{22\infty} \right)}{\lambda_{1\infty} P_{11\infty} - \lambda_{2\infty} P_{22\infty}} \right) \Bigg/ \ln \left(\lambda_{1\infty}^2 \lambda_{2\infty}^4 \right) \tag{7-32}$$

$$\mu_\infty = \frac{\lambda_{1\infty} P_{11\infty} - \lambda_{2\infty} P_{22\infty}}{\lambda_{1\infty}^2 - \lambda_{2\infty}^2} \tag{7-33}$$

Considering P22=0

$$\alpha_\infty = -\ln\left(\lambda_{2\infty}^2\right) \Big/ \ln\left(\lambda_{1\infty}^2 \lambda_{2\infty}^4\right) \tag{7-34}$$

$$\mu_\infty = \frac{\lambda_{1\infty} P_{11\infty}}{\lambda_{1\infty}^2 - \lambda_{2\infty}^2} \tag{7-35}$$

$$\lambda_{1\infty} = \frac{\lambda_1}{\lambda_{1pzn}} \tag{7-36}$$

The parameters of the Hyperelastic elastic component μ_∞ and α_∞ are then calculated.

7.2.2 Parameters determination - spring of Maxwell component

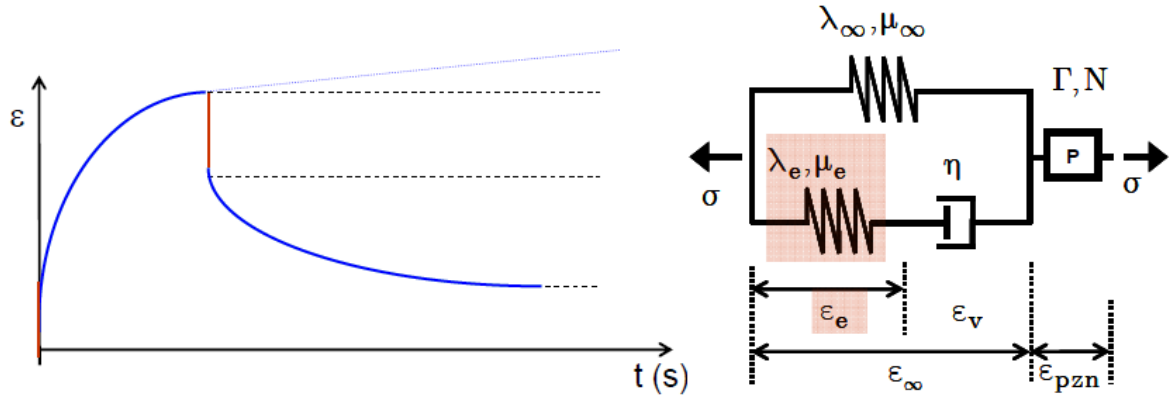

Figure 7-5 Schematic of the contribution of the Maxwell spring on the rheological behaviour of asphaltic material under Creep & Recovery tests

From the previous equation, considering the formulation already used for the hyperelastic component, the following equations can be obtained:

$$\hat{P}_{11M} = P_{11M} = \mu_M \lambda_{1M} \left[1 - \frac{1}{\lambda_{1M}^2 \left(\lambda_{1M}^2 \lambda_{2M}^4\right)^{\alpha_M}} \right] \tag{7-37}$$

$$\hat{P}_{22} = P_{22M} = \mu_M \lambda_{2M} \left[1 - \frac{1}{\lambda_{2M}^2 \left(\lambda_{1M}^2 \lambda_{2M}^4\right)^{\alpha_M}} \right] \tag{7-38}$$

Since no viscous deformations take place and that the total stress applied is zero and it is the sum of the stress that goes through the Maxwell component and the stress that goes through the infinite spring, Equations (7-37) and (7-38) can be rewritten as:

$$\frac{P_{11}}{\lambda_1} = {}_M\mu\left[1-\frac{1}{\lambda_1^2\left(\lambda_1^2\lambda_2^4\right)^{M\alpha}}\right]+{}_\infty\mu\left[1-\frac{1}{\lambda_1^2\left(\lambda_1^2\lambda_2^4\right)^{\infty\alpha}}\right] \tag{7-39}$$

$${}_M P_{22} + {}_\infty P_{22} = 0 \tag{7-40}$$

$${}_M\mu\,{}_M\lambda_2\left[1-\frac{1}{{}_M\lambda_2^2\left({}_M\lambda_1^2\,{}_M\lambda_2^4\right)^{M\alpha}}\right]+{}_\infty\mu\,{}_\infty\lambda_2\left[1-\frac{1}{{}_\infty\lambda_2^2\left({}_\infty\lambda_1^2\,{}_\infty\lambda_2^4\right)^{\infty\alpha}}\right]=0 \tag{7-41}$$

$${}_M\mu\lambda_2\left[1-\frac{1}{\lambda_2^2\left(\lambda_1^2\lambda_2^4\right)^{M\alpha}}\right]+{}_\infty\mu\lambda_2\left[1-\frac{1}{\lambda_2^2\left(\lambda_1^2\lambda_2^4\right)^{\infty\alpha}}\right]=0 \tag{7-42}$$

Equations (7-39) and (7-40) can be solved for α_M and μ_M .

$$\mu_M = -\frac{\mu_\infty\left[1-\frac{1}{\lambda_2^2\left(\lambda_1^2\lambda_2^4\right)^{\alpha_\infty}}\right]}{1-\frac{1}{\lambda_2^2\left(\lambda_1^2\lambda_2^4\right)^{\alpha_M}}} \tag{7-43}$$

$$\alpha_M = \frac{\ln\left[\frac{A_2\lambda_1^2-A_1\lambda_2^2}{\lambda_1^2\lambda_2^2\left(A_2-A_1\right)}\right]}{\ln\left(\lambda_1^2\lambda_2^4\right)} \tag{7-44}$$

Where A_1 and A_2 can be calculated as follows:

$$A_1 = \mu_\infty \left[1 - \frac{1}{\lambda_2^2 \left(\lambda_1^2 \lambda_2^4 \right)^{\alpha_\infty}} \right] \tag{7-45}$$

$$A_2 = \mu_\infty \left[1 - \frac{1}{\lambda_1^2 \left(\lambda_1^2 \lambda_2^4 \right)^{\alpha_\infty}} \right] - \frac{P_{11}}{\lambda_1} \tag{7-46}$$

The parameters of the Maxwell elastic component μM and □M are then calculated.

The elastic stretches during the unloading phase can be calculated starting from the in time Piola Kirchhoff tensor Equation (7-38):

$${}_M\hat{P}_{11} = \left(\frac{{}_M\lambda_1}{{}_M\lambda_{1e}} \right)^2 {}_MP_{11} = {}_M\mu \, {}_M\lambda_{1e} \left[1 - \frac{1}{{}_M\lambda_{1e}^2 \left({}_M\lambda_{1e}^2 \, {}_M\lambda_{2e}^4 \right)^{M\alpha}} \right] \tag{7-47}$$

$${}_M\hat{P}_{22} = \left(\frac{{}_M\lambda_2}{{}_M\lambda_{2e}} \right)^2 {}_MP_{22} = {}_M\mu \, {}_M\lambda_{2e} \left[1 - \frac{1}{{}_M\lambda_{2e}^2 \left({}_M\lambda_{1e}^2 \, {}_M\lambda_{2e}^4 \right)^{M\alpha}} \right] \tag{7-48}$$

Equations (7-47) and (7-48) can be rearranged as follows:

$$\frac{{}_M\lambda_1^2 \, {}_MP_{11}}{{}_M\mu} = {}_M\lambda_{1e}^3 \left(1 - \frac{1}{{}_M\lambda_{1e}^2 \left({}_M\lambda_{1e}^2 \, {}_M\lambda_{2e}^4 \right)^{M\alpha}} \right) \tag{7-49}$$

$$\frac{{}_M\lambda_2^2 \, {}_MP_{22}}{{}_M\mu} = {}_M\lambda_{2e}^3 \left(1 - \frac{1}{{}_M\lambda_{2e}^2 \left({}_M\lambda_{1e}^2 \, {}_M\lambda_{2e}^4 \right)^{M\alpha}} \right) \tag{7-50}$$

In order to determine the elastic stress, the system of Equations (7-49) and (7-50) and can be used. Rewriting Equation (7-48) in the way is shown in Equation (7-50) allows calculating the elastic stretches via an iterative solver.

$$ {}_{M}\lambda_{2e} = \left(\frac{ {}_{M}\mu \, {}_{M}\lambda_{1e}^{1-2{}_{M}\alpha} }{ {}_{M}\lambda_{1e}^{3} \, {}_{M}\mu - {}_{M}\lambda_{1}^{2} \, {}_{M}P_{11} } \right)^{1/4{}_{M}\alpha} \tag{7-51} $$

$$ \frac{ {}_{M}\lambda_{2}^{2} \, {}_{M}P_{22} }{ {}_{M}\mu } - \left({}_{M}\lambda_{2e}^{3} - \frac{ {}_{M}\lambda_{2e}^{3} }{ {}_{M}\lambda_{2e}^{2} \left({}_{M}\lambda_{1e}^{2} \, {}_{M}\lambda_{2e}^{4} \right)^{{}_{M}\alpha} } \right) \to 0 \tag{7-52} $$

7.2.3 Parameters determination - dashpot of Maxwell component

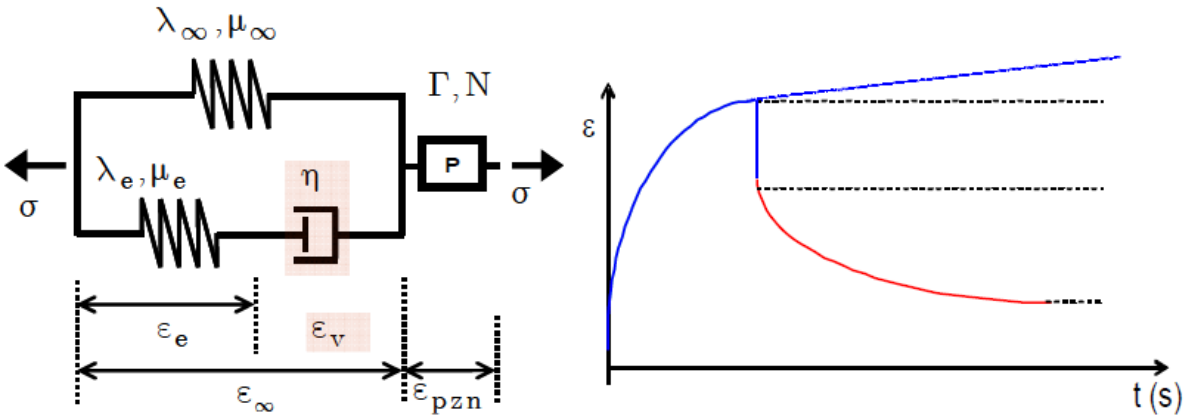

Figure 7-6 Schematic of the contribution of the Maxwell dashpot on the rheological behaviour of asphaltic material under Creep & Recovery tests

The viscous stretches can be calculated from the elastic stretches:

$$ {}_{M}\lambda_{1} = {}_{M}\lambda_{1e} \, {}_{M}\lambda_{1v} \tag{7-53} $$

From the viscous stretches the viscosity coefficient can be calculated using the relationship between the velocity ratio and the Mandel tensor. The viscosity coefficient can be divided between the deviatory component and the volumetric component. In order to consider a non-linear evolution of the viscosity coefficient ${}_{M}\lambda_{1v}$ is calculated as a function of the viscous component of the second Piola Kirchoff tensor.

7.2.4 Parameters determination - Perzyna component

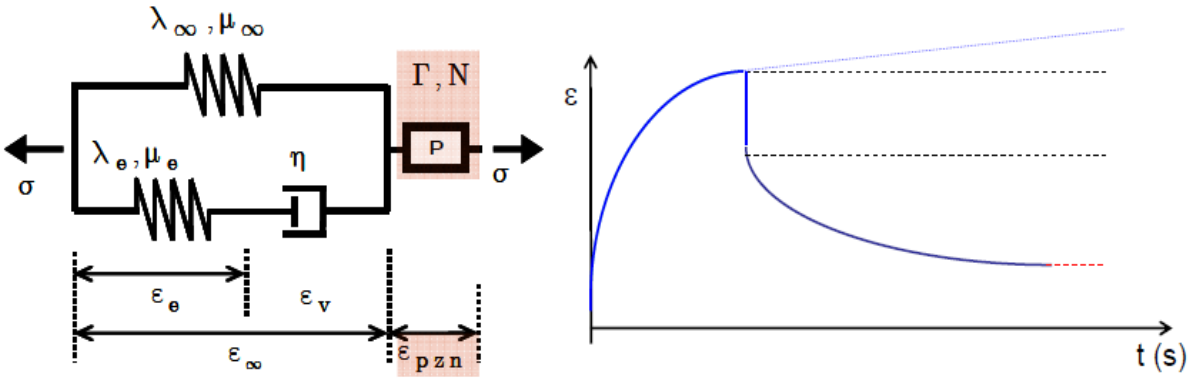

Figure 7-7 Schematic of the contribution of the Perzyna component on the rheological behaviour of asphaltic material under Creep & Recovery tests

In case of asphaltic materials subjected to constant stress the response can be divided in three ranges. Immediately after load application the material responses elastically to load application (primary or elastic creep), then, if the sample is kept loaded with the same load after some time the secondary creep phase starts and the material exhibits permanent visco-plastic strain. The last phase that leads to failure is called tertiary creep. This behaviour is typical of visco-plastic solids, that according to Lamaitre are 'those which exhibit permanent deformation after the application of loads but which continue to undergo a creep flow as a function of time under the influence of the applied load'.

Different approaches can be used in order to model this type of materials:

- demarcation of an elastic domain by means of a yield surface
- uniform formulation of evolution Equation without yield surface and case distinction
- decomposition of the total stress into rate independent equilibrium stress and rate independent overstress

In the model defined in this report the last approach has been considered and the viscoelastic material is characterized by the following viscoelastic evolution Equation:

$$L_{vp}=\Gamma\langle J_2\rangle^N \tag{7-54}$$

Where Γ is the fluidity parameter, $\langle\phi\rangle^N$ is the flow function that can be calculated as a function of the second stress invariant as follows:

$$\langle\phi\rangle^N = J_2^N \tag{7-55}$$

The evolution problem can be solved in the time interval $[t,t+\Delta t]$ to give a first order accurate estimate for ${}^{t+\Delta t}F_p = {}^{t+\Delta t}F_{pzn}$:

$$ {}^{t+\Delta t}\mathbf{F}_{pzn} = \exp^{t+\Delta t}\left[-\Delta\lambda\, \bar{\mathbf{N}} \right] {}^{t}\mathbf{F}_{pzn} \qquad (7\text{-}56) $$

Considering the axial component of the deformation gradient:

$$ {}^{t+\Delta t}\lambda_{1pzn} = \exp^{t+\Delta t}\left[\Delta t\, \Gamma J_2 \mathbf{N} \right] {}^{t}\lambda_{1pzn} \qquad (7\text{-}57) $$

The fluidity parameter Γ is calculated by considering $\Delta\lambda = \Delta t \Gamma \langle \phi \rangle^N$.

7.3 Model Calibration

In this section the parameter determination procedure detailed in section 7.2, will be applied to Material I,II and III, in order to extrapolate input parameters. Determination of the failure stress levels for each material will be followed by the calibration procedure which will provide a step-by-step explanation that will make use of the experimental results (Creep & Recovery curves) obtained with the modalities explained in section 4.1.2 and section 5.1.2.

7.3.1 Failure stress levels

Monotonic constant strain rate (CSR) tests were initially performed in order to establish the stress and strain levels at which failure occurs. These results (Figure 7-8 Failure stresses in compression CSR tests) provide mechanical references to perform further tests in a stress/strain region representing the usual range at which the road pavements are subjected.

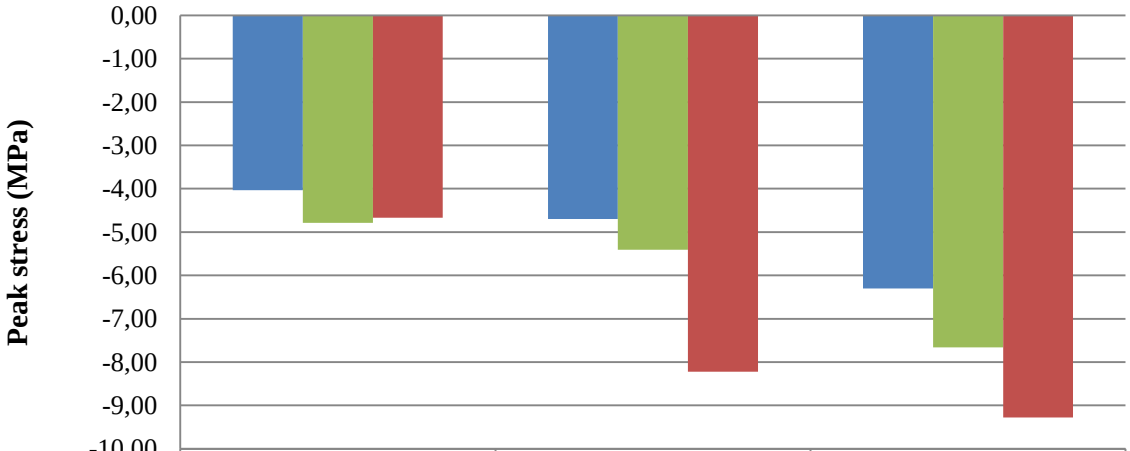

	(C)0.0005	(C)0.001	(C)0.005
Mat I	-4,03	-4,70	-6,30
Mat II	-4,79	-5,41	-7,66
Mat III	-4,67	-8,22	-9,28

Figure 7-8 Failure stresses in compression CSR tests

7.3.2 Creep & Recovery tests

In order to extrapolate the input parameters for the model it is necessary to perform Creep & Recovery tests at different stress levels. In fact in order to simulate the behavior of a working pavement in service, the applied stress levels have to be chosen within a range far from the failure state previously determined. In our experimental program, 20% of the failure stress has been chosen has the highest value to be applied during the Creep & Recovery tests. At least three levels of stress need to be chosen within the above mentioned range, although higher is the number of experimental tests more accurate will be the calibration.

In the present study, Creep Recovery tests were conducted for the three materials at several different stress levels below the 20% of the failure peak stresses previously obtained in the constant strain rate tests at the 0.0005 strain level. These tests were carried out as the recovery curves, generated from the secondary creep region of the test, allow the elastic, delayed elastic and viscous strain components to be separated. Further details on how to accurately perform the testing are explained in section 4.1.2 and section 5.1.2. Creep & Recovery curves for the materials tested in WP5 are reported below.

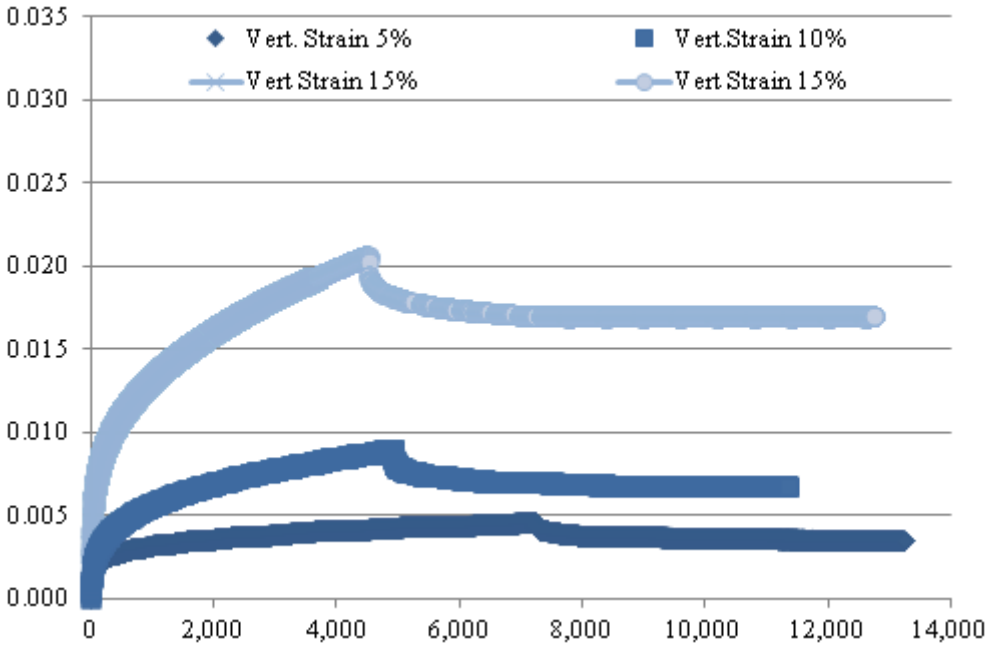

Figure 7-9 Material I: Plot of the vertical strain of the Creep & Recovery tests in compression

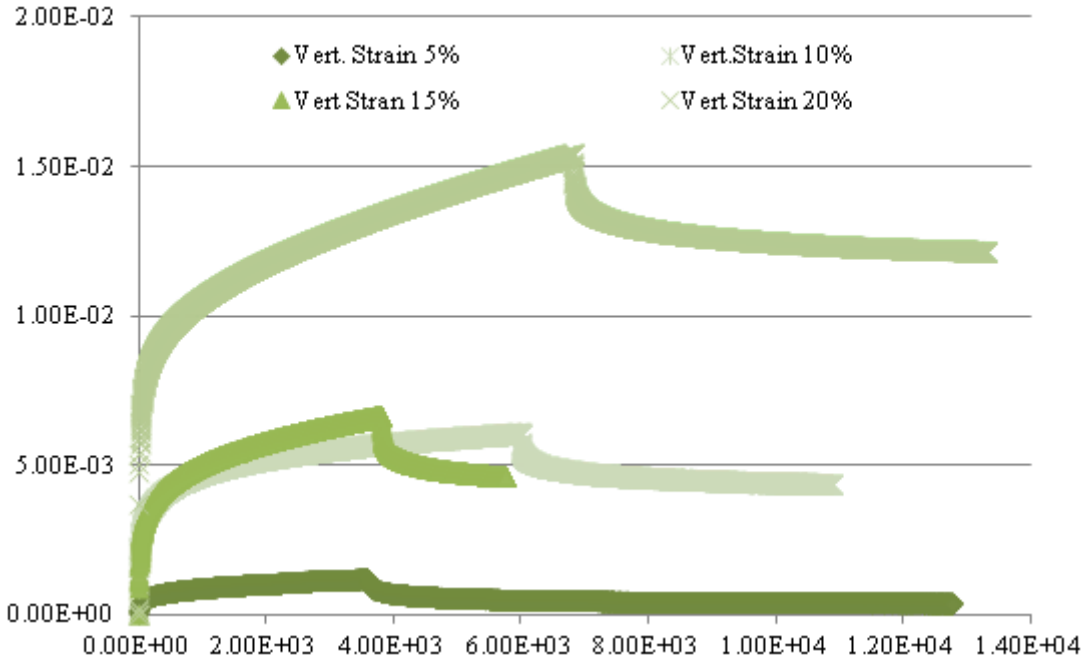

Figure 7-10 Material II: Plot of the vertical strain of the Creep & Recovery tests in compression

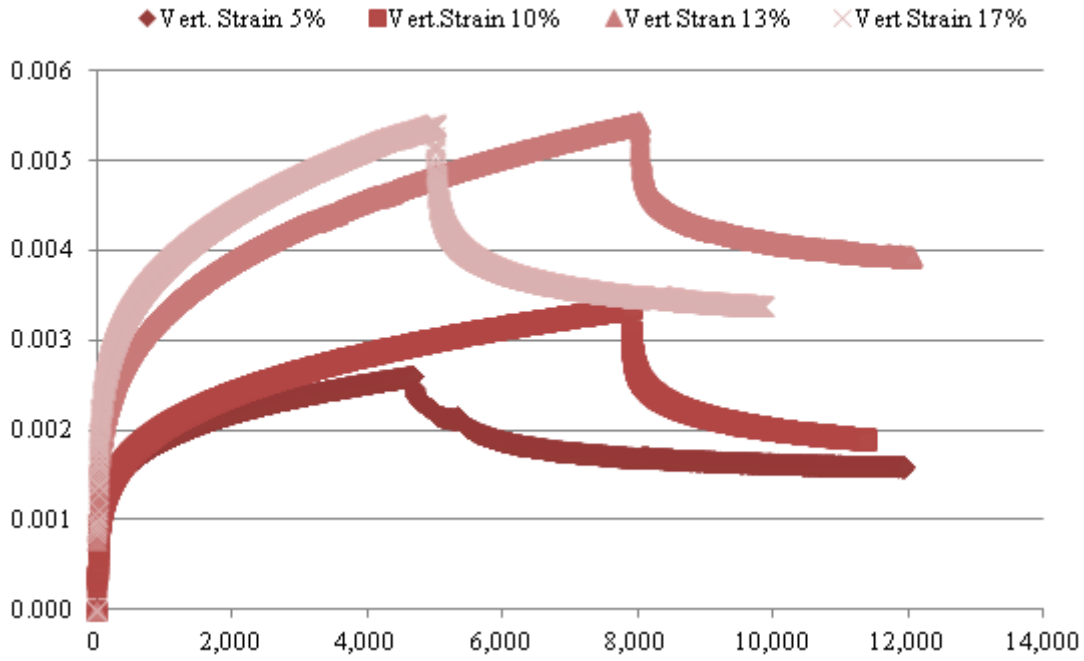

Figure 7-11 Material III: Plot of the vertical strain of the Creep & Recovery tests in compression

7.3.3 Calibration procedures

The model calibration procedure consists in the analysis of the results of laboratory test in order to extract parameters related to some critical points of the Creep&Recovery curves. These separate the regions in which the asphalt material shows a less complex behavior (see Figure 7-12).

Point A, identifies the begin of the secondary creep region; Point B is the begin of the unloading phase; Point C starts the purely visco-elastic recovery after the purely elastic recovery (B-C); Point D identifies the achievement of the permanent deformation while Point E is a measured or extrapolated point which proves that viscous phenomenon are expired at point D.

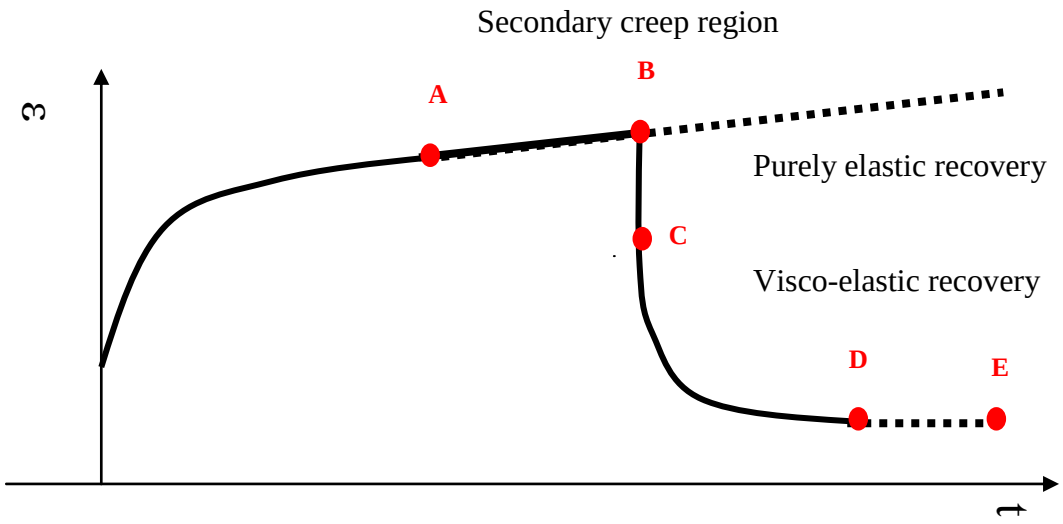

Figure 7-12 Calibration procedures: instants to be identified

The above mentioned points could be obtained already during the experimental test by an appropriate planning or, as it has been done in this study, they can be identified in post-processing by looking at the displacement-time plots to establish the time-instants at the point indicated in Figure 7-12 and in turn extract the relative stress and strain values. Table 7-1, Table 7-2 and Table 7-3 report the results of the calibration procedure performed on the tested materials. It is important to underline that tables do not show point A because it is not used for the parameters' determination. In fact, point A which has been taken always 600 sec before point B, has been used only to check that point B falls within the secondary creep region (constant displacement/time ratio which provides a constant slope of the higher dotted line in Figure 7-12).

Table 7-1 Material I: calibration procedure

	point	P11	epsilon 1	epsilon 2	t
5% PS (-1.61 kN)	B	*-0.2037183*	-0.0045833	-0.00225	*7244.021*
	C	0	-0.0043333	-0.0021667	*7250.024*
	D	0	-0.0035833	-0.0015	12000.024
	E	0	-0.0035475	-0.001485	
10% PS (-3.16 kN)	B	*-0.402343696*	-0.009	0.007916667	*4914.014*
	C	0	-0.008416667	0.007666667	*4929.909*
	D	0	-0.00675	0.0055	10500.008
	E	0	-0.0064125	0.005225	
13% PS (-4.75 kN)	B	*-0.604368615*	-0.020666917	0.008273333	*4512.091*
	C	0	-0.019486417	0.008338333	*4521.104*
	D	0	-0.017073917	0.007794167	7001.003
	E	0	-0.016220221	0.000681667	

Table 7-2 Material II: calibration procedure

	point	P11	epsilon 1	epsilon 2	t
5% PS (-2.15 kN)	B	-0.27416667	-0.001203333	0.000933333	3850.152
	C	0.00186746	-0.001120833	0.00095	3850.177
	D	0	-0.0003875	0.000344167	13014.003
	E	0	-0.00034875	0.00030975	
10% PS (-4.3 kN)	B	-0.54663993	-0.006066667	0.002543333	5999.651
	C	-0.007639437	-0.005714167	0.002365833	5999.676
	D	0	-0.004385	0.001539167	10890.002
	E	0	-0.0042973	0.001508383	
15% PS (-6.45 kN)	B	-0.82022091	-0.00667	0.036444167	3780.153
	C	-0.000254648	-0.006264167	0.035333333	3780.203
	D	0	-0.004629167	0.024485833	5541.203
	E	0	-0.00416625	0.02203725	
20% PS (-8.61 kN)	B	-1.09438758	-0.015416667	0.020371083	6776.183
	C	0.003649996	-0.014925	0.0201725	6776.233
	D	0	-0.012173333	0.014716667	13260.008
	E	0	-0.011929867	0.014422333	

Table 7-3 Material III: calibration procedure

	point	P11	epsilon 1	epsilon 2	t
5% PS (-2.45 kN)	B	-0.31423552	-0.0026025	0.001060833	4669.226
	C	0.003310423	-0.0024775	0.001048333	4669.251
	D	0	-0.0015925	0.000681667	11390.001
	E	0	-0.001576575	0.00067485	
10% PS (-4.9 kN)	B	-0.62312343	-0.003360833	0.003116667	7880.013
	C	0.004333216	-0.00304	0.00291	7880.038
	D	0	-0.001900833	0.0017325	11339.288
	E	0	-0.001805792	0.001645875	
13% PS (-6.42 kN)	B	-0.81640119	-0.005426667	0.0036575	7989.385
	C	-0.005856902	-0.005336667	0.003439167	7989.511
	D	0	-0.0039325	0.0020875	12000.011
	E	0	-0.003814525	0.002024875	
17% PS (-8.55 kN)	B	-1.09142094	-0.005409167	0.004245833	4945.581
	C	0	-0.005195833	0.004055	4945.682
	D	0	-0.003388333	0.0024125	9810.007
	E	0	-0.0032528	0.002316	

7.3.3.1 Input parameters calculation

The analysed experimental curves can then be imported on spreadsheets with implemented the automated procedures based on the algorithms showed in section 7.2. The outputs of this calculations lead to establish the input parameters to be provided to the model in order to predict the mechanical behavior of asphaltic material incorporating reclaimed asphalt.

Table 7-4, Table 7-5 and Table 7-6 report the input parameters. These parameters have been further as materials' properties of each mixture analysed during the validation procedure showed in section 5.1.2. The several undertaken simulations highlighted that all the parameters resulted to be stress-dependent but with different proportions.

Table 7-4 Model's Input parameters of Material I

	5% PS (-1.61 kN)	10% PS (-3.16 kN)	15% PS (-4.75 kN)
P11 (MPa)	-0.20	-0.40	-0.60
Hyperelastic spring			
MU_INF	70	67	55
Lambda_INF	280	270	220
Maxwell			
MU_M	221	191	134
Lambda_M	883	763	537
ETA_M	25000	35000	40000
Perzyna			
K	10000	10000	18000
GAMMA_MIN	-2.00E-07	-5.00E-07	-1.19E-07
GAMMA_MAX	-4.00E-04	-4.00E-04	-5.00E-03

Table 7-5 Model's Input parameters of Material II

	5% PS (-2.15 kN)	10% PS (-4.3 kN)	15% PS (-6.45 kN)	20% PS (-8.61 kN)
P11 (MPa)	-0.27	-0.54	-0.82	-1.09
Hyperelastic spring				
MU_INF	114	110	117	112
Lambda_INF	456	438	463	442
Maxwell				
MU_M	1072	443	605	683
Lambda_M	4289	1774	2419	2731
ETA_M	150000	150000	120000	180000
Perzyna				
K	10000	10000	18000	18000
GAMMA_MIN	-8.00E-08	-1.00E-07	-4.00E-07	-6.00E-07
GAMMA_MAX	-7.00E-05	-4.00E-04	-6.00E-04	-2.00E-03

Table 7-6 Model's Input parameters of Material III

	5% PS (-2.45kN)	10% PS (-4.9 kN)	13% PS (-6.42kN)	17% PS (-8.55 kN)
P11 (MPa)	-0.27	-0.54	-0.82	-1.02
Hyperelastic spring				
MU_INF	109	143	180	180
Lambda_INF	436	569	717	717
Maxwell				
MU_M	788	550	3058	1646
Lambda_M	3513	2202	12235	6586
ETA_M	150000	150000	240000	240000
Perzyna				
K	10000	10000	18000	18000
GAMMA_MIN	-1.19E-07	-1.10E-07	-2.00E-07	-2.41E-07
GAMMA_MAX	-3.70E-03	-1.21E-03	-4.00E-03	-7.00E-04

8 Model Validation

Model validation was carried out by comparing the results achieved with the Hamburg and Dublin wheel tracking test.

8.1 Circular Wheel Tracking Tests at UC Dublin

The circular wheel tracking facility was developed previously at University College Dublin (see Picture 8-1 and Picture 8-3) (Hartman et al 2001, Tabakovic et al 2010).

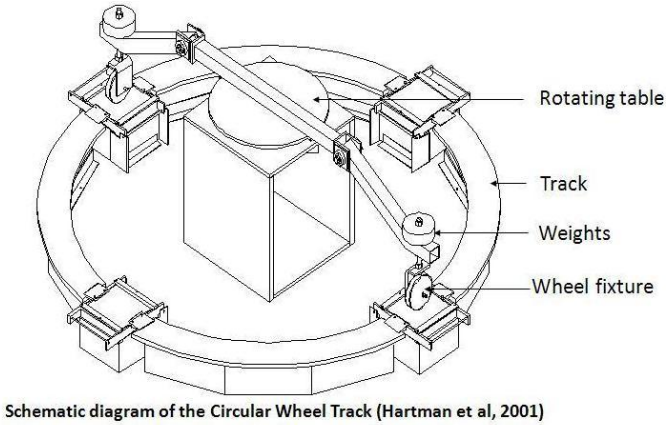

Figure 8-1 UCD circular wheel tracker - original layout

Picture 8-1 UCD circular wheel tracker - redesigned track

It was originally used to study fatigue crack growth in asphalt. The design of the circular wheel tracking device consists of a circular motor driven table onto which a beam is attached. The beam has a wheel fixture connected at each end, via a

hinged joint, which is driven around the track. The wheel tracker uses solid rubber wheels which have a diameter of 200 mm and are 36 mm wide. The wheel fixtures are loaded through a dead load system by placing steel weights on to each of them. The turntable rotates at a speed of 6.515 rpm, resulting in 13.03 wheel passes per minute. The wheel path circumscribes a circle of 1.327 m in radius.

The speed of the wheel is 3.259 km/h. The original track layout is shown below in Picture 8-1.

The facility has been redesigned to enable its use in the examination of asphalt for resistance to permanent deformation. As part of this work, the facility was rebuilt in a temperature controlled chamber, which can maintain a temperature between 10 °C and 40 °C (±1 °C).

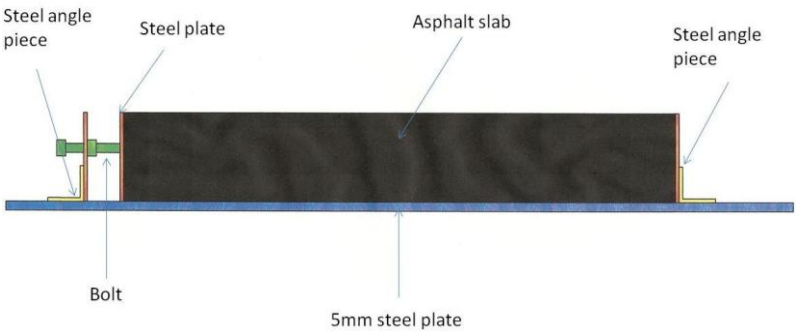

Picture 8-2 Specimen Holder – diagram

Picture 8-3 Specimen Holder - in use

As part of the redesign process, a new track was constructed, as shown in Picture 8-3. The new track included four additional specimen testing stations specifically for resistance to deformation testing. The specimens are recessed into the track and are retained in place by a steel frame. The steel frame consists of a 5mm thick base plate and 2 mm thick side plates, as shown Picture 8-5. These stations accommodate specimens with the dimensions of 305 mm x 305 mm x 100 mm. The specimen depth of 100mm, along with the solid steel base, was selected so as to

limit slab flexure and promote failure of the specimen through densification and shear flow.

8.1.1 Light Detection and Ranging (LiDAR)

LiDAR is a widely used laser scanning technique in creating 3-D models. In recent years it is becoming increasingly used in surveying applications. LiDAR, which is also known as terrestrial laser scanning, is a non contact method of making physical surface measurements. A laser pulse is emitted onto the surface of interest and through using known information such as the angular components of the laser beam path from a reference position and the time taken for laser pulse to be reflected back, a 3-D visualisation of the surface can be created. The quality and intensity of the laser pulse that bounces back to the LiDAR unit is dependent on the characteristics of the surface being scanned (Laefer & Lennon, 2008).

In adapting the UCD circular wheel tracking device to allow assessment of resistance to deformation testing, it was also necessary to select a method to record the deformation of the specimens at various intervals of wheel loadings. This method should result in minimal interference with the specimens. It was also strongly desirable to be able to record additional features of the specimen surface rather than just the rut depth as is the case with other wheel tracking tests. A LiDAR measurement system was selected as it appeared to have the potential to be ideally suited to this task.

8.1.1.1 LiDAR evaluation

The first step in investigating the suitability of a measurement tool was to examine if it could scan an asphalt surface in sufficient detail.

Picture 8-4 LiDAR unit positioned above the test surfaces

A sample slab was constructed and it was found that the laser pulse reflected back from the asphalt surface was of a low intensity, resulting in poor quality scans. This was expected, as it is well known that black surfaces have the ability to absorb energy.

To overcome this, it was decided to spray paint the surface of the specimens white. This ensured that the returned laser pulse was of sufficient intensity to provide good quality scans.

The LiDAR unit used in this work was a Trimble GS200 3-D scanner. It is generally used with a tripod in a set-up of a similar nature to other standard road surveying equipment. This set-up however was considered unsuitable for use with the circular wheel tracker as it was not possible to achieve sufficient height above the test samples. As such, it was necessary to manufacture a simple frame to position the scanner unit above the turntable of the wheel tracking device to provide setup that would enable each of the specimen station locations to be scanned in a time efficient manner. This setup is shown in Picture 8-4.

8.1.2 Test Methodology

8.1.2.1 Specimen manufacture

The premixed SMA material was heated in an oven at 160 °C for 5 hours. The required mass of material was then compacted into a preheated steel mould of dimensions 305 mm x 305 mm x 100 mm using a Cooper Technology Roller Compactor. The bulk density of each of the mixes was 2391kg/m3. This resulted in the design mass of the specimens being 22.242 kg.

The temperature of the mix in the mould prior the compaction was in excess of 140 °C and in excess of 90 °C subsequent to compaction. After the mould and specimen had been allowed to cool for 30 minutes, the mould was removed and the specimen was allowed to cool further to ambient temperature. The mass of the specimen was then recorded. The top surface of the specimen was then spray painted white.

8.1.2.2 Test set-up

In each test run, three specimens were tested with one specimen from each mix type. The mix types were Material I (SMA with 0% RA), Material II (SMA with 15% RA) and Material III (SMA with 30% RA). The testing station chosen as the location of the specimen of each mix was rotated in each test run so as to minimise any effects of possible slight differences in the testing stations. This however was not considered to be an issue. The specimens were placed in the testing stations and secured in place. The temperature chamber was then preheated to the test temperature (40 °C) for a 24 hour period prior to the start of the test. Picture 8-5 shows a specimen secured in the testing station.

Steel plates were then placed on to the wheel arms to apply a deadweight load to each of the wheels, as shown below in Picture 8-6. The load on each wheel was

0.95 kN. The wheel contact area when this load was applied was 1426.2 mm^2, resulting in a contact stress of 669.6 kPa being applied to the specimen with each wheel pass.

Picture 8-5 Specimen secured in testing station

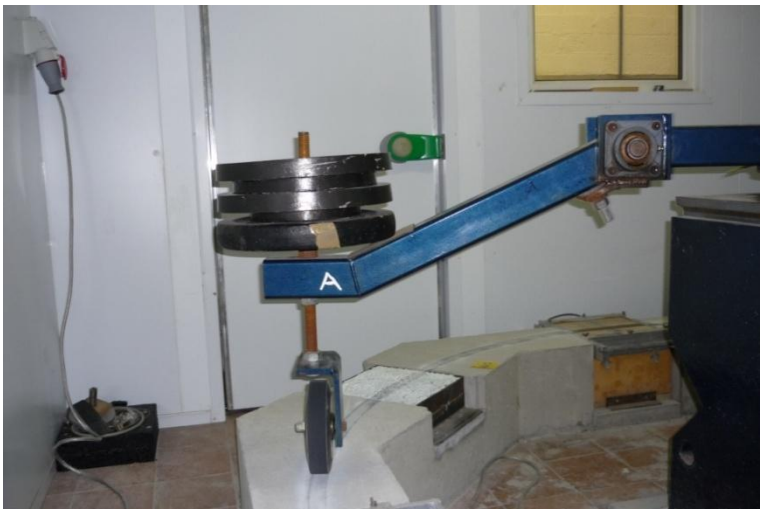

Picture 8-6 Wheel loaded by steel plates

8.1.2.3 Test procedure

Before any wheel passes were applied to the specimens, an initial scan of the surface of each of the specimens was recorded with the LiDAR scanner. The scanner unit was controlled through Trimble Pointscape software on a laptop and was set to record points at a 1 mm interval across the top surface of the specimen. The scan is recorded as a point cloud, a large data set containing information on the coordinates of the scanned surface.

A set number of wheel passes were then applied to the asphalt specimens. The specimens were then cleared of any debris and were scanned again. The duration of this operation was approximately 45 minutes. A further number of wheel passes were then applied before the specimens were scanned again. This process was repeated until the test reached completion – a pre-determined limit of 150,000 wheel passes (approximately days after the start of test). The number of wheel passes applied to the specimens between each scanning interval is set out in Table 8-1.

Table 8-1 Scanning schedule for LiDAR measurements

Scan Name	Number of Wheel Passes Applied	Cumulative Number of Wheel Passes Completed
0c	-	0
5000c	5000	5000
10000c	5000	10000
20000c	10000	20000
30000c	10000	30000
50000c	20000	50000
70000c	20000	70000
90000c	20000	90000
110000c	20000	110000
130000c	20000	130000
150000c	20000	150000

Photographs of the first set of specimens tested are shown in Picture 8-7. The image on the left is of the sample before the test, where as the image on the right is after 150,000 wheel passes. Images are shown for 1 sample representing mixes with 0% RA, 15% RA and 30% RA. The depth of the rut in the specimens due to permanent deformation caused by the passing wheel was also then measure manually.

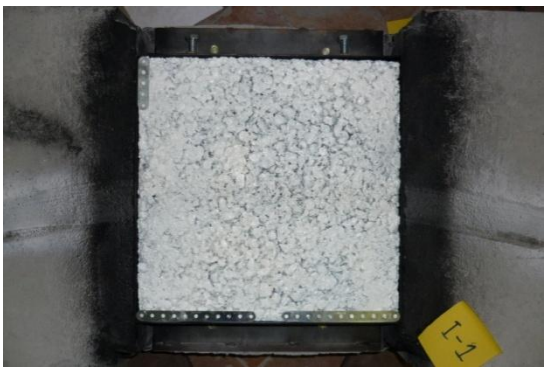

(a)

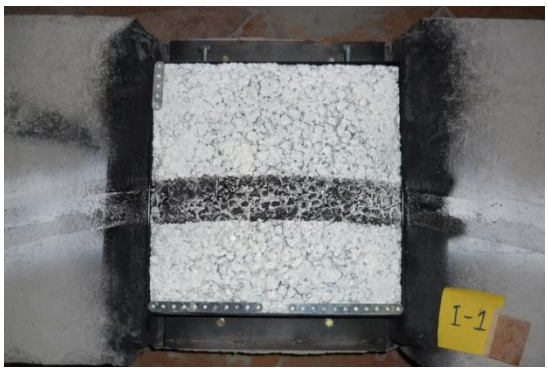

(b)

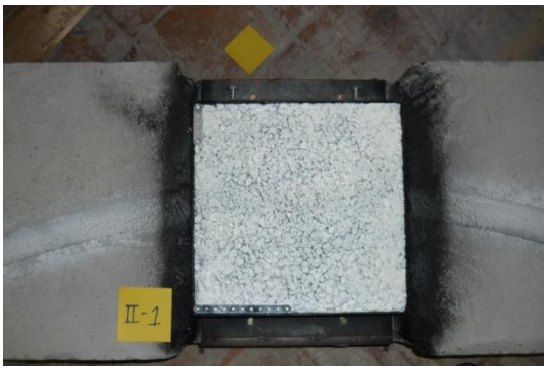

(c)

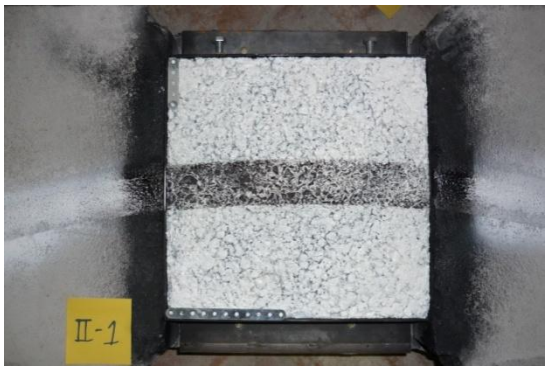

(d)

(e)

(f)

Picture 8-7 Material I (a) before testing and (b) after 150,000 wheel passes; Material II (c) before testing and (d) after 150,000 wheel passes; Material III (e) before testing and (f) after 150,000 wheel passes

8.1.3 LiDAR Data Analysis

The output of each LiDAR scan is represented in the form of a point cloud file. The file structure represents each data point in the scan with five numerical values. The first 3 numbers represent the X, Y and Z coordinates of the point, followed by the RGB true colour and return intensity. The point cloud for each LiDAR scan is in turn imported into Trimble RealWorks Survey software where a 3-D visualisation of the point cloud can be viewed. In the process of scanning the surface of the asphalt specimens, some of the adjoining concrete track and surrounds is also scanned. It is possible to isolate only the surface of the asphalt specimen and to export just these data points as text file format containing just the X, Y and Z values for each data point.

The LiDAR scanner records the X, Y, Z values of the data points based on the location of the LiDAR scanner unit being the reference or (0,0,0) point. In order to simplify the comparisons of the initial and subsequent scans of the same asphalt specimens, it is necessary to adjust location of the reference point of each scan. The desired coordinate system is such that:

The bottom left hand corner of the specimen surface is the origin (represented by a (0,0,0) coordinate). The following conventions were used:

- X values represent distance along the bottom side of the specimen surface.
- Y values represent distance along the left side of the specimen surface.
- Z values represent the elevation of the specimen surface.

This is illustrated below in Figure 8-2.

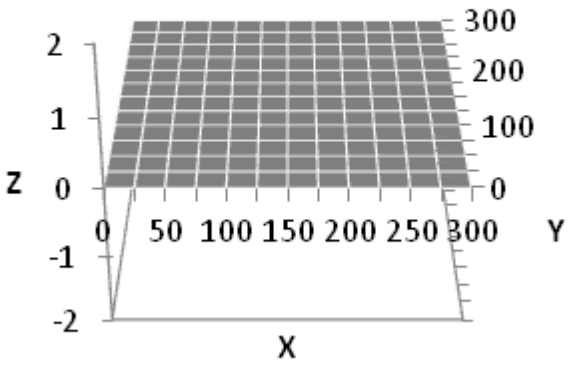

Figure 8-2 Slab specimen coordinate system

The necessary translation and rotation about each of the axes necessary to achieve this coordinate system was calculated for each individual scan by selecting three target points on the specimen scan in the RealWorks software that represent the desired reference point and points on the X – Y plane. It should be noted that in excess of 60,000 data points were recorded in the area of each of the specimen slab

surfaces. The translation and rotation operations were applied to each of these data points. In order to apply this transformation in an expedient manner, it was decided to utilise a MATLAB program. An algorithm was written in a .m file to conduct this operation. As part of this operation a low pass filter was applied to the data points, reducing any measurement noise that was present in the point cloud.

Subsequent to the point clouds data being processed and filtered, the next step was to plot the surfaces. This allows the user to observe the progression of the permanent deformation at different intervals of wheel passes. These plots are shown below in Figure 8-3 and Figure 8-4. The graphs shown below are effectively contour plots, whereby high to low points are coloured red to blue respectively.

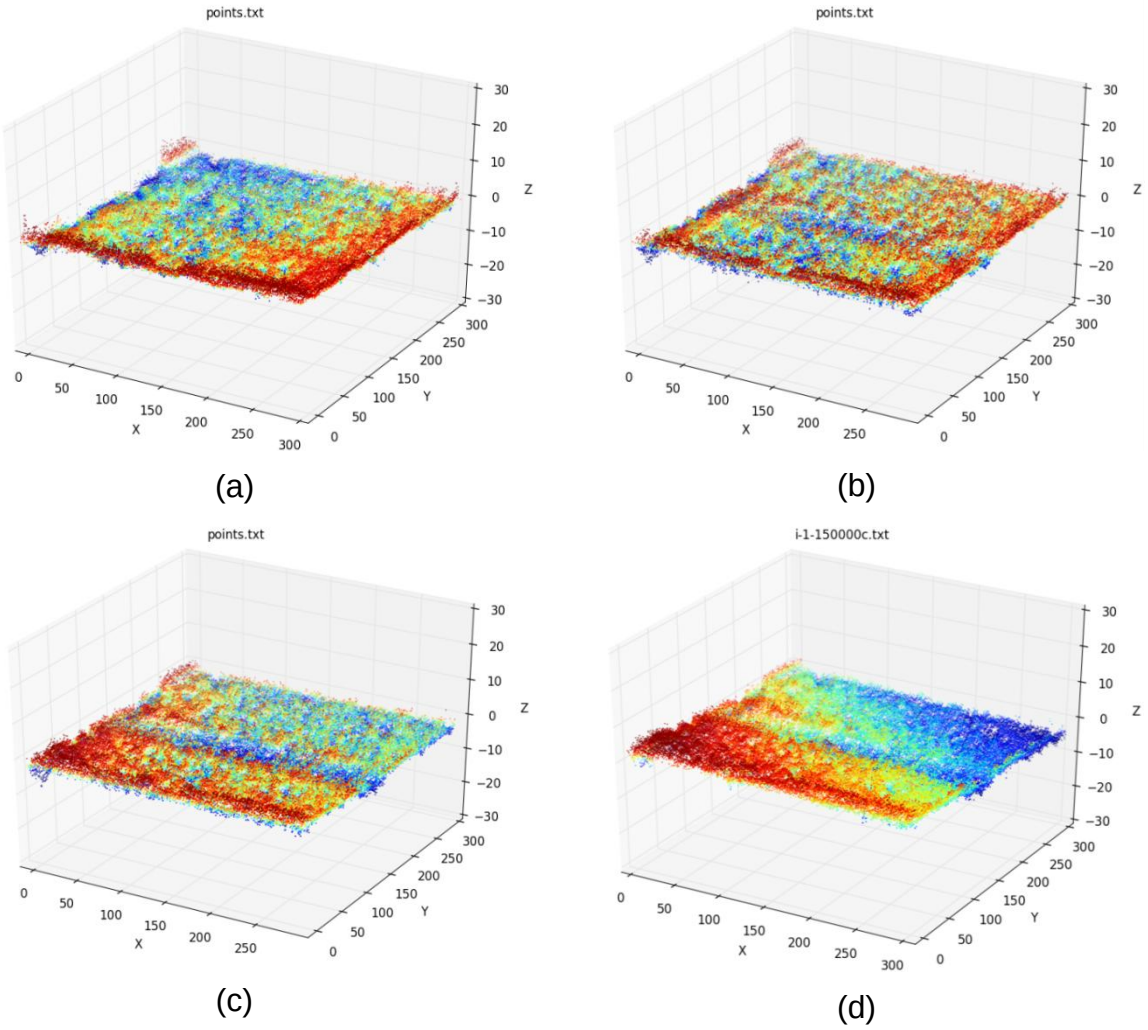

Figure 8-3 LiDAR scans for the Material I after (a) 0 wheel passes (b) 20,000 wheel passes, (c) 90,000 wheel passes and (d) 150,000 wheel passes

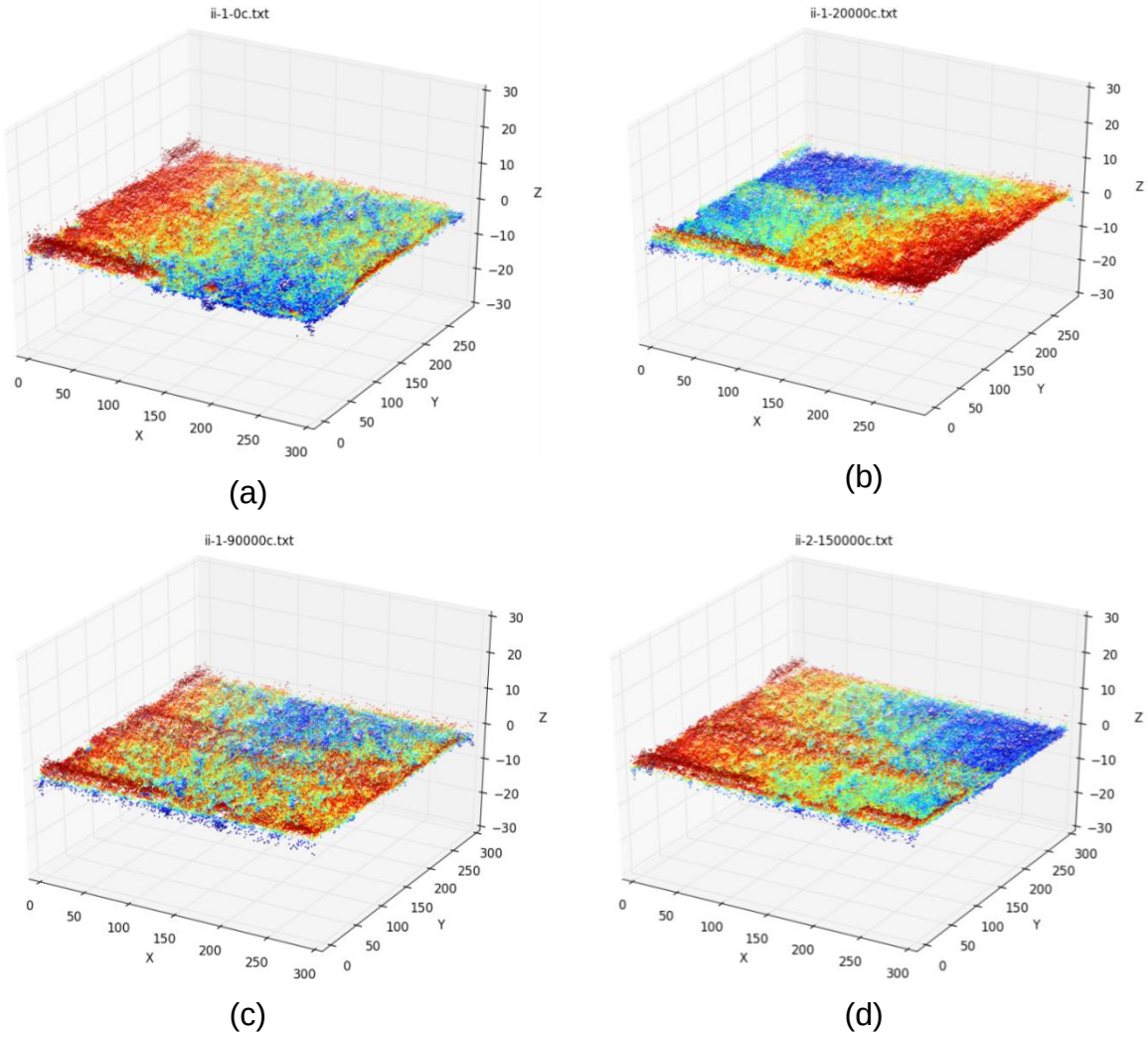

Figure 8-4 LiDAR scans for the Material II after (a) 0 wheel passes (b) 20,000 wheel passes, (c) 90,000 wheel passes and (d) 150,000 wheel passes

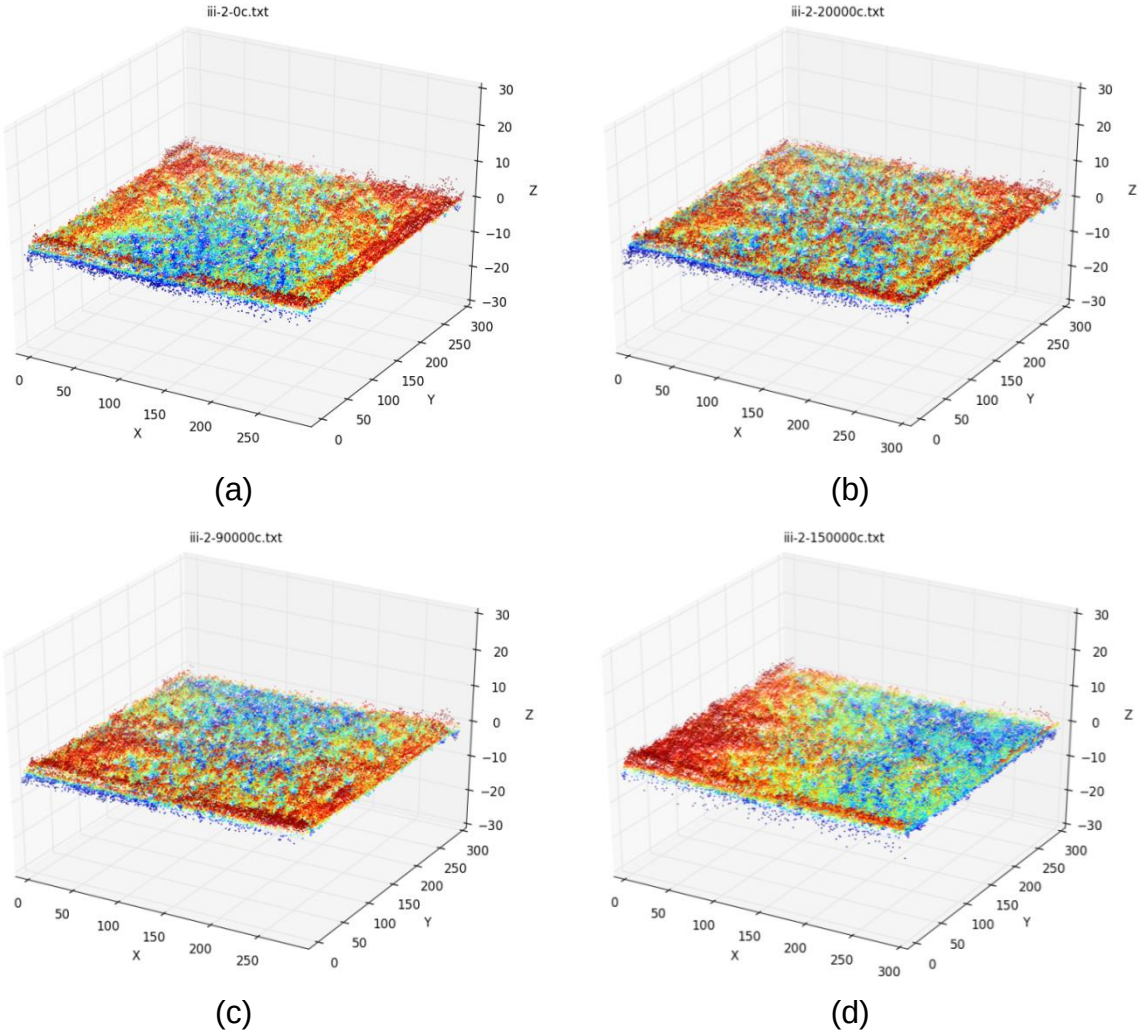

Figure 8-5 LiDAR scans for the Material III after (a) 0 wheel passes (b) 20,000 wheel passes, (c) 90,000 wheel passes and (d) 150,000 wheel passes

For the case of Material I, the development of a rut can be clearly observed. However for Material II and III, the situation is less clear. Despite the low levels of rutting observed, the wheel track testing may be considered as successful, in that a number of key strategic requirements were satisfied:

- Each mix was tested at a different location in the wheel-tracker and the observed performance levels were consistent;
- Despite the tests being of significant duration (greater than 2 weeks), a consistent test environment was maintained throughout;
- The manufacture and subsequent performance of each reference mixture was consistent, as reflected in the repeatable results.

8.1.4 Measurement of Permanent Deformation

8.1.4.1 Using LiDAR scanning

The data points in the output file could be adjusted so as to remove the data either side of the lines corresponding to Y=25 mm and Y=280 mm (i.e. 25 mm from either edge). By removing edge effects it was possible to remove any unevenness from the selection of the target point and enable a more accurate comparison of the scans at different intervals of loading.

Using these levelled scans, a 15 mm x 100 mm band, called the track path, was located. This area was located directly under the path of the passing wheel and was located in the middle 100mm of the specimen. This area was isolated for detailed analysis. In this area, the mean of the Z values of the track path were calculated as the Z coordinates of the wheel path. The values of the track path were compared across the different scans from the various loading intervals. In this way the accumulation of permanent deformation in the specimens could be observed. The results of the track path analysis are shown below in Table 8-2. For the Reference Material I, minor deformation could be observed along the track width, as can be seen in Figure 8-5 (d). For the case of Material II and III, the deformation is much more difficult to detect. This can be clearly seen in Figure 8-5 (d), where there is no visible sign of any rut development. It should be noted that it was not possible to detect a rut using LiDAR in any of the test specimens.

Table 8-2 Average permanent deformation calculated using LiDAR

Mix Type	Average LiDAR Calculated Track Path Depth (mm)
Reference Material I (0% RA)	0.89
Reference Material II (15 %RA)	0.16
Reference Material III (30% RA)	-

8.1.4.2 Using manual measurement

The rut depth or the permanent deformation accumulated in the specimens was also measured manually after the completion of the test and the specimens had been subjected the 150,000 wheel passes. The results of these measurements are shown below in Table 8-3.

Table 8-3 Average permanent deformations using manual measurements

Mix Type	Average Measured Rut Depth (mm)
Reference Material I (0% RA)	1.11
Reference Material II (15 %RA)	0.52
Reference Material III (30% RA)	0.31

As can be seen from these figures the level of permanent deformation observed was very low. Nonetheless, the following comments can be made:

- The use of increased levels of RA in the asphalt mixtures resulted in increased resistance to permanent deformation. Based on the average reported vales, it can be seen that the use of 15 % RA resulted in a 53 % reduction in permanent deformation and the use of 30 % RA resulted in a 72 % decrease.
- The LiDAR proved to be a useful tool in evaluating the surface characteristics of asphalt surfaces. Although some surface preparation was needed, the system did prove useful and can provide full surface scans showing the rut details such as depth and width.
- For the Material III, the LiDAR was unable to detect the low levels of rutting observed. This does represent a shortcoming of the method, although it should be noted that the mix tested was very resistant to rutting.
- Significant processing of the LiDAR data was needed to produce scans with the level of detail needed to detect details in the asphalt surface. These processes included filtering, re-alignment and interpretation. While the technique has proven useful for this laboratory study, significant development work is needed before it can be used for this purpose in the field.
- The material used for testing has proven to be extremely resistant to deformation, as evidenced by the high fatigue lives reported in section 5.1.3 and the very low levels of rutting exhibited during this test. The low rutting levels are most likely due to the nature of the material (SMA), high compaction density and low voids content. A weaker material may have proven more appropriate for distinguishing between levels of performance across the various mixtures.

8.2 Hamburg Wheel Tracking Tests at TU Dresden

The Hamburg Wheel Tracking Test (HWTT) measures the effects of rutting by rolling a rubber or a pneumatic wheel across the surface of an asphalt slab under defined temperature conditions. The laboratory test might be carried out in a water bath instead or an air bath to ensure for the required test temperature. Susceptibilities to rutting are based on pass/fail criteria (see Picture 8-8).

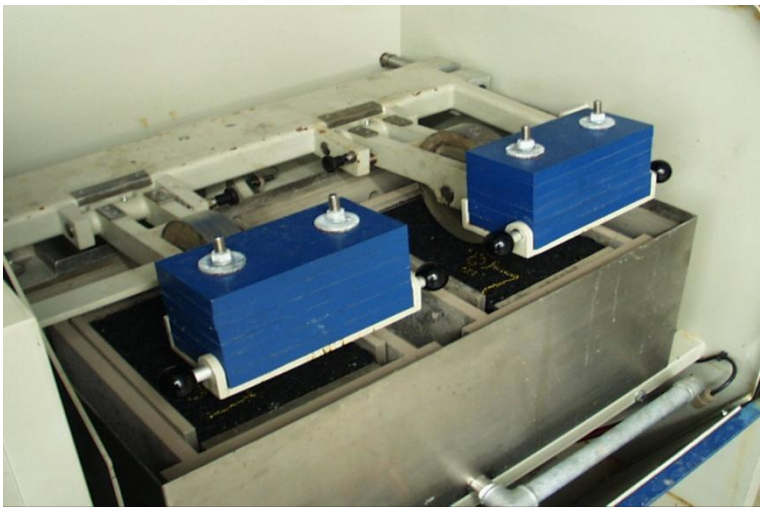

Picture 8-8 Hamburg Wheel Tracking Test Device in the Pavement Engineering Laboratory of TU Dresden

Results obtained from the HWTT include:

- rut depth,
- post-compaction and
- creep slope.

8.2.1 Test Parameter

In addition to the initial testing program described in the research proposal, HWTT at TU Dresden were conducted using a small rubber wheel with an outer diameter of 200 mm and a width of 20 mm. Table 3-1 shows the test parameters.

Table 8-4 HWTT parameter

Width of the wheel	45 mm
Contact length	23 mm
Contact patch	45 mm x 23 mm = 1035 mm^2
Applied load	630 N
Contact pressure	0,608 N/mm^2
Internal dimensions of the asphalt slab	320 mm x 260 mm x 40 mm

Photographs from the contact patch measurements are presented in Picture 8-9. The left photograph shows the measurement of the width of the contact patch, whereas the right one documents the measurement of length of the contact patch.

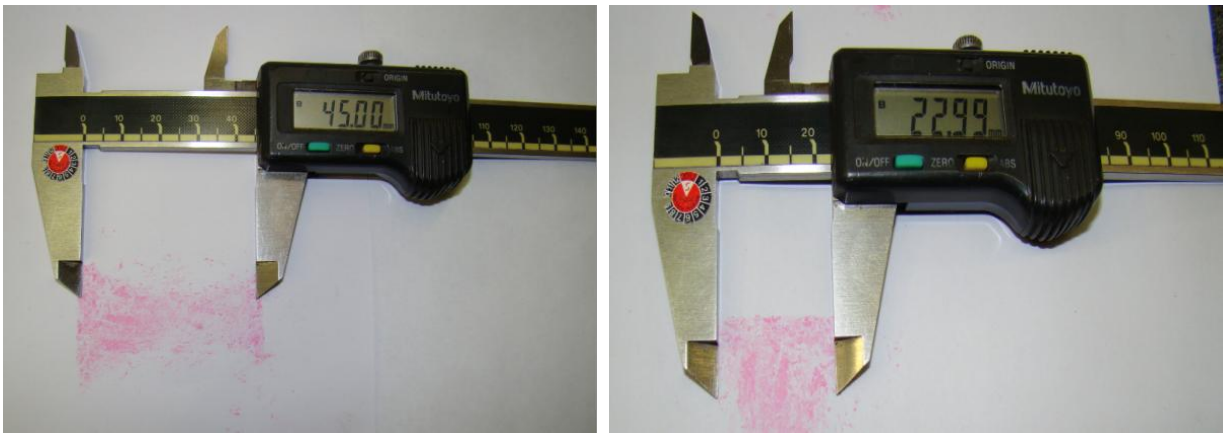

Picture 8-9 Contact patch measurements

8.2.2 HWTT results

To compare the permanent deformations from HWTT with the permanent deformations calculated with the plastic model, rededications of the tests were conducted on three asphalt materials (Material I, Material II and Material III). The development of permanent deformations in dependency on the number of wheel passes is presented in Figure 3-3.

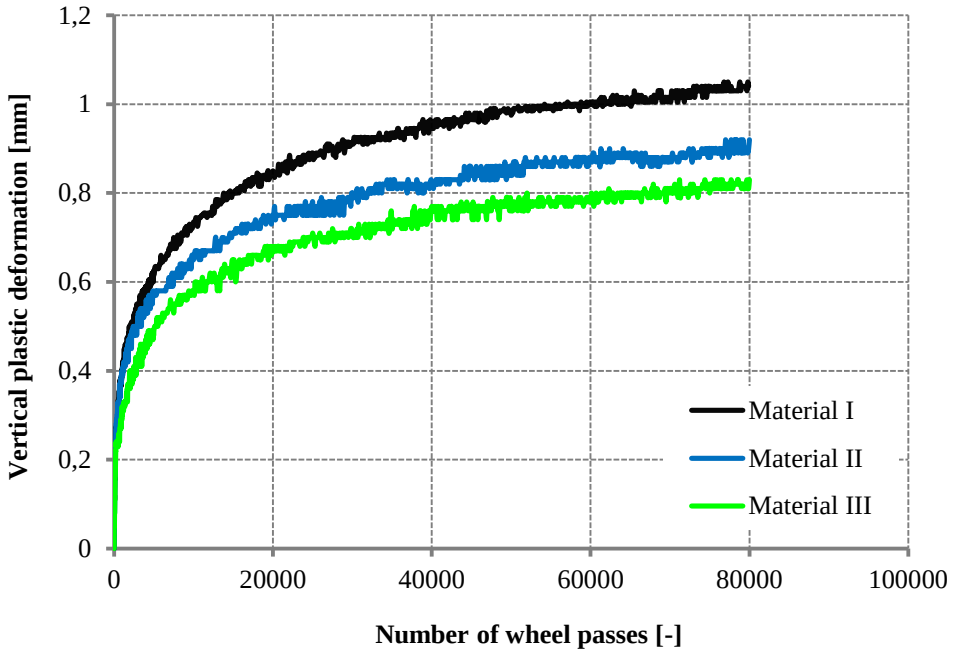

Figure 8-6 HWTT results for Material I, Material II and Material III

As can be seen from Figure 8-6, the level of permanent deformation observed was relatively low. Nonetheless, the following conclusions can be made:

- The use of increased levels of RA in the asphalt mixtures resulted in increased resistance to permanent deformation.
- Relatively high plastic deformations were observed during the post compaction period.
- Similar deformation tendencies were observed from the circular wheel tracking tests carried out at UC Dublin.

8.3 Model Validation at TU Dresden

8.3.1 Numerical Calculation of the Rut Depth

The rut depth is calculated as follows:

- Hydrostatic and deviatoric stresses at the centroid of each element are obtained from the finite element model.
- The strains at each element are calculated with the plastic model.
- The vertical permanent deformation of each element is calculated.
- The rut depth is the determined by summing up the vertical permanent deformation of all elements in the loading axis in vertical direction.

In this section, a numerical example is presented showing the permanent deformation behaviour of the asphalt mixes with RA in comparison with the Material I. The effect of the cycling vertical load leading to the permanent deformation of the asphalt is the main goal of this example. The tire rolling effects are not taken into account since no time dependent effects are considered in the model.

8.3.2 FE Model

The test track is discretized with a FE mesh of 1610 finite elements (20-node isoparametric elements). The finite element model considers only one-fourth of the pavement structure and loading area, taking advantage of symmetry. The computation is carried out with the in-house Finite Element (FE) code ReFEM. The discretized FE model is shown in Figure 8-7. It can be seen in Figure 8-7, the mesh is finer in the vicinity of the load where stress concentration and large deformation gradients are expected.

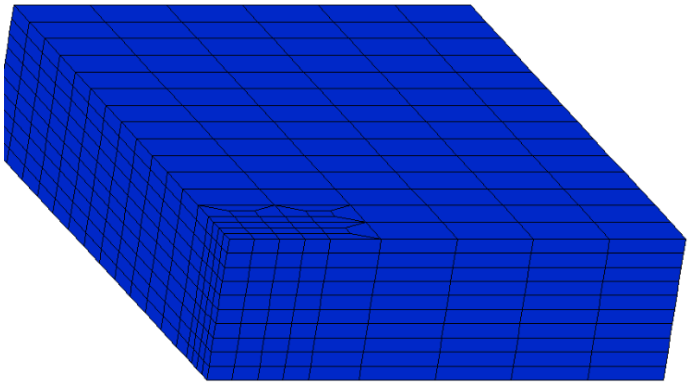

Figure 8-7 FE mesh of the HWTT - Quarter of the total system in its initial configuration

The boundary conditions are as follows:

- The base of the slab is fixed in all directions.
- Movements perpendicular to the symmetry planes are not permitted.

8.3.3 Input values for the FE calculation

For the calculation of strain and stresses a linear elastic model is used. This assumption constitutes a rough approximation of the real visco-elastic material behaviour.

As the material is considered isotropic, the two parameters of a linear elastic material law are the absolute modulus |E| and Poisson ratio. The |E| values are obtained from the master curves at a temperature of T = 40°C, and at a load frequency of 1Hz. The results are presented in Table 8-5.

Table 8-5 Material parameter for the FE model

Material	Absolute Modulus $\|E_1\|$ (T=40°C) [N/mm^2]	Poisson's ratio μ [-]
Material I	1406	0.4
Material II	2081	0.4
Material III	2760	0.4

Figure 8-8 presents the FE mesh of the test sample.

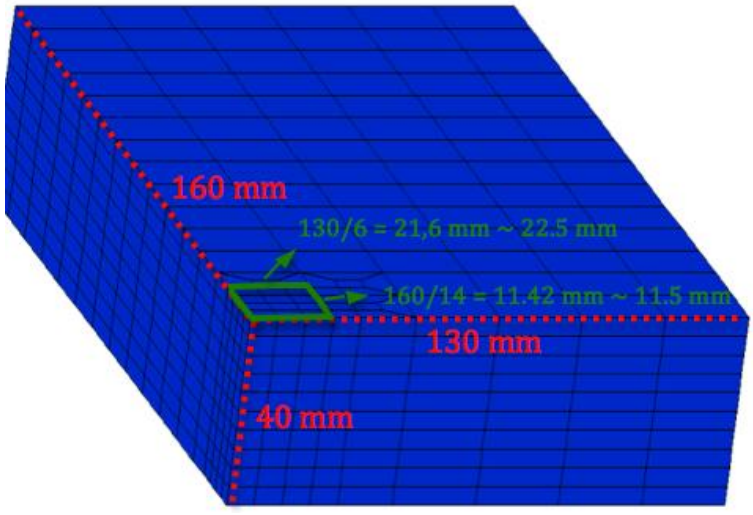

Figure 8-8 FE mesh of the sample - geometry and loaded area

The tire footprint is represented by a rectangular area of 45 mm x 23 mm with a uniformly distributed vertical contact pressure of 0.608 N/mm^2 (see Figure 8-8). Perfect contact between the wheel and the pavement was assumed for the analysis.

8.3.4 Results of the FE calculation

The inputs of the plastic model are the deviatoric and hydrostatic stresses at the centre of each element. These stresses are illustrated qualitatively in Figure 8-9.

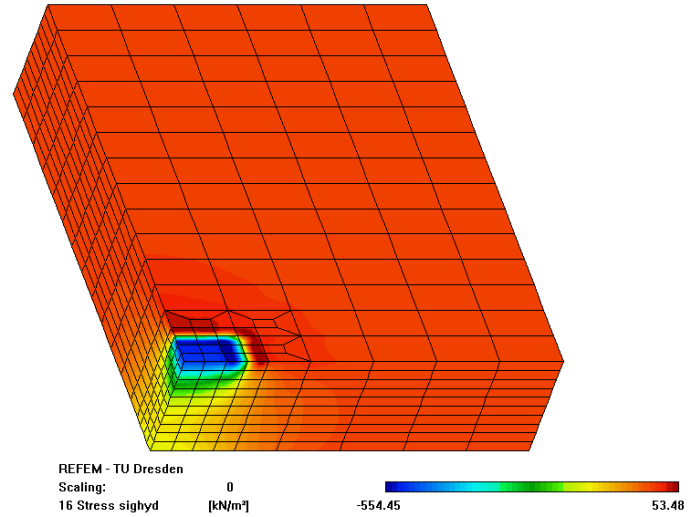

(a)

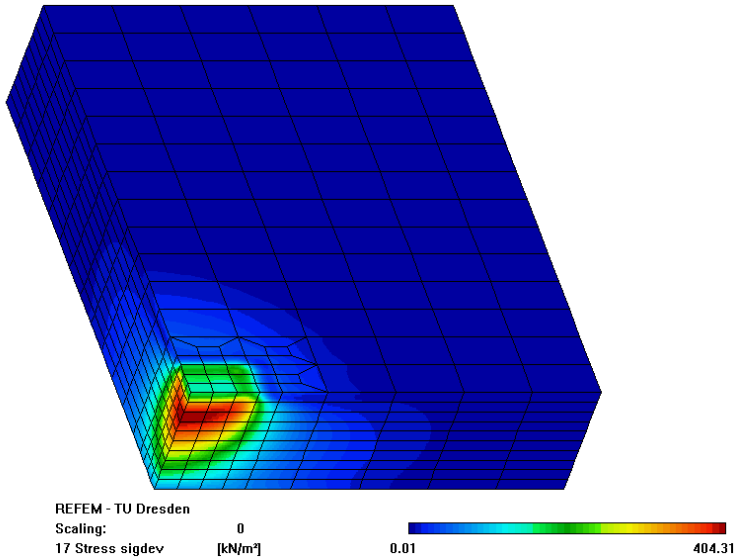

(b)

Figure 8-9 FE deformed configurations (a) hydrostatic stresses (b) deviatoric stresses

Analogous, by the deviatoric and hydrostatic stresses in the loading axis, where the maximum permanent deformation occur, are plotted in Figure 8-10 and Figure 8-11.

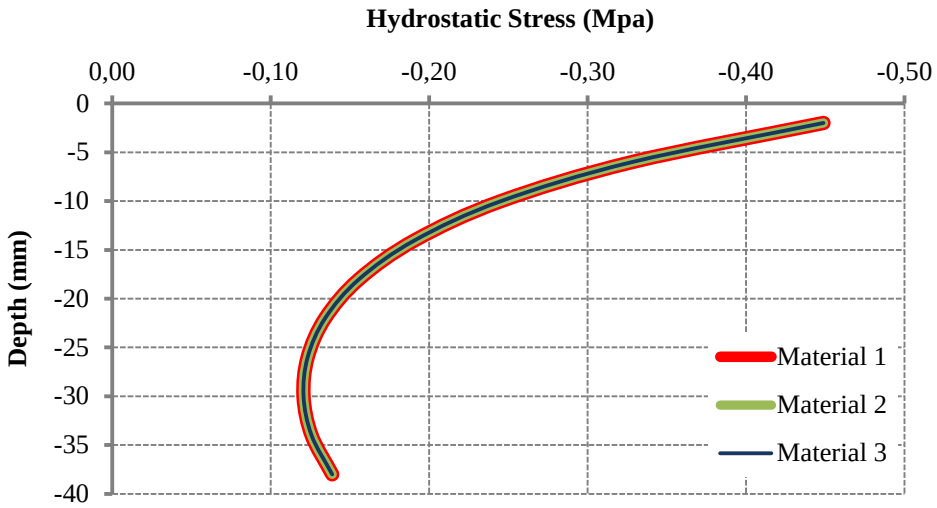

Figure 8-10 Hydrostatic stresses in the loading axis

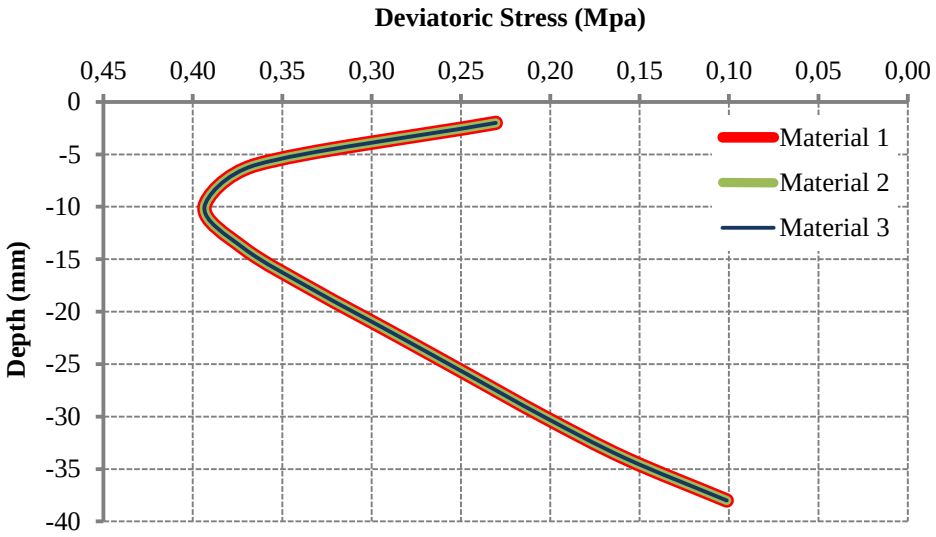

Figure 8-11 Deviatoric stresses in the loading axis

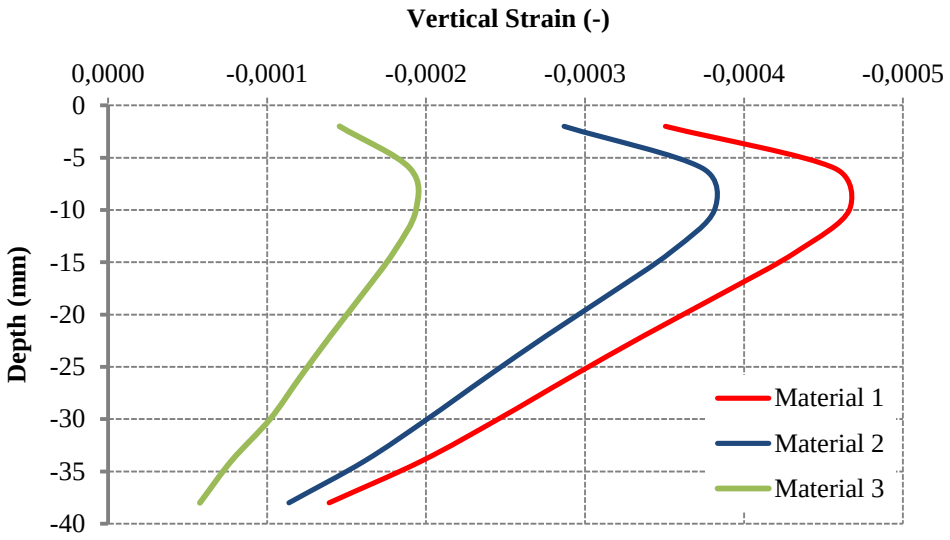

Figure 8-12 Vertical strains in the loading axis

The rut depth at 80,000 load cycles was calculated using the plastic model described previously in Equation (6-50) and (6-51). The results obtained from the models and the rut depth measured during the HWTT are compared in Figure 8-13 and Figure 8-14.

For the calculation the steady state phase was considered only and the post compaction period was excluded. The reason for this was to concentrate on the long term plastic deformation performance of the asphalt mixes.

The results of the simulation show the lowest plastic deformation in terms of a calculated rut depth for Material III followed by Material II. Material I exhibits the highest plastic deformation using the strain approach. This agrees with the results from the HWWT and the theory that postulated that the existence of RA in the mix improves the resistance against rutting of the mix. Additional investigation suggests that a stress approach provides a better fit with the experimental data compared to the elastic strain approach. The results of the simulation show the lowest plastic deformation in terms of a calculated rut depth for Material I followed by Material II and III. However, further experimental data is needed to improve and fine tune the model in order to confirm the validity of the plastic model.

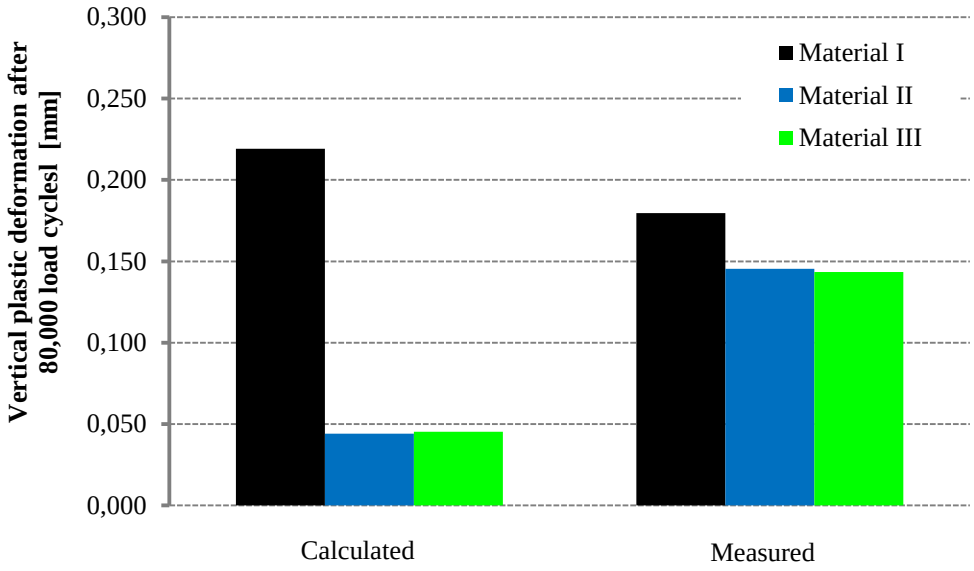

Figure 8-13 Results obtained from the model (Equation (6-50)) and the HWTT at 40°C - calculated and measured

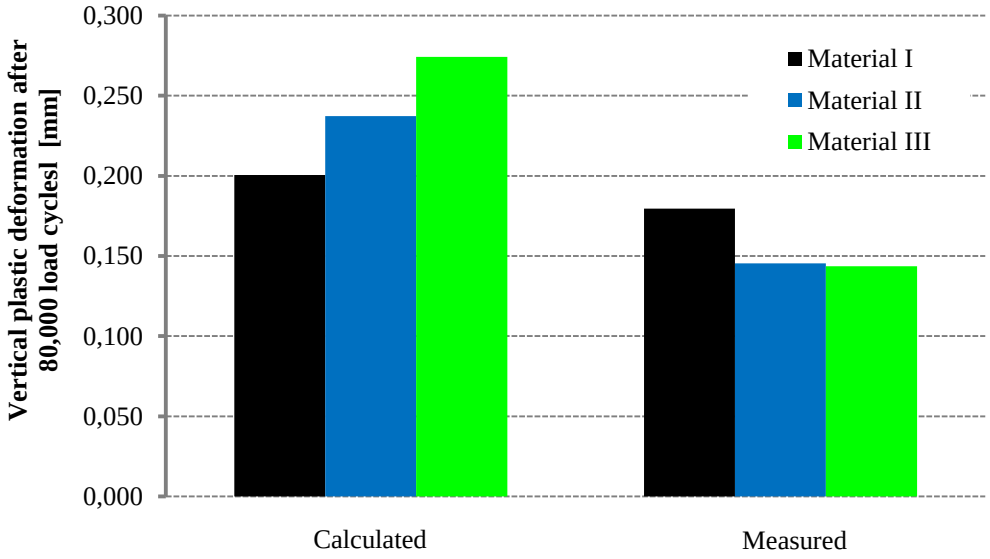

Figure 8-14 Results obtained from the model (Equation (6-50)) and the HWTT at 40°C - calculated and measured

8.4 Model Validation at University of Nottingham

The model has been verified by simulating the laboratory tests on the basis of which material parameter determination was performed. The validation has been performed by using finite element system CAPA-3D, developed at the Section of Structural Mechanics of TU Delft. The achievement of this result will prove the ability of the model to predict reclaimed asphalt mixes behavior under a wide range of in-service stresses and strains.

CAPA-3D is a system that has got an open library of materials, so it allows the customisation of new materials by implementing new constitutive relations. In order to simulate the mechanical behaviour of the Re-Road materials, the group of UNOTT/TUDelft has therefore preliminary defined the proposed model into the material library of CAPA-3D, then material properties have been specified by providing the input parameters (Table 7-4, Table 7-5 and Table 7-6) the software and a simulation of the Creep&Recovery tests provided the model predictions.

Figure 8-15 to Figure 8-25 show the results of the simulation for each test performed on the Re-Road materials, within the range of strain and stress at which a road pavement is usually subjected in service. The results show that the model provides outcomes comparable with the experimental curves. In particular, the model is therefore able to predict very well the visco-elastic behaviour in the recovery phase, but overall it is able to accurately predict the accumulated permanent deformation which is one of the main causes affecting the durability of an asphalt road pavement.

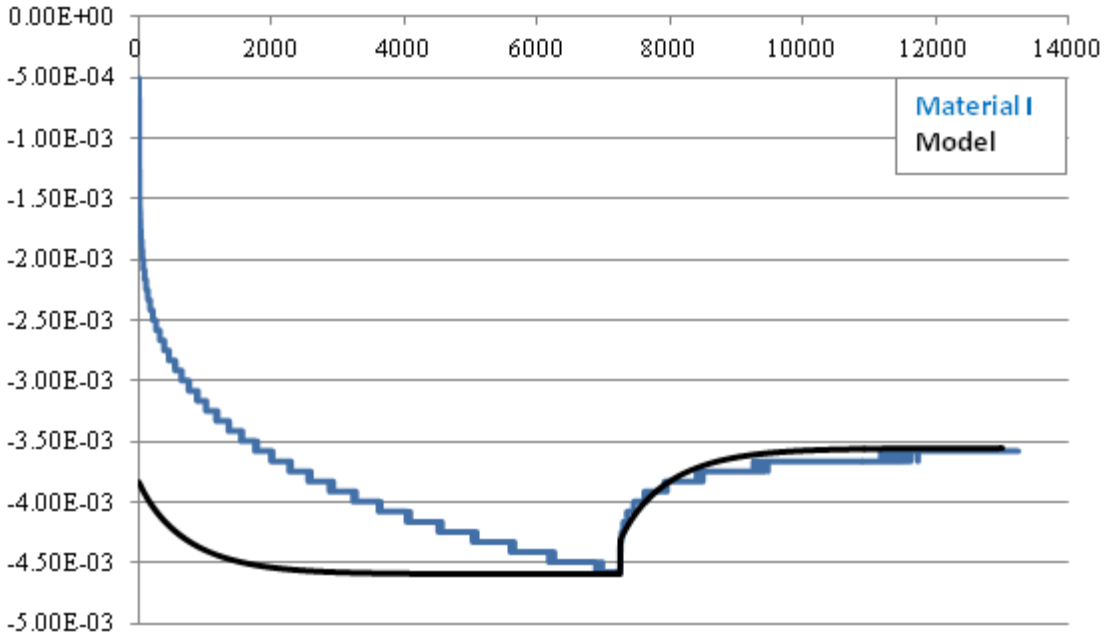

Figure 8-15 Material I – 5% PS: Experimental curve vs model output

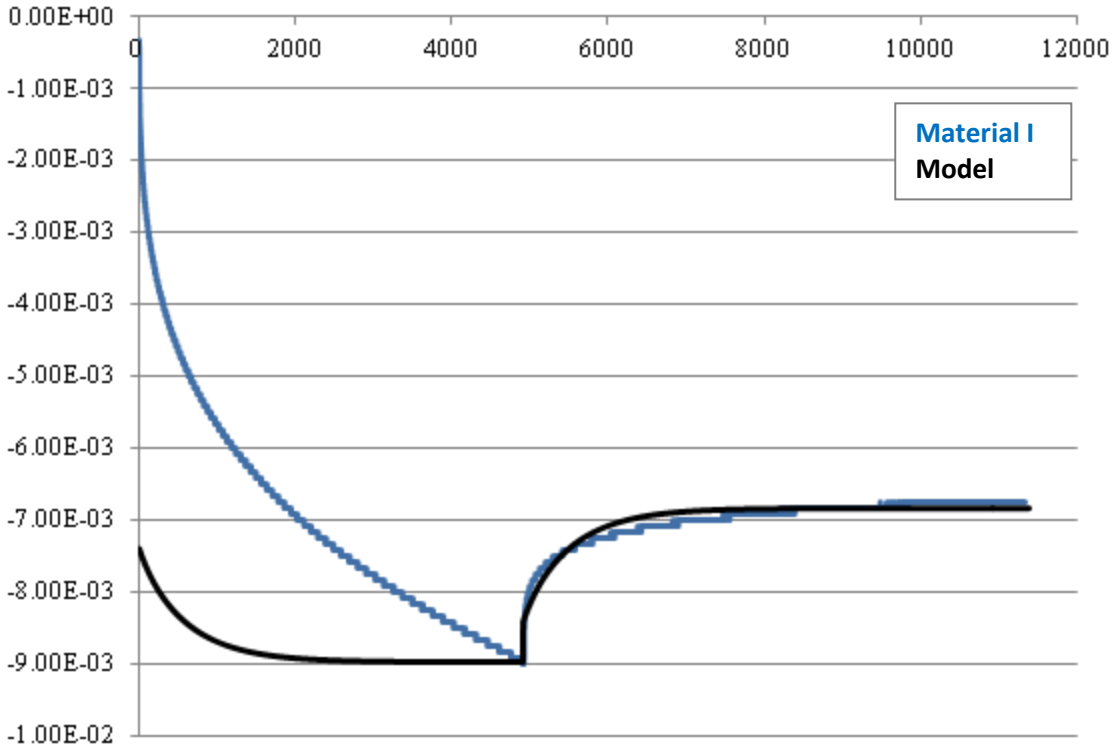

Figure 8-16 Material I – 10% PS: Experimental curve vs model output

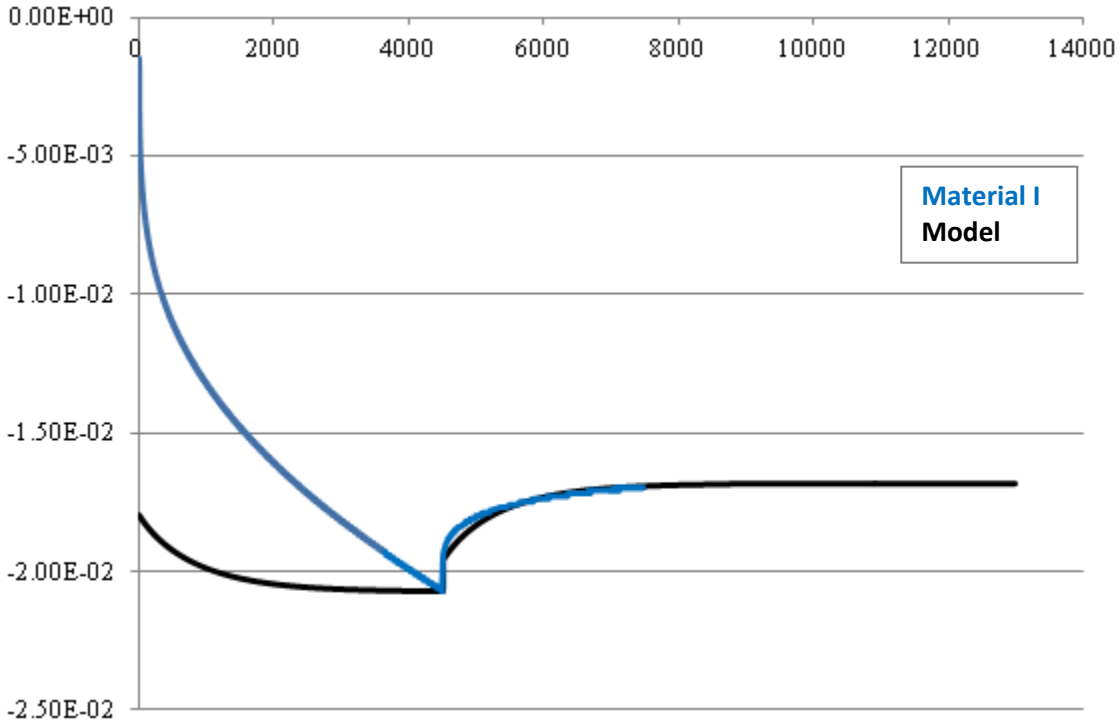

Figure 8-17 Material I – 15% PS: Experimental curve vs model output

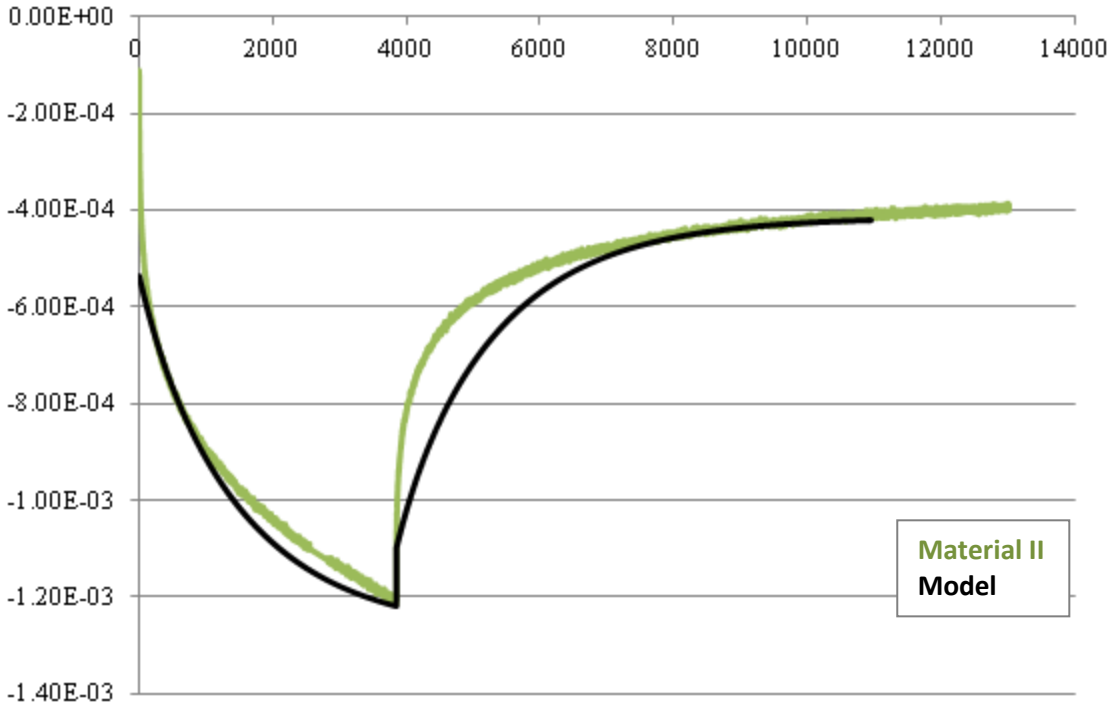

Figure 8-18 Material II – 5% PS: Experimental curve vs model output

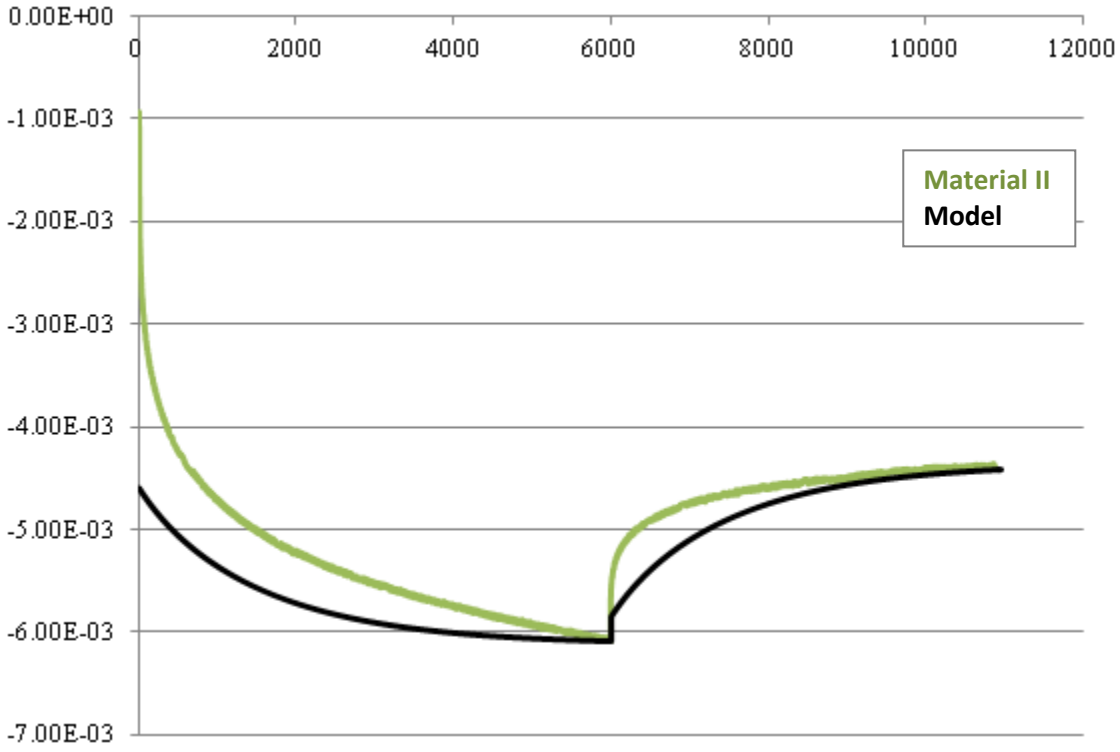

Figure 8-19 Material II – 10% PS: Experimental curve vs model output

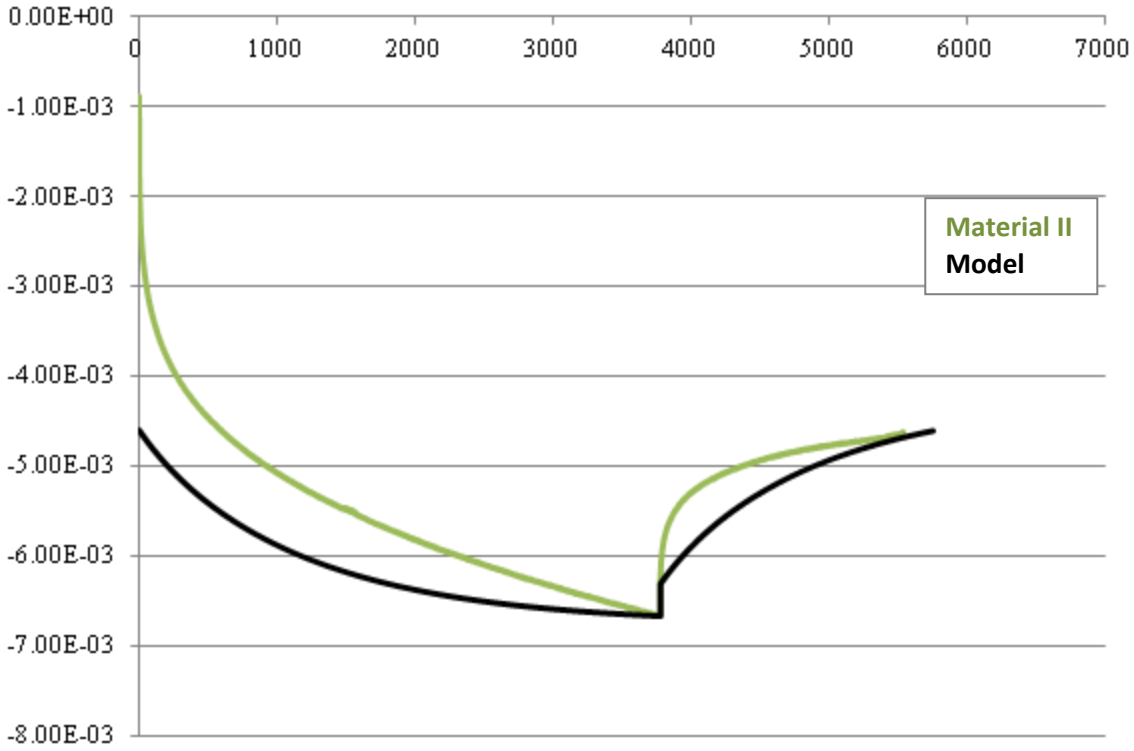

Figure 8-20 Material II – 15% PS: Experimental curve vs model output

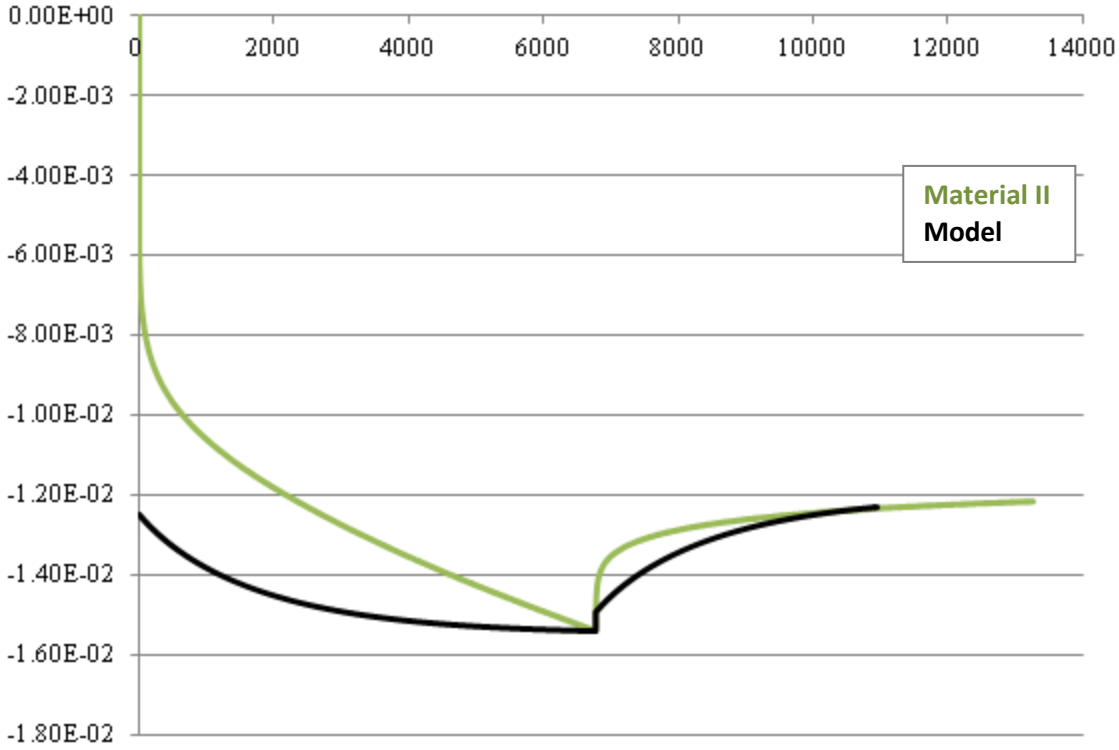

Figure 8-21 Material II – 20% PS: Experimental curve vs model output

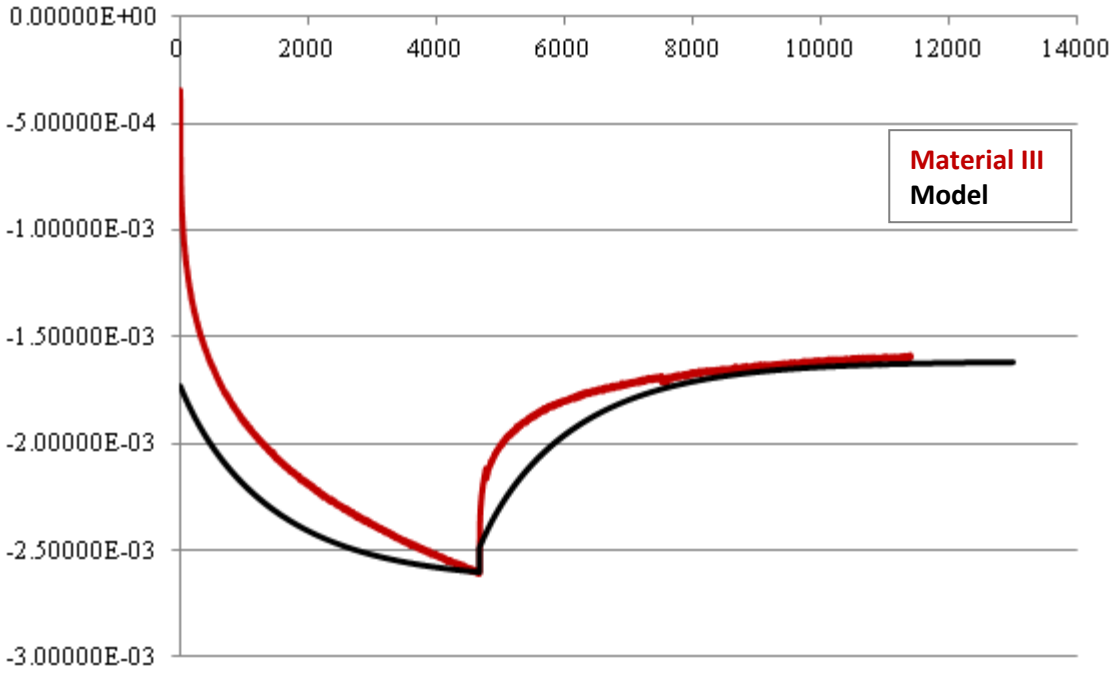

Figure 8-22 Material III – 5% PS: Experimental curve vs model output

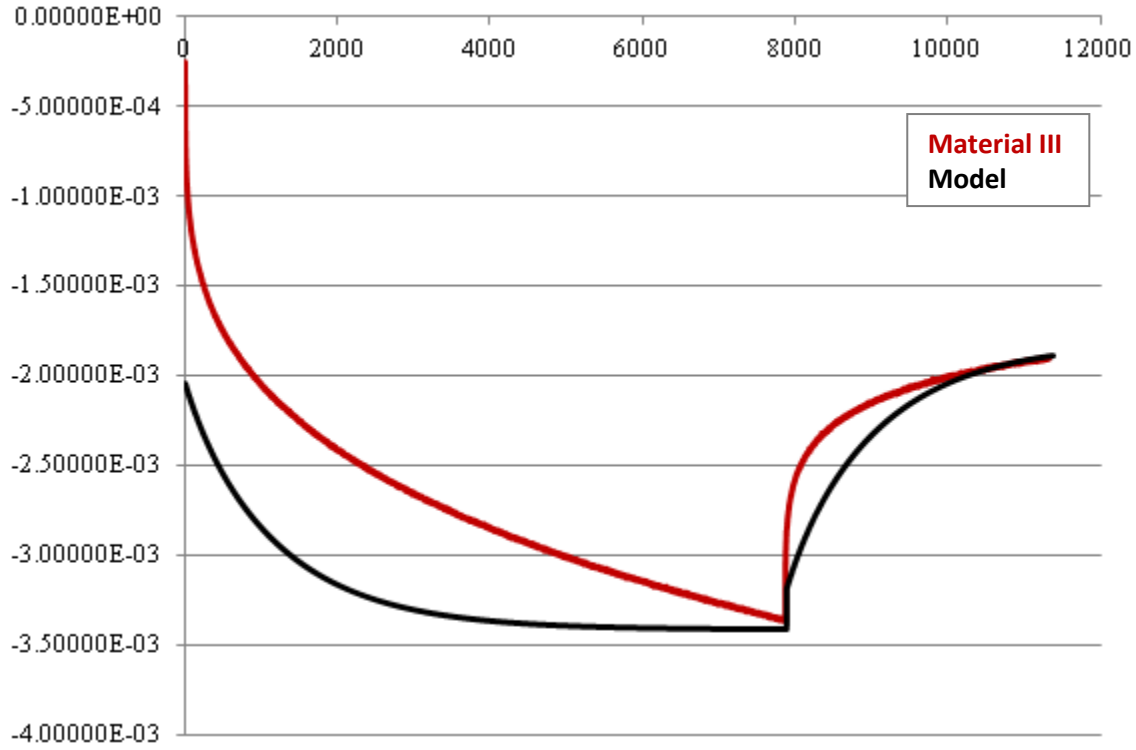

Figure 8-23 Material III – 10% PS: Experimental curve vs model output

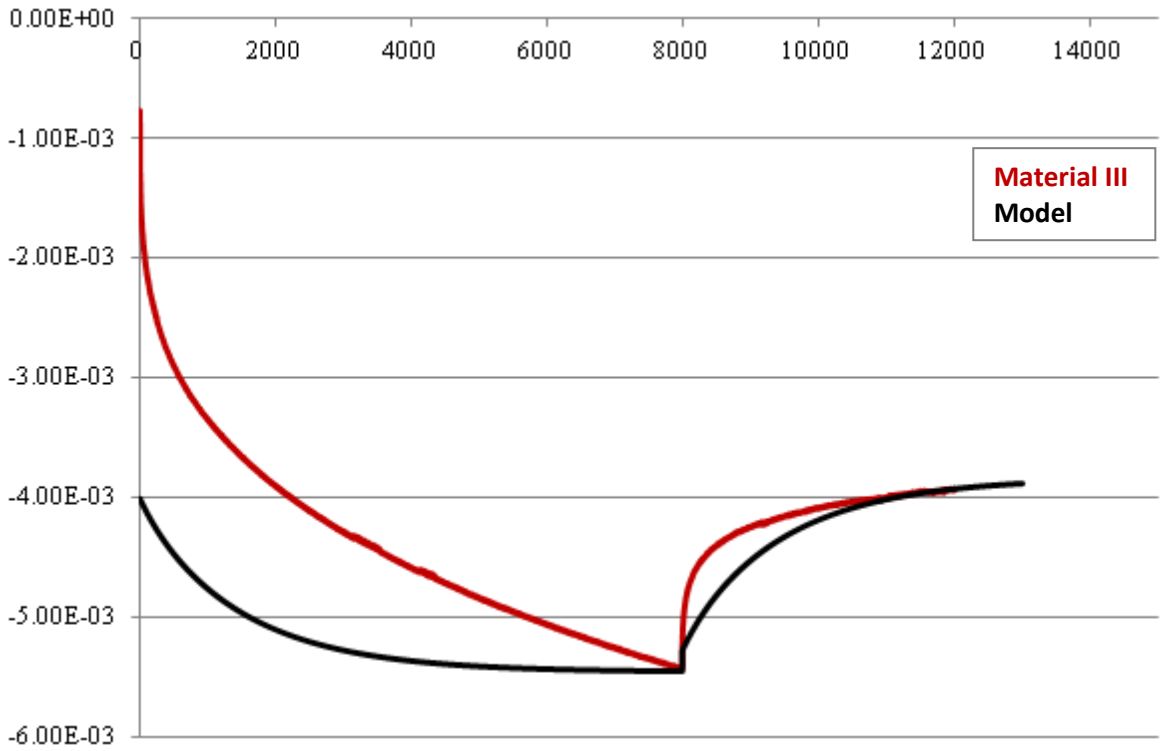

Figure 8-24 Material III – 13% PS: Experimental curve vs model output

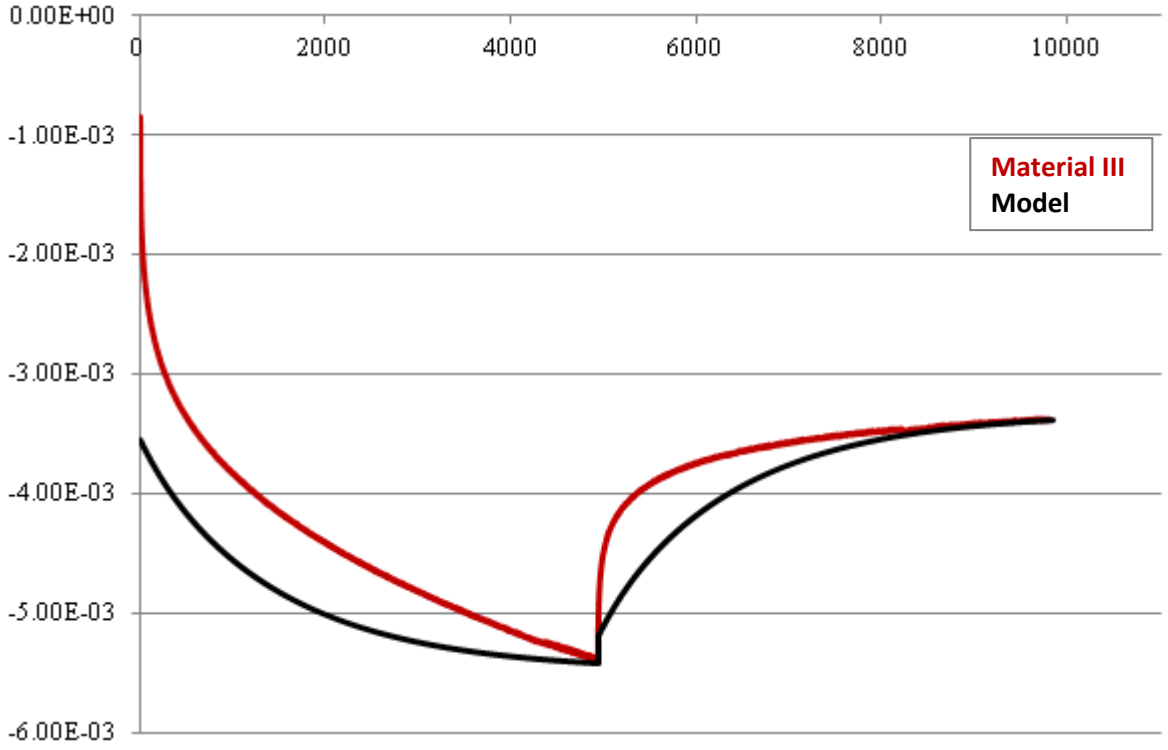

Figure 8-25 Material III – 17% PS: Experimental curve vs model output

In summary, the model presents the following advantages:

- It is an available formulation could be implemented in any FE code with an open library of materials
- It requires few experimental tests: Single Uniaxial Creep&Recovery tests within the in-service range of strains and stresses
- it provides a very accurate estimation of the accumulated permanent deformation even when 30% of RA is incorporated into the asphalt mixtures

Despite more efforts toward an improvement of the inelastic formulation of the model could provide a more accurate prediction of the loading phase and of the overall behaviour of the asphaltic materials, the proposed formulation of the model showed to adapt very well to reclaimed asphalt mixes and it represent a valid support to allow road pavement designer to determine the pavement life of asphalt pavement with and without RA.

9 Pavement Design Life Calculations conducted at TU Dresden

Different repeated load test methods have been established worldwide to investigate the stiffness and fatigue characteristics of asphalt mixes. The results of the fatigue tests can be used as input parameters for a mechanistic-empirical pavement design procedure. For the pavement design procedure the stiffness and the fatigue resistance of the asphalt mixes should be known in order to estimate the appropriate lifetime of the pavement structures. These characteristics can be obtained by various fatigue tests like bending, direct and indirect tensile tests. Fatigue parameters of asphalt mixes are commonly determined using the results of repeated load tensile tests. These parameters and the E-Modulus-temperature-function are required for the pavement design process. Different repeated load tests have been established in Germany and worldwide to determine the fatigue behaviour of asphalt mixes.

Within WP5 indirect tensile tests were carried out to determine the required parameters for the pavement design process. A detailed description of the used testing device and test conditions is presented in section 4.1.3. Figure 5-31 shows exemplary the results of the investigated fatigue tests.

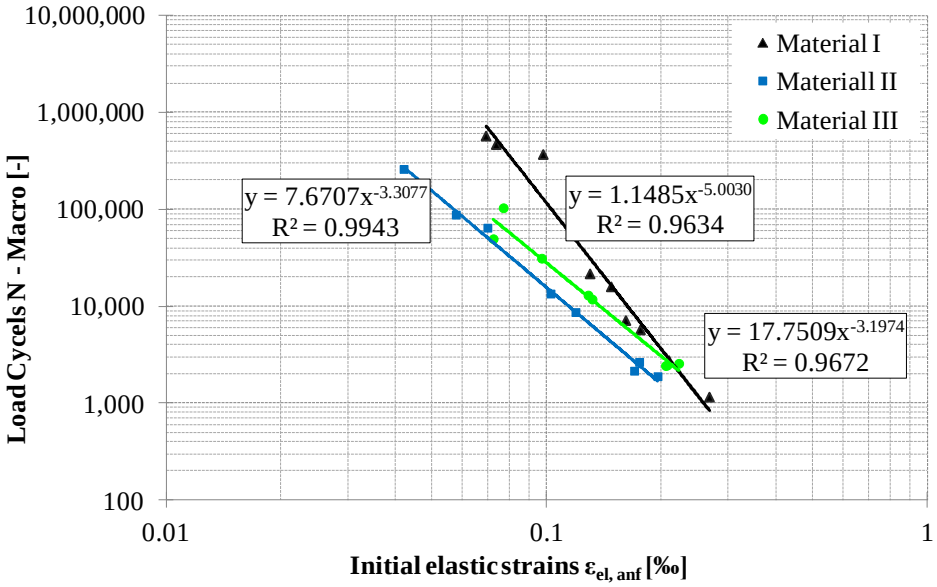

Figure 9-1 Fatigue relations obtained for the asphalt mixes

From this diagram it becomes quite clear that the intercept value K2 of the fatigue relation is changing significantly due to the RA content of the asphalt and/or the different binder contents of the three asphalt mixes investigated. However, it seems that the resistance against fatigue is decreasing by adding RA.

The laboratory test results in terms of the stiffness values and the fatigue curves were used as input values for pavement design life calculations.

The pavement design life calculations were conducted using an estimation of the tensile strains at the bottom of the asphalt layer. Based on the results of the pavement design process (in accordance to the German analytical design procedure for asphalt pavements RDO Asphalt (RDO, 2009)) the fatigue life of the pavements was calculated. The fatigue life is defined by the occurrence of the macro-crack at the bottom of the asphalt layer.

9.1 Input Values for the Calculation

In order to be able to design a pavement structure, comprehensive knowledge on the material properties is essential. The laboratory tests presented in chapter 4 and chapter 5 as well as the constitutive model presented in part 2 of this document are important pre-requisites for the design calculations using the pavement design software TISAD (Zeißler, 2012). This design software is based on multilayered elastic analysis and proceeds according to the German analytical design procedure for asphalt pavements RDO Asphalt (RDO, 2009). The fatigue curves used for the calculation process were presented earlier. Two fictive pavement structures were investigated, one with a 10 cm and one with a 20 cm thick asphalt surface layer (each containing different amounts of reclaimed asphalt).

Figure 9-2 shows the pavement structure of the “fictive” pavement investigated with a surface layer of 20 cm asphalt. The unbound granular layer was modeled with a stiffness of 150 MPa and the subgrade with a stiffness of 120 MPa.

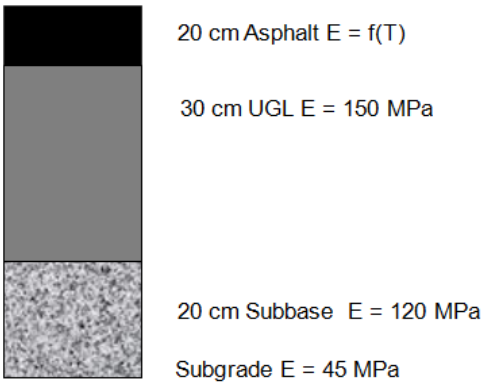

Figure 9-2 Pavement structure investigated (surface layer: 20 cm)

In the RDO Asphalt (RDO, 2009) typical frequency distribution of the axle load class in Germany are listed. For this project, the relative frequency distribution of the axle load class “highway - close to cities” was chosen. For the calculation process an average daily traffic for heavy vehicles (> 3.5 t total weight) of 1000 was assumed.

Within the analytical design process of asphalt pavements the climatic conditions play an important role due to the temperature dependant performance of asphalt layers. According to RDO Asphalt (RDO, 2009) thirteen standardized characteristic temperature gradients dependant on the asphalt surface temperatures are defined for Germany. In addition, 4 different temperature zones for Germany (a temperature

zone map for Germany is also included in (RDO, 2009)) with the corresponding frequency distribution for the asphalt surface temperatures were specified. Within this research, the frequency distribution of the asphalt surface temperatures of temperature zone 3 according to RDO Asphalt (RDO, 2009) was used (Figure 9-4).

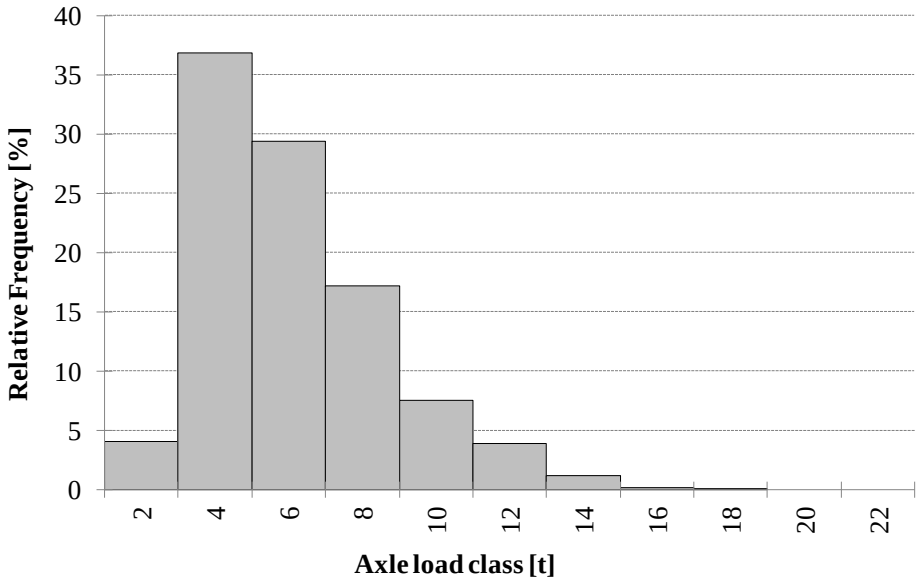

Figure 9-3 Relative frequency distribution of the axle load classes

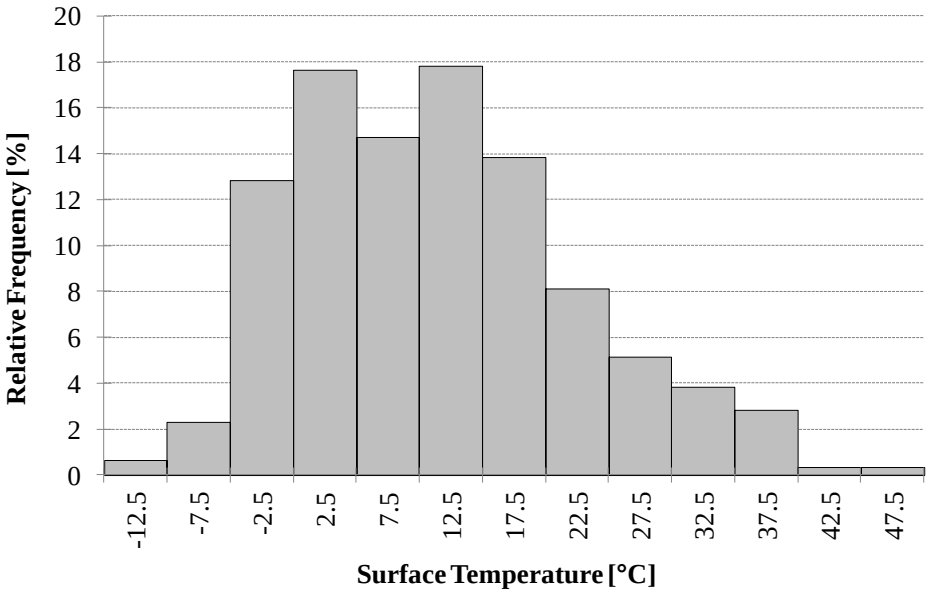

Figure 9-4 Representative frequency distribution of the asphalt surface temperatures – temperature zone 3 according to RDO Asphalt

9.2 Analysis of the Calculation Results

Using the software TISAD the fatigue status after 30 years of the pavements was determined. The fatigue status expresses the “consumption” of the pavement service life for the traffic volume expected. It can be emanated that a fatigue status of 100 % is equal to the end of pavement service life. The results of the pavement structure with a surface layer of 20 cm thickness show that for the pavement with 15 % RA the shortest remaining pavement life (high fatigue status) can be expected and for the pavement with 0 % RA the longest life (low fatigue status) (Figure 9-5 and Figure 9-6).

As Figure 9-5 shows, the fatigue performance of the pavement declines by adding RA to the asphalt mixes which is indicated by an increase in the fatigue status. Hence, the pavement fatigue life decreases.

However, by the supposed increase in fatigue life of the pavement with asphalt layers containing 30 % RA compared to the pavement 15 % RA the aging process of the asphalt mixes should be considered.

An accelerated aging process of the asphalt mixes containing RA that occurs in reality, leads to shorter pavement life as calculated here.

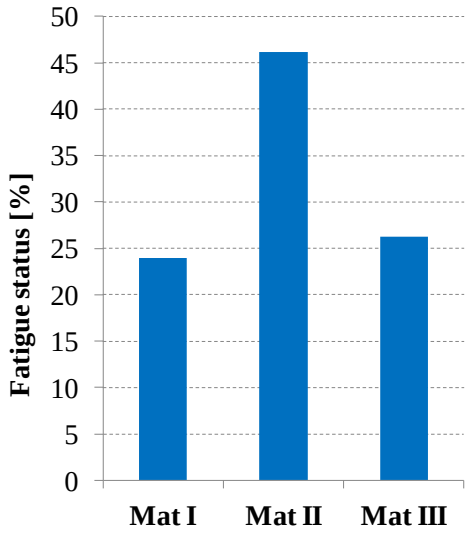

Figure 9-5 Fatigue status for the pavements investigated (20 cm asphalt surface layer)

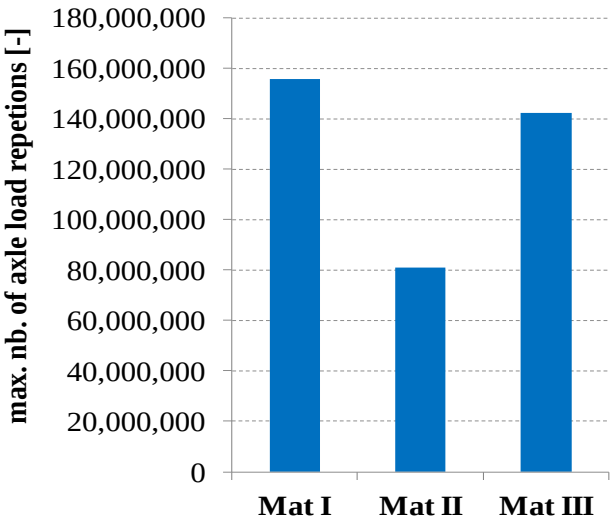

Figure 9-6 Maximum number of axle load repetitions for the pavements investigated (20 cm asphalt surface layer)

The results of the pavement structure with a surface layer of 10 cm thickness are presented in Figure 9-7 and Figure 9-8. The investigated materials show here another behavior than presented in Figure 9-5 and Figure 9-6. This can be explained as follows. The thinner asphalt surface layer cause higher strains at the bottom of the asphalt layer what leads to a lower number of calculated axle load repetitions as

well as to a lower fatigue status for the three materials. The order of the investigated materials in Figure 9-5, Figure 9-6, Figure 9-7and Figure 9-8 can be explained by the fatigue relations obtained for the three asphalt mixtures (Figure 5-31). An application of higher stresses leads to higher initial strains and following to a new order of the fatigue curves.

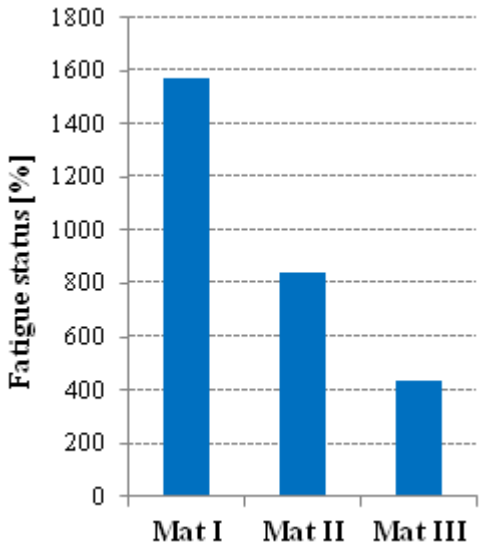

Figure 9-7 Fatigue status for the pavements investigated (10 cm asphalt surface layer)

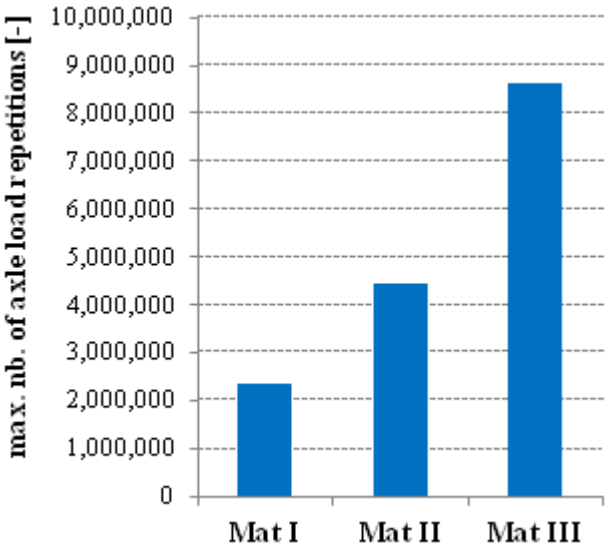

Figure 9-8 Maximum number of axle load repetitions for the pavements investigated (10 cm asphalt surface layer)

10 Numerical Tool developed at TU Dresden

For the performance models, input parameter such as plastic strains, elastic strains, stresses are required. These parameter were determined using the results of laboratory tests on asphalt mixes. Within this research project, cyclic triaxial tests were carried out at TU Dresden. In particular, the mechanical properties and the performance characteristics of three asphalt mixes containing different amouts of RA were determined and used for the numerical investigations.

10.1 Numerical tool to determine the Elastic Model Parameters

The complex modulus IE*I representsf the stiffness of viscoelastic materials, such as asphalt mixtures, under the action of cyclic loads. The complex modulus of asphalt materials is temperature and time dependent. The time dependency is evidenced in Figure 3-1 in which the strain lags behind the input stress. This lag is known as the time lag Δt from which the phase lag $\Delta\delta$ may be determined.

E* is a complex number comprising a real and an imaginary. The real part represe the storage modulus E' that characterizes the elastic portion (measures the stored energy) and the imaginary part represent the loss modulus E'' that symbolizes the viscous portion (measures of the energy dissipated as heat). In Figure 3-2, the complex modulus and its relationship with the phase lag is illustrated. The complex modulus E* in vector representation is known as absolute modulus |E*| (see chapter 3).

The complex modulus can be plotted in the complex plane, where E'' is the loss modulus and E' is the storage modulus; are drawn as functions of the phase lag δ and the absolute value of the complex modulus IE*I. Figure 3-3 shows a typical asphalt Cole-Cole plot determined at different frequencies and temperatures. It can be seen that at high temperatures and low frequencies the behavior of the material is mainly viscous and at high frequencies and low temperatures the asphalt behaves like an elastic solid (see chapter 3).

If the absolute modulus follows a single curve in the Cole-Cole plane then the time temperature superposition principle (TTSP) applies and a master curve can be constructed. The TTSP states that the same |E*| can be found for different frequency- temperature combinations. When the TTSP applies, |E*| values at different temperatures (isochrone of |E*|) can be translated by applying a multiplier (shift factor) to the frequency at which the measurement is taken so that they are combined to form a single curve of frequency versus stiffness. This curve is known as master curve. Figure 3-4 shows an absolute modulus master curve and its temperature-frequency relationship (see chapter 3). The parameter for the Cole-Cole plot and the master curve for Material I, II and III can be determined automatically using the numerical tool ReRoadToolTUD developed at TU Dresden.

Installation prerequisites

In order to use this algorithm, the following programs and packages need to be installed:

- Python 2.7 (www.python.org)
- Scipy (www.scipy.org)
- Numpy (numpy.scipy.org)
- Matplotlib (matplotlib.sourceforge.net).
- Wxpython

After starting the program **ReRoadToolTUD**, the laboratory test data (elastic strains, stresses) for a particular material can be loaded (Figure 10-1).

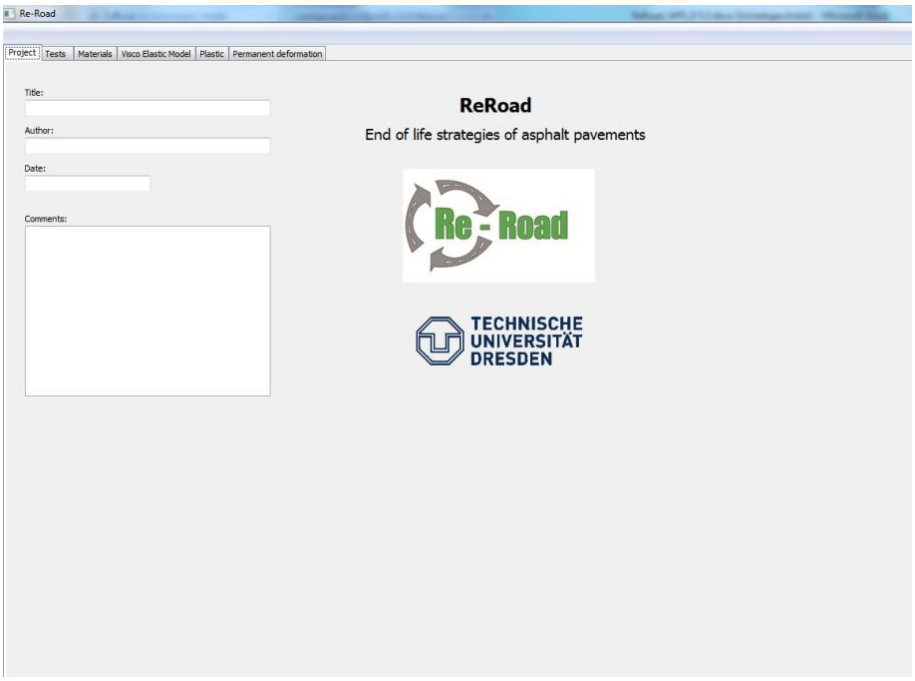

Figure 10-1 Screenshot of the cover page

In a second step, the data regression will be conducted (Figure 10-2).

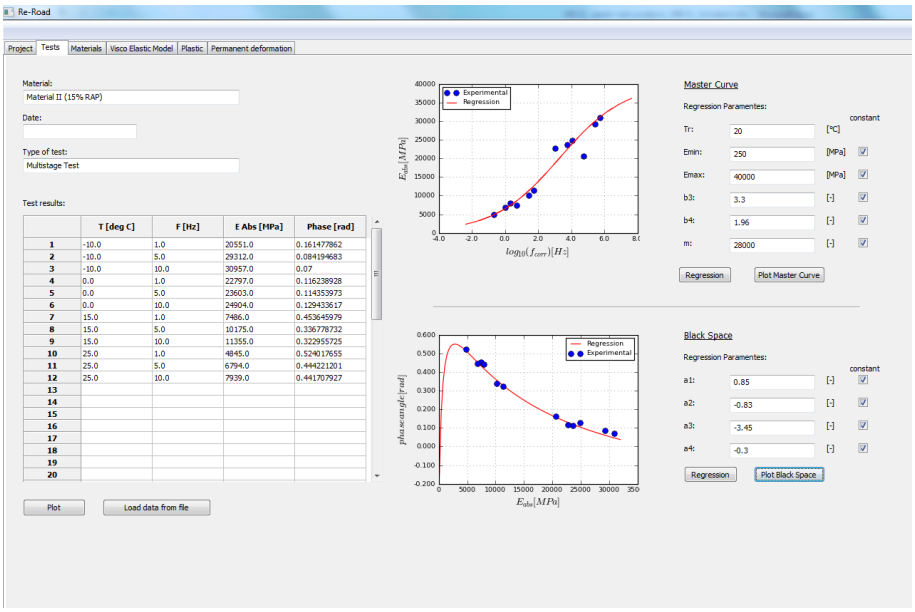

Figure 10-2 Screenshot of the data regression procedure

As a result of the regression process the parameter of the Cole-Cole plot and the master curve can be determined (Figure 10-2, Figure 10-3 and Figure 10-4).

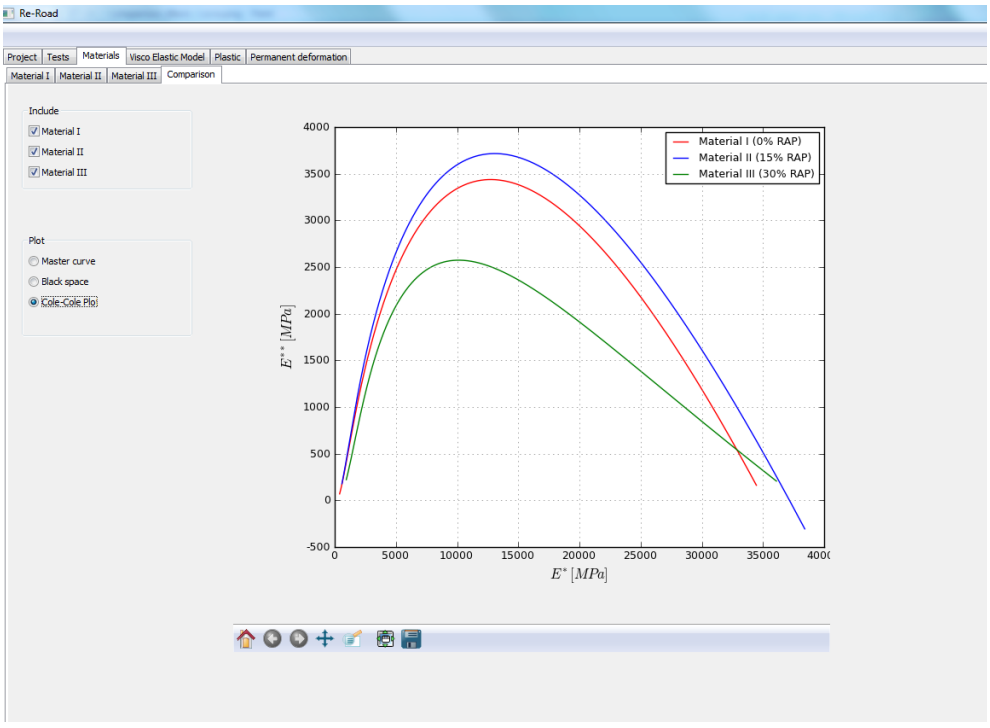

Figure 10-3 Screenshot of the Cole-Cole plots

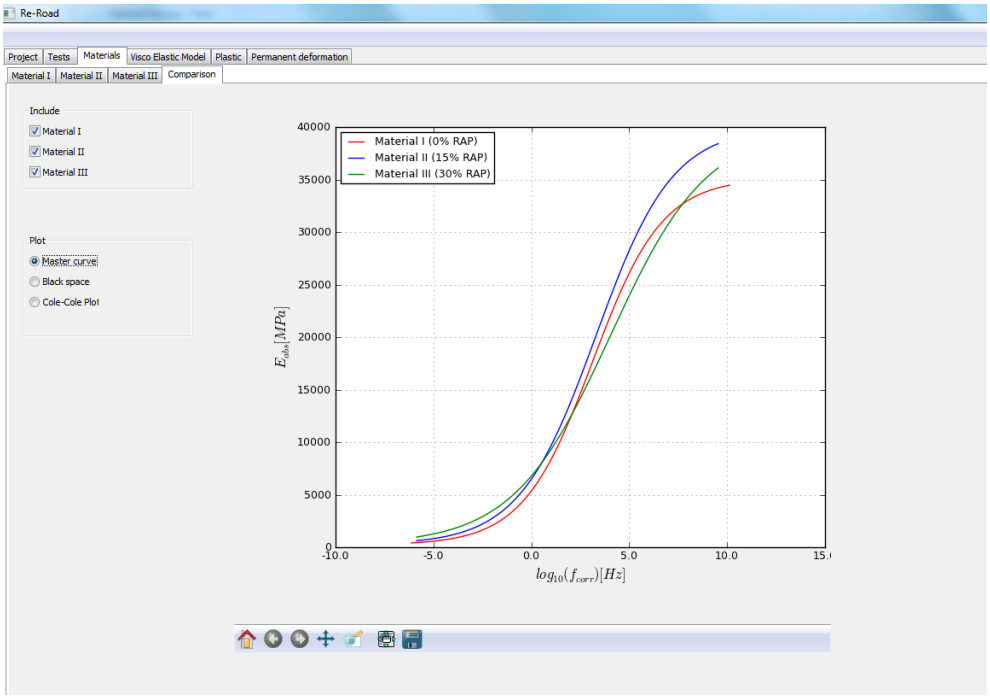

Figure 10-4 Screenshot of the master curve plots

10.2 FE Code used

Previous research at the TU Dresden was aimed to develop a computational model for flexible multilayer pavements based on the FE method. In order to forecast the load-bearing behaviour of pavements and satisfy the above-mentioned demands posed on suitable numerical models, existing mechanical and mathematical fundamental concepts were reformulated and extended, and algorithms to account for the nonlinear material behaviour of asphalt were developed and calibrated on the basis of laboratory experiments. Within the constitutive model the deformation behaviour of asphalt is modelled with the aid of so-called rheological bodies. A special body (HOOKEAN, KELVINIAN, NEWTONIAN body) is assigned to each deformation component (elastic, viscoelastic, viscoplastic). Non-monotonic damage-healing processes are described phenomenological and taken into consideration with the aid of a newly-developed damage-healing body. The rheological bodies are dependent on free values; these permit the computation of deformation increases. This material model exists in a differential form in one and three-dimensional configuration.

For a detailed investigation of pavement response, a 3-D computational model is required. Oeser (2004) has developed a 3D-FE Program ReFEM with a special tool for pavements. ReFEM is a complex and general FE program and experience is needed to utilise its full capabilities. It can simulate a very broad range of soil and pavement engineering materials under a range of loads, both dynamic and static (Bathe 2002). The ReFEM Program was used to carry out this investigation. Special

isoparametric finite elements (Bathe 2002) were used applying 60 degrees of freedom and tri-quadratic displacement shape functions.

Using the results of the numerical tool in terms of the elastic properties (stiffness values for the asphalt) it was possible to determine the input values for the FE calculations using the ReFEM. Any other FE code can be used as well.

Any pavement structure can be now modelled using a suitable FE code. As a result of the FE calculation, the elastic strain values in the asphalt layer in the loading axis can be defined. This forms the input values for the second part of the numerical tool to determine the plastic deformation of the asphalt layer.

10.3 Numerical Tool to predict Plastic Deformations

The plastic model predicts the plastic deformation using a correlation between resilient and plastic strains and /or stresses and plastic strains. This simplified approach can be used to predict the plastic deformation in the loading axis. The model build on an exponential law that links the vertical plastic strain rate $\varepsilon_{1;p;rate}$ to the vertical resilient strain $\varepsilon_{1;r}$ and the stresses respectively. More details about the model can be found in section 6.3.

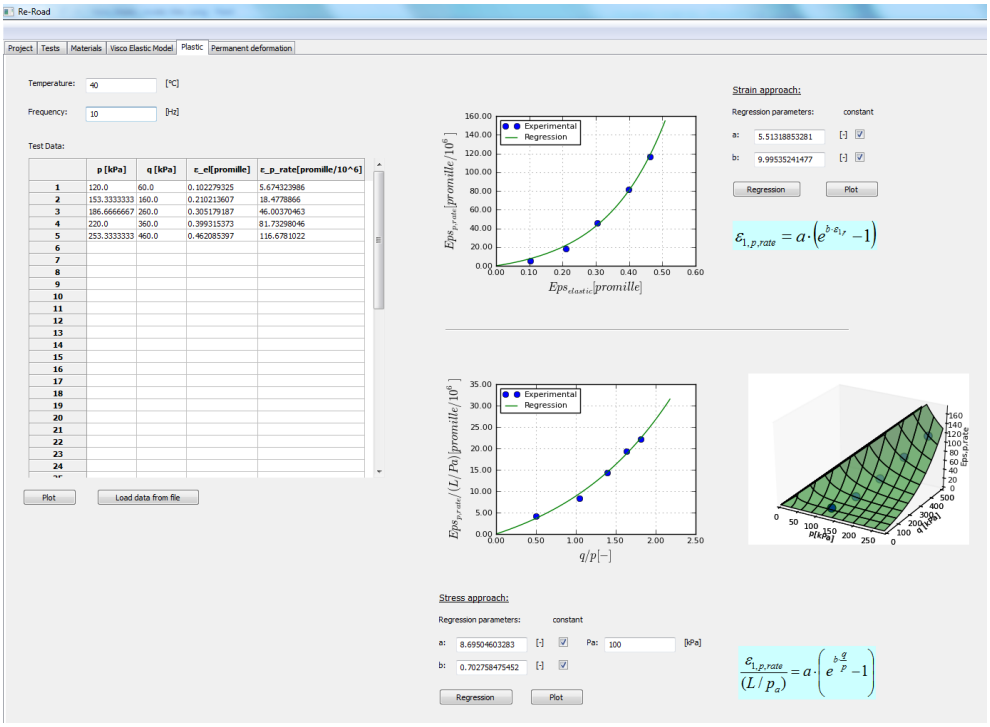

Figure 10-5 Screenshot of the determination of the plastic model parameter

The model is fitted with the results of long term repeated load triaxial tests in which stresses as well as resilient and permanent strain are recorded. The plastic strain rates, $\varepsilon_{1;p;rate}$, are determined from the permanent strain curve (permanent strains vs. load cycles) using the slope of the secant line between 25,000 and 50,000 cycles.

Figure 2-9 presents the results of the parameter determination process using the stress approach (Equation (6-50)) and strain approach (Equation (6-51)).

Finally, the plastic deformation for a defined asphalt layer thickness in dependence on the number of load applications can be calculated for a defined pavement condition (loading and asphalt temperature distribution) – see Figure 10-6. It is possible to incorporate this procedure in an analytical pavement design process in order to predict pavement life in terms of rutting.

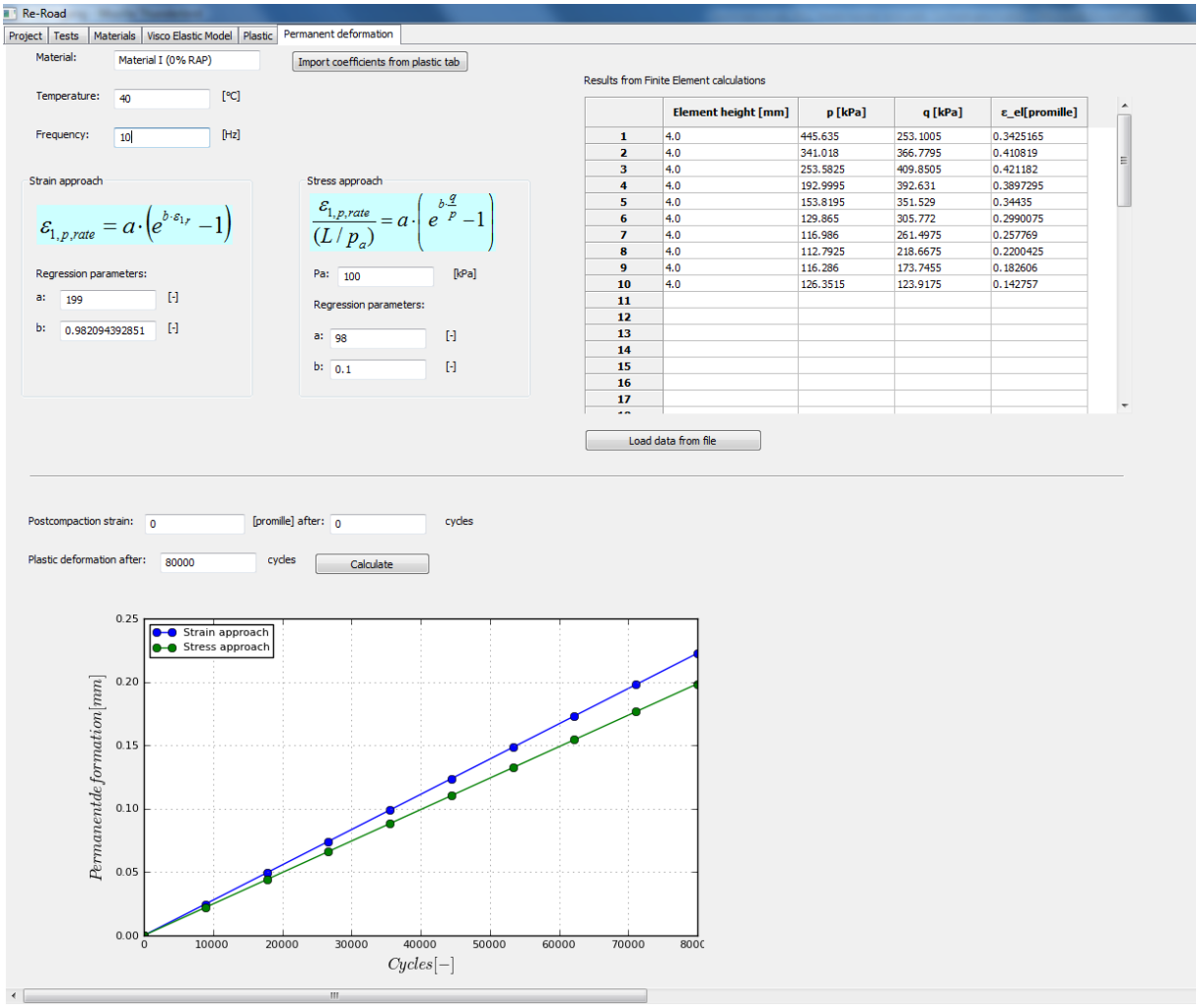

Figure 10-6 Screenshot of the prediction of the plastic deformation - rutting in dependence on the number of load cycles

11 Conclusions

Using conventional testing procedures, such as the ring and ball test and needle penetration, it is impossible to comprehensively study the behaviour of asphalt binders especially if the materials consist of new and reclaimed components. The results obtained from DSR-tests indicate that if a significant amount of reclaimed binder is used in the mix, the mixed binder ages at an accelerated rate. In order to verify those test results and to provide more proof for this, additional rheological tests such as creep recovery tests would need to be carried out.

Compared to the reference asphalt with 0% reclaimed material, the asphalt mixes with recycled components (RA-mixes) exhibited a higher stiffness and lower visco-elastic deformation even for high temperatures and low frequencies. The plastic deformation characteristics were also influenced by the amount of recycled material in the asphalt mix in such a way that the resistance to plastic deformation was higher in RA-mixes when low stresses and consequently low elastic strains were applied. However, for high stresses and high elastic deformation the permanent deformation in the RA-mixes were higher than what was obtained for the reference asphalt.

The resistance to fatigue also varies significantly with the amount of RC-material in the RA-mixes. This result was observed by comparing fatigue testing results of RA-mixes to results obtained on reference material. The RA-specimens that were used for those tests were subjected to the same loads and would exhibit the same granulometric characteristics and binder contents as the specimens made of reference material. To assess the materials resistance to fatigue, the fatigue characteristics as well as the stiffness characteristics should always be jointly considered. This is necessary, since a high resistance to fatigue crack formation may be achieved through a high stiffness at lower fatigue resistance or alternatively, through a lower stiffness at high fatigue resistance.

In addition to the knowledge created through the research project, experiences in regards to the use of RC-material for asphalt surface courses as well as for asphalt binder courses are to be aimed at. In the opinion of the authors, the performance characteristics of asphalt mixes containing RC-material should not only be assessed by means of experimental procedures, but also by numerical simulations such as the ones suggested in the RDO Asphalt (RDO Asphalt, 2009).

Problems observed when conducting the tests arose from material in-homogeneities due to the special grain size distribution of the aggregates used for the mixes, from the binder content as well as from the special rheological characteristic of the binder.

Based on the investigation conducted within this study it can be concluded that an equality of the pavements with and without RA could not be assessed. No equivalent conditions in terms of the mix composition could be reached due to the inhomogeneity of the asphalt mixes containing RA. This leads to a change in stiffness and fatigue performance of the asphalt materials.

12 Suggestions for implementation

12.1 Research needs identified

Research indicates that recycling of asphalt is a beneficial approach both from an economical as well as an ecological point of view (Lu et. al. 2002). Further, recycling of asphaltic materials may help to conserve diminishing resources of aggregates and petroleum products, save energy and reduce carbon dioxide emissions created during the production process of the material (Karlsson et. al., 2006).

Asphalt pavements age after several years in service. The aging is mainly caused by a change in the chemical composition of the binder. Binder consists of solid components as well as viscous components. Both components are constituted by molecular substances of different structure. These substances mainly consist of carbon, hydrogen, nitrogen oxygen and sulphur. Due to oxidation and distillation processes the molecular structure of these substances changes. This change generally leads to a transformation of viscous components into solid components, which in turn causes the binder to behave more solid-like (more brittle) with time (Karlsson et. al., 2007). A graphical representation of this process is given in Figure 12-1.

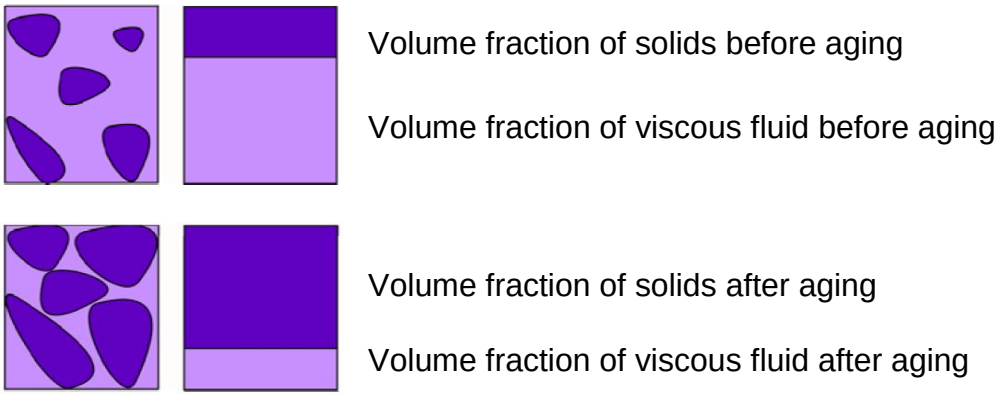

Figure 12-1 Volumetric composition of binders before and after aging

Almost all of the pavement design guides worldwide do not adequately consider the effect of aging within the design procedure of pavements. This generally leads to an overestimation of the viscous potential of pavements in the later stages of service life and to accelerated pavement failure. Hence, the asphalt aging process should be properly incorporated into the pavement design process.

Another issue that has been discovered during the research is the accelerated aging of the fresh material components in RC-mixes when larger quantities of recycled asphalt are present in the mix. Aging during construction (short term aging) and service (long term aging) has been associated with six major mechanisms (Roberts,

1996; Tyrion, 2000; Karlsson & Isacsson 2006):

- Oxidation through diffusive reaction between the binder and oxygen in the air;
- Volatilization through evaporation of the lighter components especially during
- construction;
- Polymerization through chemical reaction of molecular components;
- Thixotropy due to the formation of a structure within the asphalt binder over a long
- period of time;
- Syneresis due to the exudation of thin oily components; and
- Separation through the removal of oily constituents, resins, and asphaltenes by
- absorptive aggregates.

The level of aging that asphalt binder experiences during service also depends on the amount of aged binder present in the mix. This occurs, presumably, because the aged binder in the mix acts like an oxidation accelerator. The chemical reactions that trigger this accelerated oxidation are widely unknown so far and need to be research.

Another problem discovered during the research is that RC-mixed are often very inhomogeneous. This means that the fresh and recycled components may be incompletely mixed. Similar results were found by Oliver (2001) who investigated the blending process between aged and virgin asphalt binders using mechanical testing. To prevent incomplete blending between aged and virgin asphalts in RC-mixes, new procedures need to be developed that guarantee for homogeneous properties of RA-mixes. First ideas on how this could be realized were formulated in Stephens et al. (2001) who studied the effect of preheating (including varying in preheating times) of the recycled asphalt on the homogeneity of the RC-mix.

12.2 Implementations of the research

The implementation of the research in a pavement engineering environment may be achieved by publication and seminars. It is planned to have sessions on recycling of asphalt and the characteristics of RC-mixes at the following conferences:

- Braunschweiger Straßenbau Aktuell, 2013
- Aachener Straßen- und Verkehrstage, 2013
- Dresden Straßenbaukolloquium 2013

The (diverse) healing factor of bituminous mixtures with and without reclaimed asphalt is important to implement in pavement design, since this healing factor will affect directly the estimated pavement design life. DSR tests on binder and mastic are more practicable than tests on asphalt mixtures (faster, less expensive). The fatigue and healing test results on binders and mastic will be compared to the fatigue and healing tests of the asphalt mixtures, provided by UC Dublin. An abstract is submitted for a paper at Fourth International Conference on Self-Healing Materials ICSHM2013.

13 References

[1] Arrhenius, S.: (In German) Zeitschrift für Physikalische, Chemie 1:285, 1887

[2] Arnold, G.: Rutting of Granular Pavements. Dissertation, University of Nottingham, Nottingham,U.K, 2004

[3] Bathe, K.J.: Finite Element-Methods. Berlin, Springer Verlag, 2002

[4] Caputo, M. – Mainardi, F.: Linear Models of Dissipation in Anelastic Solids. Rivista del Nuovo Cimento, Vol. 1, No.2, 1971

[5] Celauro, C. – Bernardo, C. – Gabriele, B: Production of innovative, recycled and high-performance asphalt for road pavements. Resources, Conservation and Recycling 54(6): 337–347, 2010

[6] Chailleux, E. – Ramond, G. – Roche, C.D.L.: A Mathematical-based Master Curve Construction Method Applied to Complex Modulus of Bituminous Materials. Road Mater. Pav. Des., Vol. 7, pp. 75-92, 2006

[7] Craiem, D.O. – Rojo, F.J. – Atienza, J. M. – Guinea, G.V.: Fractional Calculus Applied to Model Arterial Vico-elasticity, Latin American Applied Research, Vol. 38, pp 141-145, ISSN 0327-0793, 2008

[8] Davison, R.R. – Bullin, J.A. – Glover, C.J. – Chaffin, J.M. – Peterson G.D. – Lunsford, K.M. – Lin, M.S. – Liu M. & Ferry: M.A. 1994. Verification of an asphalt aging test and development of superior recycling agents and asphalts, Texas Transp. Institute and Chemical Dept., Texas A&M Univ

[9] Doucet, F.: Complex Modulus Determination of Asphalt Mixes. Report, Ministry of Transport of Quebec, Quebec, Canada, 2010

[10] Dragon, I. – Malcherek, T. – Blasl, A.: Einfluss des Recyclingasphaltanteils sowie des verwendeten Zugabebindemittels auf die Ermüdungsbeständigkeit von Asphaltbefestigungen. Journal Straße + Autobahn, Issue 62, No. 4, 2011, pp. 229-237

[11] Erkens S., “Asphalt concrete response (acre): determination, modelling and prediction”, Doctoral thesis Delft University of Technology,2002

[12] Erkens S. M. G. J. – Liu X. – Scarpas A.: 3D Finite Element Model for Asphalt Concrete Response Simulation, The International Journal of Geomechanics, Vol.2, N.3, 2002

[13] Ferry, J.D.: Visco-elastic Properties of Polymers, 3rd Edition, John Wiley & Sons, New York, 1980

[14] Gidel G, et al.: A New Approach for Investigation the Permanent Deformation Behaviour of Unbound Granular Material Using the Repeated Load Triaxial

Apparatus. Report, Bulletin des Laboratorires des Ponts et Chaussees, France, 2001

[15] Grohs, S.: Bestimmung mechanischer Kenngrößen für einen SMA 0/11S mit Hilfe des dynamischen Triaxialversuchs. Diploma Thesis, TU Dresden, Germany, 2010

[16] Hajj E. – Sebaaly, P.: A Laboratory Evaluation on the Use of Recycled Asphalt Pavements in HMA Mixtures. Report, 2007, University of Nevada Reno, Nevada

[17] Harris L. – Fairchild N.: Sustainability in Transportation. Newsletter summer 2011, Kansas University Transportation Center, Kansas, United States

[18] Hartman, A.M. – Gilchrist, M.D. – Nolan, D.: Wheeltracking fatigue simulation of bituminous mixtures. Road Materials and Pavement Design 2(2): 2001, pp-141-160

[19] Hveem, F.N.: Mix design method for asphalt concrete MS-2. The Asphalt Institute, College Park, Md., USA, 1974

[20] Jones, D.I.G.: Handbook of Viscoelastic Vibration Damping, Chapter 5: Numerical Analysis of Measured Complex Modulus Data, pp 109-138, Wiley & Sons, UK, ISBN 0721492485, 2001

[21] Kandhal P.S. – Rao S.S. – Watson D.E. – Young B.: Performance of recycled hot mix asphalt mixtures in State of Georgia. National Center for Asphalt Technology, NCAT Report 9501, 1995

[22] Karlsson, R. – Isacsson, U.: Material-Related Aspects of Asphalt Recycling—State-of-the-Art. Journal of Martials in Civil Engineering 18(1): 81-92, 2006

[23] Karlsson, R. – Isacsson, U. – Ekblad, J.: Rheological characterisation of bitumen diffusion. Journal of Material Sciences 42:101–108, 2007

[24] Kim, R.: Modeling of Asphalt Concrete. McGraw-Hill, United States of America, 2009

[25] Kim, W. – Labuz, J.: Resilient Modulus and Strength of Base Course with Recycled Bituminous Material. Report, Minnesota Department of Transportation, Maplewood, 2007

[26] Laefer, D. – Lennon, D.: Viability assessment of terrestrial LiDAR for retaining wall monitoring. In: Proceedings of GeoCongress 2008: Geosustainability and Geohazard Mitigation, GSP 178, New Orleans, Louisiana, American Society of Civil Engineering, 2008

[27] Lee E. H. – Liu D. T.: Finite- Strain Elastic-Plastic Theory with Application to Plane- Wave Analysis, Journal of Applied Physics, Volume 38, Issue 1, 1967

[28] Lee E. H.: Elastic-Plastic Deformation at Finite Strains. Journal of Applied Mechanics, Volume 36, Issue 1, 1, 1969

[29] Lo Presti et al., “Use of Gyratory Compactor to Manufacture Asphalt Test Specimens Containing Reclaimed Asphalt”, ISAP TC 2012 conference proceedings, 2012

[30] Lo Presti D. – Brown L. – Kranthi K. – Airey G. – Collop A. – Scarpas A.: Mechanical characterisation of reclaimed asphalt mixes for modelling purposes. Proceeding, MAIREPAV 7, 7th International Conference on Maintenance and Rehabilitation of Pavements, New Zealand, 2012

[31] Lu, X. – Isacsson, U. Effect of ageing on bitumen chemistry and rheology. Construction and Building Materials 16(1): 15–22, 2002

[32] Malcharek, T.: Einfluss von Recyclingasphalt auf die Ermüdungsbeständigkeit von Asphaltbefestigungen. Diploma Thesis, TU Dresden, Germany, 2010

[33] Neifar, M. – Di Benedetto, H.: Thermo-Viscoplastic Law for Bituminous Mixes, Road Materials and Pavement Design, Vol. 2, Issue 1, 2001

[34] O'Brien, D.J. – Mather, P.T. – White, S.R.: Viscoelastic Properties of an Epoxy Resin during Cure, Journal of Composite Materials, Vol. 35, Issue 10, pp 883 – 904, 2001

[35] Oeser M.: Nichtlineare numerische Simulationsmodelle für Verkehrswegebefestigungen unter Berücksichtigung von mechanischen, thermischen und hydraulischen Einwirkungen. Habilitation Thesis, TU Dresden, Germany, 2009

[36] Oeser, M. – Freitag, S.: Modelling of Materials with Fading Memory Using Neural Networks, International Journal for Numerical Methods in Engineering, Vol. 78, pp. 843-862, 2009

[37] Oeser, M. – Pellinen, T. – Scarpas, T. – Kasbergen, C.: Studies on creep and recovery of rheological bodies based upon conventional and fractional formulations and their application on asphalt mixture, International Journal of Pavement Engineering, Vol. 9, Issue 5, pp 373 – 386, 2008

[38] Olard, F. – Di Benedetto, H.:, General “2S2P1D” Model and Relation Between the Linear Visco-elastic Behaviors of Bituminous Binders and Mixes”, Road Materials and Pavement Design, Vol.4, Issue 2, 2003

[39] Olard, F. – Di Benedetto, H. – Eckmann, B. – Triquigneaux, J-P.: Linear Visco-elastic Properties of Bituminous Binders and Mixtures at Low and Intermediate Temperatures, Road Materials and Pavement Design, Vol. 4, Issue 1, 2003

[40] Oliver, J. W. H.: The Influence of the Binder in RAP on Recycled Asphalt Properties. International Journal of Road Materials and Pavement Design, Vol. 2, No. 3, pp. 311-325, 2001

[41] Pellinen, T. – Christensen, D.W. – Bonaquist R.F.: Hirsch Model for Estimating the Modulus of Asphalt Concrete, Journal of the Association of Asphalt Paving Technologists, Vol.72, pp.121-151, 2003

[42] Powels, J.G.: Cole-Cole Plots as they should be, Journal of Molecular Liquids, Vol. 56, pp. 35-47. Elsevier Science Publishers B.V., Amsterdam, 1993

[43] RDO Asphalt 09, Richtlinien für die rechnerische Dimensionierung des Oberbaues von Verkehrsflächen mit Asphaltdeckschicht. RDO - Asphalt 09 – FGSV 2009, Germany, Köln

[44] Re-Road FP7 project, Delivarable 2.2 – Internal report, 2010

[45] Roberts F.L. – Kandhal, P.S. – Brown, E.R. – Lee, D. – Kennedy T.W.: Hot Mix Asphalt Materials, Mixture Design and Construction. Second Edition, National Asphalt Pavement Association, Lanham, MD, 1996

[46] Rossikhin, Y.A.: Reflections on Two Parallel Ways in the Progress of Fractional Calculus in Mechanics of Solids, Applied Mechanics Reviews 63:1-12, 2010

[47] Rowe, G.: Alternate shift factor relationship for describing the temperature dependency of the viscoelastic behaviour of asphalt materials. UK, 2010

[48] Scarpas, A.: A Mechanical based Computational Platform for Pavement Engineering, PhD-Thesis, Technical University of Delft , 2004

[49] Stephens, J. E., J.: Mahoney, and C. Dippold, Determination of the PG Binder Grade to Usein a RAP Mix, Report No. JHR 00-278, Connecticut Department of Transportation, Rocky Hill, CT, 2001

[50] Tabaković, A., Gibney, A., McNally, C. & Gilchrist, M.D. Influence of recycled asphalt pavement on fatigue performance of asphalt concrete base courses. Journal of Materials in Civil Engineering 22(6) 2010, 643-650

[51] TU Dresden, Faculty of Civil Engineering: Computational Modeling and Experimental Testing of Tire-Pavement Interation-Phenomena under Consideration of Flexible Pavement Structures, Report, Dresden, 2010

[52] Van den bergh, W.: The Effect of Ageing on the Fatigue and Healing Properties of Bituminous Mortars, PhD. Thesis, TU Delft, The Netherlands, 2011

[53] Valdes, G. , et al, Experimental Study of Recycled Asphalt Mixtures with High Percentages of Reclaimed Asphalt Pavement (RAP), Report, University of Catalonia

[54] Werkmeister, S. – Wellner, F. – Oeser, M.: Study on the Fatigue Behaviour of Asphalt Mixes Using the Dynamic Indirect Tensile Test within the Scope of Analytical Design. ISAP Conference, Canada 2006

[55] Wulandari, D.: The Use of Reclaimed asphalt in Pavements. Master Thesis, TU Dresden, Germany,2009

[56] Yusoff, M.: The 2S2P1D: An Excellent Linear Viscoelastic Model, UNIMAS e-Journal of civil Engineering, Vol 1: Issue 2, 2012

[57] Zeißler, A.: TISAD Pavement Design Software. TU Dresden, Germany, 2012

[58] Zeißler A.: Untersuchungen zum spannungsabhängigen Materialverhalten von Asphalt. Manuscript PhD. Thesis, TU Dresden, Germany, 2012

Notes

[1] http://www.01db-metravib.com

14 Acknowledgements

The research leading to these results has received funding from the European Community's Seventh Framework Program (FP7/2007-2013) under grant agreement n° 218747.

15 Appendix

A Materials tested

Table A1: Volumetric characteristics of Material I (0% RA, reference material)

Asphalt mixture	Percentage of RA
Binder content	6,5 M.-%
Soluble binder content	6,95 M.T.
Binder volume	15,4 Vol.-%
Maximum density	2,454 g/cm³
Bulk density*1	2,391 g/cm³
Void content	2,6 Vol.-%
Fictitious void content	18,0 Vol.-%
Voids filled with binder	85,6 %

*1 Buoyancy method for determination of density

B Model development at TU Dresden

To obtain the coefficients and exponents of fractional derivatives of simpler combinations of springs and dashpots, the instructions given in Figure B1 may be followed. Table B2 to Table B5 contain a complete set of exponents and coefficients for all elements shown in Figure B1. Rows where both coefficients, b_j, and, c_j, are zero have been omitted in tables.

Table B1: Exponents and coefficients of the 2S3P-element

Exponents	Stress-coefficients	Strain-coefficients
$\beta_1 = \alpha_{11} + \alpha_{12}$	$b_1 = M_1 / \left(p_{13} \cdot \alpha_T^{\alpha_{13}} \right)$	$c_1 = M_0 \cdot M_1 / \left(p_{13} \cdot \alpha_T^{\alpha_{13}} \right)$
$\beta_2 = \alpha_{11} + \alpha_{13}$	$b_2 = M_1 / \left(p_{12} \cdot \alpha_T^{\alpha_{12}} \right)$	$c_2 = M_0 \cdot M_1 / \left(p_{12} \cdot \alpha_T^{\alpha_{12}} \right)$
$\beta_3 = \alpha_{12} + \alpha_{13}$	$b_3 = M_1 / \left(p_{11} \cdot \alpha_T^{\alpha_{11}} \right)$	$c_3 = M_0 \cdot M_1 / \left(p_{11} \cdot \alpha_T^{\alpha_{11}} \right)$
$\beta_4 = \alpha_{11} + \alpha_{12} + \alpha_{13}$	$b_4 = 1$	$c_4 = M_0 + M_1$

The variable, α_T, in Table B1 denotes the temperature shift factor. The temperature shift factor can be calculated from the Arrhenius type Equation (B1), where, T_0, represents the reference temperature, T, is the material temperature and, C_1, and, C_2, denote material parameters.

$$\log(\alpha_T) = \frac{C_1 \cdot (T_0 - T)}{C_2 + (T - T_0)} \quad \text{(B1)}$$

Table B2 Exponents and coefficients of the standard solid element

Exponents		Stress-coefficients	Strain-coefficients
A2a	A2b		
$\beta_3 = 0$	$\beta_3 = 0$	$b_3 = M_1 / \left(p_{11} \cdot {\alpha_T}^{\alpha_{11}}\right)$	$c_3 = M_0 \cdot M_1 / \left(p_{11} \cdot {\alpha_T}^{\alpha_{11}}\right)$
$\beta_4 = \alpha_{11}$	$\beta_4 = 1$	$b_4 = 1$	$c_4 = M_0 + M_1$

Table B3 Exponents and coefficients of the Maxwell element

Exponents		Stress-coefficients	Strain-coefficients
A3a	A3b		
$\beta_3 = 0$	$\beta_3 = 0$	$b_3 = M_1 / \left(p_{11} \cdot {\alpha_T}^{\alpha_{11}}\right)$	$c_3 = 0$
$\beta_4 = \alpha_{11}$	$\beta_4 = 1$	$b_4 = 1$	$c_4 = M_1$

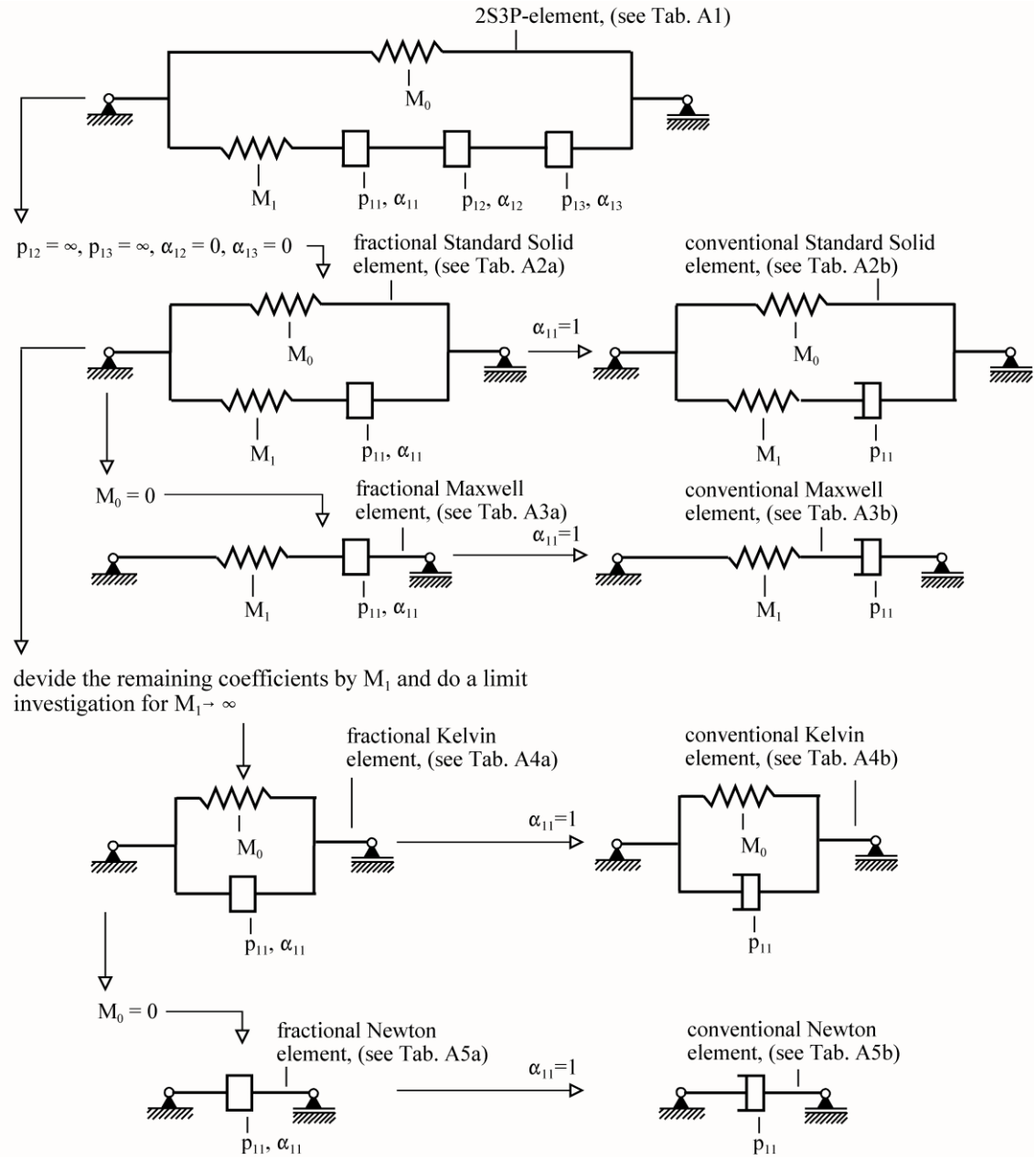

Figure B1 Fractional and conventional rheological elements

Table B4 Exponents and coefficients of the Kelvin element

Exponents		Stress-coefficients	Strain-coefficients
A4a	A4b		
$\beta_3 = 0$	$\beta_3 = 0$	$b_3 = 1/\left(p_{11} \cdot {\alpha_T}^{\alpha_{11}}\right)$	$c_3 = M_0/\left(p_{11} \cdot {\alpha_T}^{\alpha_{11}}\right)$
$\beta_4 = \alpha_{11}$	$\beta_4 = 1$	$b_4 = 0$	$c_4 = 1$

Table B5 Exponents and coefficients of the Newton element

Exponents		Stress-coefficients	Strain-coefficients
A5a	A5b		
$\beta_3 = 0$	$\beta_3 = 0$	$b_3 = 1/\left(p_{11} \cdot {\alpha_T}^{\alpha_{11}}\right)$	$c_3 = 0$
$\beta_4 = \alpha_{11}$	$\beta_4 = 1$	$b_4 = 0$	$c_4 = 1$

To obtain the exponents and coefficients of the 2S2P1D, 1S2P1D, Huet-Sayegh and Huet element the mathematical operations indicated in Figure B2 must be carried out. A complete set of exponents and coefficients for the above mentioned elements is given in Table B6 to Table B9. Rows where both coefficients, b_j, and, c_j, are zero have been omitted in the tables.

Table B6 Exponents and coefficients of the 2S2P1D-element

Exponents	Stress-coefficients	Strain-coefficients
$\beta_1 = 1 + \alpha_{12}$	$b_1 = M_1/\left(p_{13} \cdot {\alpha_T}^{\alpha_{13}}\right)$	$c_1 = M_0 \cdot M_1/\left(p_{13} \cdot {\alpha_T}^{\alpha_{13}}\right)$
$\beta_2 = 1 + \alpha_{13}$	$b_2 = M_1/\left(p_{12} \cdot {\alpha_T}^{\alpha_{12}}\right)$	$c_2 = M_0 \cdot M_1/\left(p_{12} \cdot {\alpha_T}^{\alpha_{12}}\right)$
$\beta_3 = \alpha_{12} + \alpha_{13}$	$b_3 = M_1/\left(p_{11} \cdot {\alpha_T}^{\alpha_{11}}\right)$	$c_3 = M_0 \cdot M_1/\left(p_{11} \cdot {\alpha_T}^{\alpha_{11}}\right)$
$\beta_4 = 1 + \alpha_{12} + \alpha_{13}$	$b_4 = 1$	$c_4 = M_0 + M_1$

Table B7 Exponents and coefficients of the 1S2P1D-element

Exponents	Stress-coefficients	Strain-coefficients
$\beta_1 = 1 + \alpha_{12}$	$b_1 = M_1/\left(p_{13} \cdot {\alpha_T}^{\alpha_{13}}\right)$	$c_1 = 0$
$\beta_2 = 1 + \alpha_{13}$	$b_2 = M_1/\left(p_{12} \cdot {\alpha_T}^{\alpha_{12}}\right)$	$c_2 = 0$
$\beta_3 = \alpha_{12} + \alpha_{13}$	$b_3 = M_1/\left(p_{11} \cdot {\alpha_T}^{\alpha_{11}}\right)$	$c_3 = 0$
$\beta_4 = 1 + \alpha_{12} + \alpha_{13}$	$b_4 = 1$	$c_4 = M_1$

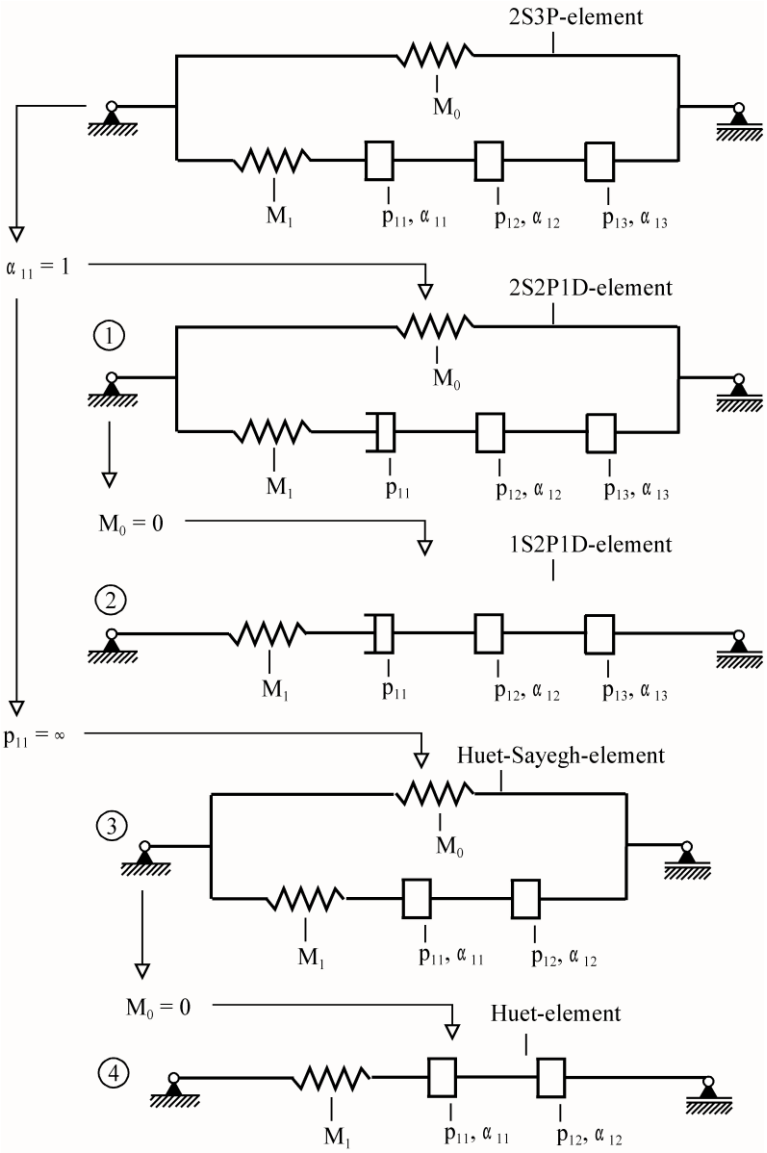

Figure B2 2S2P1D-, 1S2P1D-, Huet-Sayegh- and Huet-element

Table B8 Exponents and coefficients of the Huet-Sayegh-element

Exponents	Stress-coefficients	Strain-coefficients
$\beta_1 = \alpha_{11}$	$b_1 = M_1 / \left(p_{13} \cdot \alpha_T^{\alpha_{13}}\right)$	$c_1 = M_0 \cdot M_1 / \left(p_{13} \cdot \alpha_T^{\alpha_{13}}\right)$
$\beta_3 = \alpha_{13}$	$b_3 = M_1 / \left(p_{11} \cdot \alpha_T^{\alpha_{11}}\right)$	$c_3 = M_0 \cdot M_1 / \left(p_{11} \cdot \alpha_T^{\alpha_{11}}\right)$
$\beta_4 = \alpha_{11} + \alpha_{13}$	$b_4 = 1$	$c_4 = M_0 + M_1$

Table B9: Exponents and coefficients of the Huet-element

Exponents	Stress-coefficients	Strain-coefficients
$\beta_1 = \alpha_{11}$	$b_1 = M_1 / \left(p_{13} \cdot \alpha_T^{\alpha_{13}}\right)$	$c_1 = 0$
$\beta_3 = \alpha_{13}$	$b_3 = M_1 / \left(p_{11} \cdot \alpha_T^{\alpha_{11}}\right)$	$c_3 = 0$
$\beta_4 = \alpha_{11} + \alpha_{13}$	$b_4 = 1$	$c_4 = M_1$

Although the rheological concept adopted by Olard, di Benedetto, Sayegh and Huet and those presented in this paper are identical, the parameters of the rheological models established by Olard, di Benedetto, Sayegh and Huet are different from the parameters used in Table B1 to Table B9. To determine the parameters used in Table B1 to Table B9 from the parameters used by Olard, di Benedetto, Sayegh and Huet, the equations listed in Table B10 and Table B11 may be employed.

Table B10 Parameters used here vs. Olard-, di Benedetto-parameters

2S2P1D	1S2P1D
$M_0 = E_0$	
$M_1 = E_\infty - E_0$	$M_1 = E_\infty$
$\alpha_{12} = h$	$\alpha_{12} = h$
$\alpha_{13} = k$	$\alpha_{13} = k$
$p_{11} = \eta$ with $\eta = \left(E_\infty - E_0\right) \cdot \beta \cdot \tau$ and with $\tau = \alpha_T \cdot \tau_0$	$p_{11} = \eta$ with $\eta = E_\infty \cdot \beta \cdot \tau$ and with $\tau = \alpha_T \cdot \tau_0$
$p_{12} = \left(E_\infty - E_0\right) \cdot \tau^h$ with $\tau = \alpha_T \cdot \tau_0$	$p_{12} = E_\infty \cdot \tau^h$ with $\tau = \alpha_T \cdot \tau_0$
$p_{13} = \dfrac{\left(E_\infty - E_0\right) \cdot \tau^k}{\delta_0}$ with $\tau = \alpha_T \cdot \tau_0$	$p_{13} = \dfrac{E_\infty \cdot \tau^k}{\delta_0}$ with $\tau = \alpha_T \cdot \tau_0$

Table B11 Parameters used here vs. Sayegh- and Huet-parameters

Huet-Sayegh	Huet
$M_0 = E_0$	
$M_1 = E_\infty - E_0$	$M_1 = E_\infty$
$\alpha_{11} = h$	$\alpha_{11} = h$
$\alpha_{13} = k$	$\alpha_{13} = k$
$p_{11} = (E_\infty - E_0) \cdot \tau^h$ with $\tau = \alpha_T \cdot \tau_0$	$p_{11} = E_\infty \cdot \tau^h$ with $\tau = \alpha_T \cdot \tau_0$
$p_{13} = \frac{(E_\infty - E_0) \cdot \tau^k}{\delta_0}$ with $\tau = \alpha_T \cdot \tau_0$	$p_{13} = \frac{E_\infty \cdot \tau^k}{\delta_0}$ with $\tau = \alpha_T \cdot \tau_0$

The parameters used by Olard, di Benedetto, Sayegh and Huet may be interpreted as, E_0, static modulus, E_∞, glassy modulus, η, Newtonian viscosity, τ, characteristic time, τ_0, characteristic time at reference temperature, α_T, temperature shift factor, h, and, k, slopes of the Cole-Cole-graphs at the right and left intersection point (see Section 1.2) and, δ_0, as a material constant.

Re-Road

re-road.fehrl.org

THE RE-ROAD PROJECT aims to develop knowledge and innovative technologies for enhanced end of life strategies for asphalt road infrastructures. Such a strategy has an important impact on the energy efficiency and the environmental footprint of the European transport system and fits within the life-cycle thinking which is being introduced in waste policy at European level. It leads to reduction of the need for new raw materials, prevents the creation of waste and the occupation of landfills and consequently minimizes the need to transport these materials to and from the work site and hence reducing energy, pollution including CO_2-emissions.

PROJECT COORDINATOR
Björn Kalman, VTI
E-MAIL bjorn.kalman@vti.se

EUROPEAN COMMISSION DG RESEARCH
A FP7 Collaborative Project
WORK PROGRAMME Sustainable Surface Transport
SST.2007.1.2.2 End of life strategies for vehicles/ vessels and infrastructures

WORK PACKAGES

WP 1 Sampling and Characterization of RA
Virginie Mouillet

WP 2 Impact of RA quality and characteristics on mix design and performance of asphalt containing RA
Konrad Mollenhauer

WP 3 Environmental performance of RA
Anja Enell

WP 4 RA processing and RA management at the mixing plant
Erik Nielsen

WP 5 Performance modelling of RA
Sabine Werkmeister

RA = Reclaimed asphalt

TECHNISCHE UNIVERSITÄT DRESDEN · ZAG LJUBLJANA · The University of Nottingham UNITED KINGDOM · CHINA · MALAYSIA · SGI · vti · Road Directorate · artesis · CDV CENTRUM DOPRAVNÍHO VÝZKUMU · TRL · IFSTTAR · EAPA European Asphalt Pavement Association · FEHRL · UCD DUBLIN · BRRC · PEAB Peab Asfalt